

Municipal Biosolids Capillary Barrier Covers for Reactive Mine Tailings

A thesis submitted to the Faculty of Graduate and Postdoctoral Affairs
in partial fulfilment of the requirements for the degree of

Master of Applied Science

In

Environmental Engineering

by

Christopher Hey

Department of Civil and Environmental Engineering
Carleton University

Ottawa-Carleton Institute of Civil and Environmental Engineering
Ottawa, Ontario

December 2018

© Christopher Hey

Abstract

This project investigated the use of municipal biosolids as a low-cost, low-permeability material in capillary barrier covers (CBC) for reactive mine tailings.

The biosolids exhibited low saturated hydraulic conductivities ($k = 4.21 \times 10^{-7}$ cm/s @ $e = 4.01$) and an air-entry value of approximately 400 kPa. During laboratory column testing, biosolids layers within the CBCs remained highly saturated, acting as a barrier to oxygen diffusion and water flux. Pore water samples in the tailings of the monolayer cover show elevated concentrations of nitrate, potassium, and sodium relative to CBC columns. No significant change in pH was observed in any of the columns.

Numerical models showed reduction in water flux at the tailings surface by 98% and a reduction in oxygen diffusion by up to three orders of magnitude when using biosolids CBCs relative to uncovered tailings. Cover function was not significantly impacted by the characteristics of the underlying tailings.

Acknowledgements

I could not have undertaken this project, or my career transition from underground mining to environmental engineering without the support of Dr. Paul Simms. To Dr. Simms, your decision to take me on as a graduate student, and to support my research is immensely appreciated. Thank you for your patience and guidance throughout the course of my time at Carleton University.

Thank you to Marie Tudoret, Stan Conley, Jason Arnott, Ken Akhiwu, Richard Kibbee, and Steven Vickers for your patience and guidance in the lab; I couldn't have set up my experiments without you. To Dr. Nimal De Silva and Smita Mohanty, thank you for your help in analyzing ICP samples.

Portions of this project were funded through a Matics Accelerate program; I am grateful for the support of Jeff Newman from Terratec Environmental, Glen Watson and Quenitn Smith at Vale, and Michael Payne at Black Lake Environmental for supporting the Mitacs project.

Thanks to Dr. Suzanne Beauchemin and Dr. Sean Langley at Natural Resources Canada and CANMET Mining for their support in developing this project concept.

I want to thank all of my professors: Dr. Paul Simms, Dr. Banu Ormeci, Dr. Robert Delatolla, Dr. Onita Basu, Dr. Siva Sivathayalan, and Dr. Majid Sartaj for giving me the tools to succeed in an environmental engineering career.

Thank you to my fellow researchers Muhammad Asif Salam, Abdulghader Abdulrahman, Yagmur Babaoglu, and Oswaldo Hurtado for providing advice in running laboratory tests, and to Meagan Morrow, Hirlatu Peruga, David Igbinedion, and Matthieu Poulain for your assistance in testing and data collection. Thank you to all of my fellow students who made class and life at school a great experience.

Dedication

To my parents, my brother, and to Samantha: thank you for supporting my decision to return to school and pursue my passions, and for helping me navigate through this project and career change.

Table of Contents

| | |
|------------------------------------------------------------------------------------------------------|-------------|
| ABSTRACT | II |
| ACKNOWLEDGEMENTS..... | III |
| DEDICATION | IV |
| TABLE OF CONTENTS | V |
| LIST OF TABLES | VIII |
| LIST OF FIGURES | IX |
| LIST OF ABBREVIATIONS..... | XV |
| CHAPTER 1 : INTRODUCTION, BACKGROUND AND OBJECTIVES | 1 |
| 1.1 ACID ROCK DRAINAGE IN THE MINING INDUSTRY | 1 |
| 1.2 OVERVIEW OF THE RESEARCH PROJECT | 3 |
| 1.3 SCOPE OF RESEARCH AND OBJECTIVES..... | 3 |
| 1.4 THESIS OUTLINE | 5 |
| 1.5 NOVELTY OF THE THESIS..... | 6 |
| CHAPTER 2 : LITERATURE REVIEW..... | 7 |
| 2.1 HARD ROCK MINE TAILINGS | 7 |
| 2.1.1 <i>Tailings Deposition</i> | 13 |
| 2.1.1.1 Grain-Size Segregation | 14 |
| 2.1.1.2 Consolidation..... | 17 |
| 2.2 MUNICIPAL BIOSOLIDS | 19 |
| 2.2.1 <i>Wastewater Treatment Processes</i> | 20 |
| 2.2.2 <i>Sludge Treatment Processes</i> | 24 |
| 2.3 ARD IN TAILINGS AND ITS MANAGEMENT | 28 |
| 2.3.1 <i>Acid Rock Drainage Overview</i> | 28 |
| 2.3.1.1 Oxidation-Reduction Potential | 30 |
| 2.3.1.2 Oxygen Diffusion | 31 |
| 2.3.1.3 Oxygen transport in porous media & Fick’s Law | 31 |
| 2.3.2 <i>Technologies to control ARD in mine tailings</i> | 34 |
| 2.3.2.1 Water Covers..... | 34 |
| 2.3.2.2 Soil Covers | 35 |
| 2.3.2.2.1 Monolayer Covers with an Elevated Water Table..... | 35 |
| 2.3.2.2.2 Multilayer Covers – Infiltration Barriers..... | 36 |
| 2.3.2.2.3 Multilayer Covers – Store and Release..... | 37 |
| 2.3.2.2.4 Multilayer Covers - Capillary Barrier Covers | 38 |
| 2.3.3 <i>Organic Covers</i> | 41 |
| 2.4 AN UNSATURATED FLOW THEORY FRAMEWORK | 46 |
| 2.4.1 <i>Theory of Water Flow Through Porous Media</i> | 46 |
| 2.4.2 – <i>Darcy’s Law and Flow Through Saturated Soils</i> | 46 |
| 2.4.3 – <i>Hydraulic Conductivity in Unsaturated Soils</i> | 48 |
| 2.5 SOIL SUCTION THEORY..... | 49 |
| 2.5.1 – <i>Total Suction</i> | 49 |
| 2.5.2 – <i>Matric Suction</i> | 50 |
| 2.5.3 – <i>Osmotic Suction</i> | 52 |
| 2.6 WATER CONTENT – SUCTION, SATURATION – SUCTION, AND VOID RATIO –WATER CONTENT RELATIONSHIPS | 54 |

| | | |
|------------------|----------------------------------------------------------------------------------------|------------|
| 2.6.1 | <i>Hysteresis and factors affecting the Water Retention Function</i> | 56 |
| 2.6.2 | <i>Evaporation</i> | 63 |
| CHAPTER 3 | : MATERIAL CHARACTERIZATION AND EXPERIMENTAL PROCEDURES | 65 |
| 3.1 | PHYSICAL CHARACTERIZATION OF COVER MATERIALS | 65 |
| 3.1.1 | <i>Specific Gravity</i> | 67 |
| 3.1.2 | <i>Particle Size / Grain Size Distribution of Fresh Tailings and Oxidized Tailings</i> | 68 |
| 3.1.2.1 | Particle Size Distribution from Sieve Testing | 68 |
| 3.1.2.2 | Particle Size Distribution from Hydrometer Testing | 69 |
| 3.1.3 | <i>Gravimetric Water Content and Solids Content</i> | 71 |
| 3.1.4 | <i>Volumetric Water Content</i> | 72 |
| 3.1.5 | <i>Degree of Saturation</i> | 72 |
| 3.1.5.1 | Saturated Water Content | 73 |
| 3.1.6 | <i>Void Ratio and Porosity</i> | 74 |
| 3.1.7 | <i>Total Volatile Solids of Biosolids Amendment Materials</i> | 74 |
| 3.1.8 | <i>Atterberg Limits – Plastic Limit and Liquid Limit</i> | 75 |
| 3.1.8.1 | Plastic Limit | 77 |
| 3.1.8.2 | Liquid Limit | 77 |
| 3.1.8.3 | Plasticity Index | 77 |
| 3.1.9 | <i>– Compaction & Optimum Water Content</i> | 77 |
| 3.1.10 | <i>Saturated Hydraulic Conductivity</i> | 78 |
| 3.1.10.1 | Constant Head Test | 79 |
| 3.1.10.2 | Falling Head Test | 80 |
| 3.2 | DEVELOPING WATER RETENTION CURVES | 81 |
| 3.2.1 | <i>Total Suction Measurements</i> | 82 |
| 3.2.1.1 | Filter Paper Method for Total Suction Measurement | 82 |
| 3.2.1.2 | Chilled Mirror Dewpoint Hygrometer | 85 |
| 3.2.2 | <i>Matric Suction Measurements</i> | 86 |
| 3.2.2.1 | Pressure Extraction and Axis Translation | 86 |
| 3.2.2.1.1 | Displacement Sensor Calibration | 89 |
| 3.2.2.1.2 | Porous Ceramic Verification | 90 |
| 3.2.2.2 | Filter Paper Method for Matric Suction Measurement | 92 |
| 3.2.3 | <i>Osmotic Suction Measurements</i> | 92 |
| 3.2.3.1 | <i>Saturation Extract Method Electrical Conductivity</i> | 93 |
| CHAPTER 4 | : MATERIAL CHARACTERIZATION RESULTS AND DISCUSSION | 95 |
| 4.1 | SOIL-WATER CHARACTERISTIC CURVES AND WATER RETENTION PROPERTIES OF COVER MATERIALS | 97 |
| CHAPTER 5 | : COLUMN TESTING | 104 |
| 5.1 | SOIL COLUMN SETUP | 104 |
| 5.1.1 | <i>Column Design and Specifications</i> | 104 |
| 5.1.2 | <i>Instrumentation and Sensor Calibration</i> | 107 |
| 5.1.3 | <i>Simulated Boundary Conditions</i> | 110 |
| 5.1.4 | <i>Initial Conditions</i> | 111 |
| 5.1.5 | <i>Column Flushing</i> | 112 |
| 5.2 | COLUMN TEST RESULTS | 113 |
| 5.2.1 | <i>Initial Drying Period Results</i> | 114 |
| 5.2.2 | <i>Column Flushing Results</i> | 121 |
| 5.2.3 | <i>Post-Flush Drying Results</i> | 124 |
| 5.2.4 | <i>Pore-Water Quality Results</i> | 125 |
| 5.2.4.1 | Pore water metals and nutrient analysis | 133 |
| 5.2.5 | <i>Additional Results and Observations from Column Testing</i> | 138 |

| | |
|--------------------------------------------------------------------------------------|------------|
| 5.2.5.1 Column Deconstruction..... | 147 |
| 5.3 COLUMN TESTING DISCUSSION | 149 |
| 5.3.1 Volumetric Water Content..... | 149 |
| 5.3.2 Suction Profiles | 151 |
| 5.3.3 Pore Water Quality Profiles | 151 |
| 5.3.3.1 pH Profiles | 151 |
| 5.3.3.2 Electrical Conductivity Profiles | 152 |
| 5.3.3.3 ORP Profiles | 153 |
| 5.3.3.4 Metal Cation Concentration Profiles | 153 |
| 5.3.3.5 Nutrient Anion Concentration Profiles..... | 155 |
| 5.3.4 Key Findings from Column Testing..... | 156 |
| CHAPTER 6 : UNSATURATED FLOW MODELLING | 157 |
| 6.1 ONE-DIMENSIONAL MODEL PARAMETERS | 157 |
| 6.1.1 Model Dimensions | 157 |
| 6.1.2 Material Properties..... | 158 |
| 6.1.2.1 Initial Volumetric Water Content | 161 |
| 6.1.3 Boundary Conditions..... | 162 |
| 6.1.3.1 Climate Boundary | 162 |
| 6.1.3.1.1 Calculating Potential Evaporation and Calibrating Evaporation Inputs | 162 |
| 6.1.3.1.2 Calculating Actual Evaporation | 165 |
| 6.1.3.2 Constant Head Boundary | 167 |
| 6.1.4 MODEL CALIBRATION, RESULTS, AND DISCUSSION..... | 167 |
| 6.1.4.1 SV-Flux Calibration to Laboratory Column Results..... | 168 |
| 6.1.4.2 Modelling of Secondary Drying Period..... | 171 |
| 6.1.5 Simulated Cover Functionality | 174 |
| 6.1.5.1 Simulated Weather Condition Results..... | 174 |
| 6.1.5.1.1 Comparison of Cover Configuration..... | 175 |
| 6.1.5.1.2 Comparison of Cover Materials..... | 183 |
| 6.1.5.2 Simulated Extreme Drying Condition Results..... | 187 |
| 6.1.5.3 Model Input Sensitivity..... | 188 |
| CHAPTER 7 : SUMMARY AND CONCLUSIONS | 196 |
| 7.1 SUMMARY..... | 196 |
| 7.2 CHARACTERIZATION | 196 |
| 7.3 COLUMN TESTS | 196 |
| 7.3.1 Saturation and water flux..... | 196 |
| 7.3.2 Pore water analysis..... | 196 |
| 7.4 MODELLING..... | 197 |
| 6.5 OTHER FINDINGS | 197 |
| CHAPTER 8 : RECOMMENDATIONS FOR FUTURE WORK..... | 198 |
| REFERENCES | 199 |
| APPENDIX A – MATERIAL CHARACTERIZATION DATA AND RESULTS | 209 |
| APPENDIX B – COLUMN TESTING PARAMETERS, DATA, AND RESULTS | 220 |
| APPENDIX C – NUMERICAL MODELLING ADDENDA..... | 224 |

List of Tables

| | |
|------------------------------------------------------------------------------------------------|-----|
| Table 2-1. Mineralogy of Vale pyrrhotite tailings from X-Ray Diffraction analysis | 9 |
| Table 2-2. Liberation and exposure of Vale pyrrhotite tailings | 10 |
| Table 2-3. Canadian Federal wastewater sewage effluent regulations | 20 |
| Table 2-4. Typical domestic wastewater influent values | 20 |
| Table 2-5. Sludge disposal in selected countries of the European Union in 2013..... | 28 |
| Table 2-6. Permeability of major soil groups | 47 |
| Table 3-1. Summary of Experimental Protocols | 66 |
| Table 3-2. Suction measurement methods used for generation of WRC..... | 82 |
| Table 3-3. Calibrated conversion factor from mA to mm for NCDS readings | 90 |
| Table 3-4. Specifications for 5 bar porous ceramic discs used in pressure extraction technique | 91 |
| Table 4-1. Summary of material characterization test results | 95 |
| Table 4-2. Cover material water retention properties obtained from SWCC | 100 |
| Table 5-1. Port height and corresponding measurement or sampling horizon | 105 |
| Table 5-2. 5TE sensor calibration curve parameters for different soil types | 109 |
| Table 5-3. Column layer elevations, materials, and initial water content..... | 112 |
| Table 5-4. Gravimetric water content of surface samples from Column B biosolids surface ... | 118 |
| Table 5-5. Layer thickness change observed during flush period | 140 |
| Table 6-1. Cover configurations modelled in SV-Flux..... | 158 |
| Table 6-2. Scenarios initially modelled in SV-Flux | 174 |
| Table 6-3. Modelled cover nomenclature | 175 |

List of Figures

| | |
|------------------------------------------------------------------------------------------------------------------------------------------------------------------------------------------------------------|----|
| Figure 1-1. Global production of zinc, copper, and aluminum from 1900–2012 | 1 |
| Figure 2-1. Simplified flow-chart of a mineral processing operation in which ore is processed to yield an ore mineral concentrate and tailings..... | 8 |
| Figure 2-2. Particle Size distribution of Sudbury area pyrrhotite tailings from Vale & Glencore operations | 9 |
| Figure 2-3. Ore fragmentation and mineral liberation showing surface area exposure for the various ore materials within tailings particles..... | 10 |
| Figure 2-4. Backscattered electron images highlighting pyrite (Py) and arsenopyrite (Apy) particles and secondary goethite (Gt) alteration in tailings from the Delnite gold mine..... | 11 |
| Figure 2-5. Visualization of sulfide-mineral oxidation by diffusion of oxygen into tailings pore space (A), and subsequent diffusion of oxygen into tailings grains (B)..... | 12 |
| Figure 2-6. Image of pyrrhotite tailings grain from a backscattered electron microscope showing alterations from innermost layer of native sulfur surrounded by sulfur and sulphate bearing goethite | 13 |
| Figure 2-7. Hydraulic tailings deposition showing spigots with formation of a beach and decant pond | 14 |
| Figure 2-8. Particle size distribution of tailings sampled at the same depth (7-8m) but at varying distance from the discharge point (distance in meters shown as “/XX”)..... | 15 |
| Figure 2-9. Grain-size segregation observed in analyzed cross section | 15 |
| Figure 2-10. Conceptual variation in permeability along a cross section of a tailings beach..... | 16 |
| Figure 2-11. Grain-size distribution of copper tailings at sampled at various depths..... | 16 |
| Figure 2-12. Conceptualization of soil volume and mass in (a) natural state, and (b) partitioned by phases of solids, water, and air | 17 |
| Figure 2-13. Stages of consolidation in typical soil samples | 18 |
| Figure 2-14. Tailings profiles with depth for void ratio (A), Bulk density (B), and Sand to Fines Ratio (C)..... | 19 |
| Figure 2-15. Typical wastewater treatment process..... | 21 |
| Figure 2-16. Microbial growth patterns in a batch reactor | 22 |
| Figure 2-17. Activated sludge treatment schematic | 23 |
| Figure 2-18. Unit processes available for sludge treatment | 25 |
| Figure 2-19. Anaerobic conversion of wastewater organics to byproducts..... | 26 |
| Figure 2-20. Mid-Halton wastewater treatment plant schematic..... | 27 |
| Figure 2-21. Pourbaix diagram of iron in water showing change of oxidizing and reducing conditions with variation in pH | 30 |
| Figure 2-22. The relationship between soil saturation and the calculated effective oxygen diffusion coefficient..... | 33 |
| Figure 2-23. Conceptual model of an elevated water table within reactive tailings for reducing acid rock drainage | 35 |
| Figure 2-24. Example of a multilayer cover designed with a saturated barrier layer | 37 |
| Figure 2-25. Degree of Saturation profile in a simulated capillary barrier cover | 38 |

| | |
|--------------------------------------------------------------------------------------------------------------------------------------------------------------------------------------------------------------------------------------------------|----|
| Figure 2-26. Schematic showing hydraulic functions of a silt (fine grained soil) and sand (coarse grained soil)..... | 39 |
| Figure 2-27. Density of Lolium perenne var.nui plants on experimental treatments. | 42 |
| Figure 2-28. Metal concentrations in shoots of red fescue grown in control plots (white bars) and in plots treated with sewage sludge (grey bars) | 44 |
| Figure 2-29. Copper and zinc contents in shoots of Lolium perenne var. nui plants on experimental treatments. | 45 |
| Figure 2-30. Forces acting on capillary tube..... | 50 |
| Figure 2-31. Physical model of capillarity..... | 51 |
| Figure 2-32. Presence of ions affecting partial pressure of water in soil pore spaces (b) compared to pure water in pore space (a)..... | 53 |
| Figure 2-33. Pressure difference induced by osmotic suction across a semi-permeable membrane | 54 |
| Figure 2-34. Typical Water Retention Curve (drying and wetting path) for a fine-grained soil ... | 55 |
| Figure 2-35. Illustration of hysteresis as a result of changes in pore space distribution after drying | 57 |
| Figure 2-36. SWCC for a silty sand at two levels of compaction | 58 |
| Figure 2-37. SWCC for till compacted to OWC | 59 |
| Figure 2-38. Soil-water characteristics for specimens compacted at different initial water contents | 60 |
| Figure 2-39. Effect of Stress State on SWCC..... | 61 |
| Figure 2-40. Shrinkage curve and volume-mass relation for slurry soil | 62 |
| Figure 2-41. Relationship between actual evaporation and potential evaporation with changing soil saturation..... | 64 |
| Figure 3-1. Vale Copper Cliff Tailings Area | 66 |
| Figure 3-2. Soil hydrometer bulb dimensions | 70 |
| Figure 3-3. Fall cone test results showing liquid limit and plastic limit of Leaf and Yard Waste.. | 76 |
| Figure 3-4. Data regression at water contents above inflection point to determine Atterberg limits (test data for unoxidized tailings) | 76 |
| Figure 3-5. Permeameter used for constant and falling head tests..... | 78 |
| Figure 3-6. Constant head test permeameter and reservoir setup..... | 79 |
| Figure 3-7. Experimental setup for suction equilibration in total and matric suction filter paper tests..... | 83 |
| Figure 3-8. Calibration curve for suction determination using Whatman 42 filter paper compared to calibration curve provided in ASTM document. | 84 |
| Figure 3-9. Chilled mirror dew point hygrometer internal sensor block..... | 86 |
| Figure 3-10. Pressure extractor vessel schematic and photograph | 87 |
| Figure 3-11. Calibration of NCDS using bench micrometer..... | 89 |
| Figure 3-12. Electrical conductivity and total suction as a function of NaCl concentration in water | 93 |
| Figure 4-1. Particle size distribution of cover materials..... | 96 |
| Figure 4-2. Combined results of Hanging Column (Method A), Porous Plate Pressure Extraction (Method B), and Chilled Mirror Hygrometer (Method D) to construct a soil-water characteristic curve spanning a large range of suction pressures..... | 97 |

| | |
|------------------------------------------------------------------------------------------------------------------------------------------------------------------------------------------------------------|-----|
| Figure 4-3. Soil-water characteristic curve for characterized cover materials (volumetric water content on y-axis)..... | 98 |
| Figure 4-4. Soil-water characteristic curve for characterized cover materials (degree of saturation on y-axis)..... | 99 |
| Figure 4-5. SWCCs of cover materials showing potential establishment of capillary barrier at elevated suctions with desaturated sand layer and saturated biosolids in agreement with conceptual model..... | 100 |
| Figure 4-6 . Shrinkage curve for pre-oxidized tailings from axis translation test results | 101 |
| Figure 4-7. Shrinkage curve of municipal biosolids from weighed, measured, and dried cubes | 102 |
| Figure 5-1. Column schematic indicating layer thicknesses from the column bases for the Capillary Barrier and Monolayer Covers. | 105 |
| Figure 5-2. Schematic indicating column instrumentation type, elevations, and locations..... | 106 |
| Figure 5-3. Photograph of instrumented columns at start of test period..... | 107 |
| Figure 5-4. 5TE sensor volumetric water content calibration curve for unoxidized tailings | 109 |
| Figure 5-5. Volumetric water content profile of Column A (calibrated) | 114 |
| Figure 5-6. Calculated saturation profile for Column A..... | 115 |
| Figure 5-7. Volumetric water content profile of Column B (calibrated)..... | 115 |
| Figure 5-8. Electrical Conductivity profile of Column B from 5TE sensors | 116 |
| Figure 5-9. Calculated saturation profile of Column B | 116 |
| Figure 5-10. Cracking observed in the surface of the CRM biosolids in monolayer cover of Column B | 117 |
| Figure 5-11. Biosolids monolayer shrinkage and separation from walls of Column B | 117 |
| Figure 5-12. Volumetric Water content profile of Column C (calibrated)..... | 120 |
| Figure 5-13. Saturation Profile of Column C (calibrated) | 120 |
| Figure 5-14 - A. Volumetric water content profile of Column A throughout flush period (calibrated) | 122 |
| Figure 5-15. Volumetric water content profile of Column B throughout flush period (calibrated) | 122 |
| Figure 5-16. Volumetric water content profile of Column C throughout flush period (calibrated) | 123 |
| Figure 5-17. Volumetric Water Content profile of Column C at start of flush period (calibrated) | 123 |
| Figure 5-18. Drying of monolayer cover biosolids throughout duration of column testing..... | 125 |
| Figure 5-19. Electrical conductivity profile in Column A measured from pore water samples.. | 126 |
| Figure 5-20. Electrical conductivity profile in Column A reported by 5TE sensors..... | 126 |
| Figure 5-21. Electrical conductivity profile in Column B measured from pore water samples .. | 127 |
| Figure 5-22. Electrical conductivity profile in Column B reported by 5TE sensors..... | 127 |
| Figure 5-23. Electrical conductivity profile of Column C measured from pore water samples.. | 128 |
| Figure 5-24. Electrical conductivity profile of Column C reported by 5TE sensors | 128 |
| Figure 5-25. pH profile in Column A | 129 |
| Figure 5-26. pH profile of Column B | 130 |
| Figure 5-27. pH profile of Column C | 131 |
| Figure 5-28. ORP profile of Column A | 131 |
| Figure 5-29. ORP profile of Column B..... | 132 |

| | |
|-------------------------------------------------------------------------------------------------------------------------------------------------------------------------------------------------|-----|
| Figure 5-30. ORP profile of Column C..... | 132 |
| Figure 5-31. Concentration profiles for cations and anions throughout test duration..... | 138 |
| Figure 5-32. Suction profile in Column A measured by Teros 21 sensors throughout test duration..... | 139 |
| Figure 5-33. Suction profile in Column B measured by Teros 21 sensors throughout test duration..... | 139 |
| Figure 5-34. Suction profile in Column C measured by Teros 21 sensors throughout test duration..... | 140 |
| Figure 5-35. Volumetric Water Content profile of Column A throughout column test duration reported by 5TE sensors without calibration adjustment..... | 141 |
| Figure 5-36. Volumetric Water Content profile of Column A throughout column test duration reported by 5TE sensors adjusted using determined calibration curves..... | 141 |
| Figure 5-37. Volumetric Water Content profile of Column B throughout column test duration reported by 5TE sensors without calibration adjustment..... | 142 |
| Figure 5-38. Volumetric Water Content profile of Column B throughout column test duration reported by 5TE sensors adjusted using determined calibration curves..... | 142 |
| Figure 5-39. Volumetric Water Content profile of Column C throughout column test duration reported by 5TE sensors without calibration adjustment..... | 143 |
| Figure 5-40. Volumetric Water Content profile of Column C throughout column test duration reported by 5TE sensors adjusted using determined calibration curves..... | 143 |
| Figure 5-41. Paired VWC and Suction readings in the sand layers of laboratory columns overlying the characterized sand SWCC..... | 144 |
| Figure 5-42. Paired VWC and Suction readings in the unoxidized tailings of laboratory column C overlying the characterized unoxidized tailings SWCC..... | 145 |
| Figure 5-43. Paired VWC and Suction readings in the pre-oxidized tailings of laboratory columns A & B overlying the characterized pre-oxidized tailings SWCC..... | 145 |
| Figure 5-44. Paired VWC and Suction readings in the CRM biosolids of laboratory columns A, B, and C overlying the characterized CRM biosolids SWCC..... | 146 |
| Figure 5-45. Advection of biosolids particles within the pore spaces of the pre-oxidized tailings in monolayer cover of Column B indicating slight preferential flow along the column wall..... | 147 |
| Figure 5-46. Water content profiles of Column A from soil sampling during deconstruction ... | 148 |
| Figure 5-47. Water content profiles of Column B from soil sampling during deconstruction ... | 148 |
| Figure 5-48. Water content profiles of Column C from soil sampling during deconstruction ... | 148 |
| Figure 5-49. Surface crust formation in the CRM biosolids of the monolayer Column B..... | 150 |
| Figure 6-1. SV-Flux 1-D CBC column model setup..... | 158 |
| Figure 6-2. Fredlund-Xing fit used in SV-Flux modelling of pre-oxidized tailings..... | 159 |
| Figure 6-3. Brooks-Corey fit for determining unsaturated hydraulic conductivity calculation parameters of unoxidized tailings..... | 160 |
| Figure 6-4. Fredlund-Xing-Huang function of unsaturated hydraulic conductivity used in SV-Flux for unoxidized tailings..... | 161 |
| Figure 6-5. Sensitivity of Potential Evaporation calculation to various parameters..... | 165 |
| Figure 6-6. Calculation of AE/PE using Modified Wilson Limiting Equation relative to measurements in various soil types..... | 167 |

| | |
|-----------------------------------------------------------------------------------------------------------------------------------------------------------------------------------------------------------------------------------------|-----|
| Figure 6-7 . Calibration of boundary conditions applied to simulation of Laboratory Column A in SV-Flux. -2m constant head boundary applied (a), and no-flux boundary condition (b). ... | 169 |
| Figure 6-8. Column A Model results overlaid on initial drying profiles. Adjusted VWC (a) and unadjusted VWC values (b). | 170 |
| Figure 6-9. Column B Model results overlaid on initial drying profiles. Adjusted VWC (a) and unadjusted VWC values (b) | 170 |
| Figure 6-10. Column C Model results overlaid on initial drying profiles. Adjusted VWC (a) and unadjusted VWC values (b) | 170 |
| Figure 6-11. Matric Suction profiles for Column A (a) and Column C (b) from SV Flux modelling of initial drying period | 171 |
| Figure 6-12. Volumetric Water Content profile of Column A with original hydraulic conductivity (a) and a lowered hydraulic conductivity (b)..... | 172 |
| Figure 6-13. Volumetric Water Content profile of Column B with original hydraulic conductivity (a) and a lowered hydraulic conductivity creating a drying front (b)..... | 172 |
| Figure 6-14. Volumetric Water Content profile of Column C with original hydraulic conductivity (a) and a lowered hydraulic conductivity (b)..... | 173 |
| Figure 6-15. Saturation profile of Cover CBC-1A | 176 |
| Figure 6-16. Saturation profile of Cover Mono-1A..... | 176 |
| Figure 6-17. Reported flux at the sand/tailings interface of Cover CBC-1A | 177 |
| Figure 6-18. Reported flux at the biosolids/tailings interface of Cover Mono-1A | 177 |
| Figure 6-19. Flux at the tailings surface when no cover is applied over pre-oxidized tailings and -2m constant head boundary at the base of the tailings..... | 178 |
| Figure 6-20. Saturation profile of Cover TBS-1A | 179 |
| Figure 6-21. Reported flux at the biosolids/tailings interface of Cover TBS-1A | 179 |
| Figure 6-22. Saturation profile of Cover CBC-1B | 180 |
| Figure 6-23. Saturation profile of Cover Mono-1B..... | 180 |
| Figure 6-24. Flux at the tailings interface of Cover CBC-1B..... | 181 |
| Figure 6-25. Flux at the tailings interface of Cover Mono-1B..... | 181 |
| Figure 6-26. Saturation profile of Cover TBS-1B..... | 182 |
| Figure 6-27. Flux at the tailings interface of Cover TBS-1B | 183 |
| Figure 6-28. Saturation profile of TA-ML..... | 184 |
| Figure 6-29. Flux at the tailings interface of Cover TA-ML | 184 |
| Figure 6-30. Saturation profile of Cover TA-1B | 185 |
| Figure 6-31. Flux at the tailings interface in Cover TA-1B | 186 |
| Figure 6-32. Flux at the tailings interface in Cover TA-1A | 186 |
| Figure 6-33. Comparison of saturation profiles for CRM biosolids CBC with -20m constant head boundary at the base of the pre-oxidized tailings. Precipitation applied (a) compared to extreme drying conditions (b). | 187 |
| Figure 6-34. Comparison of saturation profiles for CRM monolayer covers with -20m constant head boundary at the base of the pre-oxidized tailings. Precipitation applied (a) compared to extreme drying conditions (b)..... | 187 |
| Figure 6-35. Saturation profile of CBC covers with identical inputs (-2m constant head boundary at base), with the exception of initial saturation conditions. Unsaturated (a) compared to initial Fully Saturated (b) conditions. | 188 |

Figure 6-36. Flux at the tailings interface for identical CBC covers (-2m constant head boundary at base of tailings) with unsaturated initial conditions and fully saturated initial conditions. 189

Figure 6-37. Saturation profile of CBC covers with identical inputs (-20m constant head boundary at base), with the exception of initial saturation conditions. Unsaturated (a) compared to initial Fully Saturated (b) conditions. 189

Figure 6-38. Flux at the tailings interface for identical CBC covers (-20m constant head boundary at base of tailings) with unsaturated initial conditions and fully saturated initial conditions 190

Figure 6-39. Comparison of CBC saturation profiles with unoxidized tailings (a) and pre-oxidized tailings (b) with a -2m constant head boundary at the base of the tailings..... 191

Figure 6-40. Flux at the tailings interface in a CBC cover with CRM biosolids and a -2m constant head boundary at the tailings base 191

Figure 6-41. Comparison of saturation profiles of CBCs using CRM biosolids with a -20m constant head boundary at the base of the tailings layer 192

Figure 6-42. Water flux at the tailings interface of CBCs using CRM biosolids with a -20m constant head boundary with covers placed over pre-oxidized and unoxidized tailings... 192

Figure 6-43. Comparison of saturation profiles of monolayer covers using CRM biosolids with a -2m constant head boundary at the base of the tailings layer 193

Figure 6-44. Comparison of water flux at the tailings interface when using a monolayer CRM cover with a -2m constant head boundary at the base of the tailings..... 193

Figure 6-45. Comparison of saturation profiles of monolayer covers using CRM biosolids with a -20m constant head boundary at the base of the tailings layer 194

Figure 6-46. Comparison of flux at the tailings interface for monolayer cover over unoxidized and pre-oxidized tailings using CRM biosolids with a -20m constant head boundary at the base of the tailings 194

List of Abbreviations

AOB – Ammonia Oxidizing Bacteria
AEV – Air-Entry Value
ARD – Acid rock drainage
BOD - Biological oxygen demand
CBC – Capillary barrier cover
CBOD – Carbonaceous Biochemical Oxygen Demand
COD - Carbonaceous oxygen demand
CRM – Custom Reclamation Mix
DO – Dissolved Oxygen
DTPA - Diethylenetriaminepentaacetic Acid
EPA – Environmental Protection Agency
LL – Liquid Limit
MEND – Mine Environment Neutral Drainage
ORP – Oxidation-Reduction potential
OWC – Optimum Water Content
PAO – Phosphorous Accumulating Organisms
PHA - Poly-Hydroxyalkanoates
PL – Plastic Limit
SEM - Scanning electron microscope
SWCC – Soil-Water Characteristic Curve
TS – Total solids
VS – Volatile Solids
WRC – Water Retention Curve
WSER - Wastewater Sewage Effluent Regulations

Chapter 1 : Introduction, Background and Objectives

1.1 Acid Rock Drainage in the Mining Industry

Mining and mineral processing play a significant role in the Canadian economy; in 2016 minerals and mineral products accounted for 19% of total domestic exports (“Minerals and metals facts | Natural Resources Canada,” n.d.). Globally the demand for minerals and metals continue to grow as shown in Figure 1-1.

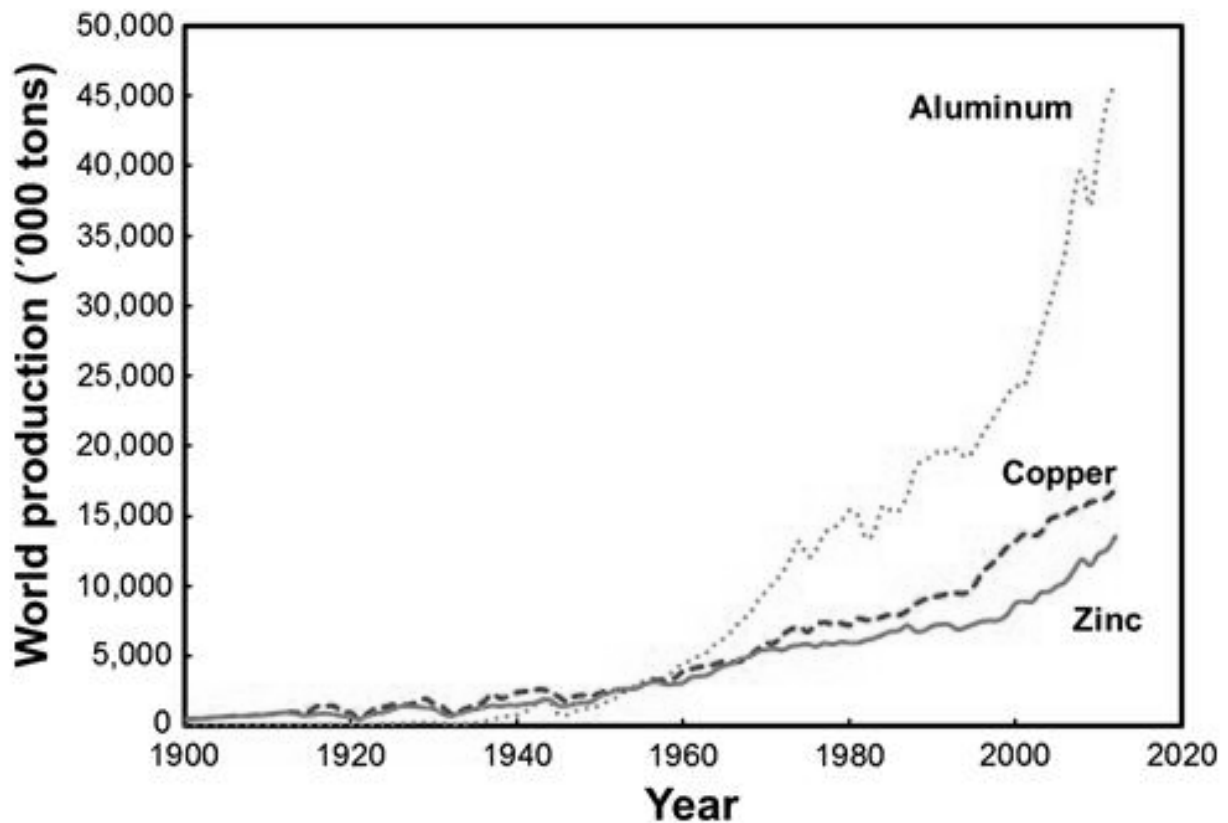


Figure 1-1. Global production of zinc, copper, and aluminum from 1900–2012 (Wills & Finch, 2015)

Waste rock and residual material from mineral processing, referred to as mine tailings, are produced on an extraordinary scale, often representing fifty to ninety-eight percent of total material extracted during mining, depending on the type of ore extracted (Nagaraj, 2005). The country of Chile at one time produced an estimated 1 MT of tailings per day (Villavicencio, Espinace, et al., 2014).

Extraction of metals through mining and mineral processing produces large quantities of waste materials in the form of waste rock and tailings. Waste rock refers to the rock removed in order to access metal and mineral bearing ores and is generally unprocessed waste material resulting from blasting operations. Tailings refer to the gangue waste created through crushing, grinding, and separation processes. Crushing is used to reduce blasted ore to 5-20 cm in size, while subsequent grinding and milling further reduces particles sizes to 10-100 μm , which corresponds to the typical size of hard rock tailings particles. For hydraulic transportation and deposition of tailings slurries, the water content of the tailings is in the range 150 to 100 per cent by mass of dry solids. The corresponding relative density for the slurry is between 1.3 to 1.5 (Blight & Bentel, 1983). The wastes of further metallurgical processes to extract metals are referred to as slag or leached ores. Waste rock, leached ores, slag, and tailings all have the potential to create acidic conditions depending on their chemical composition and exposure to oxidizing conditions.

Acid Rock drainage (ARD) refers to the generation of low pH conditions in tailings soil matrices and mine waters, and results from the oxidation of sulfide minerals (Singer & Stumm, 1970). Due to the volumes of mine wastes generated, the potential negative effects of acid generation on surrounding communities and ecosystems are significant. Environmental impacts of ARD include acidification of aquatic ecosystems, generation of airborne tailings dusts, and mobilization of heavy metals in soil leading to potential bio-accumulation in ecosystem food-chains. The deleterious effects of ARD arise from the discharge and disposal of water contaminated with solids, heavy metals, sulfur compounds, and mill reagents (Chalkley, 1989). It is estimated that total worldwide liability related to ARD exceeds \$10 billion USD. Source control of sulphide oxidation limits the generation of ARD, and subsequently reduces the costs associated with later treatment (Lottermoser, 2007).

ARD can be controlled by limiting availability of oxygen which reduces the acid produced by tailings oxidation. The minimization of oxygen available for tailings oxidation can be achieved by either submerging the tailings below a suitable depth of water, or by constructing a solid soil cover which limits the ingress of precipitation and diffused oxygen through to the tailings (Elberling, Nicholson, et al., 1994).

Several methods exist for construction of soil covers to mitigate acid rock drainage. Capillary barrier covers utilize differences in the water retention properties of layered cover materials to maintain a saturated barrier layer which prevents oxygen transport through to the tailings, limiting oxidation reactions and acid generation (Yanful 1993).

1.2 Overview of the research project

This research project seeks to determine if municipal biosolids may be used to replace costly clay and geotextile materials as the oxygen impermeable layer in capillary barrier covers. Utilizing biosolids instead of clays would provide an additional means of biosolids disposal for municipalities, and divert valuable carbon and nutrient materials from landfills. Using biosolids may eliminate the need to disturb sites to source clay, and can reduce the overall cost of cover construction by providing a low cost and easily deployed material.

Tailings from the Vale Copper Cliff Tailings Facility have been obtained with samples of both a freshly deposited and weathered tailings material. Municipal biosolids from the region of Halton, and biosolids mixed with Leaf & Yard waste from Sudbury were also obtained. All materials were characterized in order to develop soil-water characteristic curves; these properties were used in computer simulation of cover configurations. Column tests of selected cover configurations were used to prove the effectiveness of the biosolids in creating a capillary barrier cover at a laboratory scale, and to calibrate numerical models for further simulation.

1.3 Scope of Research and Objectives

The objectives of this project are to:

1. Evaluate the hydrogeological characteristics of municipal biosolids for use in engineered soil cover applications.
2. Assess the effectiveness of municipal biosolids in maintaining saturation and controlling water flux in engineered capillary barrier soil covers.

3. Determine the suitability of municipal biosolids as a replacement for conventional low permeability materials (such as clays) in the construction of capillary barrier covers for reactive mine tailings to limit oxygen diffusion and water flux through the cover.

In order to achieve these objectives, the following experimental work was performed:

1. Characterization tests of municipal biosolids and amended biosolids mixes, unoxidized and pre-oxidized tailings, and sand. These included specific gravity, Atterberg limits, saturated hydraulic conductivity, grain size distribution.
2. Development of soil-water characteristic curve and shrinkage curves for biosolids and cover materials by conducting axis translation, filter paper, and dewpoint hygrometer tests.
3. Column testing of capillary barrier covers and a monolayer cover over tailings to observe physical water retention properties, suction development, and water quality throughout column profiles.
4. Numerical model calibration with laboratory results to develop predictive capability for assessing hypothetical cover application in field situations. Simulated “what if” scenarios utilized calibrated model parameters to assess effectiveness of biosolids covers to mitigate oxygen diffusion and water flux under varying applied conditions.

The project is limited in scope to establishing proof of concept for use of municipal biosolids in capillary barrier covers. The project does not examine the ageing and decomposition of biosolid materials, or the effects of vegetation on the efficacy of the cover. The project does not evaluate lateral transport within the cover or the effects of erosion on cover integrity. The interaction between tailings and biosolids is only evaluated by assessing water quality within the cover as measured by pH, nutrient content, and metals concentrations. The effects of hysteresis, and freezing and thawing on covers are not investigated.

1.4 Thesis Outline

The outline of this thesis is presented below:

Chapter Two: Literature Review – This section briefly describes the generation hard rock mine tailings and acid rock drainage, as well as the generation and processing of municipal biosolids. A review of existing acid rock drainage mitigation practices and the theory of flow in unsaturated soils is presented.

Chapter Three: Material Characterization and Experimental Procedures – This section describes the laboratory characterization of tailings and cover materials used throughout this project.

Chapter Four: Material Characterization Results and Discussion – This section presents results of characterization tests for the tailings, biosolids, and sand materials.

Chapter Five: Column Testing – This section provides a detailed description of the column tests carried out in the laboratory. Column design and sensor calibration, as well as water content and pore water quality results are shown and described.

Chapter Six: Unsaturated Flow Modelling – This section covers the development and calibration of numerical models for use as a predictive tool of capillary barrier cover effectiveness. The numerical model parameters and calculations are described in detail, and results of several “what if” simulations are shown.

Chapter Seven: Summary and Conclusion – This section summarizes results and significant findings from all phases of this project.

Chapter Eight – Recommendations for Future Work – This section provides recommendations for future work related to biosolids covers which was outside of the scope of work of this project.

1.5 Novelty of the thesis

This is the first publically reported study on the use of municipal biosolids in capillary barrier covers. Furthermore, characterization of the hydrogeological and water retention of municipal biosolids has not been undertaken with the intent of using these materials in multilayer engineered soil covers, and no laboratory testing or numerical modelling of biosolids capillary barrier covers has been found through review of relevant literature. Previous research and industrial application has focused solely on the direct land application of biosolids to mine tailings, usually with a focus of revegetating tailings areas, and studies have highlighted areas of concern with direct land application. One focus of this research is to determine if capillary barrier cover configurations may limit the deleterious effects previously reported during previous study of monolayer covers. Proof of concept may generate significant opportunity for the use of biosolids capillary barrier covers in control and mitigation of acid rock drainage, and for use in other applications such as landfill covers.

Chapter 2 : Literature Review

The literature review comprises: (i) a brief background in hard rock mine tailings generation, processing, and deposition (Section 2.1); (ii) a description of municipal biosolids processing (Section 2.2) (iii) ARD management strategies, including biosolids application and capillary barrier covers (Section 2.3); (iv) a background in unsaturated flow theory (Section 2.4); (v) technical overview of soil suction (Section 2.5); and (vi) further geotechnical soil/water relationships (Section 2.6).

2.1 Hard Rock Mine Tailings

Hard rock mining utilizes drilling and blasting to liberate metal bearing ores in open-pit or underground mining operations. Ore is processed through crushing and milling followed by physical and chemical separation processes to extract targeted metals. Crushing is typically conducted in multiple stages, followed by milling which can also comprise of several stages. Water is typically added to the ore material prior and/or during milling to facilitate transportation of the material as a slurry. Crushing typically reduces or fragments to a particle size between 5-20 cm, while milling reduces or particles to sizes between 10-100 um (Wills & Finch, 2015). Material is typically classified between stages of crushing and milling using screens and hydrocyclones to recirculate oversized material and allow undersized material to proceed through the comminution circuit (Metso, 2015). A simplified comminution process is shown in Figure 2-1.

Following size reduction, ore materials can be processed through a variety of methods which serve to separate the valuable metal particles from gangue and waste rock. A common separation technique is froth flotation, whereby chemical conditioners are added to the ore slurry to selectively change the surface properties of the metal bearing ore particles. In froth flotation, conditioned ore particles are rendered hydrophobic, and the slurry is aerated; the metal bearing particles attach to the air bubbles and float to the surface of the aeration basin where they are collected as a metal concentrate (Wills & Finch, 2015). The particles which do not float report to the waste underflow.

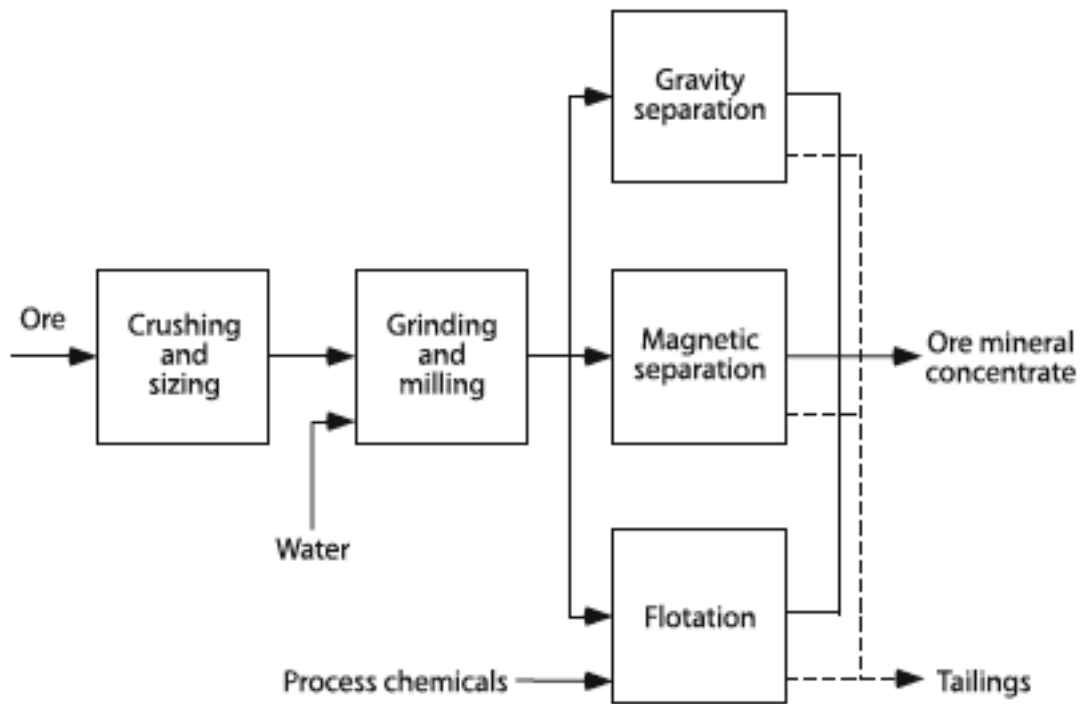


Figure 2-1. Simplified flow-chart of a mineral processing operation in which ore is processed to yield an ore mineral concentrate and tailings
(Lottermoser, 2007)

Tailings particle size and mineralogical composition vary depending on the mineral of interest in the ore being extracted and processed; in the case of this project the tailings were sampled from Vale property in Sudbury at the Copper Cliff Tailings Facility. The metals of interest in the Vale operations are copper and nickel, which are extracted from pentlandite, chalcopyrite, and pyrrhotite ores of the Sudbury Basin. Figure 2-2 provides particle size distributions of tailings phases from two tailings from the Sudbury area from Vale & Glencore operations. It can be seen that Pentlandite (Pn) particles are finer than the Pyrrhotite (Po) tailings at both operations.

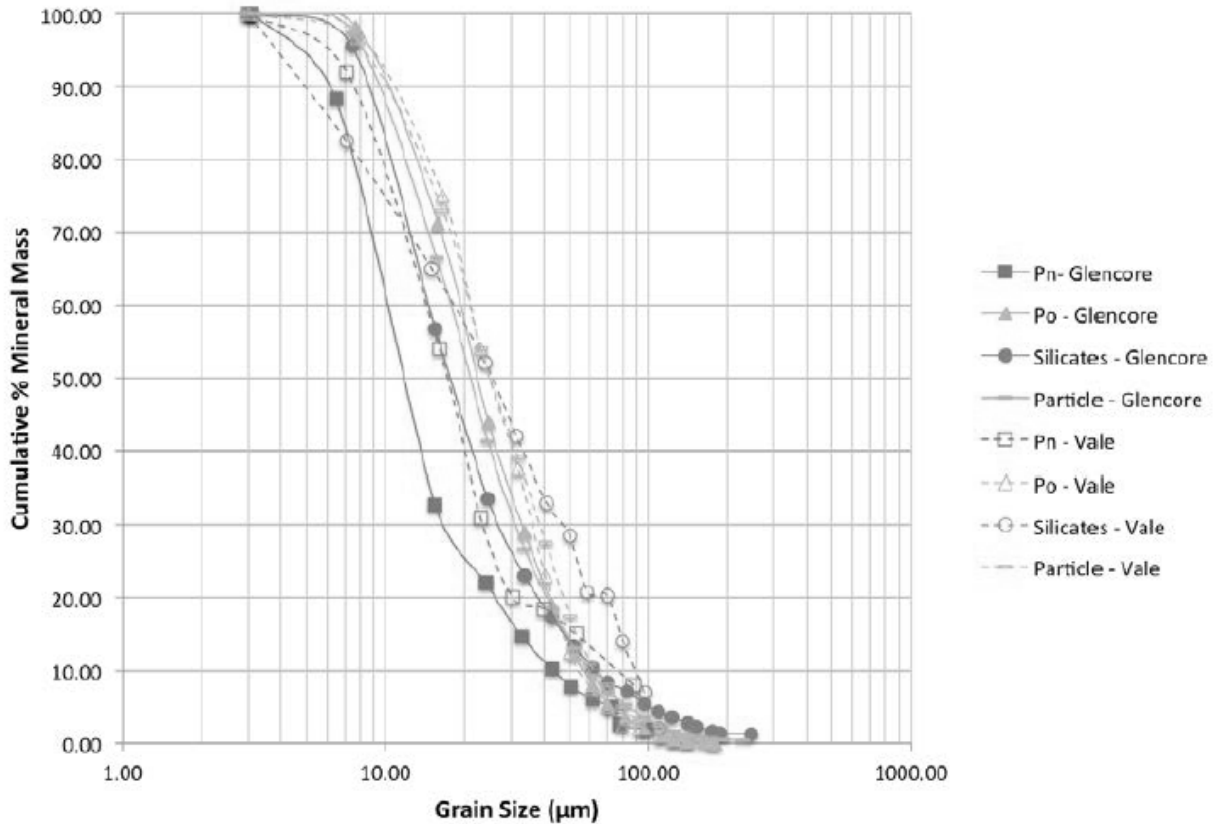


Figure 2-2. Particle Size distribution of Sudbury area pyrrhotite tailings from Vale & Glencore operations
(Duffy, Garg, et al., 2015)

Table 2-1. Mineralogy of Vale pyrrhotite tailings from X-Ray Diffraction analysis
(Duffy et al., 2015)

| Mineral / Compound | wt% |
|-------------------------|------|
| Quartz | 1.0 |
| Chalcopyrite | 0.2 |
| Pentlandite | 0.6 |
| Magnetite | 3.3 |
| Pyrrhotite (Hexagonal) | 35.9 |
| Pyrrhotite (Monoclinic) | 55.8 |
| Calcite | 0.3 |
| Szomolnokite | 2.9 |

As seen in Table 2-1, tailings may be composed either partly or primarily of sulphide materials. These sulphides can be acid forming when oxidized. The oxidation of sulphide materials is highly dependent upon the exposure of the sulphides to oxygen. The same principle of maximizing

exposed surface area in froth flotation to condition and float valuable metals has an equal and adverse effect with regards to acid generation. The finer the particles are ground (assuming a spherical particle shape) the greater the surface area to volume ratio of the particles (Little, Mainza, et al., 2016). This increased exposure of sulphides to oxygen at the surface of the tailings particles can lead to an increase in acid generation due to greater contact and reaction surface area. Figure 2-3 shows the effect of comminution on liberation of minerals and the exposure of particle surface area.

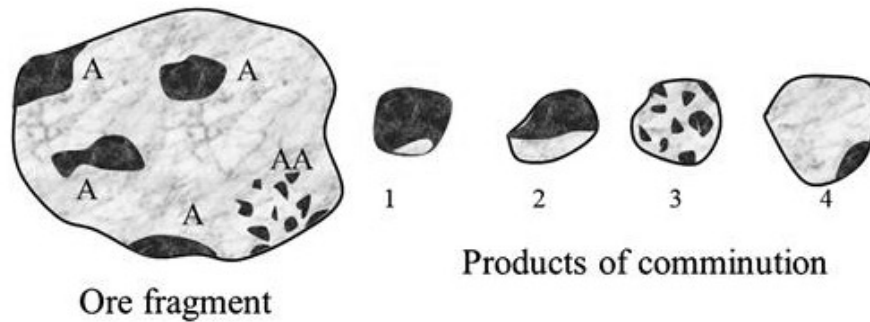


Figure 2-3. Ore fragmentation and mineral liberation showing surface area exposure for the various ore materials within tailings particles
(Wills & Finch, 2015)

Studies of the Vale tailings indicate that the pyrrhotite tailings have a high degree of liberation and exposure as shown in Table 2-2 (Duffy et al., 2015). The high degree of pyrrhotite tailings liberation and exposure indicate the significant leaching potential of the Vale tailings.

Table 2-2. Liberation and exposure of Vale pyrrhotite tailings
(Duffy et al., 2015)

| Material | Liberated | Exposed |
|-------------|-----------|---------|
| Pentlandite | 48 % | 45 % |
| Pyrrhotite | 97% | 96% |

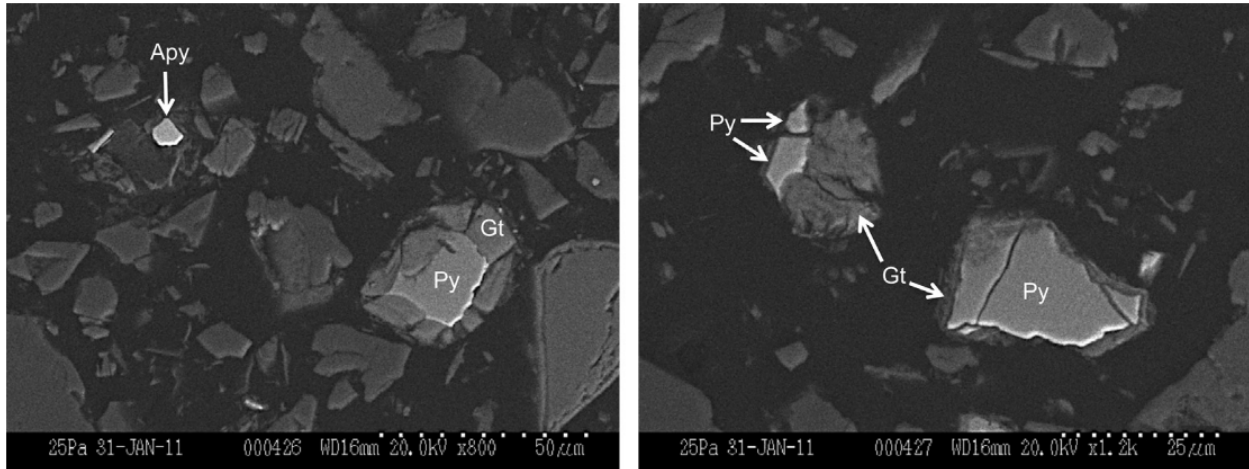


Figure 2-4. Backscattered electron images highlighting pyrite (Py) and arsenopyrite (Apy) particles and secondary goethite (Gt) alteration in tailings from the Delnite gold mine (Paktunc, 2013)

Oxidation of tailings particles can form a surficial layer of oxidized and chemically altered materials surrounding the inner, unaltered tailings grains. Oxidation and secondary precipitation of metals can significantly impact groundwater and local ecosystems. Arsenopyrite shown in Figure 2-4 is one mineral of concern when dealing with gold tailings as the release of arsenic into ground and surface water can have detrimental effects on ecosystems beyond the acidifying effects of ARD.

The macroscopic oxidation front moves through the tailings deposit where atmospheric oxygen reacts with exposed sulfide tailings particle surfaces as shown in Figure 2-5 (A). Sulfide grains continue to oxidize from the exposed surface inwards towards the center of the tailings particle, creating outer reacted rims of oxidation products as seen in Figure 2-5 (B).

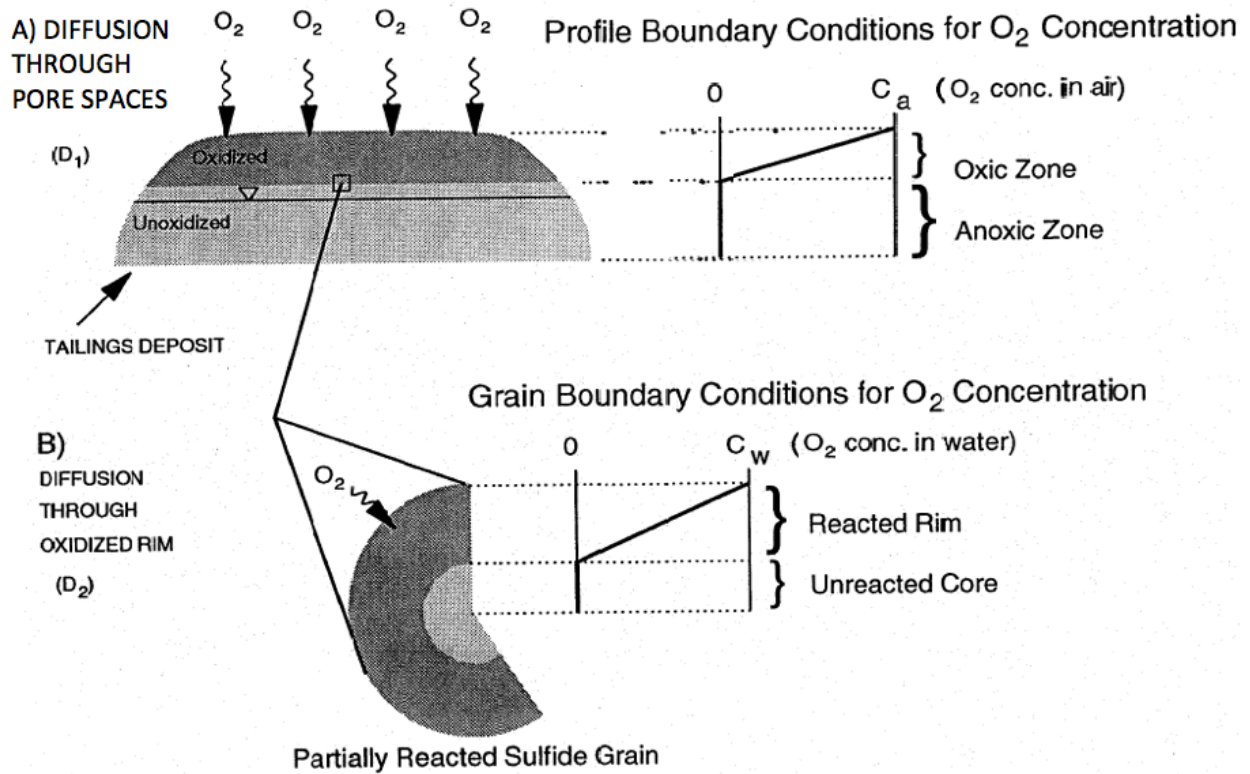


Figure 2-5. Visualization of sulfide-mineral oxidation by diffusion of oxygen into tailings pore space (A), and subsequent diffusion of oxygen into tailings grains (B) (Al & Blowes, 1995).

Figure 2-6 shows scanning electron microscope (SEM) images of tailings alteration in pyrrhotite tailings. The reacted outer layers are visible in the SEM images of the pyrrhotite grain as previously depicted in Figure 2-4 and Figure 2-5.

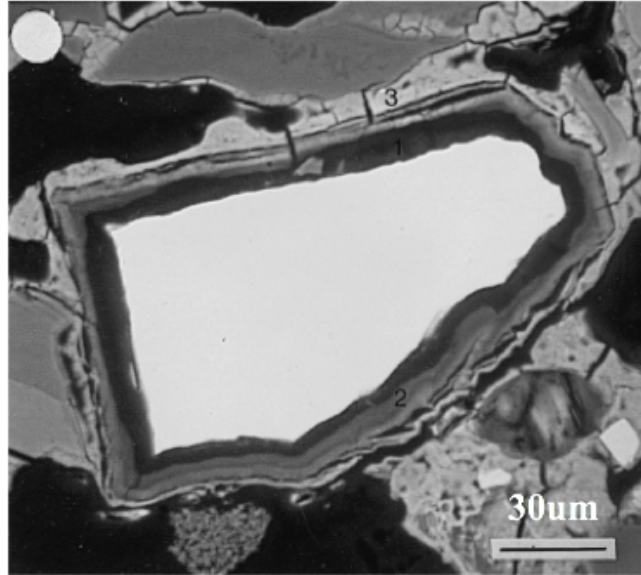


Figure 2-6. Image of pyrrhotite tailings grain from a backscattered electron microscope showing alterations from innermost layer of native sulfur surrounded by sulfur and sulphate bearing goethite
(McGregor, Blowes, et al., 1998).

2.1.1 Tailings Deposition

Tailings can be deposited in various ways depending on their water content. Hydraulic deposition of tailings is most prevalent due to the ability to pump tailings slurry over long distances and achieve high rates of deposition. De-watered tailings can be pumped as a paste, or dried and stacked, however, these methods are less common but are employed for site-specific reasons, such as high cost of water, poor foundation conditions that limit dam height, and in mountainous or hilly areas where dam construction is difficult (Simms, Daliri, et al., 2016). Tailings can be dewatered using belt presses and pressure filters; water removed can often be re-used in the milling process. Thickeners can be added to the tailings slurry to convert the slurry into a paste which can be pumped to deposition areas, or mixed with cement and used as a backfilling agent in underground operations. It is generally most cost effective to transport tailings hydraulically provided that sufficient water is available and sufficient storage volume is available to receive tailings (Vick, 1983).

Hydraulic deposition of tailings slurry is typically conducted using water contents between 150 to 100 percent by mass of dry solids with a relative density for the slurry typically between 1.3-1.5

(Blight & Bentel, 1983). The tailings typically form a beach of material from which the water decants or bleeds out of the saturated soil matrix. Hydraulic deposition requires that a berm or dam be constructed, or naturally available, to contain the tailings and water during the deposition and drainage process. Spigotting and sub-aerial discharge of tailings are common methods of depositing hydraulically transported tailings. The tailings are discharge from pipes along a sloped embankment where sufficient space is available for tailings to form a beach and decant as shown in Figure 2-7.

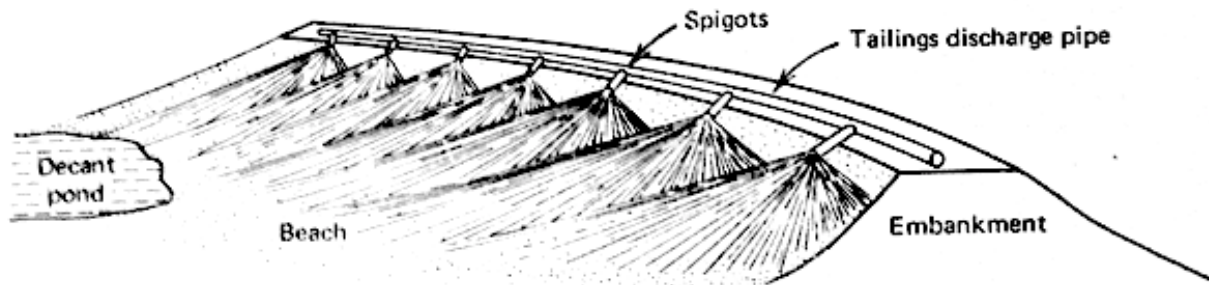


Figure 2-7. Hydraulic tailings deposition showing spigots with formation of a beach and decant pond
(Vick, 1983)

2.1.1.1 Grain-Size Segregation

Grain-size segregation in following tailings deposition is of concern when planning tailings impoundments as dams are the structural planning and design of the tailings areas are often reliant on the geotechnical properties of the tailings. Tailings particles have been shown to exhibit different degrees of segregation depending on the type of tailings deposited, however, general behaviour is for large particles to settle early after deposition, while finer particles are carried further from the discharge point (Vick, 1983). Figure 2-8 and Figure 2-9 show results of tailings sampling from copper tailings conducted in Poland at the Zelazny Most tailings pond.

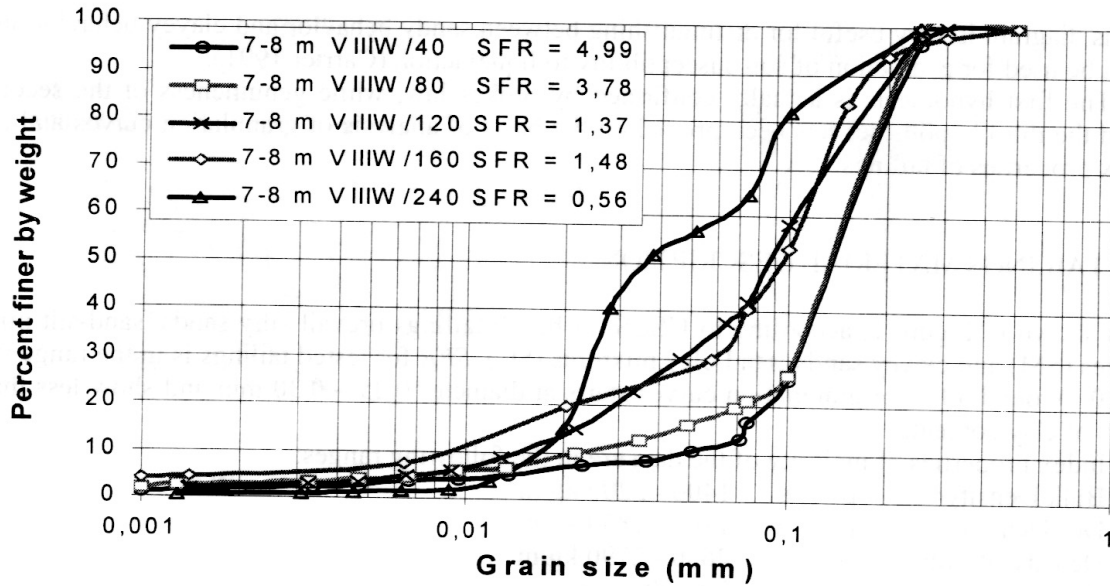


Figure 2-8. Particle size distribution of tailings sampled at the same depth (7-8m) but at varying distance from the discharge point (distance in meters shown as “/XX”)
(Lipinski & Golebiewska, 2000)

The lateral grain-size segregation of tailings particles from the point of discharge is easily visualized when viewing Figure 10. wherein it can be seen that the tailings become finer (decreasing sand to fines ratio) at greater distances from the discharge point.

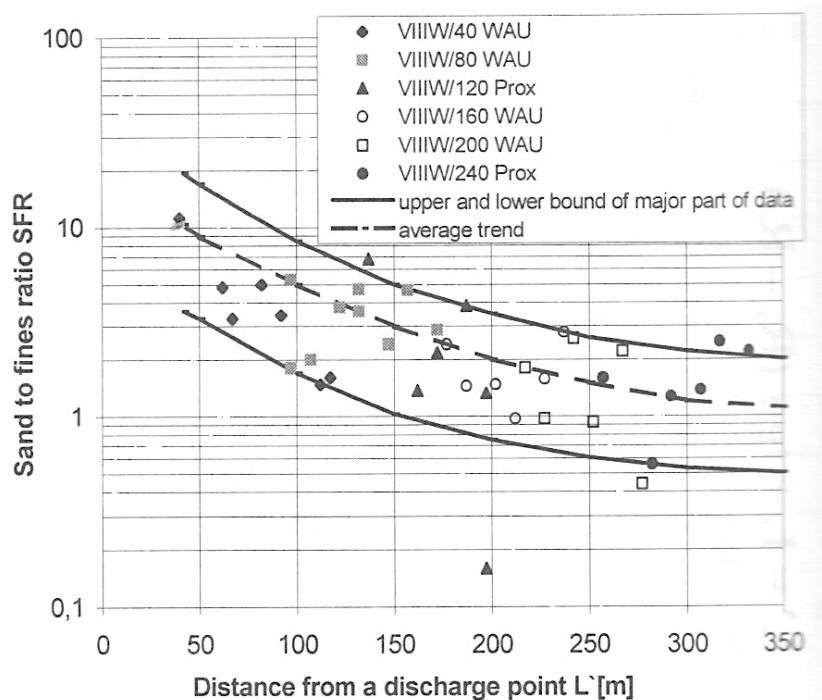


Figure 2-9. Grain-size segregation observed in analyzed cross section
(Lipinski & Golebiewska, 2000)

The segregation behaviour of the tailings generally leads to the development a distribution of permeability within the tailings impoundment similar to that shown in Figure 2-10 permeability due to the grain-size distribution of the deposited tailings along the beach.

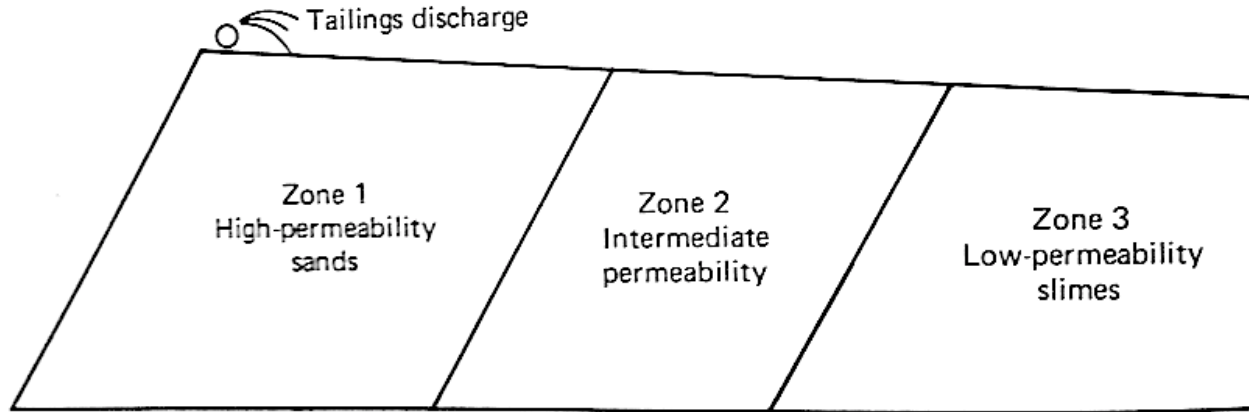


Figure 2-10. Conceptual variation in permeability along a cross section of a tailings beach (Vick, 1983)

Grain-size segregation also occurs vertically; Figure 2-11 shows the particle size distribution of samples taken at the same distance from a tailings discharge point at various depths within the tailings impoundment. It is shown in Figure 2-11 and Figure 2-14 (C) that the tailings are finer at depth, with a greater sand-to-fines ratio near the surface of the tailings, and finer material below.

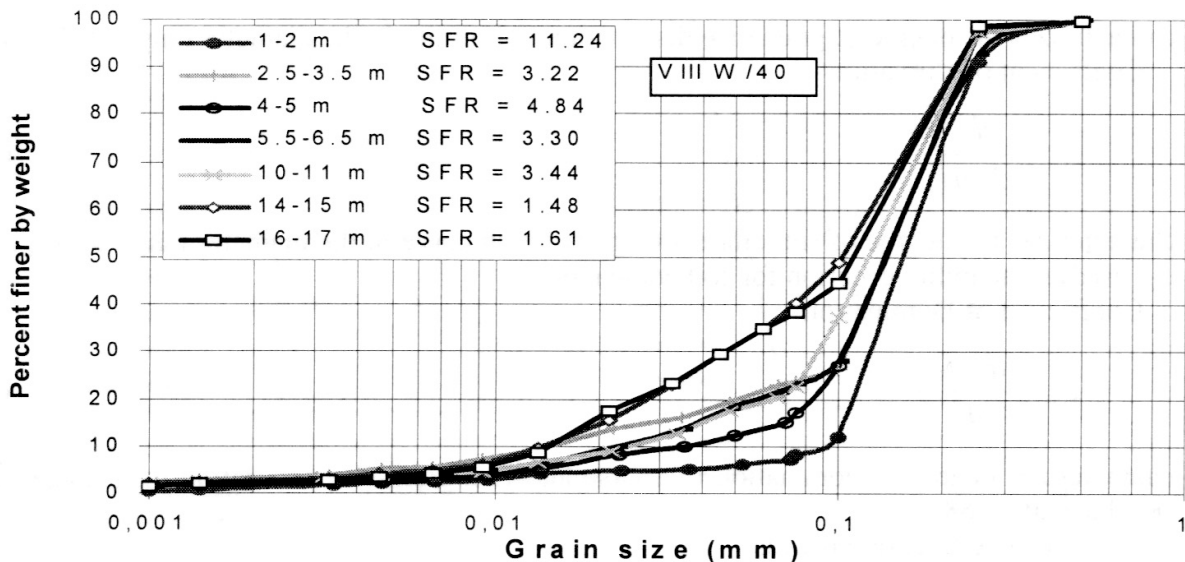


Figure 2-11. Grain-size distribution of copper tailings at sampled at various depths (Lipinski & Golebiewska, 2000)

2.1.1.2 Consolidation

The process of soil consolidation refers to a decrease in water content of a saturated soil without replacement of the water by air (Terzaghi, 1943). Consolidation of tailings occurs following hydraulic deposition as the tailings particles settle and re-arrange under normal stress conditions. Free water is pushed through the soil pore spaces to the surface as void space in the soil is reduced by stresses pushing down on the tailings from newly deposited overlying material, displacing the pore-water. The free water flows upwards to the surface where it may be decanted, while at the same time the tailings experience settlement and a reduction in total volume.

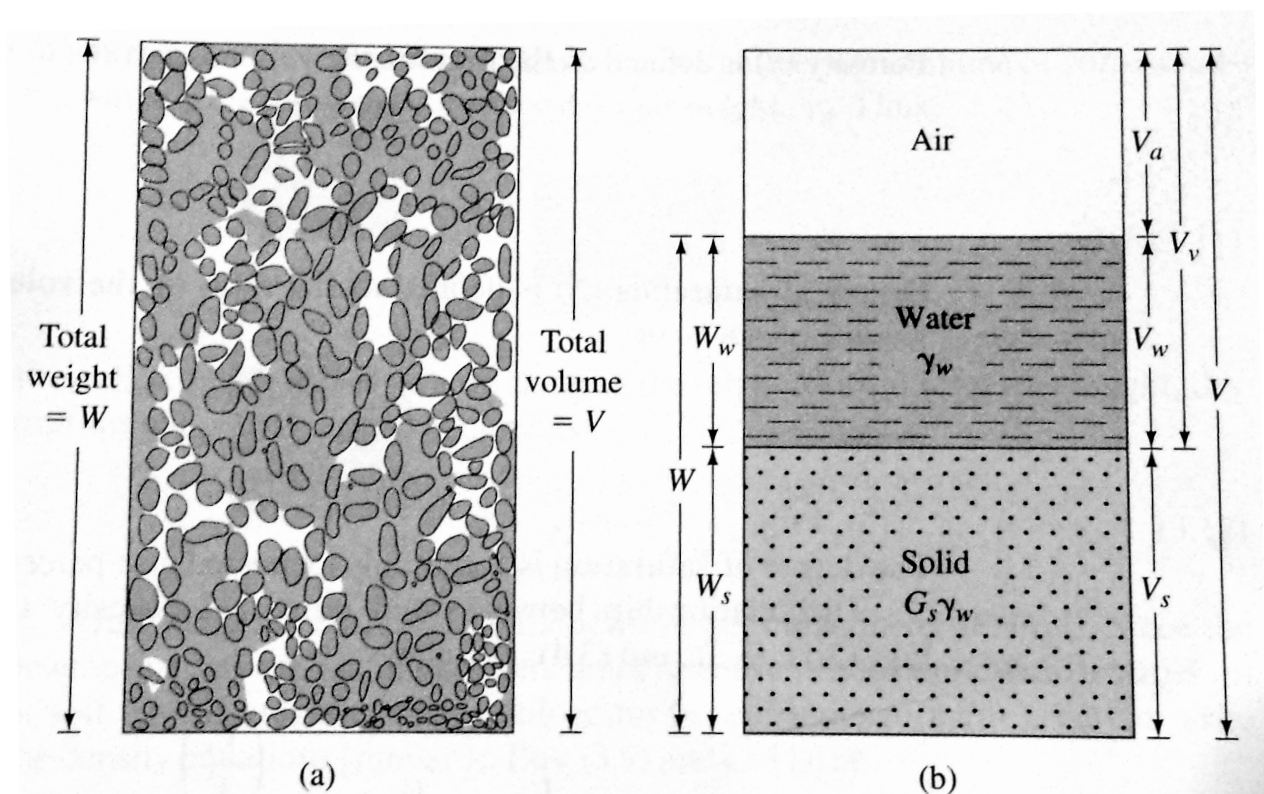


Figure 2-12. Conceptualization of soil volume and mass in (a) natural state, and (b) partitioned by phases of solids, water, and air (Das & Sivakugan, 2017).

The void ratio (e) is the volume of void spaces (V_v) in a soil as a fraction of the volume of solids (V_s) as shown in Equation 2-1. The volume coefficient of compressibility (m_v) can be determined mathematically by subjecting soil samples to incremental normal stress ($\Delta\sigma$) and observing the resultant change in void ratio (where e is the initial void ratio) as shown in Equation 2-2. With the volume coefficient of compressibility, the coefficient of consolidation (c_v) can be calculated

using the soil permeability (k), and the unit weight of water (γ_w) as shown in Equation 2-3 (Das, 2008).

$$e = \frac{V_v}{V_s} \quad \text{Equation 2 - 1}$$

$$m_v = \frac{\Delta e}{\Delta \sigma(1+e)} \quad \text{Equation 2 - 2}$$

$$c_v = \frac{k}{\gamma_w m_v} \quad \text{Equation 2 - 3}$$

Consolidation is a time dependent process, and occurs in multiple stages as shown in Figure 2-13. Initial compression is caused primarily by pre-loading of soil where air is expelled and solid particles are compressed. Primary consolidation occurs as excess pore water pressure dissipates through drainage of water from the soil, while secondary consolidation occurs due to plastic deformation, re-arrangement, or creep of the soil particles. Primary consolidation of hard rock mine tailings occurs rapidly, and coefficients of consolidation (c_v) typically vary from 5×10^{-1} to 5×10^{-2} cm^2/s for beach tailings (Vick, 1983).

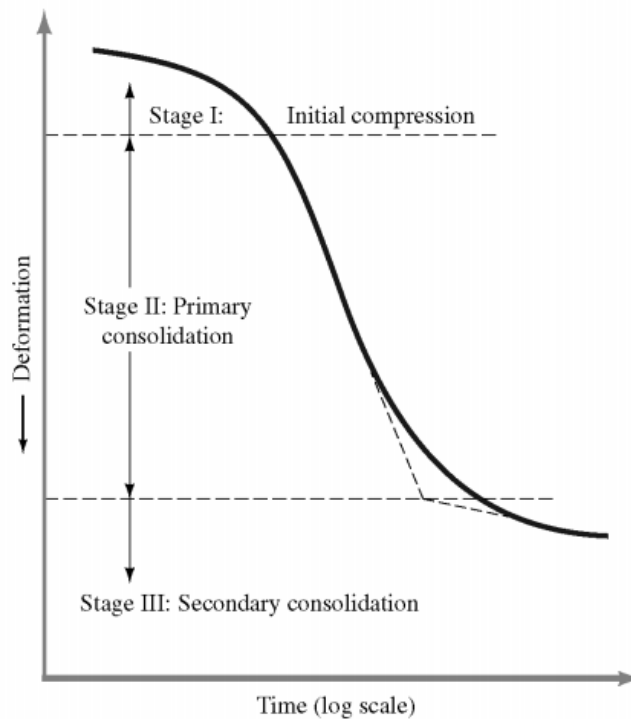


Figure 2-13. Stages of consolidation in typical soil samples (Das & Sivakugan, 2017).

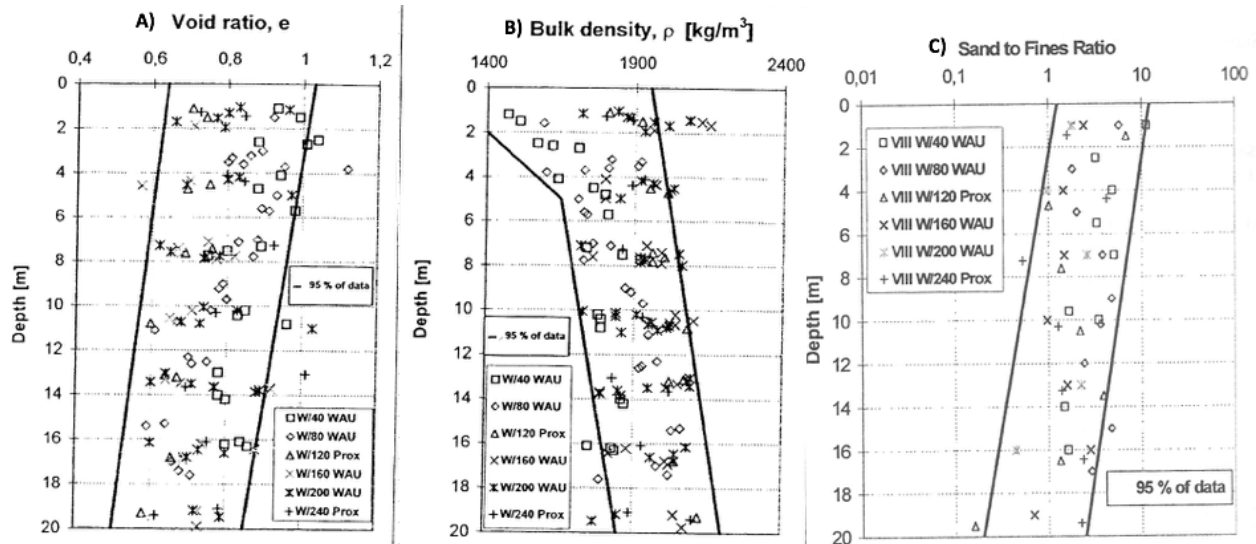


Figure 2-14. Tailings profiles with depth for void ratio (A), Bulk density (B), and Sand to Fines Ratio (C)

(Lipinski & Golebiewska, 2000).

Particle size segregation and consolidation result in tailings profiles which exhibit non-uniform properties with depth such as void ratio and permeability. From the tailings profiles plotted in Figure 2-14 the tailings void ratio decreases at depth (A), the bulk density increases with depth (B), and the material becomes more homogeneous at depth. When viewed in conjunction with Figure 2-11 it can be seen that the tailings become finer at depth. It can also be inferred that tailings lower in the profile experience a greater degree of consolidation due to the reduced void ratio observed, and a displacement of water from the soil leads to a higher bulk density.

2.2 Municipal Biosolids

Municipal biosolids are the solid residuals from municipal wastewater and sludge treatment. Solids are settled out and removed from wastewater processes and treated to reduce pathogen and bacterial counts such that the material meets regulatory thresholds. Wastewater treatment produces solid residuals in the form of sludges which are further treated to create biosolids which may be used beneficially.

Untreated wastewater discharge can cause severe environmental degradation, ranging from algal blooms caused by elevated levels of ammonia, to human deaths from E.coli contamination of drinking water. In Canada, wastewater effluent must pass basic conditions according to the Federal

wastewater sewage effluent regulations (WSER) as shown in Table 2-3. The values for typical domestic wastewater constituent concentrations are shown in Table 2-4.

Table 2-3. Canadian Federal wastewater sewage effluent regulations
 (“Wastewater Systems Effluent Regulations,” 2012)

| Deleterious Substance | Condition |
|--------------------------------|----------------------------------------------------------|
| Average CBOD | 25 mg/L |
| Average Total Suspended Solids | 25 mg/L |
| Average residual chlorine | 0.02 mg/L |
| Maximum unionized ammonia | 1.25 mg/L expressed as nitrogen (N) at 15 ⁰ C |

Table 2-4. Typical domestic wastewater influent values
 (Metcalf & Eddy, Tchobanoglous, et al., 2014)

| Constituent | Concentration (mg/L) |
|---------------------------------|-----------------------------|
| COD | 430 |
| BOD | 190 |
| Total Suspended Solids | 210 |
| Volatile Suspended Solids | 160 |
| Total Kjeldahl Nitrogen | 40 |
| NH ₄ ⁻ -N | 25 |
| NO ₃ ⁻ -N | 0 |
| Total Phosphorous | 7 |
| Alkalinity | 200 (as CaCO ₃) |

2.2.1 Wastewater Treatment Processes

Municipal wastewater is a combination of sewage, domestic wastewaters, industrial wastewater, and in some areas, storm water. Wastewater is treated to remove solids and biological components which can adversely affect the environments to which waste waters and treated effluents are discharged. The main functions of wastewater treatment are the removal of solids, the reduction of Biological Oxygen Demand (BOD), Carbonaceous Oxygen Demand (COD), Total Solids (TS),

Volatile Solids (VS), Nitrogen (Nitrates, Nitrites, Ammonia, Ammonium), and Phosphorous (P) (Wang, Shamma, et al., 2007).

Municipal wastewater treatment varies in configuration and design based upon the volume and composition of water treated, as well as effluent regulations and budget of the operating municipality, however, most plants follow the same general processes as shown in Figure 2-15. Sewage enters the plant where preliminary screening and grit removal separates large and dense solids for disposal. Primary treatment of wastewater uses sedimentation and settling to separate out primary sludge from wastewater (Jones, 1978). Secondary treatment typically involves either aerobic, anaerobic, or anoxic treatment (often in combination) in aerated lagoons or activated sludge systems.

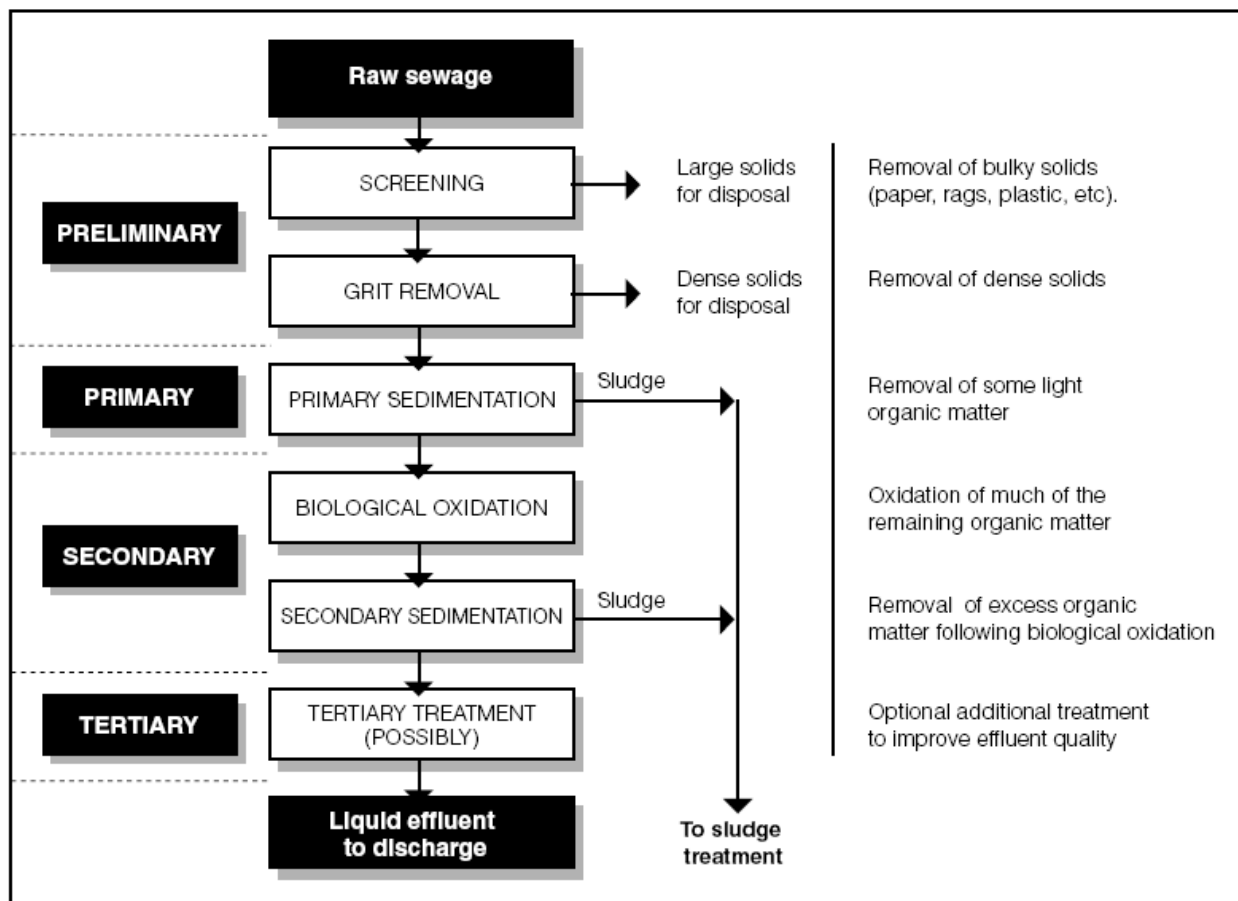


Figure 2-15. Typical wastewater treatment process (Metcalf & Eddy et al., 2014)

Secondary treatment oxidizes the biological components within the wastewater to biodegrade dissolved and particulate constituents into acceptable end products. BOD is a measure of the

amount of oxygen consumed by bacteria in the wastewater which decompose organic materials, and is typically expressed as milligrams of oxygen consumed per liter of wastewater. Reductions in BOD indicate a reduction in the bacterial activity required to break down the organic matter present which corresponds to a reduction in the quantity of organic matter remaining in the wastewater. The Carbonaceous 5-day biochemical oxygen demand (CBOD) is the biochemical oxygen demand required to oxidize carbonaceous elements only, which negates the oxygen consumption due to nitrification (which is a component of BOD).

As bacteria break down the organic matter in wastewater, the bacteria reproduce, grow, and die; this population change can be modelled by the Monod equation; an example of the bacterial growth curve is shown in Figure 2-16.

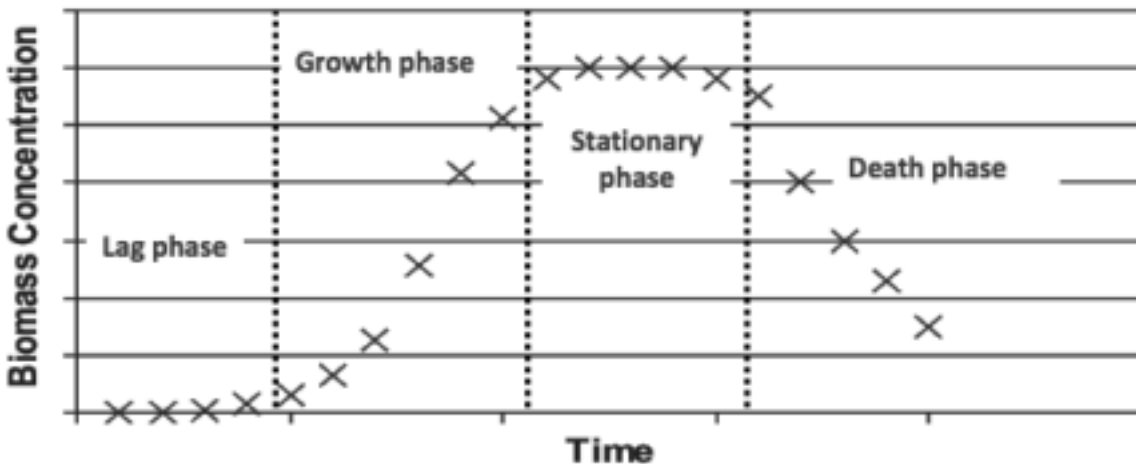


Figure 2-16. Microbial growth patterns in a batch reactor
(Metcalf & Eddy et al., 2014)

The dead bacteria, biodegraded organic matter, and other solids are removed from the wastewater through settling and flocculation, and become a sludge product as shown in Figure 2-15 and Figure 2-17.

In order to stimulate bacterial activity, several processes have been developed; one example is activated sludge treatment wherein sludge collected following secondary treatment is recirculated into the treatment train in order to seed the wastewater undergoing treatment with active bacteria. Return of activated sludge also serves to increase the solids retention time, allowing for significant reductions in the treatment basin volumes.

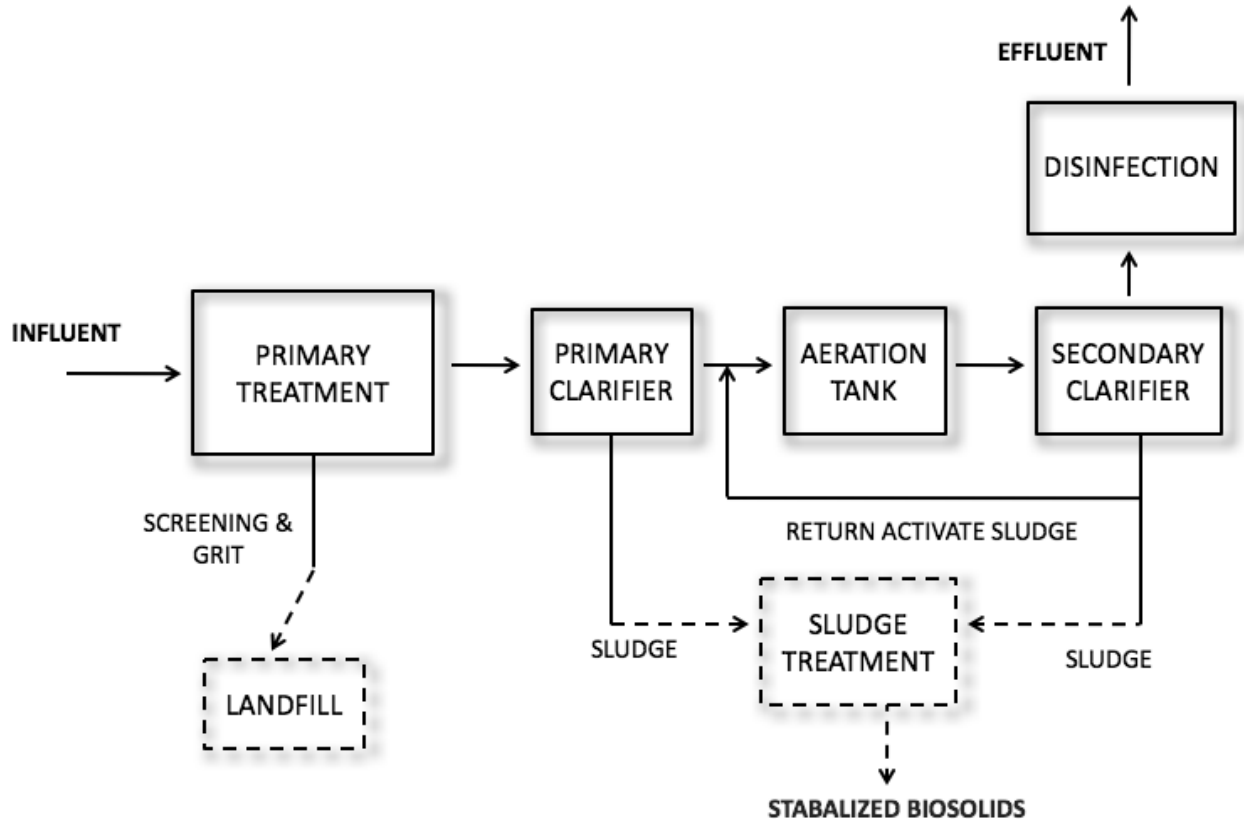


Figure 2-17. Activated sludge treatment schematic
(modified (Metcalf & Eddy et al., 2014))

Secondary treatment should also induce flocculation of otherwise suspended and non-settling colloidal solids. Nutrient removal, such as the removal of nitrogen and phosphorous is conducted as part of secondary treatment.

Nitrogen removal is achieved through nitrification and de-nitrification. Nitrification occurs via a two-step oxidation process wherein ammonia is oxidized by ammonia oxidizing bacteria (AOB) as shown in Equation 2-4 and is converted to nitrite. A common AOB is nitrosomonas. The nitrite is then oxidized and converted to nitrate by nitrate oxidizing bacteria as shown in Equation 2-5.



Denitrification is the process of converting nitrate and ammonia into di-atomic nitrogen, which is typically released to the environment as nitrogen gas. Denitrification produces alkalinity, and is an anoxic process in wastewater treatment, requiring a separate anoxic zone or tank. Proper

maintenance of anoxic conditions, and a higher mixed liquor pH value in the anaerobic stage have been shown to positively correlate with the increase in *Accumulibacter* populations (López-Vázquez, Hooijmans, et al., 2008).

The biological removal of phosphorous is driven by the presence of phosphorous accumulating organisms (PAOs) such as *Accumulibacter*, which are facultative heterotrophic bacteria. Under anaerobic conditions PAOs convert acetate or propionate into Poly-Hydroxyalkanoates (PHAs). The conversion of acetate and propionate to PHAs releases phosphates, while PAOs accumulate ortho-phosphates during anoxic or aerobic conditions, using PHAs as an electron donor and carbon source. (J. Oleszkiewicz, Kruk, et al., 2015). Where biological removal is not used, ferric chloride can be used to precipitate phosphorous from wastewater (Metcalf & Eddy et al., 2014).

Following secondary treatment, the wastewater progresses through secondary sedimentation where secondary sludge is separated from effluent water. Tertiary treatment may be implemented to further remove nutrients or chemicals.

2.2.2 Sludge Treatment Processes

Treatment of sewage sludge is done in order to stabilize the sludge mass and reduce volume, vector attraction, and to inactivate pathogens. Generally sludge treatment requires thickening and conditioning of wastewater sludge prior to stabilization processes. Thickening typically employs centrifuges, gravity belts, or other mechanical means of reducing the water content. Stabilization is commonly achieved through aerobic digestion, anaerobic digestion, composting, or alkaline treatment (Spinosa & Vesilind, 2001). Dewatering is achieved using mechanical methods, similar to thickening, after which the sludge is dewatered either through mechanical means or evaporation and subjected to high temperatures. General process options are shown in Figure 2-18.

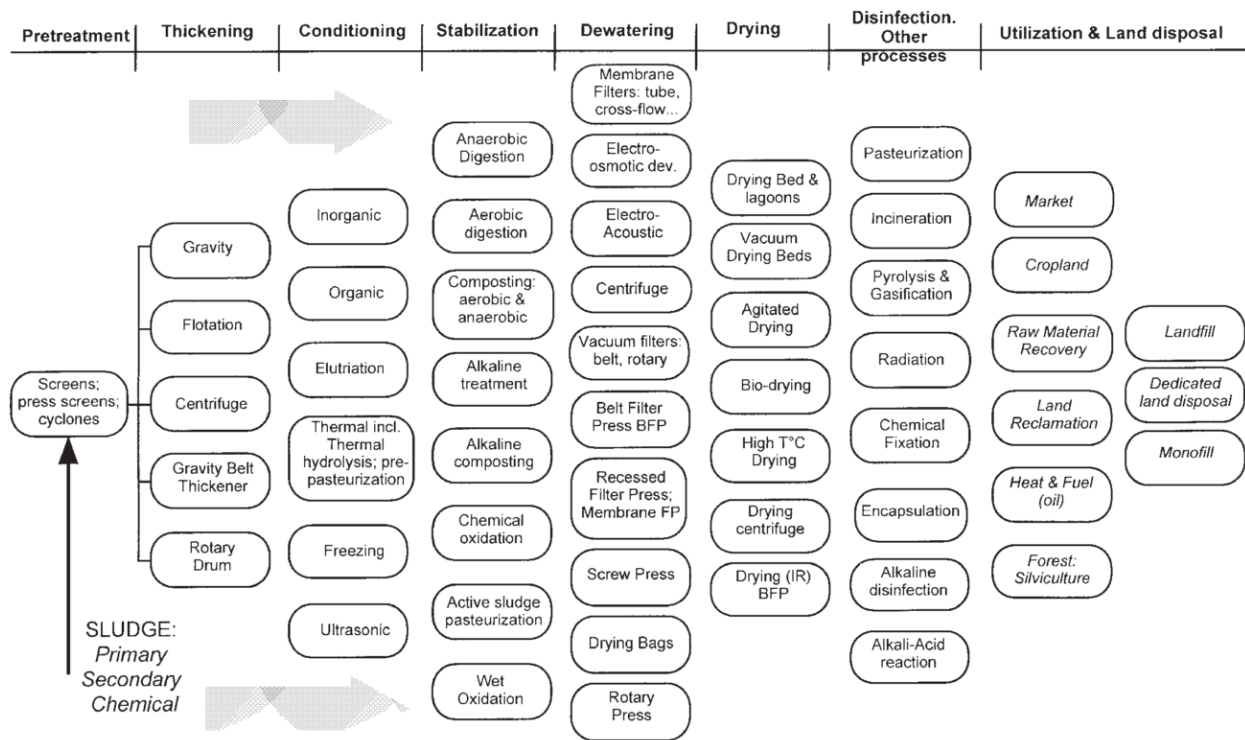


Figure 2-18. Unit processes available for sludge treatment
(J. A. Oleszkiewicz & Mavinic, 2002)

Production of municipal biosolids which do not pose a threat to human health and environmental degradation requires vector reduction and pathogen stabilization. Biosolids quality is subjective, however, the EPA has defined Class A biosolids as those which have pathogen levels which are “below detectable levels” for salmonella, bacteria, enteric viruses, and viable helminth ova. Class B biosolids refer to products where pathogens are detectable but have been reduced such that they do not pose a threat to public health and the environment when preventative measure are taken to limit exposure to the biosolids. Land application of Class B biosolids are subject to greater restriction than Class A biosolids. Municipal biosolids typically contain elevated concentrations of metals; land application of all classes of biosolids require the control of metals below specific regulatory limits. Stabilization to Class A biosolids can be accomplished using aerobic thermophilic digestion, pasteurization, composting, and lime stabilization can be used to achieve a stabilized final product. Lime addition requires that the pH be raised above 12 for a period of at least two hours, while composting requires temperature to be elevated to 55 °C for 3 days; pasteurization is achieved more quickly but requires a higher temperature of 70 °C (United States Federal Law, 1962).

Anaerobic digestion is commonly used to achieve significant reduction in pathogens and sludge volume, and has potential to produce heat and electricity through the generation of methane. Figure 2-19 shows the anaerobic process pathway for the conversion of complex organics to stabilized biosolids and digestions by-products. In the first stage of anaerobic digestion, complex organics are converted into simpler organic acids by acid forming bacteria which are obligate anaerobes; it is therefore essential to eliminate oxygen from the digestion process. The converted organics are then consumed by methanogenic bacteria which produce methane, carbon dioxide, and a moderately stabilized biosolid product.

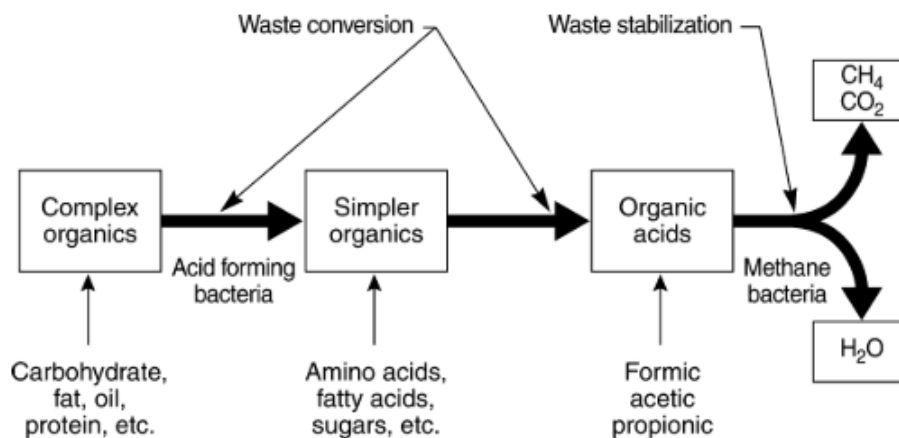


Figure 2-19. Anaerobic conversion of wastewater organics to byproducts
(Wang et al., 2007)

Detention times for anaerobic digesters typically range from 18-25 days, with influent solids concentrations in the raw sludge ranging from 3-8%. Volatile solids in the raw sludge are usually between 70-80% of the total solids, and anaerobic digestion removes between 30-35% of total solids, and 40-55% of volatile solids (Fernandes, Lopes, et al., 2007).

The Class B biosolids in this study were obtained from the region of Halton. The Mid Halton wastewater treatment plant (WWTP) is located in Oakville and a schematic of the treatment process is shown in Figure 2-20. The plant was originally constructed in 1991 with a rated capacity of 20,000 m³/d. The plant was then expanded to provide a total capacity of 75,000 m³/d. The ultimate site capacity of the Mid Halton WWTP is 400,000 m³/d based on providing conventional activated sludge treatment.

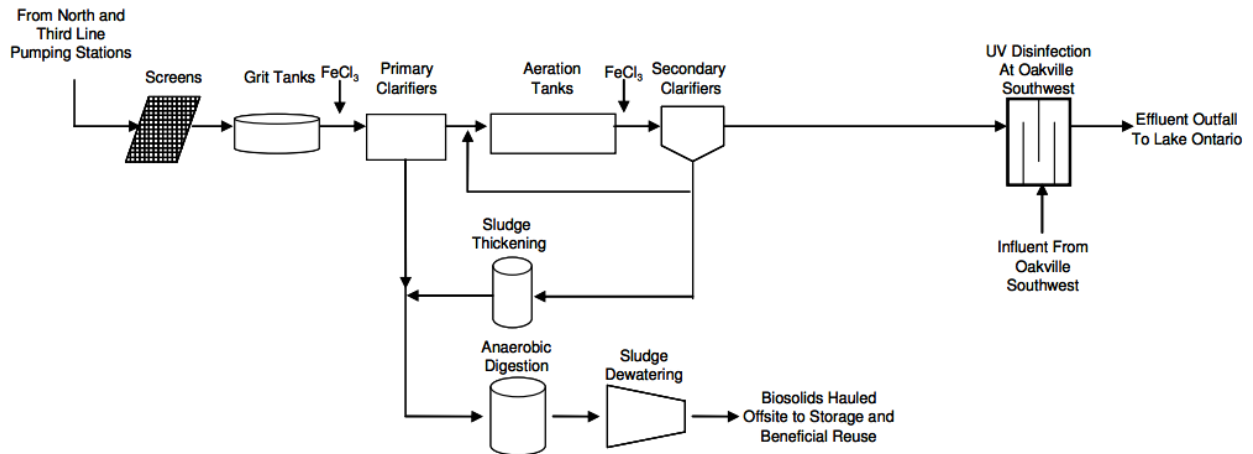


Figure 2-20. Mid-Halton wastewater treatment plant schematic
(Hatch Mott MacDonald Group, 2010)

The following is a description of the wastewater treatment processes at the Mid-Halton wastewater treatment plant (Hatch Mott MacDonald Group, 2010):

Bar screens with 25 mm clear space between bars remove materials that would be detrimental to pumps and other downstream processes. Grit removal is conducted using grit removal tanks and classifiers; material removed through screening and grit classification are collected in waste bins and hauled to a municipal solid waste landfill.

Primary clarification is conducted in four parallel tanks; primary sludge settles out and is pumped to biosolids treatment prior to disposal. Eight rectangular, and two circular aeration tanks are used for biological treatment. Eight parallel secondary clarifiers are used to settle solids following aeration, and a portion of the sludge is returned as activated sludge to maintain microbial populations in the biological treatment phase. Ferric chloride is used to precipitate, settle and remove phosphorus.

The sludge removed from the secondary clarifiers is thickened in parallel rotary drum thickeners to reduce the volume and assist in downstream dewatering processes. The solids content is increased from approximately 1% to 4%, and the volume is reduced by 75%. The thickened secondary sludge, and raw primary sludge from the primary clarifiers are mixed and anaerobically digested. Treated sludge is dewatered in two parallel centrifuges which produce biosolids with a

25-30% solids content. The biosolids are then transported for disposal and land application. Effluent from the site is disinfected with ultra-violet light prior to final discharge.

Biosolids have historically been viewed as a waste product, however, perception is shifting to view the contained nutrients as a resource. Table 2-5 presents the disposal methods in use in select European countries in 2013.

Table 2-5. Sludge disposal in selected countries of the European Union in 2013

(Neczaj, Fija, et al., 2017)

| Country | Total Disposal (10 ³ t) | Landfill (10 ³ t) | Incineration (10 ³ t) | Agricultural Use (10 ³ t) | Compost and Other (10 ³ t) | Dumping at Sea (10 ³ t) |
|-------------|------------------------------------|------------------------------|----------------------------------|--------------------------------------|---------------------------------------|------------------------------------|
| Germany | 1794.73 | 0 | 1034.77 | 491.33 | 264.4 | 0 |
| Estonia | 18.79 | 1.81 | n/a | 0.29 | 16.27 | 0.42 |
| France | 869.74 | 30.92 | 160.63 | 368.58 | 287.49 | 0 |
| Latvia | 20.74 | 0.24 | 0 | 7.48 | 2.3 | 0 |
| Poland | 540.3 | 31.4 | 72.9 | 105.4 | 32.6 | 0 |
| Slovakia | 57.43 | 6.64 | 5.01 | 0.52 | 35.21 | 0 |
| Norway | 131.2 | 18.6 | n/a | 82.6 | 29.9 | n/a |
| Switzerland | 194.5 | 0 | 188.3 | 0 | 0 | 0 |

Conventional means of disposal include incineration, which reduces volume, but can produce significant amounts quantities of ash with high concentrations of heavy metals. Biosolids are often landfilled, however, landfill tipping fees, the use of finite landfill volume, and the sequestration of valuable nutrients is prompting increased beneficial biosolids re-use. Biosolids can be land applied as a nutrient source in agricultural operations, and recent years have seen the use of municipal biosolids as a growth medium in the revegetation of industrial land such as landfill covers and reclamation of mine wastes.

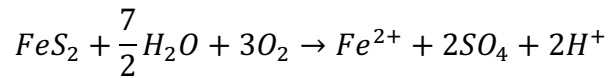
2.3 ARD in tailings and its management

2.3.1 Acid Rock Drainage Overview

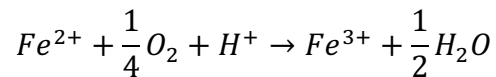
Acid rock drainage occurs due to geochemical instability in tailings, waste rock, leached ores, and slag, and is primarily caused by oxidation of iron-bearing minerals. The most common acid generating material in mine wastes is pyrite (FeS₂), which is stable in a low oxygen environment

(such as when it is underground or particles are captive in a rock matrix), but are liable to oxidize when exposed to atmosphere.

The general process for chemical oxidation of pyrite is shown in Equation 2-6 (Singer & Stumm, 1970).

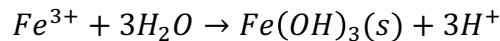


Equation 2 - 6.1

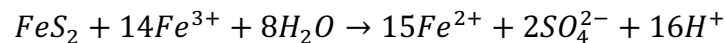


Equation 2 - 6.2

Under acidic conditions where the pH is greater than 4, ferric iron will precipitate, and may become an oxidant, accelerating the oxidation of pyrite and producing greater quantities of hydrogen ions, leading to further acidity.

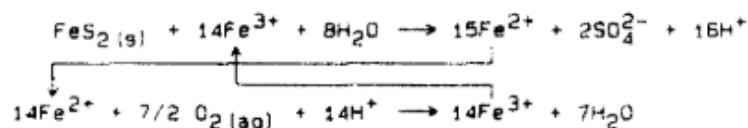


Equation 2 - 6.3



Equation 2 - 6.4

Oxidation of pyrite occurs at a much greater rate through Equation 2-6.4, and can be further accelerated by the presence of Thiobacillus Ferrooxidans bacteria. The process is initially limited by the rate of production of ferric iron but can be biologically augmented by the presence of bacteria. These bacteria typically become active in very acidic conditions when pH is approximately 1.5 to 3.5. Thiobacillus Ferrooxidans catalyzes oxidation of ferrous ions to regenerate ferric ions as shown in Equation 2 – 6.5, allowing further oxidation of the iron in solution (Moses, Kirk Nordstrom, et al., 1987).



Equation 2 - 6.5

The presence of Thiobacillus Ferrooxidans bacteria has been shown to enhance the rate of leaching of pyrite in solution (Fowler, Holmes, et al., 1999).

Weathering and oxidation of tailings typically results in complexation, metal mobility and secondary dissolution (Blowes & Jambor, 1990). The creation of hardpans can occur at or near the oxidation front, and results from precipitation of secondary sulphates and hydroxides. (McGregor et al., 1998). Secondary minerals serve as long term sources of dissolved mass, as they can dissolve and reprecipitate as pH and reduction potential change (Gambrell, Wiesepape, et al., 1991), Figure 2-21 demonstrates the change in iron speciation under varying conditions. The continued precipitation and dissolution of metals may contribute to continued contaminant discharge for decades (Johnson, Blowes, et al., 2000).

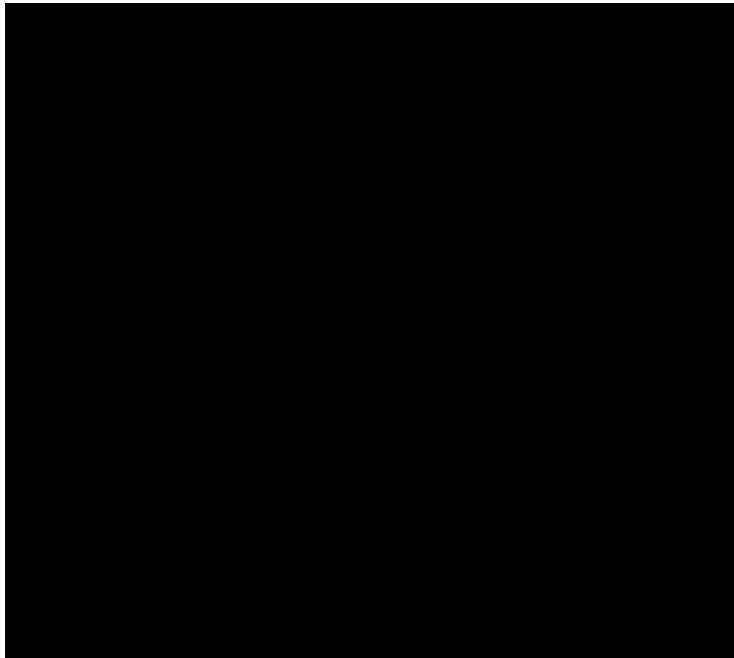


Figure 2-21. Pourbaix diagram of iron in water showing change of oxidizing and reducing conditions with variation in pH
(Pourbaix, Muylder, et al., 2009)

2.3.1.1 Oxidation-Reduction Potential

The oxidation-reduction potential (ORP) of a solution is indicative of the solution's capacity for electron transfer. The ORP is also often referred to as the REDOX potential (reduction and oxidation of the reagents in solution). In redox reactions the oxidizing agent is the reactant that is removing electrons from solution while being reduced and gaining electrons (Equation 2-7.1);

while a reducing agent is the species that is being oxidized and losing electrons (Equation 2–7.2). The redox reaction of iron and copper (ii) sulfate solution is shown in Equation 2–7.3. In this reaction copper sulfate (the oxidizing agent) is oxidizing iron while itself being reduced, while iron (the reducing agent) is reducing copper while itself being oxidized (Petrucci, Herring, et al., 2016).



The ORP of solutions is typically measured using an inactive metal electrode and measuring the electric potential of the electrode. The ORP indicates the electron activity of the solution in millivolts (mV), and whether the solution is contributing electrons to the probe, or removing electrons from the probe. An oxidizing solution will result in the probe losing electrons as the solution reduces, attracting electrons, removing them from the probe, resulting in a positive ORP. Since reducing agents shed electrons to the probe, and oxidizing agents remove electrons, the greater the magnitude of the charge measured by the ORP probe, the greater the reduction or oxidation potential.

2.3.1.2 Oxygen Diffusion

The oxidation of tailings and waste rock materials inherently requires oxygen to be available as part of the chemical reaction process. Limiting the supply of oxygen can significantly reduce the rate of oxidation and generation of acid rock drainage. Covered in greater detail in Section 2.3.3, submersion of tailings under a sufficient depth of water has been shown to greatly reduce the rate of oxidation; which is due to the low dissolved oxygen (DO) concentrations in water (8.6 mg DO/L in water and 285 mg DO/L in air) and the low oxygen diffusion coefficient of water (2.9×10^{-9} m²/s at 25 °C for water, and 1.89×10^{-5} m²/s at 25 °C for air) (Awoh, Mbonimpa, et al., 2014).

2.3.1.3 Oxygen transport in porous media & Fick's Law

The use of soil covers for controlling oxidation of reactive tailings is covered in Section 2.3.4, these cover designs rely upon the principles of oxygen transport through soil materials. While oxygen can be transported through a variety of processes such as advection of dissolved oxygen in soil pore water, the main method of gaseous oxygen transport through soils is by molecular diffusion through gas filled pores in the soil structure (Kimball & Lemon, 1970). Gaseous oxygen diffusion can be described by Fick's law expressed one-dimensionally as shown in Equation 2–8.1 where the diffusive flux of gaseous oxygen is shown as F , D_e is the effective diffusion coefficient, C is the concentration of oxygen in the gas phase, and z is the depth. (Nicholson, Gillham, et al., 1989).

$$F(t) = -D_e \frac{\partial C(t)}{\partial z} \quad \text{Equation 2 – 8.1}$$

Incorporating the porosity and degree of saturation into Equation 2–8.1 allow for the calculation of the mass flux of oxygen diffused through porous soil material at a defined degree of saturation as shown in Equation 2–8.2 and Equation 2–8.3. The air filled porosity θ_a is calculated using the total porosity of the soil (θ_t) and the degree of saturation (S_r).

$$\theta_a = \theta_t(1 - S_r) \quad \text{Equation 2 – 8.2}$$

$$F(t) = -\theta_a D_e \frac{\partial C(t)}{\partial z} \quad \text{Equation 2 – 8.3}$$

The rate of diffusion of gaseous oxygen can be reduced by several orders of magnitude depending upon the degree of saturation of the soil material as shown in Figure 2-22.

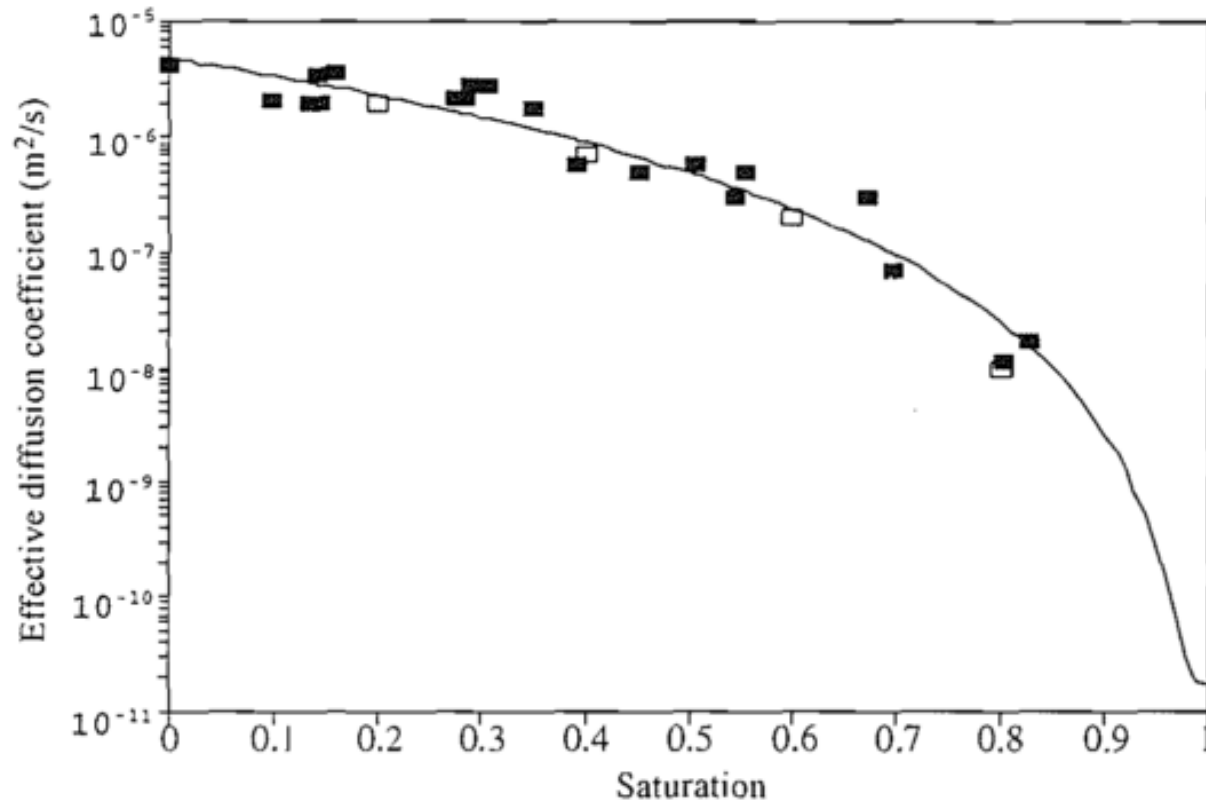
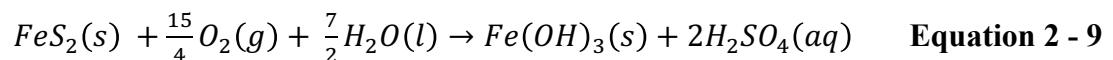


Figure 2-22. The relationship between soil saturation and the calculated effective oxygen diffusion coefficient

Data presented in Reardon and Moddle (1985) (■) and data from Elberling et al. (1993) (□) (Elberling et al., 1994)

The mass flux of oxygen through the cover into the tailings can be related to the theoretical maximum quantity of acid generated. The theoretical maximum acid flux represents the quantity of acid which would be produced were all oxygen passing through the cover to be consumed in the oxidation of sulphide tailings. The theoretical maximum acid flux can be related to the oxygen flux using the stoichiometry of the sulphide oxidation reaction shown in Equation 2 - 9.



Using the stoichiometric ratios of Equation 2-9, in the presence of water, 15 moles of gaseous oxygen (O_2) oxidize 4 moles of pyrite (FeS_2) to produce 8 moles of sulphuric acid (H_2SO_4) (E Yanful, 1994).

2.3.2 Technologies to control ARD in mine tailings

Previous studies and industrial projects have been undertaken to control the generation of ARD. The use of water covers and soil covers are outlined in the following sections.

2.3.2.1 Water Covers

Water covers of sufficient depth are effective in limiting oxygen transport and diffusion from the atmosphere to the submerged tailings. The Mine Environment Neutral Drainage (MEND) program extensively examined the effectiveness of water covers and determined that flooding tailings is the most successful method of mitigating ARD (Ernest Yanful & Simms, 1997). The addition of an inert cover layer above the tailings further prevents pyrite oxidation within the flooded tailings (Awoh et al., 2014).

While submerging reactive tailings beneath a water cover mitigates acid drainage, it presents other challenges which must be addressed. While dissolved oxygen consumption in submerged tailings can be over 2000 times less than in tailings exposed to atmosphere, metal mobility within the water cover may require that the water be treated (Vigneault & Campbell, 2001). The impoundment of a sufficient volume of water can often require dams, unfortunately, tailings dams have a rate of failure approximately 100 times more frequent than hydroelectric dams and impoundments for water reservoirs (1.2% compared to 0.01%) (Azam & Li, 2010). Cases of catastrophic tailings dam failures include the Mount Polley dam operated by Imperial Metals which failed in 2013 (Independent Expert Engineering Investigation and Review Panel, 2015), and the Fundão Tailings Dam operated by Samarco, which failed in 2015 and resulted in the deaths of 19 civilians (Bianchi, Assumpção, et al., 2016).

Tailings dams are highly vulnerable to seismic liquefaction, overtopping, erosion, and other failure methods which pose catastrophic liabilities to mining companies and the surrounding communities and environment.

2.3.2.2 Soil Covers

Soil covers can be employed to restore tailings and waste rock areas to resemble a naturally vegetated state, as well as to minimize acid rock drainage. Simple soil covers may be employed where ARD is not of concern, however, mitigation of ARD generally requires more care in cover design and construction.

2.3.2.2.1 Monolayer Covers with an Elevated Water Table

Covers can use one layer of material as a protective barrier against water infiltration and oxygen diffusion (as well as providing other benefits such as tailings dust suppression) under specific climate conditions. Monolayer covers can be effectively coupled with an elevated water table technique to ensure saturation of the tailings is maintained. So long as the depth of the water table below the surface of the tailings does not exceed the Air Entry Value (AEV) of the tailings material, then the tailings remain saturated and oxygen diffusion is minimized (see Figure 2-23). The concept of AEV and suction values will be clarified in Section 3.

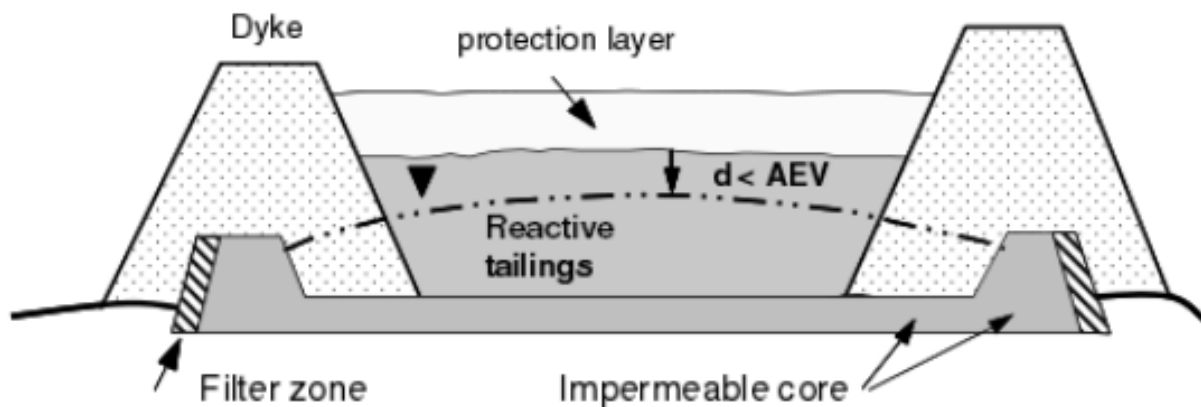


Figure 2-23. Conceptual model of an elevated water table within reactive tailings for reducing acid rock drainage
(Bussière & Aubertin, 2016)

De-sulphurized tailings have been shown to be an effective monolayer cover material to reduce the requirement for externally sourcing cover materials (Dobchuk, Nichol, et al., 2013), however, controls such as water table depth and cover material grain size were required to limit oxygen diffusion through the cover. Monolayer covers implemented without an elevated water table or additional measures to control oxygen diffusion have been shown to fail and allow oxygen

diffusion through the cover during periods of intense drying or precipitation (DeSisto, Jamieson, et al., 2017).

Laboratory scale tests have shown the potential for utilizing permeable reactive layers within tailings impoundments to neutralize pH and remove arsenic and dissolved metals from solution (Ahn, Chon, et al., 2003). The use of reactive layers has been investigated in the field and tests indicate that treatment layers containing organic carbon may be used to promote sulfate reduction and metal sulfide precipitation (Hulshof, Blowes, et al., 2006).

2.3.2.2.2 Multilayer Covers – Infiltration Barriers

Covers constructed using several materials of different hydrogeological properties can be used to reduce oxygen ingress and water flux through to the underlying tailings. The type of cover designed is contingent upon the precipitation and evaporation conditions at the tailings site.

Multilayer covers acting as infiltration barriers have been employed in the field using relatively impermeable geomembranes, geosynthetic clay liners, or fine grained soils such as compacted clay liners. The establishment of an impermeable layer prevents the physical infiltration of water during precipitation events; these covers require strict attention to the integrity of the barrier layer. Certain geotechnical risks exist when constructing infiltration barriers on inclines due to the development of macroscopic shear planes within the soil strata (Bussière & Aubertin, 2016). An example of a water barrier layer is shown in Figure 2-24.

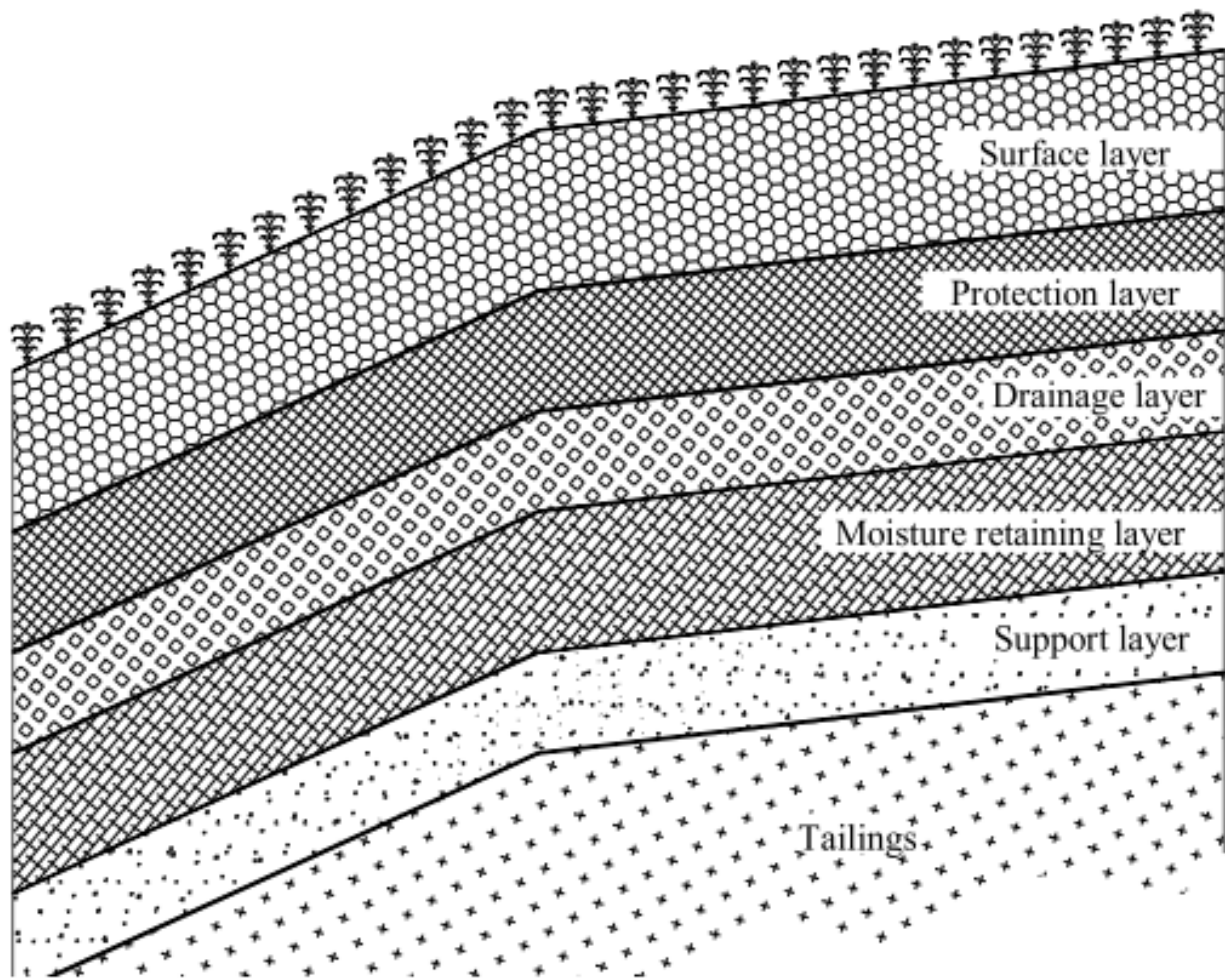


Figure 2-24. Example of a multilayer cover designed with a saturated barrier layer (Bussi re & Aubertin, 2016)

2.3.2.2.3 Multilayer Covers – Store and Release

Water retaining layers can be employed in climates with moderate precipitation; these covers store water in upper layers of the cover during precipitation events and utilize runoff and evaporation to mitigate water ingress. When combined with inclined surfaces and slopes, water multilayer store and release covers can also be used to direct water held within the cover away from the underlying tailings (Aubertin, Bussi re, et al., 2016).

2.3.2.2.4 Multilayer Covers - Capillary Barrier Covers

Capillary barrier covers are a multilayer cover designed to limit oxygen diffusion to the underlying tailings by maintaining a saturated cover layer through which oxygen does not readily diffuse. The saturated cover is generally constructed by layering a coarse material over the tailings, and topping the coarse material with a finer layer material with lower hydraulic conductivity which will remain saturated and create a capillary barrier (Nicholson et al., 1989). The establishment of a capillary barrier relies on the hydraulic conductivity and water retention characteristics of the materials used (these parameters are described in Section 2.4.2.). Briefly explained, the differences between the pore size distribution of the fine and coarse layer develop capillary and adhesion forces within the fine grained soil layer under unsaturated conditions which prevent the downward flow of water out of the fine layer (Williams, Hoyt, et al., 2011). A simplified illustration of a conventional capillary barrier cover utilizing clay is shown in Figure 2-25, and depicts the desaturation of the coarse sand layer and the highly saturated fine layer to limit water flux and oxygen diffusion. A layer of relatively coarse material overlying the saturated layer is generally employed to minimize erosion of the saturated layer (Woysner & Yanful, 1995).

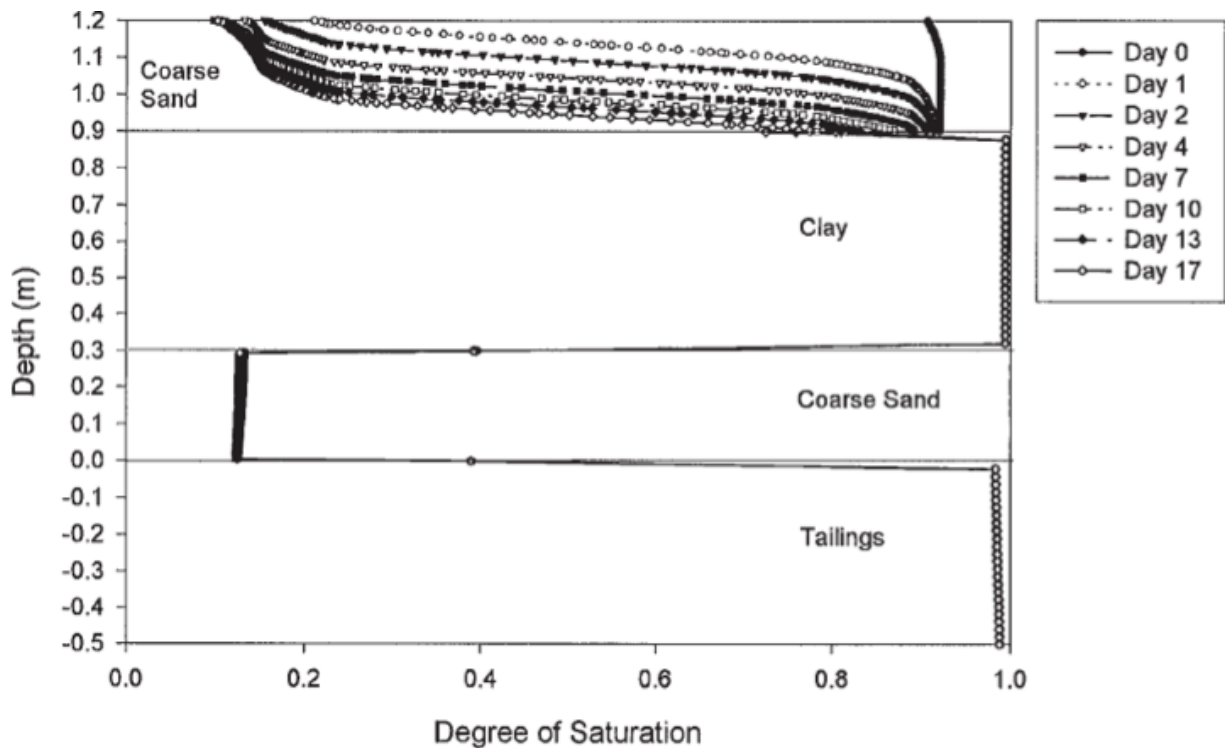


Figure 2-25. Degree of Saturation profile in a simulated capillary barrier cover (Ernest K Yanful & Choo, 1997)

The upper fine layer accumulates water during precipitation events, however, due to the low hydraulic conductivity of the upper fine soil layer the water does not readily flow down into the underlying coarse material. As water accumulates in the fine layer it becomes saturated while the lower coarse layer remains relatively unsaturated. The lower capillary barrier is established under suction conditions where the fine soil remains saturated while the underlying coarse soil desaturates as shown in Figure 2-26 (a) at point φ_a . The desaturation of the lower coarse layer results in a reduction of the unsaturated hydraulic conductivity for the lower coarse layer which limits downward drainage from the saturated fine layer. The capillary barrier effect may be overcome should the suction decrease (moving right to left in Figure 2-26 (a) along a wetting path) to such an extent that the residual water content of the lower coarse layer is exceeded (φ_r and θ_r). Should the lower coarse layer become progressively more saturated, the hydraulic conductivity of the coarse material will increase as shown by the rapid rise of the sand curve in Figure 2-26 (b) at suctions below the residual water content. The increase in hydraulic conductivity of the coarse layer allows water to move more readily between the overlying fine layer and the underlying tailings, resulting in a failure of the capillary cover.

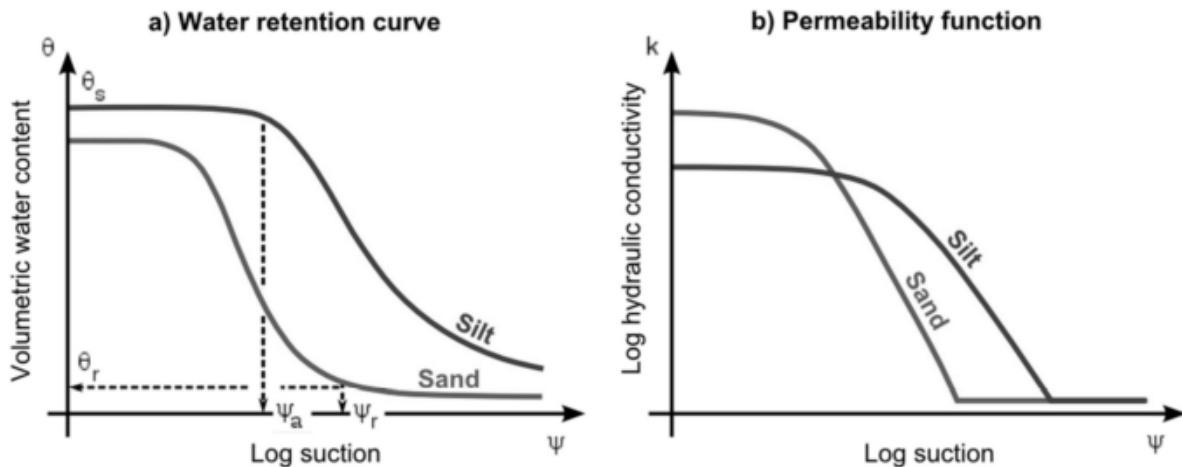


Figure 2-26. Schematic showing hydraulic functions of a silt (fine grained soil) and sand (coarse grained soil)
(Aubertin et al., 2016)

Laboratory scale testing of capillary barrier covers have shown that saturated oxygen barrier layers can be created and maintained with both overlying and underlying capillary barriers (a fine layer sandwiched between coarse layers as shown in Figure 2-25). The uppermost coarse layer has been found to minimize erosion of the saturated layer and protect the barrier layer against excessive evaporative flux from the cover surface (Woyshner & Yanful, 1995). Thicknesses of the underlying coarse layer as low as 15 cm thick have been found to be sufficient to prevent drainage of the saturated barrier layer where the air-entry value of the barrier layer is exceeded (Choo, 1996). Laboratory testing and oxygen diffusion modelling have shown that development of a fine barrier layer with a high degree of saturation and low hydraulic conductivity can be more readily achieved by placing the material at a high water content and compacting the layer (E.K. Yanful, Bell, et al., 1993).

Field evaluations have demonstrated the ability of capillary barrier covers to limit water infiltration and oxygen transport. Two 400 m² test covers on acid-generating tailings at the Waite Amulet site, near Rouyn-Noranda, were constructed with a 60 cm thick, compacted clay between two 30 cm sand layers, with the whole cover topped with a 10 cm thick gravel layer to prevent erosion. Lysimeters beneath the covers were used to capture infiltration water, and reported a net percolation through the cover of 4% of the precipitation after four years, which corresponded to the degree of percolation predicted through modelling. It was also observed that the clay barrier layer maintained a high degree of saturation throughout the monitoring period (Woyshner & Yanful, 1995).

Other field testing conducted near London, Ontario, utilizing compacted till placed between gravel layers has indicated that the degradation of cover integrity may occur due to desiccation or freezing and thawing of the cover layers. The test plots were created using a compacted till barrier between layers of gravel, with one half of the cover topped in coarse stone and the other capped in topsoil. The till under the stone cap remained unchanged over the study period. It was observed that desiccation occurred in the till beneath the topsoil as the capillary barrier created between the topsoil and the gravel prevented water infiltration through to the till barrier layer to enable recharge. It was observed that the hydraulic conductivity of the till layer under the topsoil increased

by two orders of magnitude (2.0×10^{-10} m/s to 1×10^{-8} m/s after one year) and water percolation through the till increased from 4.6% to 6.7%. (E. K. Yanful, Simms, et al., 1999).

The ability to maintain a saturated capillary break in soil covers is limited on slopes, and may not be an ideal cover design for steep or highly undulating terrain (Maqsoud, Bussi re, et al., 2011). Alternate cover materials such as crushed concrete have been assessed as low-cost replacements for sand in the coarse layer with apparent success in maintaining slope stability and limiting water infiltration (Rahardjo, Santoso, et al., 2013).

2.3.3 Organic Covers

Organic covers have been evaluated for their effectiveness in mitigating ARD, as well as for their ability to revegetate tailings areas. Previous studies have examined the application of liquid sewage sludge, the incorporation of biosolids into the top tailings layer, and monolayer cover surface application of biosolids.

The results shown in Figure 2-27 were obtained from a greenhouse scale study conducted on tailings from the El Teniente copper mine in Chile which were subjected to various treatment (lime stabilization, inoculation with fungal spores, mixed with biosolids, or covered with surface applied biosolids). The biosolids used in the study were obtained from El Trebal municipal water treatment plant.

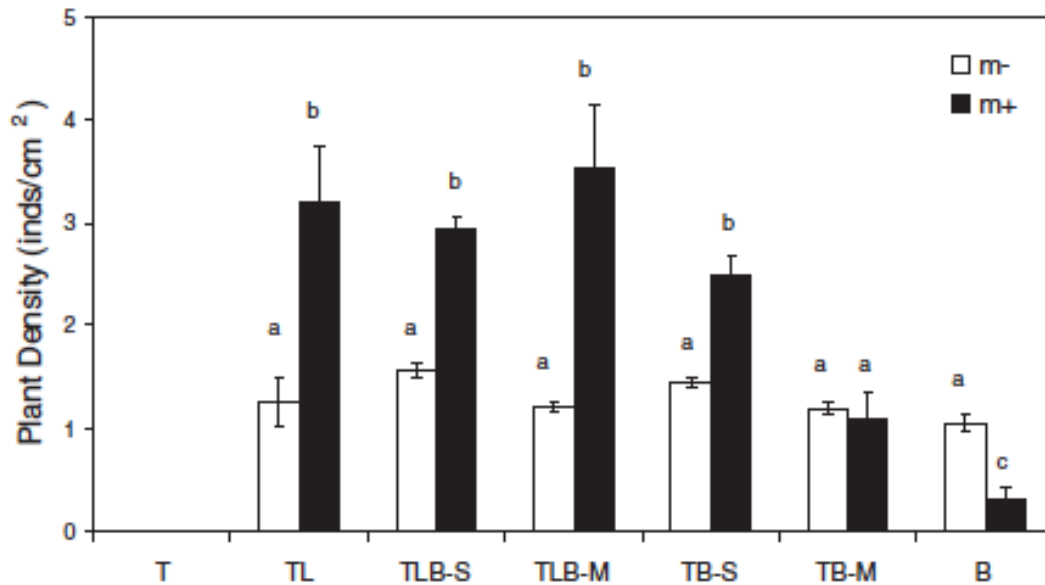


Figure 2-27. Density of *Lolium perenne* var. *nui* plants on experimental treatments. White and black bars represent the treatments (m-) without and (m+) with inoculation of mycorrhiza, respectively. Mean and standard deviation are given. T = tailings, L = Lime, B= Biosolids, S = surface application of biosolids, M= mixing of biosolids with tailings. (Verdugo, Sánchez, et al., 2011)

Shoot biomass was highest on tailings with surface application of biosolids, with or without liming. Inoculation with mycorrhiza resulted in a significant and positive effect on shoot biomass in treatments TLB-S and TB-S. Highest root biomass for non-inoculated substrates occurred on treatments TL, TLB-S and TB-S. Roots were thick, short and restricted to the upper organic matter layer on treatments TLB-S and TB-S. The restriction of roots to the upper organic layer was attributed to metal toxicity avoidance from the plants and also due to the high nutrient levels in the biosolids which negate the need for “root-foraging” responses. (Verdugo et al., 2011)

Neutralizing the pH of acid generating mine tailings is of significant importance in closure planning; low pH environments may promote growth of metal oxidizing bacteria such as *thiobacillus ferrooxidans* which can greatly increase acid generation of tailings and waste rock.

Tests utilizing kinetic weathering cells were conducted to observe the results of biosolid application to weathered copper mine tailings (pH 3.3). Neutralization of acid generating tailings

was apparent as pH values as high as 6.3 were observed following application. Biosolids applied to circumneutral tailings resulted in no change in tailing or leachate pH (Pond, White, et al., 2005).

Monitoring of covers developed at Thompson Mine in Pennsylvania revealed that concentrations of metals in vadose water samples (<5 m depth) from sludge-treated spoil (pH 5.9) were not elevated relative to untreated spoil (pH 4.4). This study was conducted on an area of reclaimed coal mine workings which were producing acidic groundwater (Cravotta, 1998).

There is a potential for nitrate leaching when mine tailings are amended with biosolids, especially at high rates of biosolids application. The potential for nitrate leaching from biosolids-amended mine tailings can be reduced by establishing a permanent plant cover. Mixing the biosolids with the tailings has been shown to reduce nitrate transport. (Santibáñez, Ginocchio, et al., 2007).

Metal mobility within tailings impoundments is of significant importance as leaching metals into the surrounding environment and/or excessive uptake by plants (and subsequent accumulation in the food chain) are a possibility. Metal mobility may be increased through chemical processes such as the activation of bacteria like thiobacillus ferrooxidans which increase the rate of iron oxidation and acid generation. Thiobacillus ferrooxidans activity can be suppressed by maintaining a pH above 2.5. Addition of organic materials to sulphide tailings may induce metal mobilization, however, several studies have shown that the net effect of vegetative covers are positive with regards reducing metal mobility.

An oxidized tailings and sewage sludge cover tested at Aitik mine in Sweden was planted with barley and red fescue; the metal concentration in the plant organic matter was tested to observe plant uptake. The results indicate that the plant uptake of the metals is greatly variable between the two plant types; barley accumulates greater metal concentrations in the straw than in the grain, and both plant types generally accumulate higher metals concentrations when planted in sludge compared to on the control plots as shown in Figure 2-28. (Forsberg & Ledin, 2006).

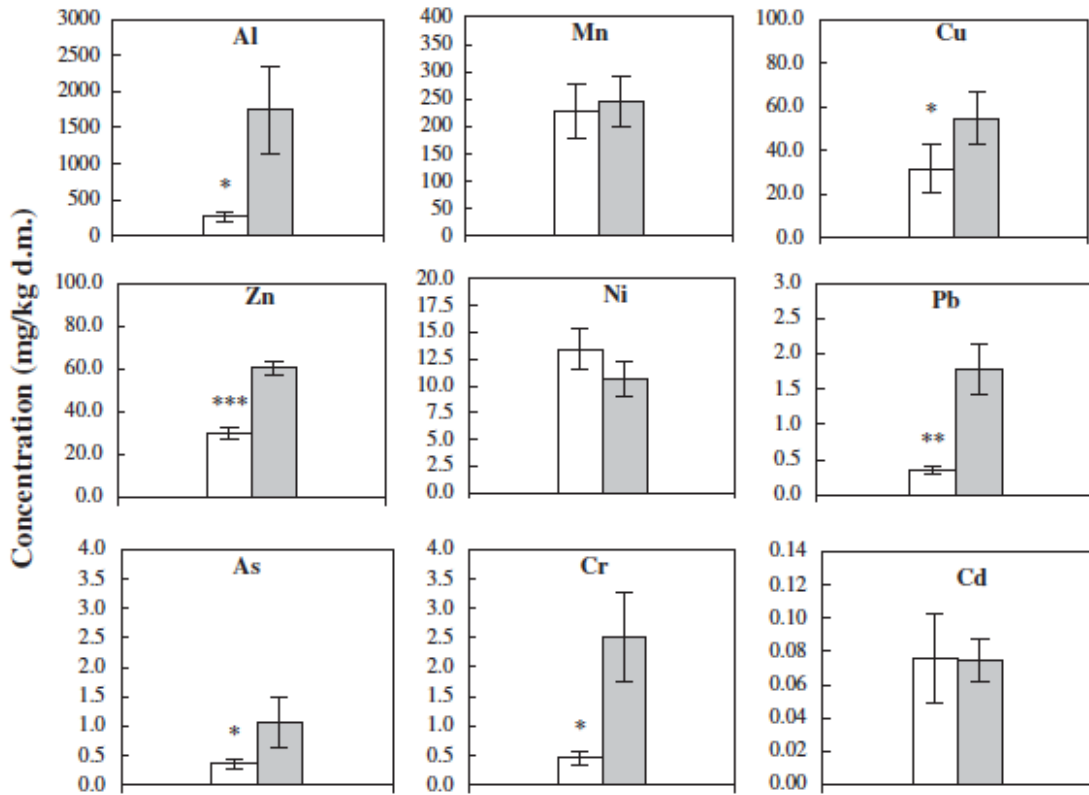


Figure 2-28. Metal concentrations in shoots of red fescue grown in control plots (white bars) and in plots treated with sewage sludge (grey bars) (Forsberg & Ledin, 2006)

Root exudates may indirectly enhance metal mobilization through stimulation of microbial activity, redox reactions, the formation and precipitation of insoluble metal compounds in the rhizosphere. In the test plots at the Dabaoshan mine, a slight trend of increasing diethylenetriaminepentaacetic acid (DTPA) extractable Zn, Cu and Cd with the time was observed, whereas DTPA extractable Pb remained steady (Yang, Liao, et al., 2016).

The Green Mines Green Energy project undertaken by CANMET Mining and Mineral Sciences Laboratories from Natural Resources Canada investigated the effects of papermill biosolids covers on soil water chemistry, metal mobility, and effluent treatability. It was noted that arsenic mobility occurred within column tests using Goldcorp's Porcupine Gold Mines tailings and Abitibi papermill biosolid cover (Tisch, Zinck, et al., 2008). Further tests using gold tailings and papermill biosolids from test plots at the Delnorte mine near Timmins revealed that the application of biosolids increased arsenic mobility (Paktunc, 2013).

In the same study as Figure 2-27 (Verdugo et al., 2011), elevated levels of copper and zinc were observed in vegetative shoots where biosolids were surface applied to tailings without the addition of lime as shown in Figure 2-29.

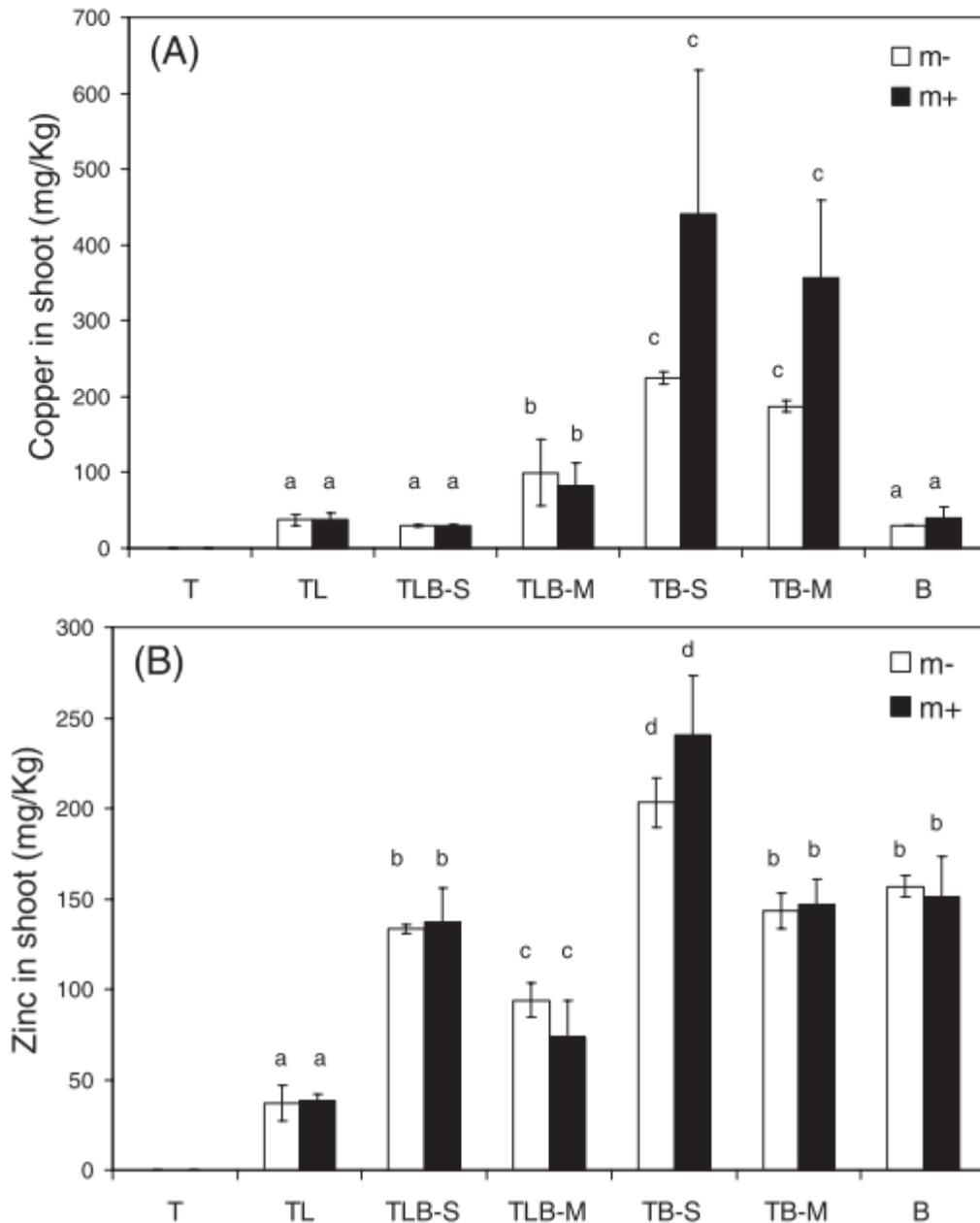


Figure 2-29. Copper and zinc contents in shoots of *Lolium perenne* var. *nui* plants on experimental treatments.

White and black bars represent the treatments without (m-) and with (m+) inoculation of mycorrhiza, respectively. Mean and standard deviation are given. T = tailings; L = lime; B = biosolids; -S = surface application of biosolids on tailings; and -M= biosolids mixed with tailings (Verdugo et al., 2011).

Application of municipal biosolids at Highland Valley Copper tailings areas observed that all elements measured except Mo and Cu remained in the range considered normal for vegetation. The elevated Cu levels were below the suggested tolerance level for agronomic crops and for cattle, however, molybdenum levels exceeded those considered safe for cattle consumption (Garnder, 2013).

Review of existing literature has not shown any study of the use of municipal biosolids or sewage sludge in capillary barrier covers.

2.4 An Unsaturated Flow Theory Framework

The development of capillary barrier covers requires an understanding of the flow of water through both saturated and unsaturated soils. This chapter provides an overview of water flow in unsaturated soils, and how these properties can be harnessed to develop a saturated barrier layer in a capillary barrier cover.

2.4.1 Theory of Water Flow Through Porous Media

Soils can be described as a porous medium wherein the inter-particle spaces allow for the advection and transport of water through the pore spaces within the soil mass.

2.4.2 – Darcy’s Law and Flow Through Saturated Soils

Water flow through soil is a result of differences in pressure head between two points. The total head at a point has three components: gravitational head, pressure head, and velocity head. In soils the velocity head is negligible when compared to the pressure head and head induced by gravity. The hydraulic head (h_w) can therefore be expressed as the water pressure head ($u_w/\rho_w g$) plus the gravitational head (γ) (Equation 2-10) (D. G. Fredlund, Rahardjo, et al., 2012).

$$h_w = \frac{u_w}{\rho_w g} + \gamma \quad \text{Equation 2 - 10}$$

The one-dimensional flow of water within porous media such as soils is governed by Darcy’s Law shown in Equation 2-11 (Darcy, 1856). Darcy’s Law states that the flow of water through a soil

mass is directly proportional to the difference in pressure between two points, and that flow is inversely proportional to the length of the distance travelled.

$$q = -k_s \frac{\partial h_w}{\partial \gamma} \quad \text{Equation 2 - 11}$$

In Equation 2-11, q is the flow rate of water (also referred to as seepage velocity or Darcy's flux), k_s is the saturated hydraulic conductivity of the soil, and $\partial h_w / \partial \gamma$ is the difference in hydraulic head between the start and end points (gradient). The negative sign in Equation 2-11 indicates that water flows from areas of high hydraulic head to areas of lower hydraulic head.

The hydraulic conductivity (k_s in Equation 2-11), also referred to as the coefficient of permeability, regulates the flow of water through soil and is generally assumed to be a constant for a given saturated soil (Bear, 1972). The hydraulic conductivity is not constant as the soil desaturates and all pore space is not available for laminar flow of water; water flow can be visualized as occurring only through channels and pore spaces which are fully saturated; as the soil desaturates, fewer pathways are available for water flow. The saturated hydraulic conductivity can be predicted via a number of methods, however, the predictive methods rely on several assumptions regarding homogeneity of the soil mass, porosity, and void distribution. Table 2-6 shows general permeability ranges for common soil types.

Table 2-6. Permeability of major soil groups
(adapted (Krumbein, 1937))

| Material | Grain size (mm) | Typical Hydraulic Conductivity (cm/s) | Drainage Properties |
|-----------------------------------|-----------------------------------------|---------------------------------------|------------------------|
| Clean gravels | 2 - 50 | $1 - 10^2$ | Good drainage |
| Clean sands, sand gravel mixtures | $2.5 \times 10^{-1} - 2$ | $1 - 10^{-3}$ | |
| Fine sands, silts, and mixtures | $2 \times 10^{-3} - 2.5 \times 10^{-1}$ | $10^{-3} - 10^{-7}$ | Poor drainage |
| Homogenous clays | $< 2 \times 10^{-3}$ | Below 10^{-7} | Practically impervious |

Several methods of predicting the hydraulic conductivity of soils have been proposed. One of the earliest methods utilizes grain size, and assumes a uniform grain size; the approximation method is shown in Equation 2-12 (Hazen, 1893).

$$k = C \cdot (D_{10})^2 \quad \text{Equation 2 - 12}$$

Where

k = saturated hydraulic conductivity (cm/s)

C = constant (between 100-150)

D_{10} = grain size at which 10% of the soil particles are finer than the specified size (cm)

The Hazen approximation shown in Equation 2-12 was developed for fairly uniform sands, where the uniformity coefficient $\left(\frac{D_{60}}{D_{10}}\right)$ is less than 2, and where D_{10} is between 0.01 cm and 0.3 cm.

Further efforts to predict hydraulic conductivity have attempted to utilize shape factors, and other parameters to account for variations within the soil pore structure which would affect the permeability of materials. The Kozeny-Carman equation utilizes semi-empirical constants to account for shape and tortuosity as shown in Equation 2-13 (Carman, 1937).

$$k = \frac{\gamma_w}{\mu} \cdot \frac{1}{C_s S_s^2 T^2} \cdot \frac{e^3}{1+e} \quad \text{Equation 2 - 13}$$

Where

k = saturated hydraulic conductivity (cm/s)

γ_w = density of water (g/cm³)

μ = viscosity of water ((N·s)/m²)

C_s = shape factor, around 2.5 for granular soils

S_s = specific surface (surface area / unit volume of solids), for uniform spheres $S_s = 6/D$ (D is the sphere diameter in cm)

T = tortuosity factor, around $\sqrt{2}$ for granular soils

e = void ratio

2.4.3 – Hydraulic Conductivity in Unsaturated Soils

As soil desaturates and pore spaces drain, fewer and smaller pathways are available for liquid to flow through; this results in a decrease in the hydraulic conductivity of the material. One method for approximating the unsaturated hydraulic conductivity of soil materials is shown in Equation 2-

14 where k_r is the unsaturated hydraulic conductivity at the specific level of suction (ψ), ψ_a is the air-entry value of the soil, and λ is a constant obtained by heuristic fitting to the soil's water retention curve (WRC) according to Equation 2-15 (Brooks & Corey, 1964).

$$k_r(\psi) = \left(\frac{\psi_a}{\psi}\right)^{2+3\lambda} \quad \text{Equation 2 - 14}$$

$$\left(\frac{\theta_w - \theta_r}{\theta_s - \theta_r}\right) = \left(\frac{\psi_a}{\psi}\right)^\lambda \quad \text{Equation 2 - 15}$$

Where the unsaturated hydraulic conductivity estimated by the Brooks-Corey method is greater than the saturated hydraulic conductivity, the saturated hydraulic conductivity is used. This change-over from saturated hydraulic conductivity to the estimated unsaturated hydraulic conductivity occurs at the suction corresponding to the AEV of the soil.

The relationship between suction and hydraulic conductivity is shown graphically in Figure 2-26 in Section 2.3.2.2.4.

2.5 Soil Suction Theory

Soil suction theory was first developed to understand water movement and holding capacity of soils for agricultural applications; it was initially observed that capillary forces within finer soil spaces were responsible for the movement or retention of water (Buckingham, 1907).

2.5.1 – Total Suction

The total soil suction is a combination of the osmotic suction due to solute potential, and matric suction due to capillary potential of the soil pore spaces (L. A. Richards, 1931). Equation 2-16 shows the relation between the total suction of water (ψ) and the relative humidity of air (\bar{u}_v/\bar{u}_{v0}) within the pore spaces using the Kelvin equation (Edlefsen & Anderson, 1943):

$$\psi = -\frac{RT}{v_w \omega_v} \ln\left(\frac{\bar{u}_v}{\bar{u}_{v0}}\right) \quad \text{Equation 2 - 16}$$

where v_w is the specific volume of water in m^3/kg at a given temperature; ω_v is the molar mass of water vapour (18.016 kg/kmol); \bar{u}_v is the partial pressure of pore-water vapour in kPa; \bar{u}_{v0} is the saturation vapour pressure of pure water over a flat surface in kPa at a given temperature, and R is the universal molar gas constant, [8.31432 J/mol·K]; and, T is the absolute temperature in Kelvin.

The total suction (ψ) can also be expressed as the sum of matric ($u_a - u_w$) and osmotic (π) suction as shown in Equation 2-17, where u_a is the pore-air pressure and, u_w is the pore-water pressure, both in kPa.

$$\psi = (u_a - u_w) + \pi \quad \text{Equation 2 - 17}$$

2.5.2 – Matric Suction

Pore spaces within partially saturated soils can be simplistically represented by a capillary tube model, in which the pore spaces act in a similar fashion as a capillary tube.

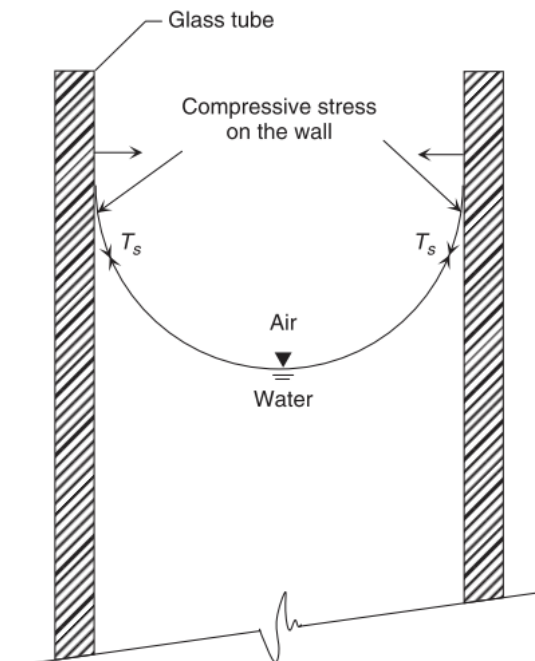


Figure 2-30. Forces acting on capillary tube
(D. G. Fredlund et al., 2012)

The surface tension and capillary forces generated within the pore structures give rise to matric suction, wherein water is retained within the soil pore spaces. A simplified capillary tube model is shown in Figure 2-31 where Equation 2-18 is used to express the pressure differential between the air and water phase developed within the capillary tube as a function of the surface tension (T_s), curved meniscus radius (R_s), and the contact angle (α) between the solid surface and gas-liquid interface.

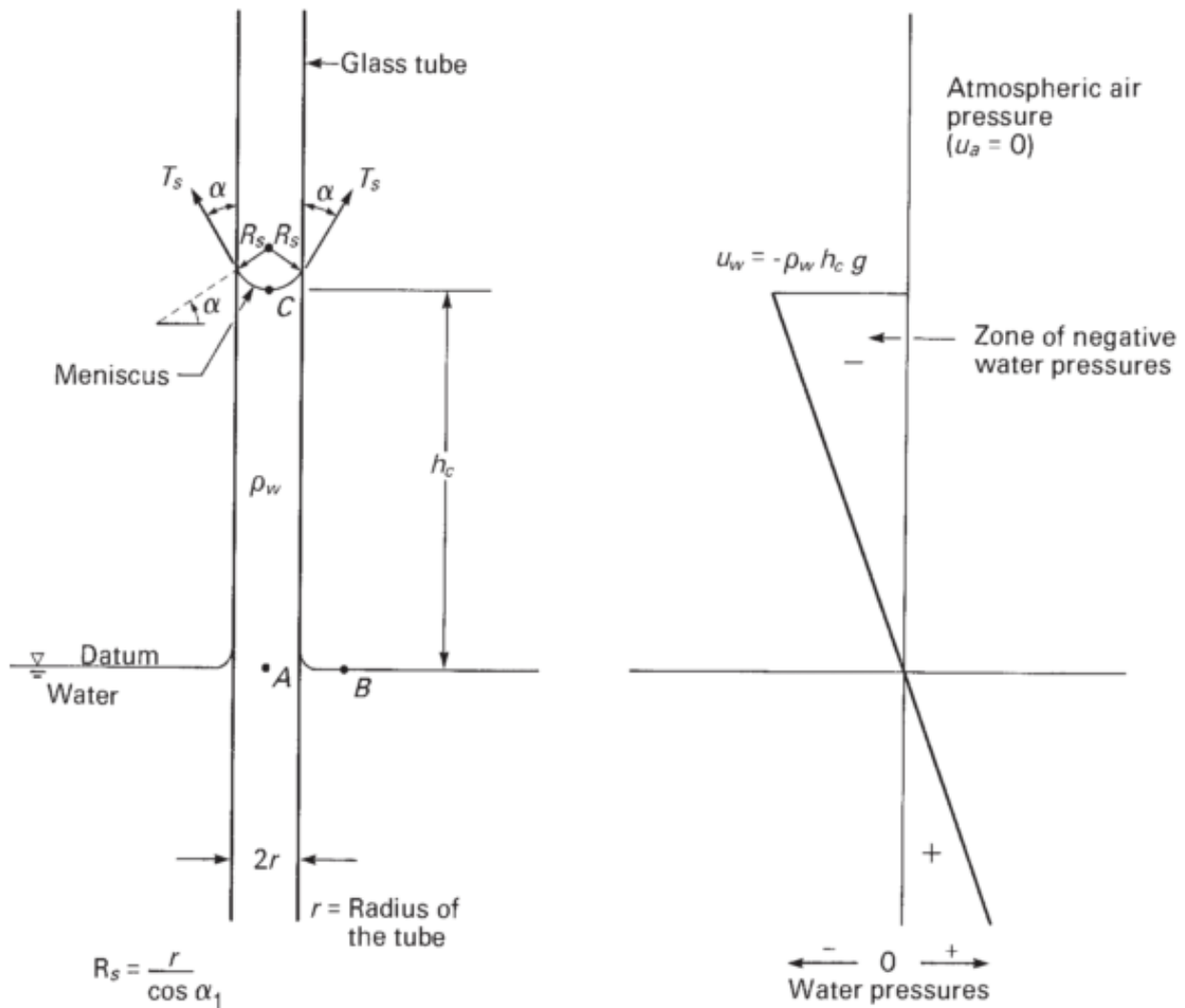


Figure 2-31. Physical model of capillarity
(D. G. Fredlund et al., 2012).

$$\Delta u = (u_a - u_w) = \frac{2T_s \cos \alpha}{R_s} \quad \text{Equation 2 - 18}$$

The contact angle of the liquid can be used to describe the behaviour of the liquid; a liquid with a contact angle less than 90° can be described as “wetting”, and will spread when applied on a solid surface. When the contact angle is less than 90° capillarity occurs wherein water rises within the soil pore spaces (Marinho, Take, et al., 2008). Figure 2-31 demonstrates the surface tension, the amplitude of which is dependent upon the material comprising the capillary tube wall, and adhesion between air and water at the interface. The contact angle for pure water and clean glass is zero (ie. $\alpha = 0$, $\therefore \cos\alpha = 1$), and under atmospheric conditions the pore-air pressure (u_a) is equal to zero, so Equation 18 can be simplified to Equation 2-19 and Equation 2-20.

$$(u_a - u_w) = \frac{2T_s}{R_s} \quad \text{Equation 2 - 19}$$

$$-u_w = \rho_w \cdot g \cdot h_c \quad \text{Equation 2 - 20}$$

In Equation 2-19, ρ_w is the density of water, and h_c is the height of the capillary head rise in meters. Using Equation 2-20 the absolute water pressure (u_w) is shown to be zero when air pressure is atmospheric (101.6 kPa), $T_s = 0.072$ N/m at 20°C , and the contact angle (α) is zero; indicating that zero water pressure exists at a capillary radius of $1.4 \mu\text{m}$. The resultant pore water pressure become more negative at decreasing pore radii, indicating that finer soils exert greater suction forces at a given water content (Marinho et al., 2008).

2.5.3 – Osmotic Suction

Equation 2-17 in Section 2.5.1 uses the parameter π to represent osmotic suction, which is the component of total suction attributed to changes in the partial pressure of water vapour relative to the pore water (D. G. Fredlund et al., 2012). The presence of dissolved ions in soil pore-water decreases the equilibrium soil vapour pressure relative to the partial pressure of water vapour in equilibrium with pure water, creating an ionic gradient. Osmotic suction refers to the development of the ionic gradient and subsequent movement of ions from areas of high to low concentration within the soil.

Osmotic suction affects the total suction of soil-water without affecting the matric suction which would be observed using devices such as tensiometers. Soils from specific geological strata have been found to contain a relatively constant salt content, resulting in fairly consistent osmotic

suction. The osmotic suction is often found to change most drastically near the ground surface where evaporation or excessive infiltration affects the geochemistry of the soils by accumulating or removing salts and ions in the soil pores. Evaporation can cause accumulation of ions near the ground surface, resulting in elevated osmotic suction. This is further explained in Section 2.6.2.

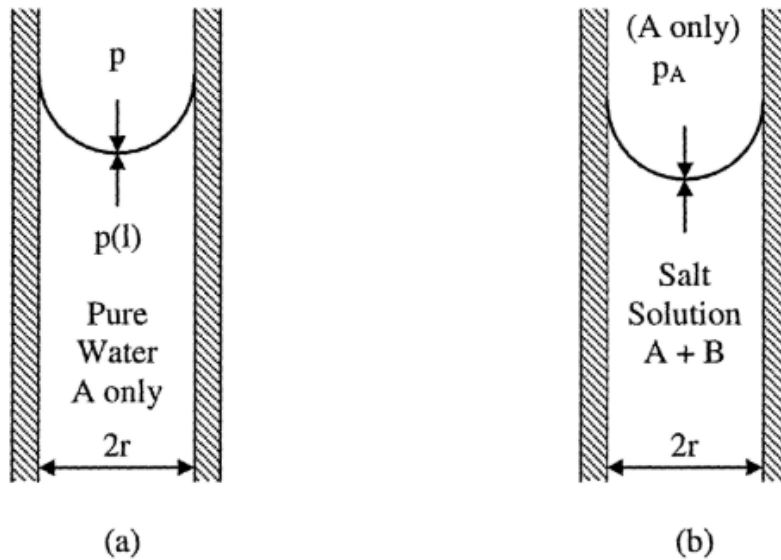


Figure 2-32. Presence of ions affecting partial pressure of water in soil pore spaces (b) compared to pure water in pore space (a)
(Miller & Nelson, 2006)

Osmotic suction can induce a pressure difference across a semi-permeable membrane, and produces similar differentials in soils with varying concentrations of ions. In Figure 2-33 water flows from the pure water side to the soil solution side to equalize the concentration of ions. The hydrostatic pressure difference (H) at equilibrium is equal to the osmotic suction induced by the ions in the soil.

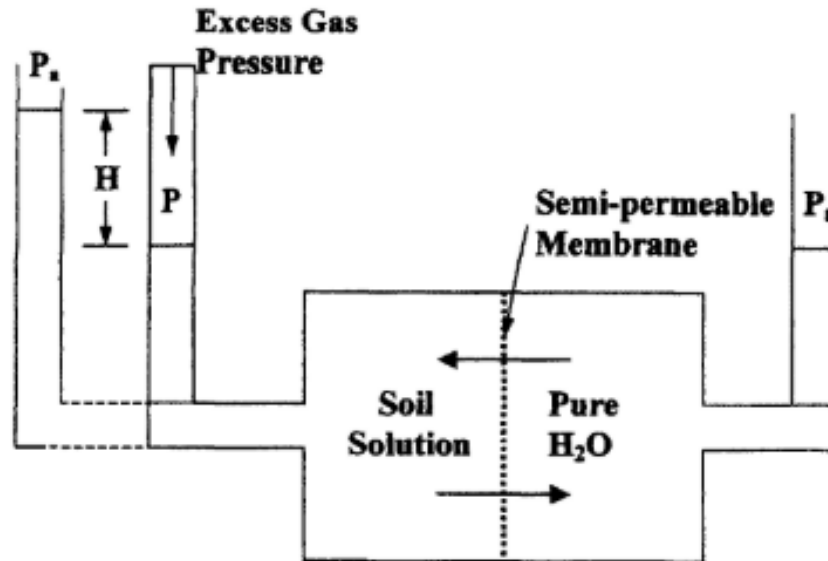


Figure 2-33. Pressure difference induced by osmotic suction across a semi-permeable membrane
(Tindall & Kunkel, 1998)

The calculation of osmotic suction can be done by multiplying the measured electrical conductivity of the pore water solution by a constant as shown in Equation 2-21 (L. Richards, Allison, et al., 1954) where EC is the electrical conductivity measured in milliSiemens per centimeter. The electrical conductivity is representative of the quantity of ions in solution; electrolytes dissociate into charged ions in the presence of water. The ions present conduct electric current, therefore the greater the concentration of ions in solution, the greater the electrical conductivity (Abedi-Koupai & Mehdizadeh, 2008).

$$\pi = 0.36 \cdot EC \cdot 101.35 \quad \text{Equation 2 - 21}$$

Where:

π = Osmotic Suction (kPa)

EC = Electrical Conductivity (mS/cm)

2.6 Water Content – Suction, Saturation – Suction, and Void Ratio –Water Content relationships

The soil-water characteristic curve (SWCC), also referred to as a water retention curve (WRC), graphically relates the water content and soil suction; a sample WRC is shown in Figure 2-34. The

WRC typically depicts the water content, either as volumetric or gravimetric water content, or the degree of saturation, at varying degrees of suction. The WRC provides valuable information regarding the water retention properties of the soil in question, such as the saturated water content, Air-Entry Value (AEV), and the Residual Water Content (θ_r).

Recall Equation 2-18 where the negative pore-water pressure is a function of pore size; this implies that the negative pore pressure of the larger pores will be overcome first, and therefore begin desaturating at lower suctions relative to the smaller pores. The AEV is the level of matric suction required to begin desaturation of the largest pore spaces.

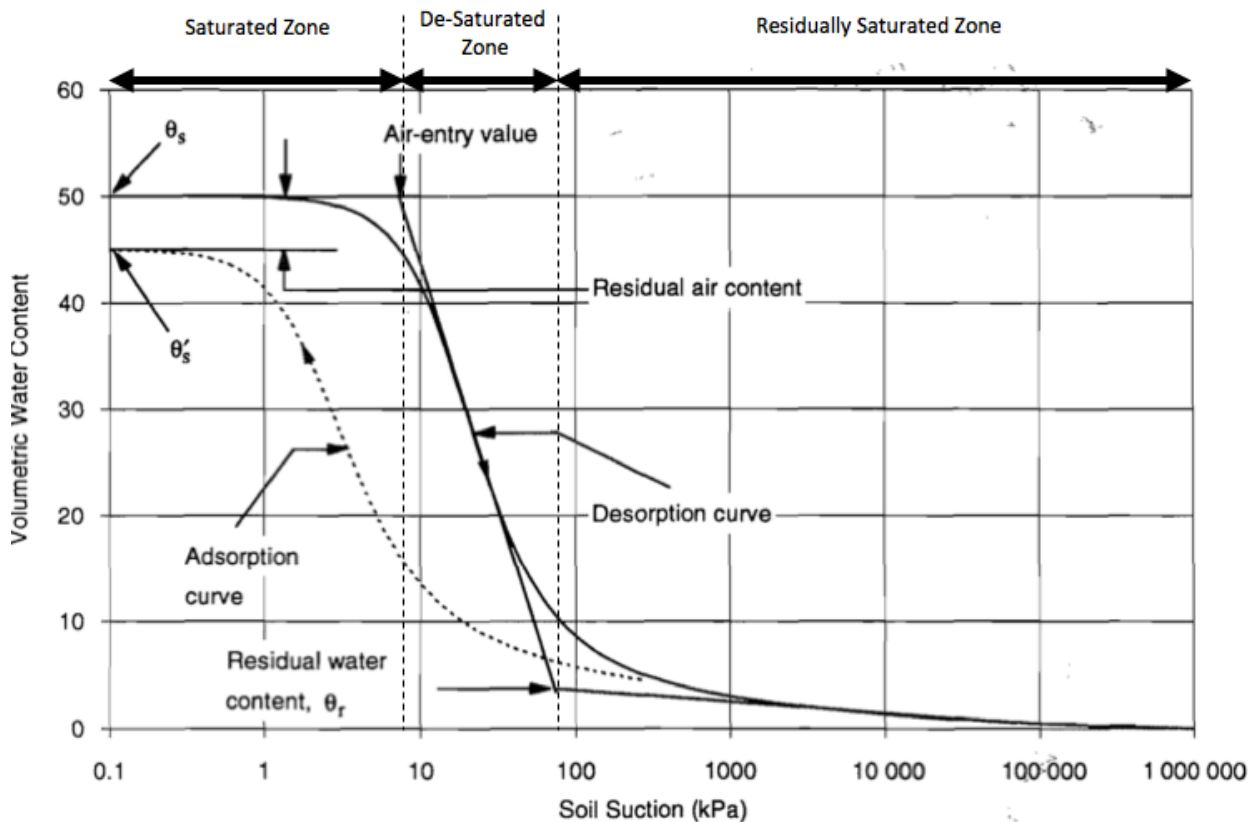


Figure 2-34. Typical Water Retention Curve (drying and wetting path) for a fine-grained soil

(adapted)(D.G. Fredlund, Xing, et al., 1994)

The residual water content (θ_r) is the water content beyond which the desorption of water from the smallest pore spaces requires significantly larger changes in suction relative to previous desaturation as shown by the change in slope of the WRC following initial desaturation.

As height above the water table increases, the gravitational potential energy acting on the pore-water increases, and requires increased matric suction to maintain saturation of the soil pore spaces. Above the water table the matric suction at a specific point in the soil needed to maintain saturation can be determined solving a nonlinear partial differential equation shown in Equation 2-22. θ is the volumetric water content, t is time, z is the elevation, k_r is the unsaturated hydraulic conductivity at z , and h is the matric suction in meters of head which can be converted into kPa (Richardson, 1922). A modification to Equation 2-22 shows the same relationship stated in terms of total head in Equation 2-23 with S_s representing the specific storage of the soil material (Witteman, 2013).

$$\frac{\partial \theta}{\partial t} = \frac{\partial}{\partial z} \left[k_r \left(\frac{\partial h}{\partial z} + 1 \right) \right] \quad \text{Equation 2 - 22}$$

$$-S_s \frac{\partial h}{\partial t} = \frac{\partial}{\partial z} \left[k_r \left(\frac{\partial h}{\partial z} + 1 \right) \right] \quad \text{Equation 2 - 23}$$

Equations 2-22 and 2-23 can be used to develop analytical solutions for determining the flow and saturation state of the soil elevation profile.

2.6.1 Hysteresis and factors affecting the Water Retention Function

As seen in Figure 2-35 and further illustrated in Figure 2-36 the water retention function may shift depending on the initial volumetric water content and whether the soil is adsorbing or desorbing water (a wetting or drying path). The change is typically attributed to permanent volumetric deformation and shrinkage of the soil as the pore spaces desaturate and the effective stress increases due to a dissipation of pore-water pressure.

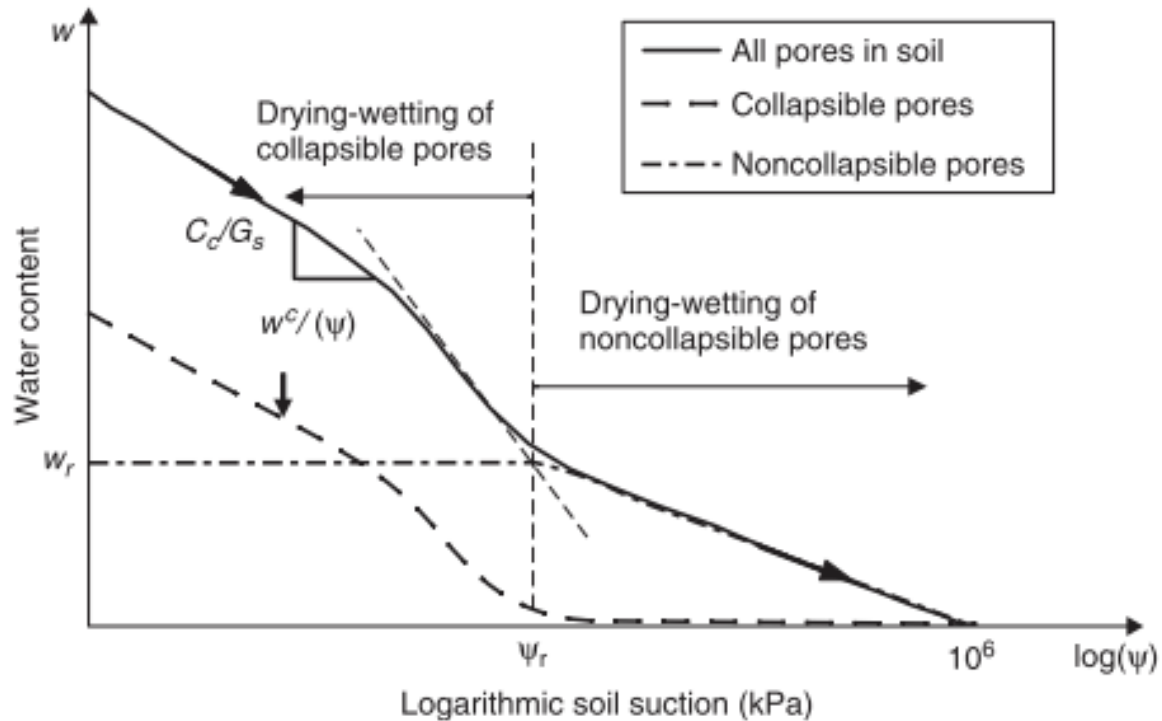


Figure 2-35. Illustration of hysteresis as a result of changes in pore space distribution after drying

(D. G. Fredlund et al., 2012)

In soil mechanics and geotechnical engineering, the Optimum Water Content (OWC) refers to the water content which results in the maximum dry density of a soil volume, indicating the water content at which the greatest degree of compaction can be achieved. At water contents which are dry-of-optimum (below the OWC) the soil will resist compaction due to shear stresses. The addition of water lubricates the soil particles, however, water contents in excess of the OWC, referred to as being wet-of-optimum, will result in elevated pore water pressures which resist compaction.

Soils compacted to different initial dry densities contain different pore-size distributions; increasing compaction causes a decrease in the saturated water content as there is less void space available. Compaction reduces the size of available pore spaces, increasing the AEV, and increasing the residual water content as water is removed from the small pore spaces less readily (Croney & Coleman, 1954). Conflicting results have been found regarding partial reduction of hysteresis between the drying and wetting curves as shown in Figure 2-36 where the hysteresis

loop is lower at a higher degree of compaction, while in Figure 2-39 the hysteresis loops are independent of applied stress.

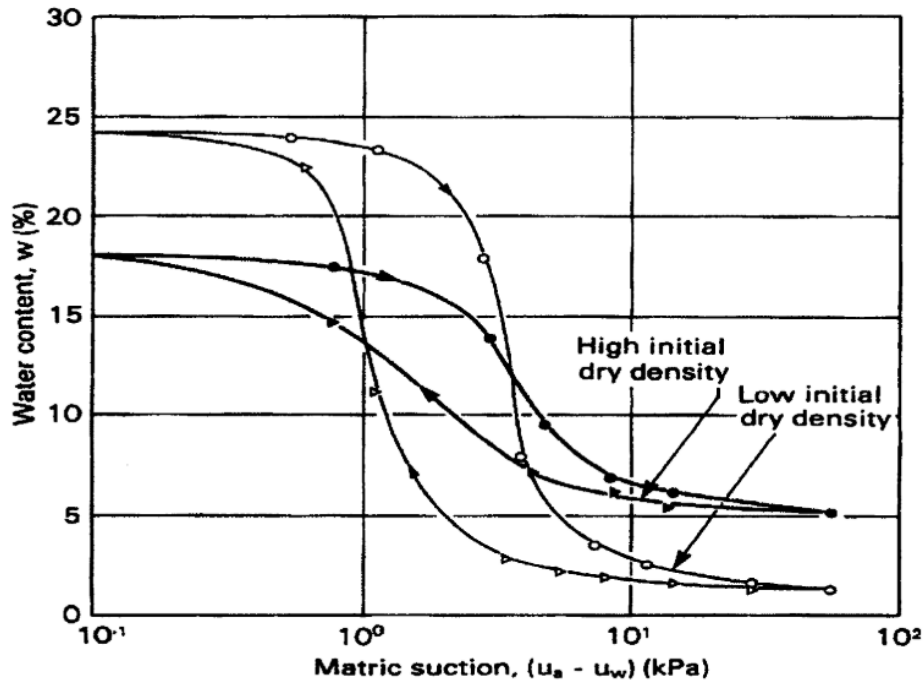


Figure 2-36. SWCC for a silty sand at two levels of compaction
(Croney & Coleman, 1954)

The effects of stress history are also shown in Figure 2-37 where a till was compacted and rehydrated to the optimum water content. It can be seen that the greater the compaction pressure applied to the soil, the greater the AEV (Vanapalli, Fredlund, et al., 1999).

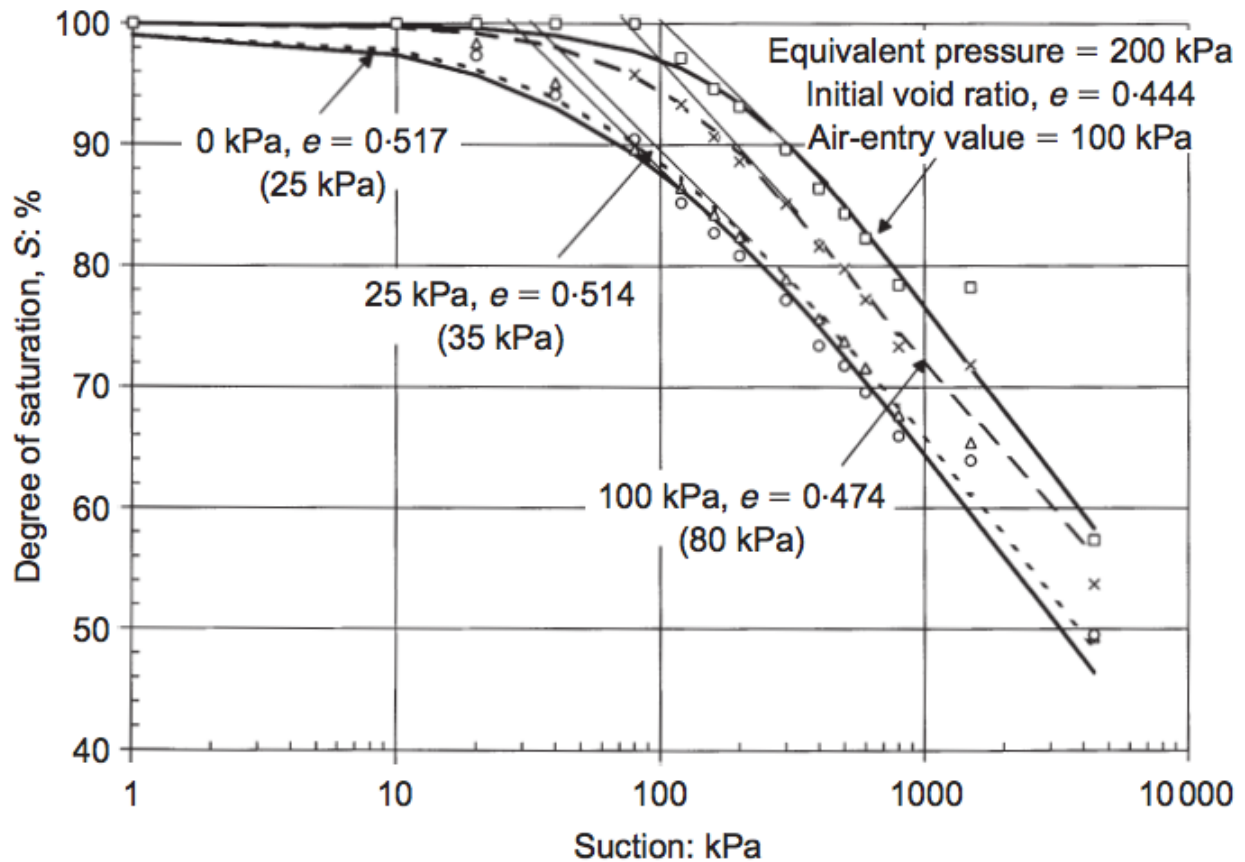


Figure 2-37. SWCC for till compacted to OWC
(Vanapalli et al., 1999)

The effect of compaction on soil macrostructure and the water retention properties can be seen in Figure 2-38 where soil compacted dry of optimum desaturates more readily than soils at optimum or wet of optimum water contents at low applied suctions. The larger pore spaces which are between the macroscopic soil agglomerations in the dry of optimum samples shed water at relatively low levels of suction. The pore spaces in the soils compacted at wet of optimum water contents are described as being occluded or lacking interconnection, and therefore offer greater resistance to desaturation relative to the soils compacted dry of optimum. Soils begin to undergo pore space occlusion near the optimum water content, which results in the SWCC for soil compacted at the OWC to lie between the wet of optimum and dry of optimum curves (Vanapalli et al., 1999)

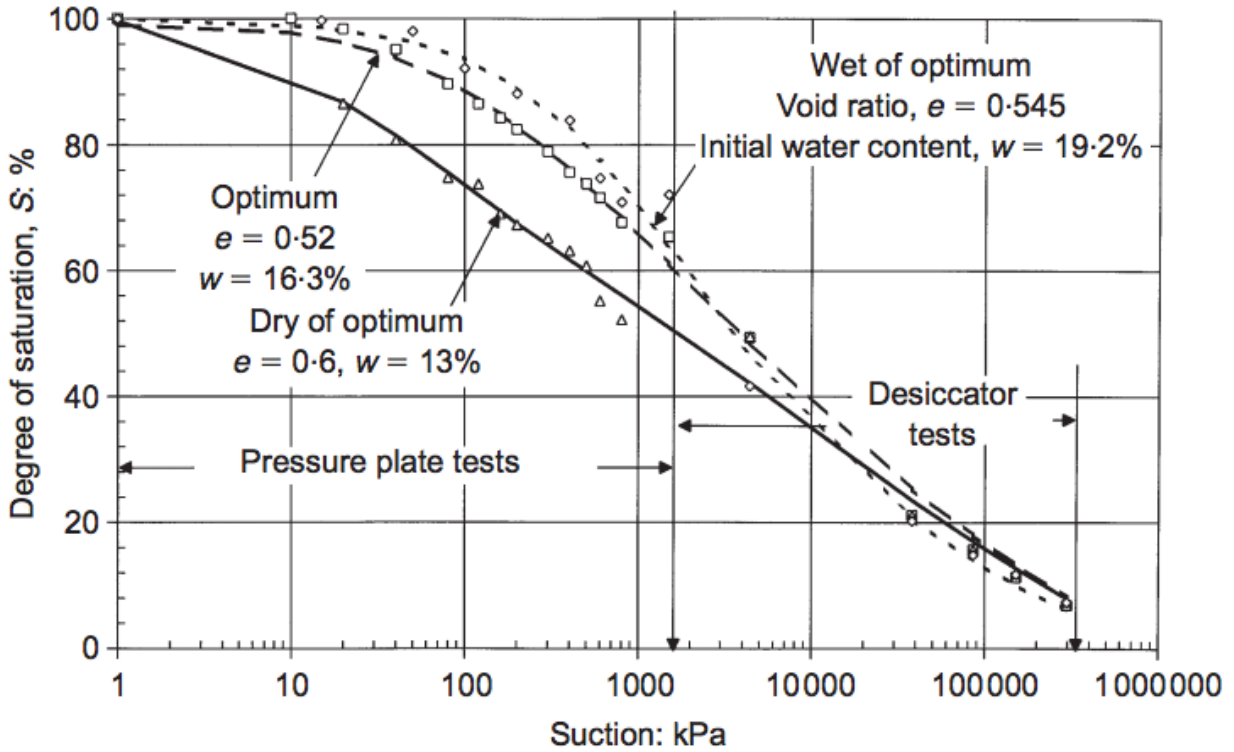


Figure 2-38. Soil-water characteristics for specimens compacted at different initial water contents

(Vanapalli et al., 1999)

Results from laboratory tests conducted on soil samples with different compaction pressures applied during axis-translation tests provide further supporting evidence that compaction pressure increases the AEV and reduces the rate of desaturation at low applied pressures.

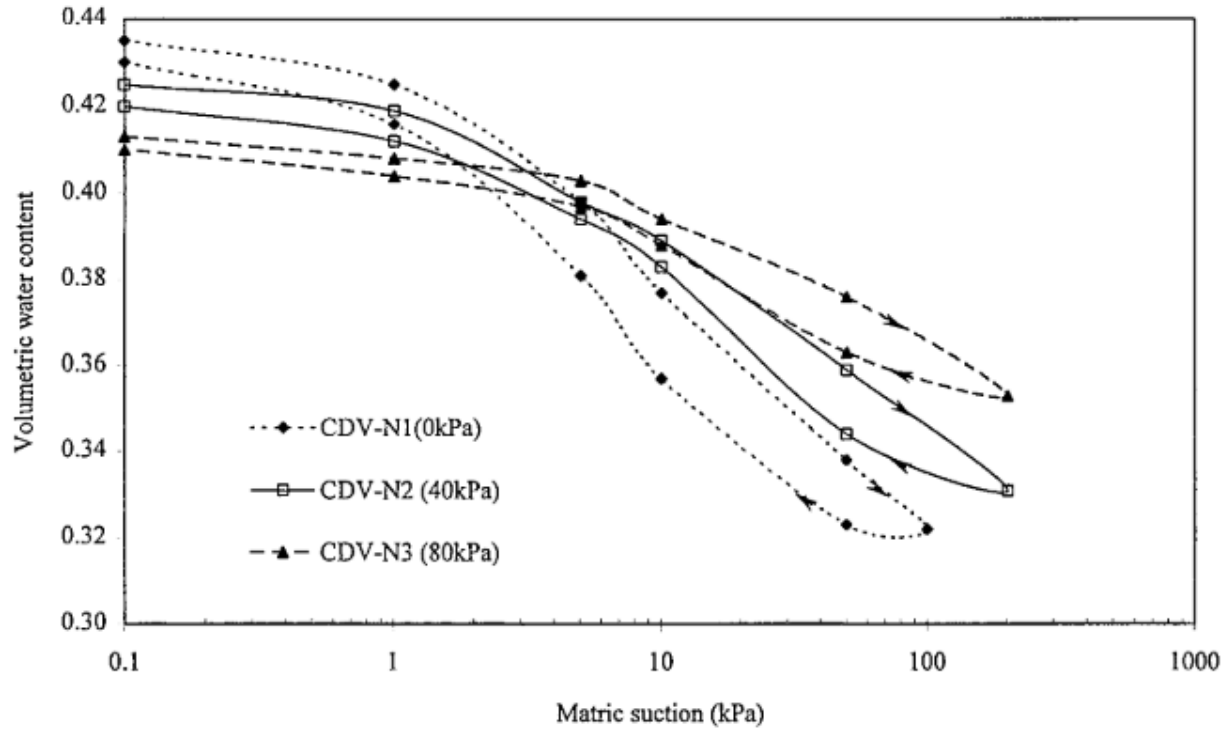


Figure 2-39. Effect of Stress State on SWCC
(Ng & Pang, 2000)

Hydraulic deposition of mine tailings is conducted at very high water contents to facilitate pumping and transport; following deposition, the oversaturated tailings shed the excess water through decanting, drying, and consolidation.

A fundamental principle of soil mechanics is the concept of effective stress initially developed by Karl Terzaghi (1923, 1925) for saturated soils (D. G. Fredlund et al., 2012). The effective stress (σ') represents the portion of the total applied stress carried by the soil particles, which is mathematically shown in Equation 2-24 as the difference between total applied stress (σ) and the pore-water pressure (μ). Equation 2-24 and the effective stress principle demonstrate the contribution of water within the soil in bearing applied loads. According to Terzaghi's principle, as the pore water pressure drops, the soil skeleton bears a greater proportion of the total applied stress.

$$\sigma' = \sigma - \mu \qquad \text{Equation 2 - 24}$$

Several models exist for calculation of effective stress in unsaturated soils; a preliminary understanding of Terzaghi's theorem is sufficient for the scope of this report.

In unsaturated soils the pore-water pressure drops as air enters the pore spaces, where the air does not have the capacity to bear stress in a similar fashion to water which is assumed to be an incompressible fluid. Due to the drop pore-water pressure which had previously supported the soil structure, the soil pores may collapse as the applied stress exceeds the bearing capacity of the soil structure leading to hysteresis as shown in Figure 2-35. There exists a limit to which the volumetric deformation of soils will occur during drying; this is known as the shrinkage limit. The shrinkage limit corresponds to the water content beyond which further drying does not result in volume change of the soil. As seen in Figure 2-40 when soils dry they deform volumetrically at a constant rate along a drying path until the air-entry value of the soil is reached, at water contents below the AEV the rate of volume change slows and eventually stops when the material reaches the shrinkage limit. Prior to reaching the shrinkage limit, the soil theoretically maintains full saturation drying from its initial state. Below the shrinkage limit the pore spaces do not change volume, but the volume of water within the pore spaces continues to drop, resulting in desaturation of the soil.

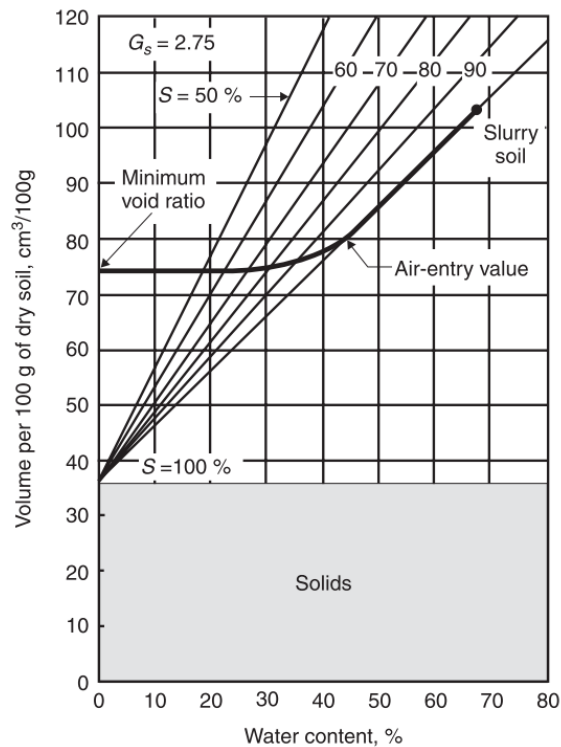


Figure 2-40. Shrinkage curve and volume-mass relation for slurry soil
(D. G. Fredlund et al., 2012)

Volumetric deformation, consolidation, and soil hysteresis are mostly beyond the scope of the predictions and numerical models used throughout this experiment. Some consideration has been given to volumetric deformation in SV-Flux modelling as the unsaturated hydraulic conductivity was developed by fitting the Brooks-Corey model to the SWCC using the degree of saturation vs. suction curve; this is explained in further detail in Chapter 6. Put simply, the model accounts for shrinkage when calculating the unsaturated hydraulic conductivity of the materials.

2.6.2 Evaporation

Evaporation from the ground surface is a significant cause of drying in soils. Evaporation is commonly defined as the vaporization of liquids into the gas phase. Evaporation is governed by the vapour pressure of the substance in question; evaporation can occur at temperatures below the boiling point of the substance in question provided that the liquid vapour pressure gradient is sufficient.

A simplified equation for calculation of the predicted evaporation is shown in Equation 2-25 (Penman, 1948).

$$E_{mass} = \frac{mR_n + \rho_a c_p (\delta_e) g_a}{\lambda_v (m + \gamma)} \quad \text{Equation 2 - 25}$$

where:

m = Slope of the saturation vapor pressure curve (Pa K^{-1})

R_n = Net irradiance (W m^{-2})

ρ_a = density of air (kg m^{-3})

c_p = heat capacity of air ($\text{J kg}^{-1} \text{K}^{-1}$)

g_a = momentum surface aerodynamic conductance (m s^{-1})

δ_e = vapor pressure deficit (Pa)

λ_v = latent heat of vaporization (J kg^{-1})

γ = psychrometric constant (Pa K^{-1})

and E_{mass} is in units of $\text{kg}/(\text{m}^2 \cdot \text{s})$

Evaporation from a saturated soil occurs according to the calculated evaporation which reflects the evaporative flux between a liquid surface and atmosphere, known as the potential evaporation (PE). Evaporation from unsaturated soils is more complex as the transport of water to the soil surface depends upon the hydraulic conductivity and pore properties of the soil. As desaturation occurs, water may no longer be able to be transported to the soil surface at a sufficient rate to match maximum potential evaporative demand, and the rate of evaporation declines and is referred to as the actual evaporation (AE).

Evaporation in soils is conventionally described in three stages. In Stage I the actual rate of evaporation is equal to PE; while actual evaporation declines in Stage II due to decreased available water at the soil surface, and a residual rate of actual evaporation is observed in Stage III (Hillel, 2004). The relationship between AE/PE and soil saturation is shown in Figure 2-41.

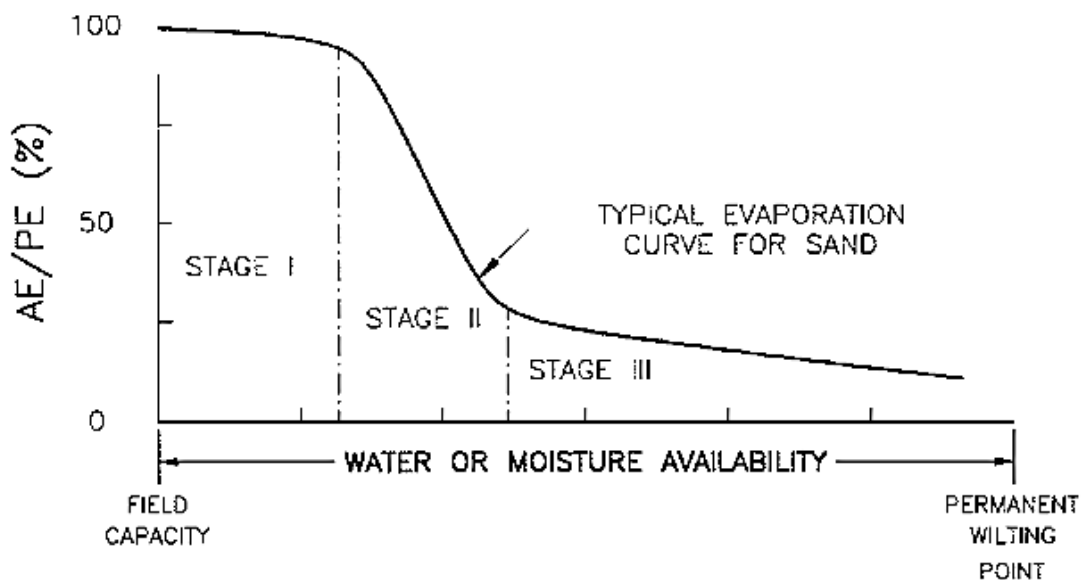


Figure 2-41. Relationship between actual evaporation and potential evaporation with changing soil saturation
(Wilson, Fredlund, et al., 1994)

State of the art understanding of evaporation has progressed in recent years, for example, it is well known that evaporation will often decrease at values of suction well-below those values predicted by the methods of Wilson et al. (1994, 1997). This phenomenon is called Stage one declining evaporation (Simms, Soleimani, et al., 2017). Osmotic suction and crack formation are also known to influence drying from particular soils or tailings (Simms et al., 2017).

Chapter 3 : Material Characterization and Experimental Procedures

To develop numerical models, simulations, and analytical predictions of cover performance, it was necessary to characterize the cover materials and determine a variety of soil parameters. The experimental method of determining the soil properties are covered in this chapter.

3.1 Physical Characterization of Cover Materials

The construction of capillary barrier covers requires materials with different water retention behaviours; it was therefore a necessity to characterize cover materials to determine key soil properties. Tailings materials, coarse sand, and biosolids samples were tested.

Two biosolid materials were tested for their suitability as construction materials in capillary barrier covers. Unamended biosolids from the Halton region were obtained from Terratec Environmental's field application site in Sudbury and are referred to as Toronto Amendment (TA); this was the name used on site for the straight biosolids where the word "amendment" refers to the material being used as a soil amendment, rather than an amended biosolids. A second biosolids material was sampled from stockpiles of biosolids blended with leaf and yard waste from the City of Sudbury on a 1:1 basis by volume. The biosolids mixed with leaf and yard waste will be referred to as the Custom Reclamation Mix (CRM). A sample of papermill biosolids from Domtar's Espanola plant (sampled following field application in Sudbury) was characterized to compare municipal biosolids to papermill biosolids. A lime treated fish compost, and leaf and yard waste from the City of Greater Sudbury were studied as potential amendment materials to be used in cover construction.

Two types of tailings were characterized for this experiment; an unoxidized pyrrhotite tailings sample and a heavily weathered and oxidized pyrrhotite tailings material; both were obtained from Vale's Copper Cliff Tailings Facility. The unoxidized tailings were obtained from the R2 area (shown in Figure 3-1) by collecting samples along the surface of the tailings beach at multiple points along the discharge area. The pre-oxidized tailings were sampled from the P area, where Vale operations had recently removed topsoil and vegetation. The tailings in P area were deposited between 1960–1989 and covers an area of approximately 405 hectares.

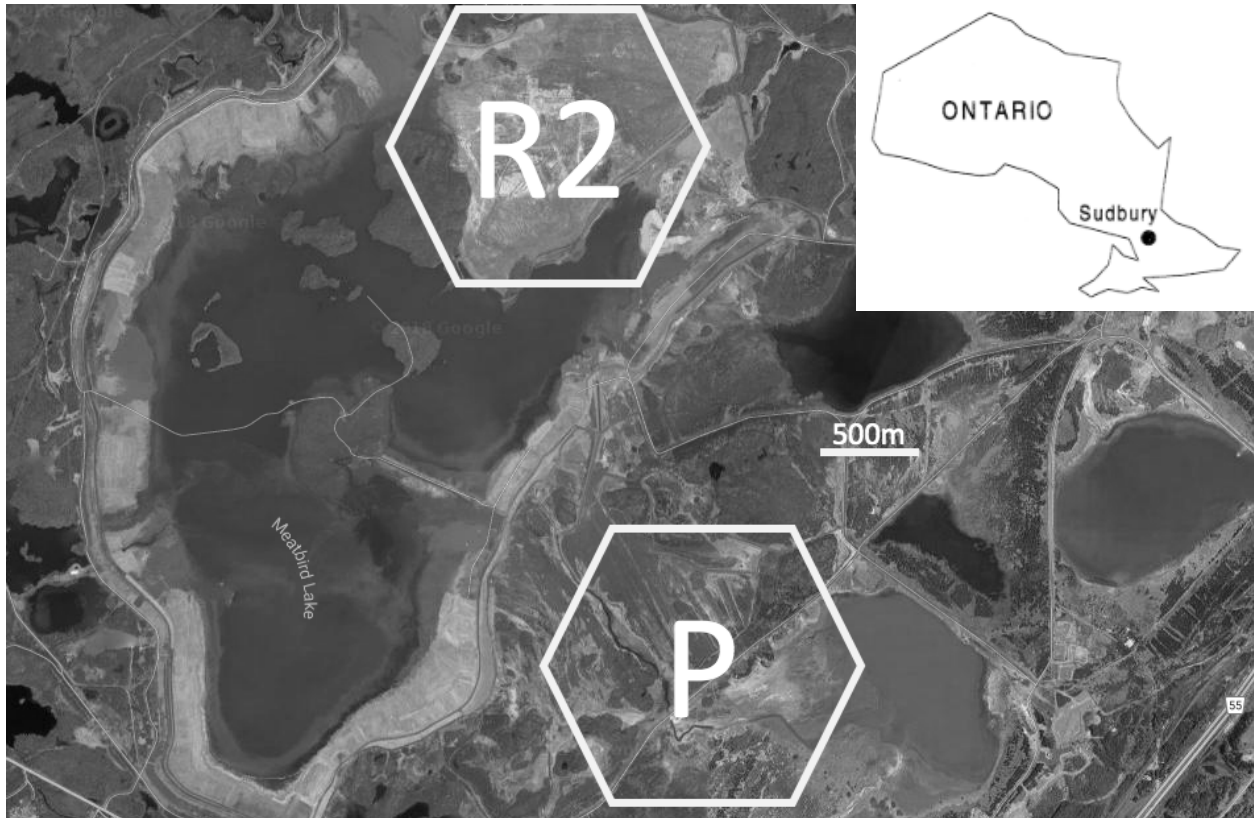


Figure 3-1. Vale Copper Cliff Tailings Area
(images from Google Maps, 2018)

A coarse sand was characterized for use as the unsaturated layer in the capillary barrier cover. The sand was obtained from Carleton University’s undergraduate civil and geotechnical engineering laboratory which purchased the sand from Merkley Supply in Ottawa, originally sourced from Ottawa quarries.

Table 3-1 provides a summary of experimental protocols used to characterize the cover materials.

Table 3-1. Summary of Experimental Protocols

| Characterization Parameter | Experimental Protocol |
|-----------------------------------|-------------------------------------------------------------------------------------------------------------------|
| Specific Gravity | Calibrated Pycnometer - ASTM D854-14 |
| Atterberg Limits | Fall Cone |
| Particle Size Distribution | Sieving - ASTM E276-13 Hydrometer - ASTM D7928-17 |
| Saturated Hydraulic Conductivity | Falling Head Test (fine grained soil) - ASTM D5856-15 Constant Head Test (coarse grained soil) - ASTM D5856-15 |

| | |
|-----------------------------------------------------|----------------------------------------------------------------------------------------------------------------------------------------------------------------------------------------------------------------|
| Determination of Soil Water Characteristic Curve | Axis Translation - ASTM D6839 – 16 Method C Dewpoint Hygrometer - ASTM D6839 – 16 Method D Filter Paper Method (matric suction) - ASTM D5298 -16 Filter Paper Method (total suction) - ASTM D5298 -16 |
|-----------------------------------------------------|----------------------------------------------------------------------------------------------------------------------------------------------------------------------------------------------------------------|

Characterization tests included determining the specific gravity of each material using calibrated pycnometers (ASTM D854-14), with sieving (ASTM E276-13) and hydrometer tests (ASTM D7928-17) for particle size distribution. Falling and constant head tests (ASTM D5856-15) were conducted to determine saturated hydraulic conductivity.

The SWCC of the cover materials was developed using combined results of multiple suction measurement techniques due to the applicable range of each method. Axis-translation was used to develop the water content – suction relationship at low levels of suction (ASTM D6839 – 16 Method C) by measuring the gravimetric loss of water through drainage at specific suction pressures with an effective range of 0-350 kPa. The axis translation technique also allowed for measurement of volumetric deformation and shrinkage for the materials during testing using a GCTS Fredlund SWC 150 device with a sonic non-contact displacement sensor.

The filter paper method of total suction and matric suction (ASTM D5298 -16) was used to develop the SWCC at suction values greater than 350 kPa; this was done by equilibrating soil samples in individual air-tight specimen jars with filter papers. A Decagon Devices WP4C dewpoint hygrometer was used according to ASTM D6839 – 16 Method D for additional total suction measurement.

3.1.1 Specific Gravity

The specific gravity of cover materials was tested using calibrated pycnometers as per ASTM D854-14. 8 volumetric flasks with volumes of 1 L, 500 mL, 250 mL, and 200 mL were thermally equilibrated in an insulated container for a period of 24 hours, and weighed to calibrate the pycnometer dry mass. The pycnometers were filled with de-aired distilled water and equilibrated

again for 24 hours, then weighed. All water used in this test was de-aired by boiling and stirring for 2 hours.

Cover materials were oven dried and ground with a mortar and pestle to reduce soil clods, then added to the dry pycnometers and weighed. De-aired water was added, and the mixture boiled to further remove air in the soil and water solution. The pycnometers were thermally equilibrated for 24 hours, and topped up to their calibrated volume with de-aired water that was stored in the same insulated container. The full mass of the pycnometers was measured.

Multiple tests were conducted for each material; the average specific gravity of the materials is shown in Table 4-1 of Chapter 4.

3.1.2 Particle Size / Grain Size Distribution of Fresh Tailings and Oxidized Tailings

The particle size distribution of the cover materials was determined using wet sieving (ASTM E276-13) and hydrometer tests (ASTM D7928-17). The results of the particle size distribution tests are shown in Figure 4-1 of Chapter 4.

3.1.2.1 Particle Size Distribution from Sieve Testing

For wet sieving, series of sieves were prepared and weighed with mesh openings of 4.5 mm, 2 mm, 850 um, 425 um, 250 um, 150 um, and 75 um. Cover materials were oven dried and clods were dispersed using a mortar and rubber pestle. Tests were conducted at each screen size, with the screen being weighed prior to each test. The screen with a fines collection pan attached underneath was tared, and the dry mass of material added was recorded. Water was used to flush tailings through the screen until water passing through the screen was free of any visible solids and material no longer passed through the screen with the addition of further water. Screens were transferred to a drying oven, and the mass recorded after 24 hours. The mass of material retained on each screen was recorded and combined with hydrometer test data to create particle size distributions as shown in Chapter 4. The percent of material passing each screen size was calculated using Equation 3-1.

$$PP = 100 \left(1 - \frac{M_{dr}}{M_d} \right) \quad \text{Equation 3-1}$$

Where

PP = Percent of particles passing specific screen size (%)

M_{dr} = dry mass retained on the sieve (g)

M_d = initial dry mass of the soil specimen (g)

3.1.2.2 Particle Size Distribution from Hydrometer Testing

Hydrometer tests were conducted to measure the fine fraction of particles in each cover material. As per ASTM D7928-17, soil samples were collected with approximately 50 g of dry soil passing through a 2 mm sieve; the dry mass was predicted using the GWC of the same material. A portion of the soil sample was split and removed to perform a GWC test to confirm the water content. 5 grams of sodium hexametaphosphate (NaPO_3)₆ dispersant (a common de-flocculating agent) was dissolved in 100 mL of water and mixed with the soil sample using a stand mixer for sixty seconds. The mixture was poured into a 1 L glass graduated cylinder of measured diameter, and filled to the 1000 mL mark with distilled water. A control cylinder was prepared with the dispersant and no soil sample. The cylinders were mixed by inverting the cylinders once per second for one minute, covered, and left to sit for 24 hours at a stable temperature. Following 24 hours, the cylinders were re-agitated by inverting them once per second for sixty seconds. A timer was started after completion of the last inversion.

A 152H hydrometer was used to measure the mass of particles; the hydrometer is calibrated to particles with a specific gravity of 2.65 at a temperature of 20⁰C. A labelled diagram of a 152H hydrometer is shown in Figure 44. Hydrometer readings were taken at specific time intervals (1,2,4,15,30,60,240 and 1440 minutes) and were completed by gently placing the hydrometer in the sedimentation cylinder such that it would not buoyantly displace when let go, and the level of the suspension was read along the marked hydrometer stem. The control cylinder was measured

in a similar fashion immediately after the soil suspension to provide a reference measurement for temperature correction.

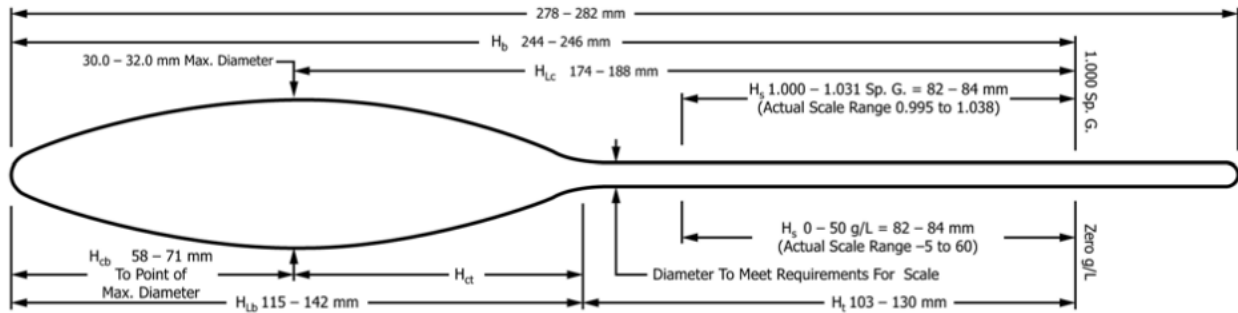


Figure 3-2. Soil hydrometer bulb dimensions
(ASTM, 2017b)

Following the final hydrometer reading, the soil suspension was sieved through a 200 mesh (75 um) screen and oven dried to determine the dry mass retained. The hydrometer test utilizes a series of calculations to determine the travel distance of particles each time the hydrometer is inserted or removed (Equation 3-2.1), which is used to calculate the percent of particles finer than a calculated maximum suspended particle diameter (Equation 3-2.2 and Equation 3-2.3).

$$H_m = H_{r2} + \left(\frac{H_{r1} - H_{r2}}{r_2 - r_1} \cdot (r_2 - r_m + C_m) \right) - \frac{V_{hb}}{2A_c} \quad \text{Equation 3 - 2.1}$$

Where

H_m = particle fall distance for reading m (cm)

H_r = distance between center of volume of the hydrometer bulb and the minimum (H_{r2}) and maximum (H_{r1}) hydrometer readings (cm)

r_m = hydrometer reading at reading number m (read in g/L)

r = minimum (r_2) and maximum (r_1) hydrometer readings on hydrometer stem (g/L)

C_m = meniscus correction on hydrometer stem (g/L)

V_{hb} = volume of the hydrometer bulb up to the base of the stem (cm³)

A_c = cross-sectional area of the sedimentation cylinder (cm²)

$$D_m = 10 \cdot \sqrt{\frac{18\mu \cdot H_m}{\rho_w g (G_s - 1) \cdot t_m}} \quad \text{Equation 3 – 2.2}$$

Where

D_m = particle diameter (mm)

μ = viscosity of water (g/cm-s)

ρ_w = mass density of water (g/cm³)

g = acceleration due to gravity (980.7cm/s²)

G_s = specific gravity of soil

t_m = elapsed fall time (s)

$$N_m = 0.06226 \left(\frac{G_s}{G_s - 1} \right) \left(\frac{V_{sp}}{M_d} \right) (r_m - r_{d,m}) \quad \text{Equation 3 – 2.3}$$

Where

V_{sp} = volume of suspension (cm³)

M_d = dry soil mass of the sedimentation specimen (g)

$r_{d,m}$ = hydrometer offset reading from reference solution at same temperature as reading m (g/L)

3.1.3 Gravimetric Water Content and Solids Content

The gravimetric water content (GWC) was tested according to ASTM D2216-10 and recorded at several stages during characterization, notably as a reference value when developing the soil-water characteristic curves. The GWC of cover materials was initially calculated following sampling to determine the in-situ water content of materials as sampled in the field.

The GWC was calculated by recording the weights of empty aluminum sample dishes, recording the weight of samples prior to drying, and recording the weight following drying. Samples were dried at $105^{\circ}\text{C} \pm 5^{\circ}\text{C}$ for 24 hours. Samples were moved to a desiccator following oven drying to ensure that moisture was not re-introduced to the samples from humidity in the laboratory.

The GWC was calculated using Equation 3-3, and the solids content calculated using Equation 3-4.

$$GWC = \frac{(m_w - m_e) - (m_d - m_e)}{(m_d - m_e)} \cdot 100\% \quad \text{Equation 3 - 4}$$

Where

GWC = Gravimetric Water Content as %

m_w = mass of the aluminum dish and sample prior to oven drying (g)

m_e = mass of the empty aluminum dish (g)

m_d = mass of the aluminum dish and sample after drying (g)

$$\% \text{ Solids} = \text{mass of solids (g)} / \text{mass of soil (g)} \times 100\% \quad \text{Equation 3 - 4}$$

3.1.4 Volumetric Water Content

Calculations for volumetric water content were conducted on materials throughout the project using Equation 3-5.

$$VWC = \frac{V_w}{V_{total}} \cdot 100\% \quad \text{Equation 3 - 5}$$

Where

VWC = volumetric water content (%)

V_w = volume of water (cm³)

V_{total} = total volume of sample which comprises of soil, air, and water in sample (cm³)

3.1.5 Degree of Saturation

The degree of saturation was calculated according to Equation 3-6 which calculates the percentage of soil pore space which is filled with water.

$$S = \frac{V_w}{V_{voids}} \cdot 100\% \quad \text{Equation 3 - 6}$$

Where

S = degree of saturation (%)

V_w = volume of water (cm³)

V_{voids} = volume voids in the soil sample (cm³)

Using calculated soil and solids unit weights, the degree of saturation can also be calculated according to Equation 3-7.

$$S = \frac{w}{\left(\frac{\gamma_w}{\gamma_d} \frac{1}{SG}\right)} \quad \text{Equation 3 - 7}$$

3.1.5.1 Saturated Water Content

The water content at saturation was determined by measuring the gravimetric water content of the soils when compacted to a known volume. With the known volume, the bulk density of the soil was determined, and the volumetric water content calculated using the specific gravity of the soil solids.

The bulk density is calculated using Equation 3-8.

$$\gamma_w = \frac{m_{soil}}{V_{soil}} \quad \text{Equation 3 - 8}$$

Where

γ_w = bulk density of the soil (g/cm³)

m_{soil} = mass of all soil components: soil, air, water (g)

V_{soil} = total volume of soil (cm³)

The dry unit weight of solids was calculated from the gravimetric water content of the samples and used to determine the dry unit weight of solids in the soil samples according to Equation 3-9.

$$\gamma_d = \frac{m_{solids}}{V_{soil}} \quad \text{Equation 3 - 9}$$

Where

γ_d = dry density of the soil solids (g/cm³)

The saturated water content was calculated using Equation 3-10.1 and setting the saturation term (S) equal to 1. Isolating for the water content w gives the equation in the form of Equation 3-10.2.

$$\gamma_d = \frac{1}{\left(\frac{w}{\gamma_w S} + \frac{1}{\gamma_w SG}\right)} \quad \text{Equation 3 - 10.1}$$

$$w = \gamma_w S \left(\frac{1}{\gamma_d} - \frac{1}{\gamma_w SG} \right) \quad \text{Equation 3 – 10.2}$$

Where

w = gravimetric water content of the soil

S = degree of saturation

SG = specific gravity of soil solids (g/cm^3)

The saturated volumetric water content calculated using Equation 3-10.2 was compared to the volumetric water content at saturation when material was compacted to the optimum water content, and to the saturated volumetric water content obtained from axis translation testing.

3.1.6 Void Ratio and Porosity

Throughout this project the void ratio of the cover materials was calculated according to Equation 3-11 which calculates the ratio of void space to soil solids volume. The void spaces are assumed to be soil pores available for water flow.

$$e = \frac{V_{voids}}{V_{solids}} \quad \text{Equation 3 - 11}$$

Where

e = void ratio

V_{voids} = volume of void space (cm^3)

V_{solids} = volume of soil solids (cm^3)

The porosity of soils (n) can be calculated from the void ratio (e) according to Equation 3-12.

$$n = \frac{e}{1+e} \quad \text{Equation 3 - 12}$$

The porosity represents the fraction of soil volume that is comprised of soil pores.

3.1.7 Total Volatile Solids of Biosolids Amendment Materials

The total volatile solids of the biosolids materials was determined using a high temperature oven which removed the friable organic content of the biosolids samples. The volatile solids content

was calculated by recording the weights of empty aluminum sample dishes, recording the weight of samples prior to high-temperature drying, and recording the weight following drying. Samples were dried at 550⁰C for two hours. Samples were moved to a desiccator following oven drying to ensure that moisture was not re-introduced to the samples from humidity in the laboratory. The calculation for Total Volatile Solids is shown in Equation 3-13 (Metcalf & Eddy et al., 2014).

$$Total\ Volatile\ Solids\ \% = \frac{(m_d - m_e) - (m_f - m_e)}{m_w - m_e} \cdot 100\% \quad \text{Equation 3 - 13}$$

Where

m_w = mass of the aluminum dish and sample prior to oven drying (g)

m_e = mass of the empty aluminum dish (g)

m_d = mass of the aluminum dish and sample after drying (g)

m_f = mass of the aluminum dish and sample after firing the sample at 550⁰C

3.1.8 Atterberg Limits – Plastic Limit and Liquid Limit

The Atterberg limits are the water contents at which soils exhibit either solid, semi-solid, plastic, or liquid behaviour. The consistency of the soil and its associated engineering properties are different in each state. The Liquid Limit (LL) and Plastic Limit (PL). Determination of the LL and PL is often conducted using ASTM D4318-17, however, the use of a fall cone to measure the LL and PL of soils is a suggested alternative which delivers consistent test results according to BS 1337-2.

The fall cone consists of a hard metal base, and a 40 g stainless steel cone with a 30⁰ tip and elongated rod base which is held in place by a height adjustable release mechanism. A displacement measurement plunger and displacement reading dial are affixed to the unit and provide readings of cone displacement in 1/10 mm increments when the plunger is brought into contact with the top end of the cone rod. The test is conducted by filling a 5 cm diameter x 3.5 cm high sample dish with soil specimens at the desired moisture content, zeroing the plunger displacement, positioning the tip of the fall cone immediately above the center of the soil specimen (ie. as close as possible without contact), and releasing the cone for 5 seconds. The release mechanism is re-engaged to hold the cone at the observed depth, and the plunger is brought into contact with the cone to measure the displacement on the measurement dial.

Test results from the fall cone are plotted on a semi-log plot of penetration depth vs. GWC to determine the liquid and plastic limits as shown in Figure 3-3, results from tests conducted for this project are shown in Table 4-1 of Chapter 4.

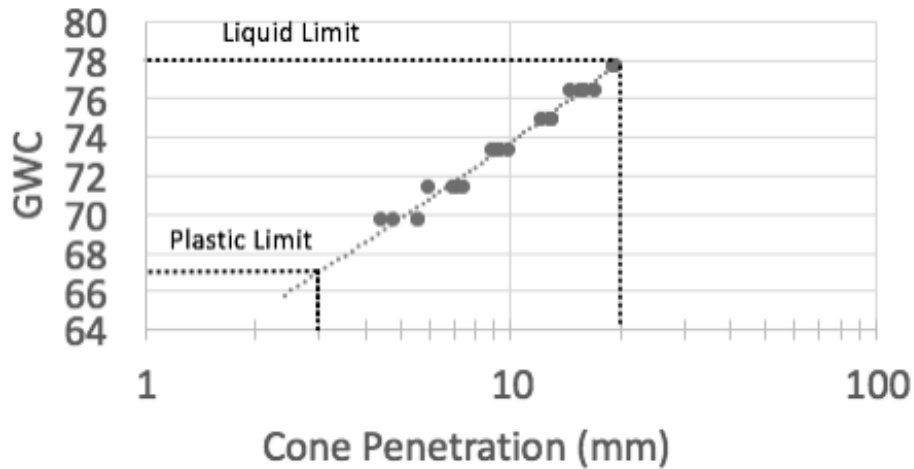


Figure 3-3. Fall cone test results showing liquid limit and plastic limit of Leaf and Yard Waste

Near the optimum moisture content, the cone penetration may data exhibit an inflection point where the cone penetration depth increases at lower water contents. This is similar to the proctor test in that there is an optimum water content below which soil particles are not lubricated sufficiently to allow for optimum compaction, and above which the water acts to retard compaction. The Atterberg limits can be obtained by regression of data at water contents above the inflection point as shown in Figure 3-4.

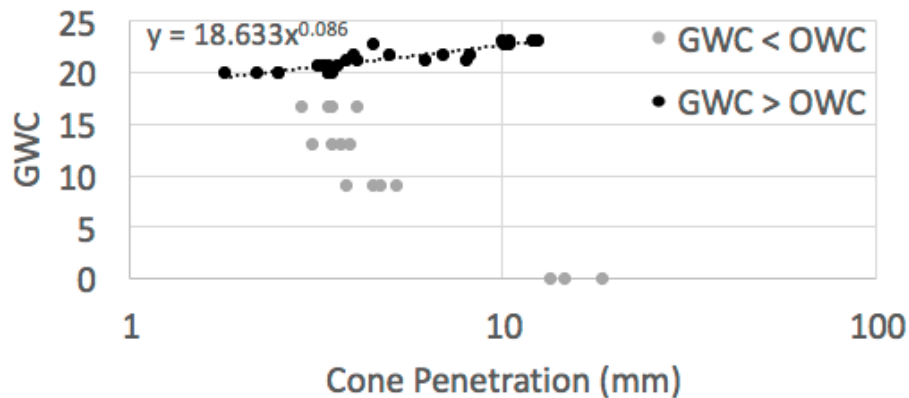


Figure 3-4. Data regression at water contents above inflection point to determine Atterberg limits (test data for unoxidized tailings)

3.1.8.1 Plastic Limit

The plastic limit is defined as the water content which delineates the boundary between plastic and semi-solid states in the soil. The plastic limit of a soil is useful in geotechnical engineering as plastic soils exhibit volumetric deformation without fracture. Using the fall cone test, the plastic limit is the water content at which the fall cone penetrates to a depth of 2 mm.

3.1.8.2 Liquid Limit

The liquid limit is defined as the water content at which the soil changes between a plastic and liquid state. Soil in a liquid state exhibits flow characteristics and does not maintain shape. Using the fall cone test, the liquid limit is the water content at which the fall cone penetrates to a depth of 20 mm.

3.1.8.3 Plasticity Index

The plasticity index (PI) is a measure of the range of water contents over which a material exhibits plastic behaviour. The plasticity index is calculated as the difference between the gravimetric water contents of the plastic limit and liquid limit (Das & Sivakugan, 2017).

3.1.9 – Compaction & Optimum Water Content

The optimum water content of soil as defined in Section 2.6.1 is often measured using ASTM D698-12, which involves conducting a Proctor test. In a Proctor test, soil samples at known water contents are compacted into a known volume using a standard effort (by dropping a standard mass from a standard height a specific number of times), and determining which water content results in the greatest dry density of the samples. The optimum water content can also be estimated by a prediction using the measured Plastic Limit (Sridharan & Nagaraj, 2005) according to Equation 314.

$$OMC = PL \cdot 0.92 \qquad \text{Equation 3 - 14}$$

Where

OMC = Optimum Moisture Content

PL = Plastic Limit

The estimation of optimum moisture content listed applies to fine grained soils and was derived from laboratory study of 10 different soils (ranging from 5% to 38% clay sized particles) and historic data of 56 fine grained soils (Sridharan & Nagaraj, 2005). This equation may therefore have a reduced degree of accuracy in the prediction of the optimum water content for the sand and unoxidized tailings materials.

3.1.10 Saturated Hydraulic Conductivity

As described in Section 2.4.3 the saturated hydraulic conductivity is a measure of the ability for a liquid to flow through a medium (water through soils in the case of this project). Both the constant and falling head test use a defined volume of soil with measured circumferential area and height and follow the directions outlined in ASTM D5856-15.

In both tests, the soil specimen is contained within a rigid compaction-mold permeameter (shown in Figure 3-5) with a ceramic disc at the top and bottom of the specimen to prevent soil swelling.

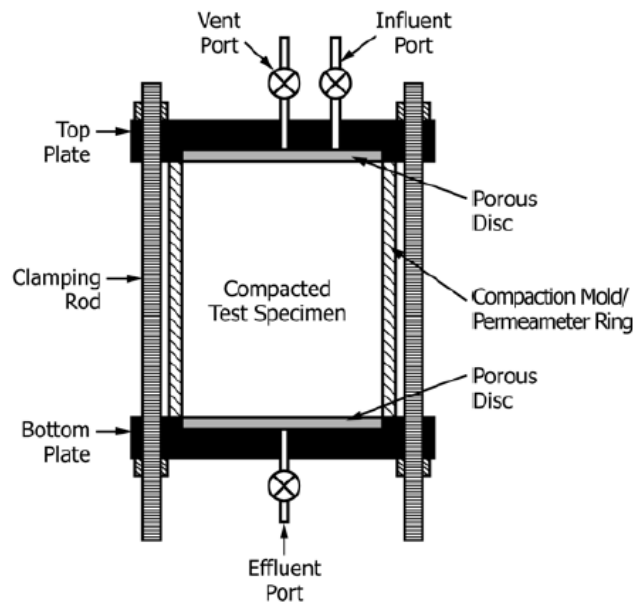


Figure 3-5. Permeameter used for constant and falling head tests
(ASTM D5856-15, 2015)

In preparing samples for both falling and constant head tests, the soil samples were compacted dynamically in three separate lifts using 25 blows of a 5.5 lb hammer falling 6 inches (half the normal proctor height to avoid fracturing of the porous disc at the permeameter cylinder base).

The compacted soil cylinders were weighted and the calculated moisture content compared to the optimum moisture content. The permeameters were connected to vacuum pumps for 15 minutes via the influent ports. Following vacuuming, water hoses were connected to the effluent ports, and the samples were hydrated with de-aired water under vacuum. Following initial hydration, all ports were closed, and all hoses were removed. A laboratory temperature of 20⁰C was recorded during testing.

3.1.10.1 Constant Head Test

The constant head test is used on coarse grained soils, and was conducted using a reservoir with a fixed intake to maintain a water column of constant height as the influent for the permeameter. The constant head test was used for determining the saturated hydraulic conductivity of the sand and unoxidized tailings. The reservoir water level was maintained throughout the test by pumping water up to the reservoir which had a large bypass drainage pipe to ensure constant head conditions as shown in Figure 3-6.

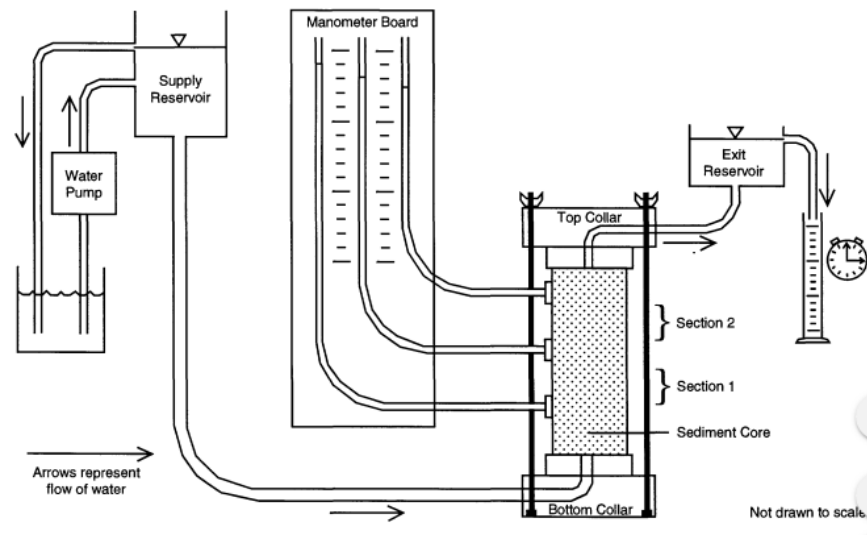


Figure 3-6. Constant head test permeameter and reservoir setup (Warren & Church, 1996).

For each test the hydrated permeameters were connected to the flowing reservoir water column and the permeameter monometers, after which the influent and effluent valves of the permeameter were opened. Test water was flushed through the sample until a constant head was observed within the monometers, after which time a stopwatch was used to measure the time taken for increments

of 200 mL of water to pass through the sample (captured and measured from the effluent). Times were recorded up until 1 L of water was captured.

The saturated hydraulic conductivity of the samples was calculated according to Equation 3-15.

$$k = \frac{\Delta Q \cdot L_f}{A \cdot \Delta t \cdot \Delta h} \quad \text{Equation 3 - 15}$$

Where

k = hydraulic conductivity (cm/s)

ΔQ = quantity of flow through the sample (mL)

L_f = Length of sample (cm)

A = Cross sectional area of sample (cm²)

Δt = time interval over which ΔQ is recorded (s)

Δh = difference in hydraulic head across the specimen (cm of water)

3.1.10.2 Falling Head Test

Falling head tests were conducted on the fine-grained cover materials with low estimated hydraulic conductivity. The falling head test was used to determine the saturated hydraulic conductivity of the pre-oxidized tailings, and all of the biosolids and soil amendment materials. Falling head tests were set up in much the same manner as the constant head tests, however, the permeameters for falling head tests did not have monometer ports, and there was no reservoir to maintain a constant head in the influent pipe. Instead, the influent pipe was a much smaller glass tube mounted on a steel frame with millimeter precise measurements (essentially a large monometer) and was open to atmosphere at the top. The influent pipe was filled with de-aired test water, and the influent pipe was connected to the hydrated permeameter influent port. The influent and effluent port of the permeameter were opened at time $t=0$ as recorded on a stopwatch. The rate of head loss was recorded at various time intervals depending on the hydraulic conductivity of the material (lower hydraulic conductivity required longer intervals between measurement to observe a change in head).

The hydraulic conductivity of the materials tested using the falling head method was calculated according to Equation 3-16.

$$k = \frac{2.3 \cdot a \cdot L_f}{A \cdot \Delta t} \log(\Delta h) \quad \text{Equation 3 - 16}$$

Where

k = hydraulic conductivity (cm/s)

a = cross sectional area of the monometer (cm²)

L_f = Length of sample (cm)

A = Cross sectional area of sample (cm²)

Δt = time interval over which Δh is recorded (s)

Δh = difference in hydraulic head shown in the monometer over time interval Δt (cm of water)

The hydraulic conductivity of the cover materials was calculated by replicating the tests multiple times; results are shown in Table 4-1 of Chapter 4.

3.2 Developing Water Retention Curves

The development of water retention curves for the cover materials was completed by measuring the water content at any given suction, where suction was measured either directly or indirectly. Several test methods exist for the determination of the water content and suction relationship, however, most methods have a range of water contents or suctions across which they are best employed for accuracy, precision, and feasibility as described in Table 3-2. A description of the test methods, and their limitations is outlined in this section (D. G. Fredlund et al., 2012). The results of the suction measurement tests are shown in Section 3.3.

Table 3-2. Suction measurement methods used for generation of WRC

| Suction Component Measured | Method | Range (kPa) | Comments |
|----------------------------|-----------------------------------------------|--------------|--------------------------------------------------------------------------------------------------------------------------------------------------------------------------------------|
| Total | Filter Paper | Entire Range | Measurement taken at low suctions (high water contents) have extreme variability due to physical retention of water droplets resulting from condensation within the sample container |
| | Chilled Mirror Dewpoint Hygrometer | Entire Range | Equipment lacks precision and accuracy at low suctions (± 0.05 Mpa from 0 to 5 Mpa, 1% from 5 to 300 Mpa) |
| Matric | Pressure Extraction (Axis Translation) | 0-1500 | Practical range between 0-350 kPa due to stress on equipment at high pressures. |
| | Filter Paper | Entire Range | Measurements taken at low suctions (high water contents) exhibited extreme variability due to physical retention large water droplets on the filter paper due to surface tension) |
| Osmotic | Saturation Extraction Electrical Conductivity | Entire Range | |

3.2.1 Total Suction Measurements

The measurement of total suction was done using a combination of the filter paper method, and a chilled mirror dewpoint hygrometer.

3.2.1.1 Filter Paper Method for Total Suction Measurement

The filter paper method for measurement of total and matric suction is described in ASTM D5298-16. The filter paper method utilizes laboratory filter papers as a passive sensor to measure the matric and total suction of soil samples which are brought to thermal and moisture equilibrium in sealed containers.

The total suction test was done by partially filling a 250 mL jar (approximately 80% full) with a soil sample, placing a rubber o-ring on top of the soil, and setting two filter papers on top of the o-ring such that there is no direct contact between the filter paper and the soil, or the walls of the jar. The experimental setup for suction equilibration is shown in Figure 3-7. The air-tight lid of the jar was closed, and the jar placed in a temperature controlled fridge at 20⁰C for one week for the soil, air, and filter paper to thermally equilibrate and come to a moisture equilibrium. Samples of varying moisture contents were tested in labelled jars.

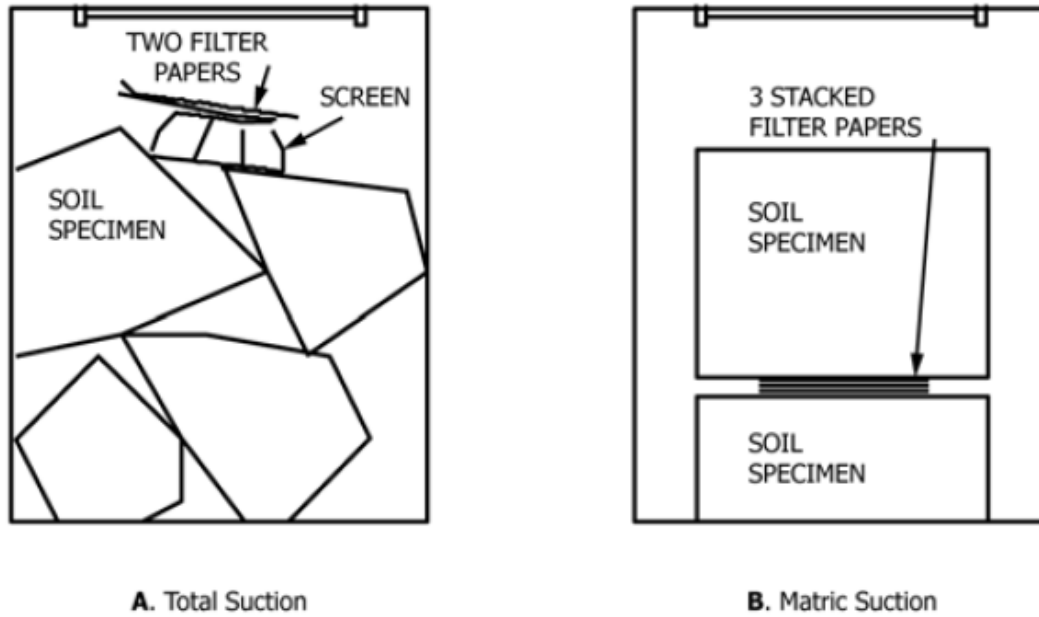


Figure 3-7. Experimental setup for suction equilibration in total and matric suction filter paper tests
(ASTM D5298-16, 2016).

Following the equilibration period, sealable plastic bags were prepared by measuring the cold-mass of the empty bags. A sample jar was removed from the fridge, and tweezers were used to transfer the filter papers to individual sealable plastic bags as quickly as possible and sealed to limit mass lost due to evaporation as per the ASTM. The mass of the filter papers within the plastic bags was recorded (M_2), and the filter papers were then transferred to a drying oven at 105⁰C for a minimum of two hours. Following oven drying, the filter papers were transferred to a desiccator to cool, and were weighed after a minimum cooling time of five minutes (M_f). The filter paper was removed, and the final mass of the plastic bag was recorded (T_h). The calculation of total suction from the recorded masses of the filter paper and plastic bag are shown in the series Equation 3-17.

$$M_f = M_2 - T_h \quad \text{Equation 3 – 17.1}$$

$$M_w = M_1 - M_2 + T_h - T_c \quad \text{Equation 3 – 17.2}$$

$$w_f = 100 \frac{M_w}{M_f} \quad \text{Equation 3 – 17.3}$$

$$h = mw_f + b \quad \text{Equation 3 – 17.4}$$

$$Suction (kPa) = 10^h \quad \text{Equation 3 – 17.5}$$

Where

T_c = initial mass of the plastic bag (g)

M_1 = total mass of plastic bag and filter paper after transferring filter paper from sample jar (g)

M_2 = total dry mass of plastic bag and dried filter paper (g)

T_h = mass of the plastic bag after removal of dry filter paper (g)

M_f = mass of dry filter paper (g)

M_w = mass of water in the filter paper (g)

w_f = water content of the filter paper (% mass)

h = \log_{10} suction value (pF)

m = slope of the filter paper calibration curve (\log_{10} kPa / % water content)

b = intercept of the filter paper calibration curve (\log_{10} kPa)

For both the matric and total suction filter paper tests a calibration relationship was required to determine the moisture retention properties of the filter papers. Whatman No. 42 ashless filter papers with a diameter of 55 mm were used in this study as per recommendation in the standard procedure, and a calibration curve was established by conducting a total suction test with varying concentrations of NaCl solution. The calibration curve for the Whatman 42 filter papers obtained through testing corresponded very well to that supplied in the ASTM document shown in Figure 3-8.

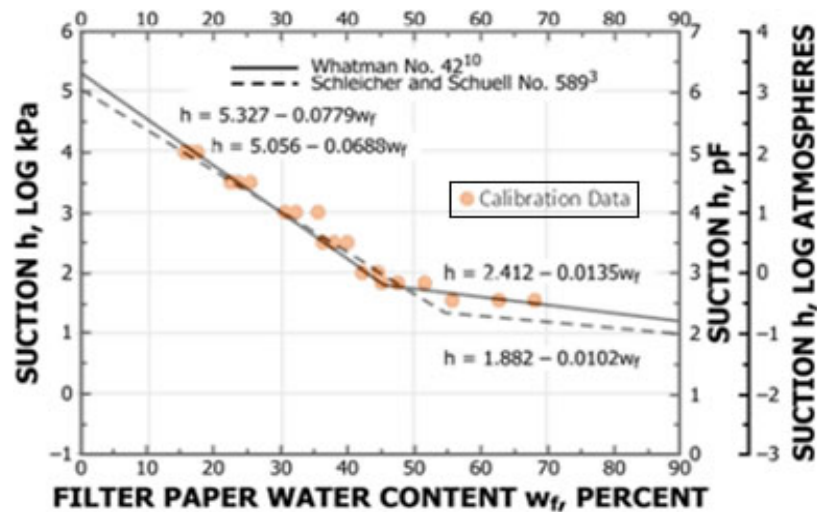


Figure 3-8. Calibration curve for suction determination using Whatman 42 filter paper compared to calibration curve provided in ASTM document. (ASTM D5298-16, 2016).

3.2.1.2 Chilled Mirror Dewpoint Hygrometer

A chilled mirror dewpoint hygrometer was used for rapid determination of total suction of soil samples according to ASTM D6836-16. The WP4C hygrometer from Decagon devices was used which measures suction by equilibrating the liquid phase water of the soil sample with the vapour phase water in a closed chamber, then measuring the vapour pressure of the chamber. The dew point hygrometer works by cooling the mirror to the dew point temperature within the chamber (the dew point is observed by an optical sensor which detects dew formation on the clean mirror) and calculating the corresponding relative humidity.

A soil sample is placed in a sample cup, which is inserted in the hygrometer and sealed against a sensor block. A fan, a dew point sensor, a temperature sensor, and an infrared thermometer are mounted inside the sensor block as shown in Figure 3-9. The fan speeds equilibration and controls the boundary layer conductance of the dew point sensor. The temperature and dew point within the sample block are measured by the dew point sensor and infrared thermometer. The hygrometer computes the vapour pressure of the air in the chamber. Once the sample suction pressure and the headspace air pressure are in equilibrium, the measurement of the headspace vapour pressure and sample temperature are used to calculate the suction of the soil sample using Equation 3-18.

$$\psi = \frac{RT}{M} \ln(a_w) \quad \text{Equation 3 - 18}$$

Where

ψ = Total Suction

R = is the gas constant

T = temperature ($^{\circ}\text{K}$)

M = molecular mass of water

a_w = water activity

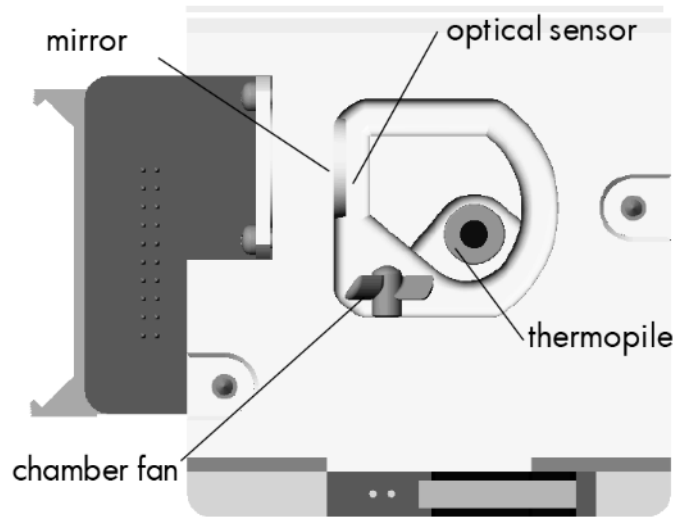


Figure 3-9. Chilled mirror dew point hygrometer internal sensor block (Meter group, 2018).

The water content of each sample tested using the hygrometer was determined by oven drying the sample as described in Section 4.1, and the results plotted on a semi-log plot of Total Suction vs. GWC.

3.2.2 Matric Suction Measurements

As defined in Section 2.5.2 the matric suction component of soil suction is primarily due to the capillary effect of soil pore spaces and the forces generated by surface tension of the pore water.

3.2.2.1 Pressure Extraction and Axis Translation

Matric suction measurement can be conducted directly by applying gas pressure to a soil sample, and measuring the quantity of water which is displaced from the soil pores. GCTS SWC-150 Fredlund devices were used to perform pressure extraction of soil samples and to determine suction via axis translation.

Axis translation utilizes the principle that matric suction can be applied to a soil by controlling the pore gas pressure, and the pore water pressure, so that the difference between the pore gas pressure and pore water pressure equals the desired matric suction according to Equation 3-19 (ASTM, 2017a).

$$\psi_m = u_g - u_w$$

Equation 3 - 19

The test setup for pressure extraction utilizes a hydrated porous ceramic with a known AEV (5 bar, or 500 kPa) and hydraulic conductivity which is placed at the base of a pressure vessel containing the soil sample. The pressure vessel is connected to a pressure source (nitrogen gas canisters with pressure regulators both at the tank and the device interface) and volume tubes as shown in Figure 3-10.

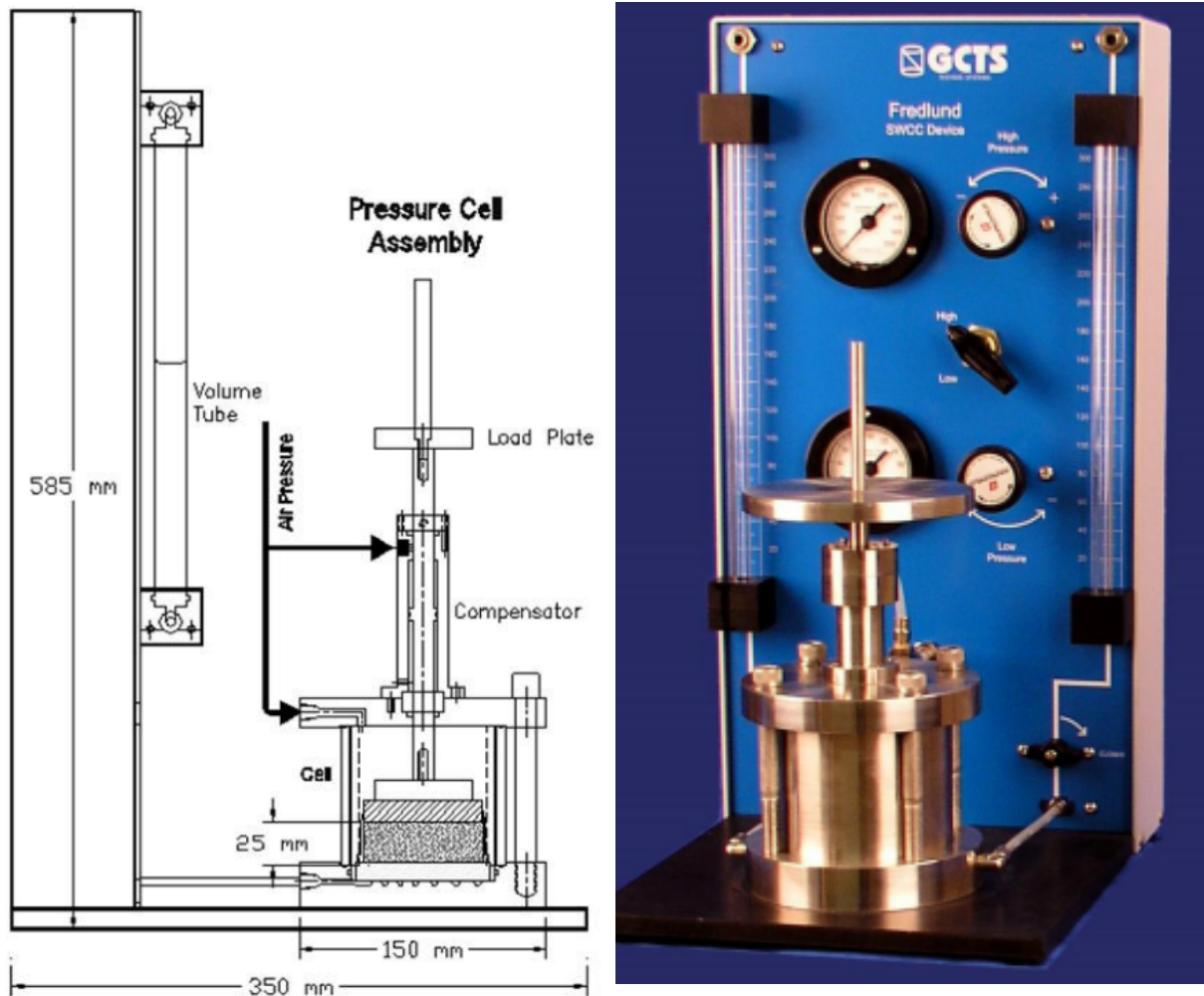


Figure 3-10. Pressure extractor vessel schematic and photograph (GCTS, 2014)

The mass of the pressure vessel with the hydrated ceramic over top of the grooved, water filled stainless steel baseplate is recorded prior to testing. The interior surface area of the pressure vessel was determined with callipers, and the depth to the top surface of the ceramic disc was measured with a non-contact displacement sensor.

Soil samples were prepared at the saturation water content and split to record the initial gravimetric water content, with the remaining sample deposited in the pressure vessel to a thickness of 2 cm, ensuring a level top surface. The full pressure vessel was weighed with the sample, and the height of the sample recorded with a non-contact displacement sensor.

The initial volume and mass of the samples were calculated along with the GWC of the sample. The stainless steel lid of the pressure vessel was screwed in place, the water drainage tubes connected to monometers, and gas pressure applied. The pressure was applied incrementally, allowing time for equilibration as determined by observation of the mass of the apparatus, volume change of the sample, and change in the volume of water displaced as measured in the monometers. The times for equilibration were on the order of several hours to days; equilibration times were longer at lower applied pressures. Following equilibration (when no further change in mass, water displacement, or sample volume change was observed), the mass of the pressure vessel and sample were recorded, as well as the monometer readings, and the sample volume. The applied pressure was increased to the next increment up to an applied pressure of 350 kPa. Beyond 350 kPa the connections on the measurement devices leaked excessively, preventing sustained application of gas pressure. Once equilibration was reached at 350 kPa, the applied pressure was reduced incrementally to observe the wetting behaviour of the materials. Prior to each mass measurement, the connecting hoses and grooved base plate beneath the ceramic disc were flushed with water to remove any air bubbles which may have formed during pressure application.

The mass of solids was assumed to be constant throughout testing and could be used as a basis for calculation of the gravimetric water content as the mass of the sample was measured at each applied gas pressure where the difference in sample mass was assumed to be equal to the change in the mass of water. The volume of soil solids was also assumed to be constant, and was calculated using the soil solids mass and soil solids specific gravity. The volume of voids was calculated by subtracting the assumed soil solids volume from the measured total sample volume. The volume of water was calculated using the calculated mass of water in the sample and the specific gravity of water. From the assumptions and calculations, the gravimetric water content, volumetric water content, void ratio, and degree of saturation could be calculated and the shrinkage limit determined.

Previous studies have recommended the simultaneous recording of volume and mass change to reduce uncertainty in interpretation of SWCC results due to changes in volume (Delwyn G Fredlund & Houston, 2013). The observation of change in volume provided improved accuracy of the unsaturated volumetric water content and degree of saturation by accounting for volumetric deformation of the samples along with changes in mass.

3.2.2.1.1 Displacement Sensor Calibration

The non-contact displacement sensor (NCDS) utilizes ultrasonic reflection to measure distance between the sensor head and a flat surface. The NCDS was connected to a power supply and output display and was calibrated using a bench micrometer to convert the NCDS output readings from milliamps (mA) to millimeters of displacement.

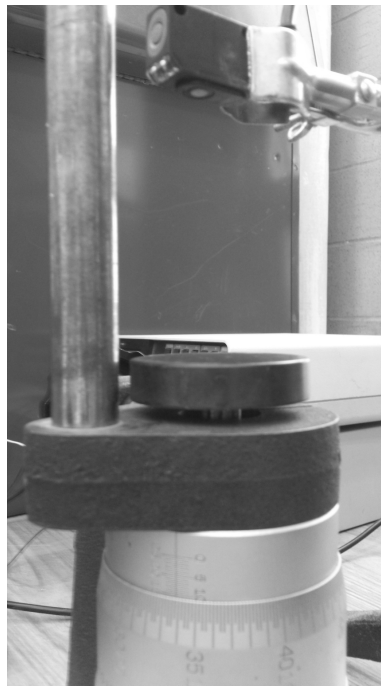


Figure 3-11. Calibration of NCDS using bench micrometer

To calibrate the sensor, a bench micrometer was used to move a flat disc up and down by 1 mm and 0.1 mm increments within the sensor reading range. The resultant mA reading was recorded over the range of the sensor at each disc location as set with the bench micrometer, and calibration was repeated. The NCDS sensor used in this project was a OMRON E4B with a precision of ± 0.1 mm as determined by repeated measurements during calibration. Plotting the displacement vs. mA allowed for determination of the conversion factor to obtain a displacement from the mA readings.

Table 3-3. Calibrated conversion factor from mA to mm for NCDS readings

| Calibration Test | Slope (mm/mA) | R ² |
|------------------|---------------|----------------|
| 1 (19 points) | 3.1369 | 0.99995 |
| 2 (16 points) | 3.1802 | 0.99985 |
| 3 (14 points) | 3.2994 | 0.99982 |
| 4 (9 points) | 3.1214 | 0.99886 |

The distance from the sensor could therefore be obtained by using Equation 3-20 which converts the milliamp reading to mm from the sensor head using the average slope.

$$\text{Distance (mm)} = 3.1845 \text{ mA} \qquad \text{Equation 3 - 20}$$

3.2.2.1.2 Porous Ceramic Verification

The porous ceramic discs used in the pressure extraction method were hydrated by placing the discs in de-aired distilled water in a vacuum chamber, and subjecting the samples to vacuum for a period of 24 hours to remove entrapped air in the ceramic pores.

The dry ceramic discs were initially weighed prior to placement in the vacuum chamber. A vacuum pump connected to the vacuum chamber was cycled on an off in 15 minute intervals until no further air bubbles or nucleation sites were observed. The disc was weighed periodically in a vessel of known mass to determine the change in mass of the disc during hydration. When no further nucleation of air bubbles was observed during pumping, and the mass of the ceramic was observed to remain constant, the disc was left under vacuum for the remainder of the 24 hour period.

The hydrated ceramic discs were installed in the pressure extraction vessels with a known mass of water overlying the samples (100 g). The vessel with 100 g of water inside was weighed, and the gas pressure was increased to 250 kPa for a period of 24 hours. The mass of the vessel and retained water was weighed after 24 hours, and the difference in mass used to calculate the water flux, and the hydraulic conductivity of the ceramic discs to ensure that they were well hydrated, and within specification.

Table 3-4. Specifications for 5 bar porous ceramic discs used in pressure extraction technique

| AEV (bar) | Bubbling Pressure (kPa) | Porosity | Maximum Pore Size (um) | Hydraulic Conductivity (cm/s) |
|-----------|-------------------------|----------|------------------------|-------------------------------|
| 5 | 552 | 0.31 | 0.5 | 1.21×10^{-7} |

The saturated hydraulic conductivity (k) of the ceramic discs was calculated according to the series shown in Equation 3-21 which is a series of substitutions of terms in Darcy's law.

Substitution of Darcy flux (q) in Equation 3-21.1 to the mass flowrate of water through the ceramic is shown in Equation 3-21.2

$$q = ki \quad \text{or} \quad k = \frac{q}{i} \quad \text{Equation 3 – 21.1}$$

where

q = Darcy's flux (m/s)

k = saturated hydraulic conductivity (m/s)

i = hydraulic gradient (m/m)

$$q = \frac{Q}{A} = \frac{m_w}{\rho_w t} \cdot \frac{4}{\pi d^2} \quad \text{Equation 3 – 21.2}$$

where

Q = mass flowrate of water through ceramic (m^3/s)

A = area of ceramic disc (m^2)

m_w = mass flux of water through ceramic disc over time interval t (kg)

ρ_w = density of water at 20°C ($1000 \text{ kg}/\text{m}^3$)

t = time interval over which mass flux occurs (s)

d = diameter of ceramic disc (m)

The gradient term (i) reflects the pressure gradient across the ceramic disc, which is equal to the applied gas pressure expressed as head in meters of water, divided by the thickness of the ceramic disc.

$$i = \frac{\partial h}{\partial L} = \frac{\psi}{\rho_w g T} \quad \text{Equation 46-3}$$

where

∂h = the change in head (m)

∂L = length of flow path (m)

ψ = applied gas pressure (kPa)

T = thickness of ceramic disc (m)

Substituting Equation 3-21.22 and Equation 3-21.3 into Equation 3-21.1 yields Equation 3-21.4 which can be used to solve for the saturated hydraulic conductivity of the porous ceramic discs.

$$k = \left(\frac{m_w}{t} \cdot \frac{4}{\pi d^2} \right) \cdot \left(\frac{g \cdot T}{\psi} \right) \quad \text{Equation 3 - 21.4}$$

3.2.2.2 Filter Paper Method for Matric Suction Measurement

The filter paper method for measurement of total suction is described in Section 3.2.1.1, and is modified only slightly for the measurement of matric suction. Samples are prepared in the same way, with the exception that filter papers are not set on top of the soil sample with no contact, but rather three filter papers are stacked together (as shown in Figure 3-7) and placed in the middle of the soil sample with good contact between the underlying and overlying soil to ensure that fluid transfer and transfer of dissolved ions can occur between the soil and filter papers. The middle filter paper may need to be trimmed to ensure that there is no direct contact with soil (ie. it should be sandwiched between the other two filter papers) to ensure that no soil solids are transferred to the filter paper. Equilibration, mass measurements and drying, and calculation of suction are conducted in the same was as when determining total suction.

3.2.3 Osmotic Suction Measurements

As outlined in Section 2.5.3 the osmotic suction is caused by the presence of dissolved ions in soil creating an ionic gradient. The measurement the dissolved ions in the soil pore-water therefore provides a measurement of the osmotic suction.

3.2.3.1 Saturation Extract Method Electrical Conductivity

Measurement of the concentration of dissolved ions in soil pore water, and therefore the osmotic suction of the soil, can be measured by the electrical conductivity of the pore water solution. The saturation extract method assumes that the electrical conductivity of the solution is representative of the concentration of electrolytic ions dissociated as charged ions in solution which conduct electricity. NaCl is often assumed to be the ion in solution which facilitates calculation of the osmotic suction as NaCl solutions have an easily determined electrical conductivity and total suction as shown in Figure 3-12. The suction relation shown on the right hand side of Figure 3-12 is the relation used to calibrate the filter paper method described in Section 3.2.1.1.

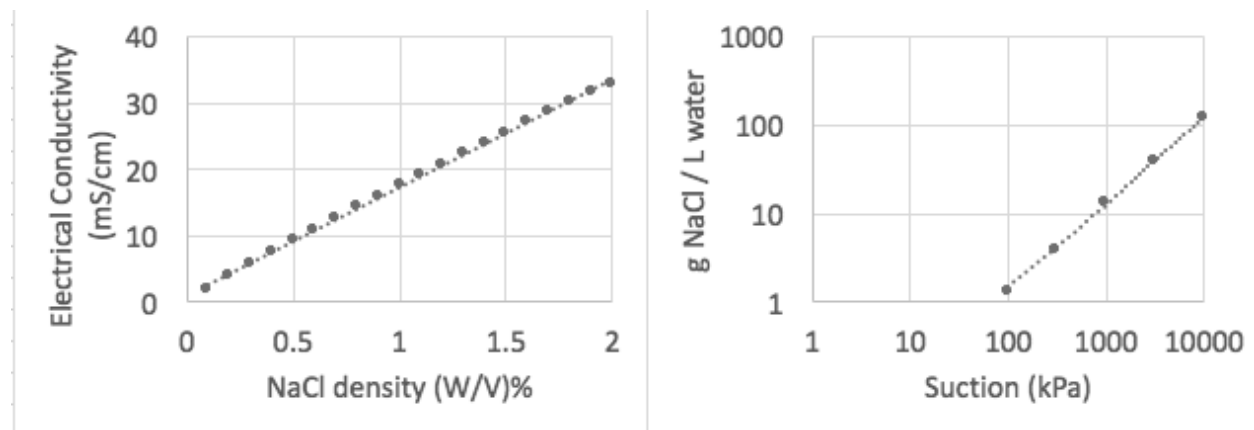


Figure 3-12. Electrical conductivity and total suction as a function of NaCl concentration in water

adapted from (Lewis, 1980) and (ASTM, 2018).

In implementing the saturation extract method a large mass of soil (several hundred grams to a few kilograms) was saturated, and spread on an impermeable plastic sheet to dry. The drying soil was sampled at several intervals (including at the time of saturation) to record the osmotic suction at progressively lower water contents. At each sampling interval, a 5 g mass of soil was taken and mixed with 15 g of de-ionized water using magnetic stirring bars for 15 minutes to ensure a complete saturation of the soil sample, as well as dilution and mixing of the pore water with the added de-ionized water. A gravimetric water content sample was also taken at the same time in order to observe the water content – suction relationship. The mixture was then centrifuged at 3000rpm for 3 minutes, and the centrate water collected. The centrate was vacuum filtered through glass 2.5 μ m filters, and an electrical conductivity probe was used to measure the EC of the filtrate in mS/cm or μ S/cm.

A dilution factor was used in order to normalize the electrical conductivity readings for soil samples of varying water contents. The osmotic suction was calculated as shown in the equation series Equation 3-22.

$$m_{ws} = m_s - \frac{m_s}{\left(1 + \frac{GWC}{100}\right)} \quad \text{Equation 3 – 22.1}$$

Where

m_{ws} = mass of water in the soil sample (g)

m_s = mass of soil sample (g)

GWC = gravimetric water content of soil sample (%)

$$m_{wf} = m_{ws} + m_w \quad \text{Equation 3 – 22.2}$$

Where

m_{wf} = total mass of water in soil-water mixture (g)

m_w = mass of de-ionized water added to soil sample (g)

$$DF = \frac{m_{wf}}{m_{ws}} \quad \text{Equation 3 – 22.3}$$

Where

DF = dilution factor

$$EC_{corrected} = EC_r \cdot DF \quad \text{Equation 3 – 22.4}$$

Where

EC_r = electrical conductivity read with EC probe (mS/cm)

$EC_{corrected}$ = electrical conductivity corrected for dilution (mS/cm)

$$\pi = 0.36 \cdot EC_{corrected} \cdot 101.35 \quad \text{Equation 3 – 22.5}$$

Where

π = osmotic suction (kPa)

Chapter 4 : Material Characterization Results and Discussion

The results of characterization testing is summarized in Table 4-1 for specific gravity, volatile solids content, saturated hydraulic conductivity, and Atterberg Limits.

Table 4-1. Summary of material characterization test results

| Material | Tailings | | Biosolids and Amendments | | | | | Sand |
|-----------------------------------------|-----------------------|-----------------------|--------------------------|-----------------------|-----------------------|------------------------|-----------------------|-----------------------|
| | Unoxidized Tailings | Pre-oxidized Tailings | Toronto Amendment | Fish Compost | Leaf and Yard Waste | Custom Reclamation Mix | Papermill Biosolids | Sand |
| Average Specific Gravity (g/cc) | 2.98 | 3.02 | 1.76 | 2.25 | 2.02 | 2.06 | 2.55 | 2.76 |
| Volatile Solids Content (%) | - | - | 15.2 | 11.4 | 13.2 | 16.4 | 8.4 | - |
| Plastic Limit (GWC, %) | 20 | 23 | 63 | 50 | 65 | 63 | 48 | 12 |
| Liquid Limit (GWC, %) | 24 | 29 | 82 | 61 | 78 | 74 | 56 | 21 |
| Plasticity Index | 4 | 6 | 19 | 11 | 13 | 11 | 8 | 9 |
| Optimum Moisture Content (GWC, %) | 18 | 21 | 58 | 46 | 60 | 58 | 44 | 11 |
| Saturated Hydraulic Conductivity (cm/s) | 5.06×10^{-3} | 1.11×10^{-4} | 1.84×10^{-6} | 2.38×10^{-6} | 4.94×10^{-6} | 4.21×10^{-7} | 3.54×10^{-5} | 1.06×10^{-2} |

From Table 4-1 it is apparent that all the biosolids possess a very high volatile organic content, and are significantly less dense than the sand and tailings materials. The surface application of biosolids at the Vale Copper Cliff Tailings Facility requires the use of specialized spreading equipment which can achieve the required traction when working on a field of biosolids, and the Atterberg limits and field water contents provide a clear indication of the highly malleable nature of the materials.

The particle size distribution for each material is shown in Figure 4-1 and combines the results of wet-sieving with hydrometer tests.

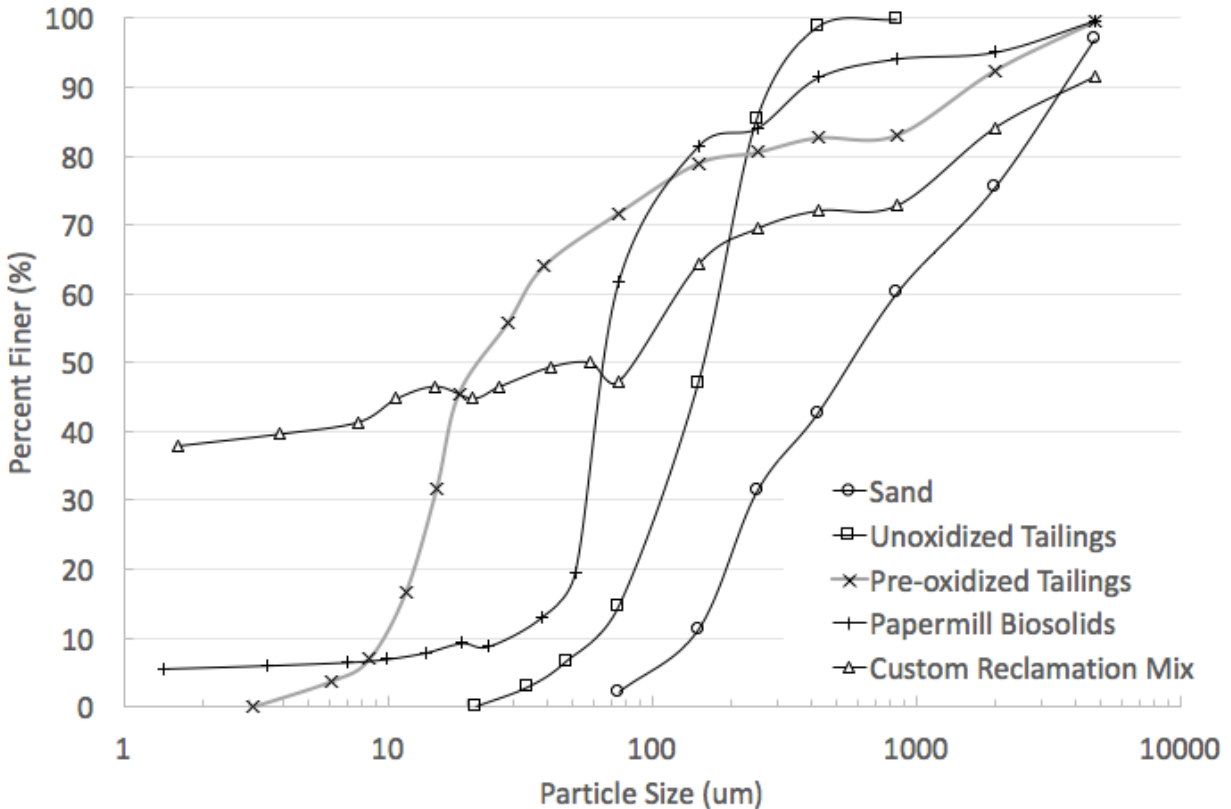


Figure 4-1. Particle size distribution of cover materials

From Figure 4-1 it is evident that the biosolids materials are very fine, with a large fraction of clay-size particles. The small average particle size of the biosolids is likely to contribute to the relative impermeability of the materials and low hydraulic conductivities. The difference in grain size between the unoxidized and pre-oxidized tailings is likely due to erosion and weathering effects over the 40 year period between deposition and sampling of the pre-oxidized tailings. Low-pH and highly oxidizing conditions within the pre-oxidized tailings materials may contribute to the reduction in grain size.

The low saturated hydraulic conductivities of the biosolids materials indicate that they may present very suitable alternatives for clay materials in the construction of the saturated layer of a capillary barrier cover from a water retention perspective, and with respect to inhibiting water flow from the ground surface through to the underlying tailings. The papermill biosolids were found to have a higher specific gravity, consisted of larger particles, and had a higher hydraulic conductivity, indicating that the municipal biosolids may present a more favourable material for an impermeable

water retaining cover. Additionally, when examining the volatile solids content, the municipal biosolids are composed of a greater fraction of volatile organics which may provide additional nutrients as a growth medium in monolayer covers compared to papermill biosolids.

4.1 Soil-water characteristic curves and water retention properties of cover materials

In developing soil-water characteristic curves it is generally accepted to combine the results of multiple test methods (described in Section 3.2) for low, medium, and high suction pressures as shown in Figure 4-2. At higher suction pressures and lower water contents the contribution of osmotic suction is generally small and the matric and total suctions are comparable (ASTM D6836-18, 2017a).

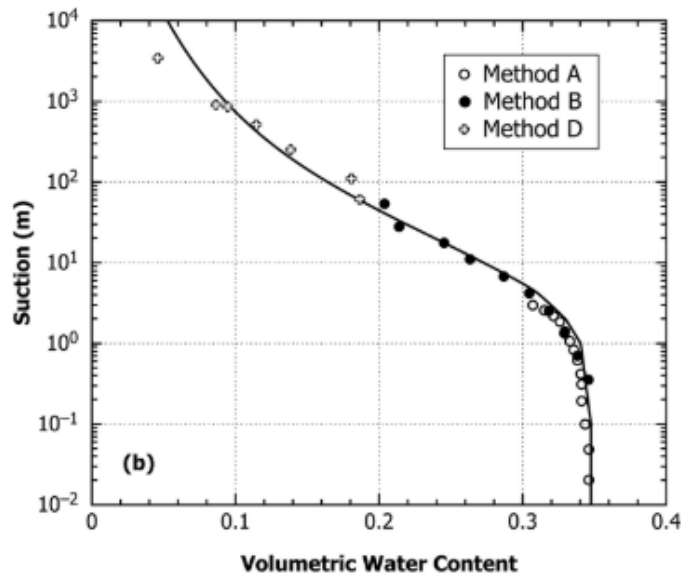


Figure 4-2. Combined results of Hanging Column (Method A), Porous Plate Pressure Extraction (Method B), and Chilled Mirror Hygrometer (Method D) to construct a soil-water characteristic curve spanning a large range of suction pressures (ASTM D6836-18, 2017a).

For axis translation tests the results were recorded with respect to gravimetric water content, volumetric water content, and degree of saturation. For total suction tests (dewpoint mirror hygrometer and filter paper method) the results are given with respect to gravimetric water content. In order to convert the results from GWC to VWC the void ratio and shrinkage limit of the materials was used to calculate the volume of voids in samples and the subsequent volumetric water content according to the series of equation shown in Equation 4-1.

$$VWC = \frac{V_{water}}{V_{solids} + V_{voids}} \quad \text{Equation 4 - 1.1}$$

$$V_{solids} = \frac{\left(\frac{m_{soil}}{GWC+1}\right)}{\rho_{solids}} \quad \text{Equation 4 - 1.2}$$

$$V_{voids} = V_{solids} \cdot e \quad \text{Equation 4 - 1.3}$$

$$S = \frac{V_{water}}{V_{voids}} \quad \text{Equation 4 - 1.4}$$

Where

VWC = Volumetric Water Content

V_{water} = volume of water in the soil sample

V_{solids} = volume of solids in the soil sample

V_{voids} = volume of voids in the soil samples

e = void ratio

S = degree of saturation

The soil-water characteristic curves for the cover materials are shown below.

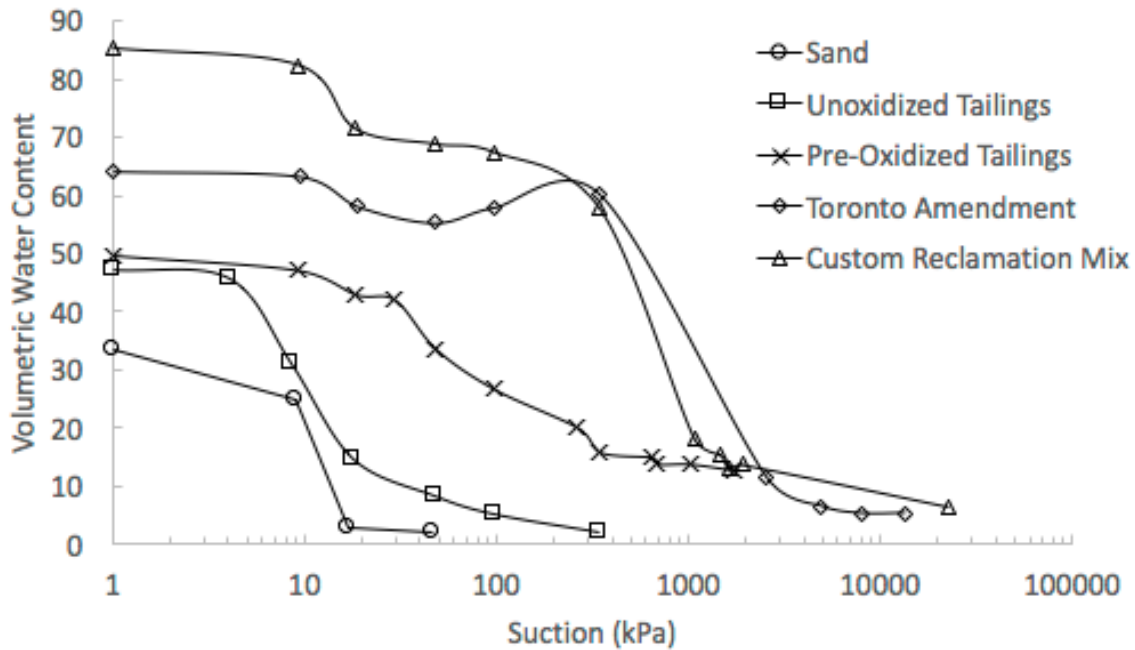


Figure 4-3. Soil-water characteristic curve for characterized cover materials (volumetric water content on y-axis)

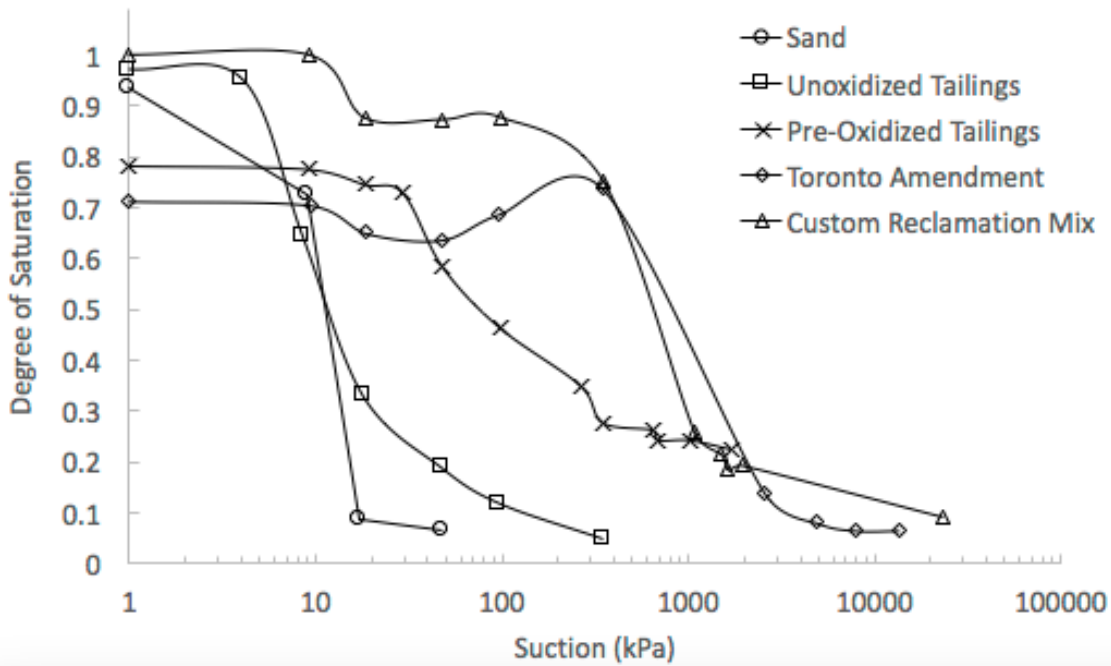


Figure 4-4. Soil-water characteristic curve for characterized cover materials (degree of saturation on y-axis)

As shown in Figure 4-3 and Figure 4-4 the sand and unoxidized tailings materials desaturate relatively easily, as reduced water contents are observed at low suction pressures. The rapid desaturation of these materials can be attributed to the large soil grain and pore size distributions. The pre-oxidized tailings demonstrate increased water retention characteristics relative to the sand and unoxidized tailings, which is attributed primarily to the reduction in grain size and soil pore size within the weathered tailings.

A degree of saturation less than 1 is observed in the pre-oxidized tailings and Toronto Amendment materials. All samples were saturated in the pressure extraction chamber, and it is suspected that inundation of the sample did not fully saturate the smallest pore spaces within the specimens, and that a vacuum saturation chamber would be required to achieve full saturation of the pre-oxidized tailings and Toronto Amendment biosolids samples (this was unavailable at the time of testing). Previous research demonstrates that the slightly lower initial degree of saturation is not likely to have significant impacts on the AEV or wetting path, and has only small effects on the overall WRC (Heidarian, 2012). Additionally, the SWCC of the tailings have little effect on the determination of cover effectiveness in this experiment as later described in Chapter 6 where it is

shown that the water retention properties of the underlying tailings have little effect on the establishment of the capillary barrier cover condition.

The biosolids materials exhibit strong water retention properties and do not experience significant desaturation until suction pressures of approximately 500 kPa are applied. Comparing the SWCCs of the sand and biosolids materials relative to the conceptual model shown in Figure 2-6 of Section 2.3.2.2.2 the requisite difference in water retention properties exists between the two materials to establish a theoretical capillary break as shown in Figure 4-5, where the sand desaturates between 10kPa and 500kPa while the biosolids remain nearly completely saturated.

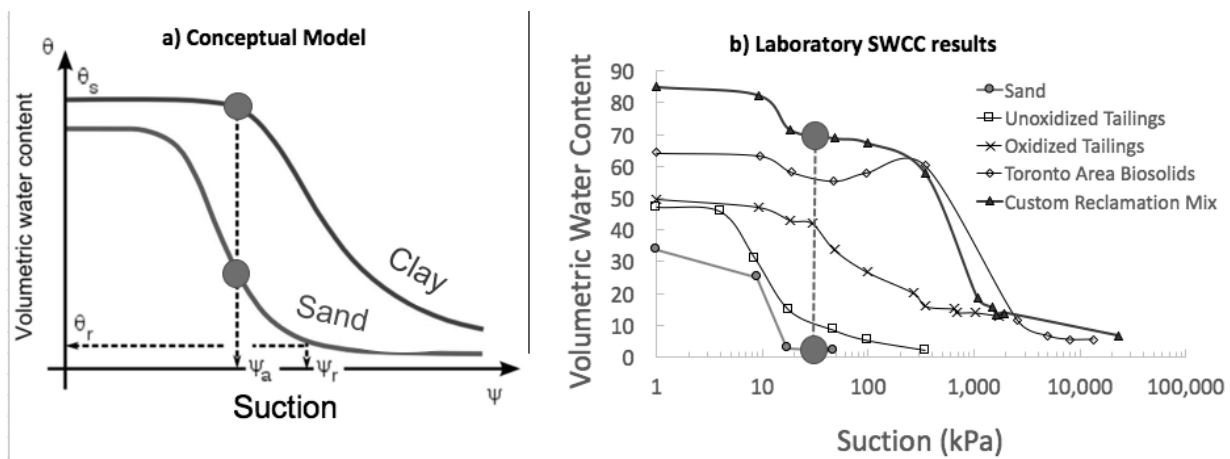


Figure 4-5. SWCCs of cover materials showing potential establishment of capillary barrier at elevated suctions with desaturated sand layer and saturated biosolids in agreement with conceptual model

Table 4-2. Cover material water retention properties obtained from SWCC

| Material | VWC at Saturation | Air Entry Value | | | Residual Water Content | | | Shrinkage Limit | |
|---------------------------|-------------------|-----------------|------|----------------------|------------------------|------|----------------------|-----------------|------------|
| | | kPa | VWC | Degree of Saturation | kPa | VWC | Degree of Saturation | VWC | Void Ratio |
| Sand | 0.32 | 10 | 0.26 | 0.98 | 50 | 0.02 | 0.05 | 0.13 | 0.34 |
| Unoxidized Tailings | 0.46 | 6 | 0.45 | 0.95 | 300 | 0.08 | 0.05 | 0.15 | 0.73 |
| Pre-oxidized tailings | 0.50 | 20 | 0.44 | 0.75 | 30000 | 0.07 | 0.10 | 0.44 | 1.36 |
| Custom Rehabilitation Mix | 0.82 | 400 | 0.75 | 0.75 | 20000 | 0.08 | 0.08 | - | - |

The water content of the materials in a saturated state compacted wet of optimum is shown in Table 4-2 along with the suction pressure, water content, and degree of saturation at the AEV and residual water content. The shrinkage limits for the granular materials (sand and tailings) were determined graphically as shown in Figure 4-6.

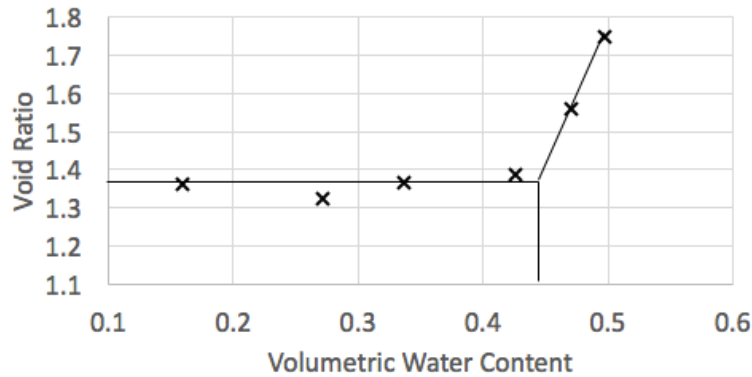


Figure 4-6 . Shrinkage curve for pre-oxidized tailings from axis translation test results

The void ratio observed during axis translation results is similar to that observed during column deconstruction described in Section 5.3 where the pre-oxidized tailings exhibit an average void ratio of 1.35 (data shown in Appendix B).

The shrinkage limit of the biosolids materials was tested, however, it was observed that the biosolids did not exhibit drying behaviour typical of granular soils where volume change ceases and soil pores begin desaturating. Instead, it was observed that the biosolids continued to volumetrically deform and shrink at extremely low water contents. Visually, the biosolids formed dried outer layers and when broken with a mortar and pestle would contain a moist core.

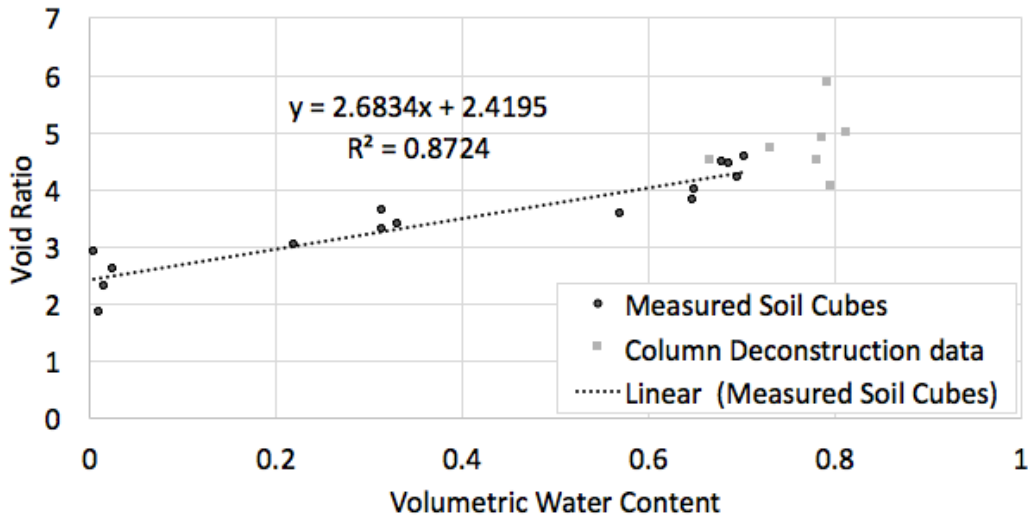


Figure 4-7. Shrinkage curve of municipal biosolids from weighed, measured, and dried cubes

The volumetric deformation of the biosolids was measured by weighing cubes of biosolids materials and measuring the dimensions with Vernier calipers. The cubes were dried, and the weight and dimensions measured and recorded at various time intervals. Following air drying and intermittent weighing and measurement, the biosolids cubes were oven-dried to determine the gravimetric water content. Using the GWC, the gravimetric solids content and volume of solids was calculated using the material’s specific gravity. The gravimetric water content and volumetric water contents were back calculated for each interim measurement. The void ratio was calculated by assuming that the difference between the volume obtained from measuring the outer dimensions of the cubes, and the calculated volume of solids was entirely attributable to void space. This assumed that there was no change in the volume of solids during drying. The method of measuring soil cubes during drying to determine shrinkage limit is described as a suitable and less labour intensive alternative to the wax method (ASTM D4943 – 18) in unsaturated soil textbooks (D. G. Fredlund et al., 2012).

Generally speaking, the municipal biosolids materials demonstrate suitable soil characteristics for use in developing a saturated layer in a capillary barrier cover. The Custom Reclamation Mix in particular displayed a very low saturated hydraulic conductivity (4.21×10^{-7} cm/s), and the SWCC developed during characterization shows good water retention properties with an AEV of approximately 400 kPa. The CRM biosolids were found to be superior to the straight biosolids (referred to as the Toronto Amendment) and were subsequently used in column testing. The

following chapters further develop the proof of concept using numerical modelling and laboratory scale column tests to observe water flux and saturation behaviour of CRM municipal biosolid capillary barrier covers.

Chapter 5 : Column Testing

Columns were commissioned based upon the mechanical application limitations of equipment used at Vale to apply 15 cm cover layers of biosolids, and supported by the results of preliminary numerical modelling in SV-Flux indicating the suitability of 15 cm layers for establishment of a capillary barrier cover.

5.1 Soil Column Setup

Acrylic columns were designed following initial 1-D modelling in SV-Flux which indicated that the proposed cover dimensions were appropriate for establishing a capillary barrier cover with sand and municipal biosolids. Chapter 6 provides greater detail on numerical modelling.

5.1.1 Column Design and Specifications

Rectangular columns were designed to simplify machining of the instrumentation ports in the column walls. The horizontal interior dimensions of the columns were 25 cm x 25 cm. The columns were constructed with an internal height of 110 cm. Two walls were cut from ½” acrylic while the other two walls were cut from ¼” acrylic. The column bases were cut from ½” acrylic. Three columns were constructed simultaneously to speed production; this allowed for instrumentation ports to be milled in three sheets of acrylic at a time and later matched with the appropriate pieces to create a completed column. Following recommendations from the employees at the Carleton Science Technology Center to provide additional strength to the column walls, the ½” walls were grooved to accommodate the ¼” walls and an acrylic bonding agent was used to ensure a strong water-tight seal.

Three types of instrumentation port were milled in the column walls. Ports were milled at heights within the column shown in Table 5-1. Circular ports with a 21 mm diameter were milled in one wall of each column, initially to fit tensiometers, however, these ports were instead used for METER Teros 21 soil suction sensors. 3mm circular holes were drilled in one of the ½” walls to accommodate Rhizosphere Rhizon Flex pore water samplers. 21 mm x 12 mm holes were milled to accommodate METER Environment 5TE soil moisture/temperature/electrical conductivity sensors.

Table 5-1. Port height and corresponding measurement or sampling horizon

| Port Height (cm from base) | Horizon in CBC | Horizon in Monolayer |
|----------------------------|----------------------------|---------------------------|
| 88 | Middle of upper sand layer | N/A |
| 73 | Middle of biosolids layer | N/A |
| 58 | Middle of lower sand layer | Middle of biosolids layer |
| 45 | Top of tailings | Top of tailings |
| 5 | Base of tailings | Base of tailings |

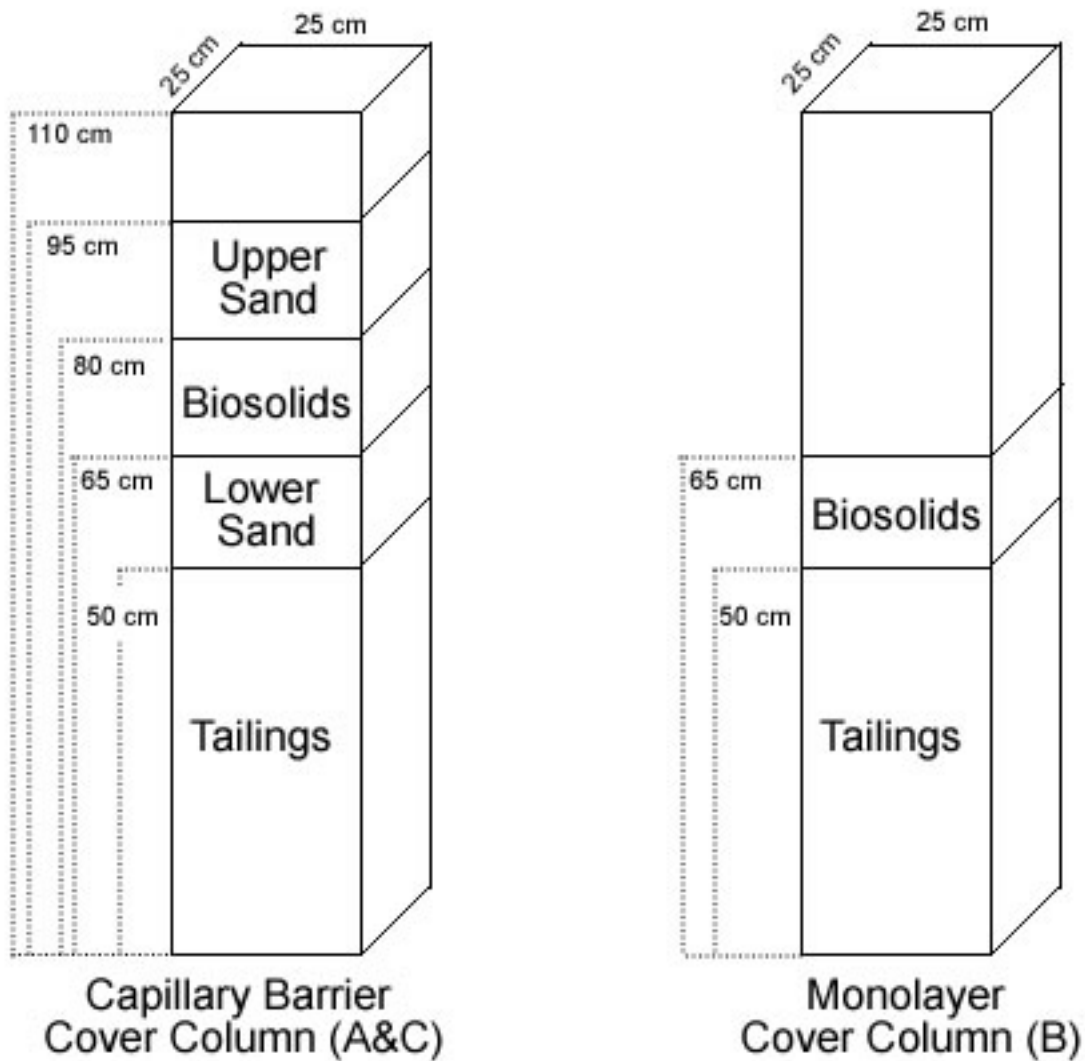


Figure 5-1. Column schematic indicating layer thicknesses from the column bases for the Capillary Barrier and Monolayer Covers.

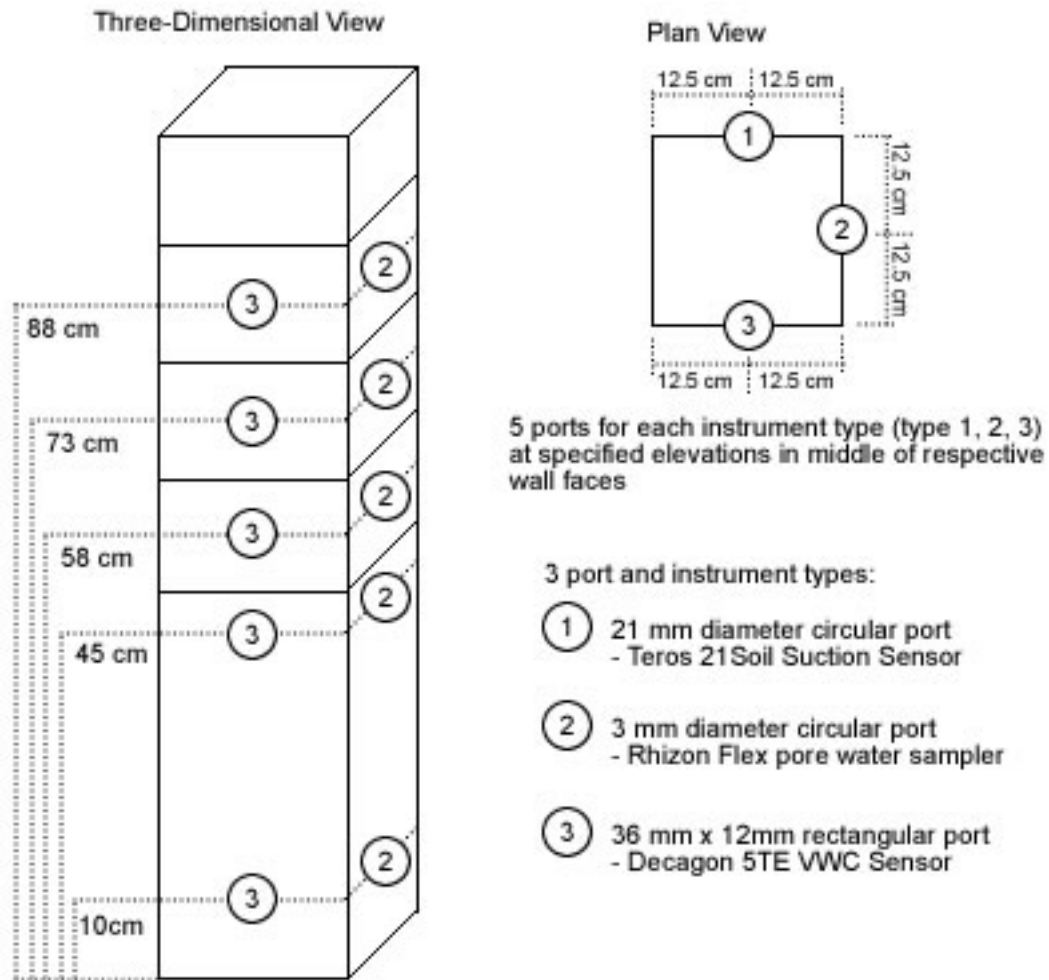


Figure 5-2. Schematic indicating column instrumentation type, elevations, and locations

One drain hole was added to the center of the base of each column to allow for the attachment of 1/4" drain tubing. The drainage port was threaded, and fittings wrapped in Teflon tape were screwed in to the base to establish a water-tight seal. Ball valves were added to provide the option to close the drainage ports. A geotextile fabric was cut to 25 cm x 25 cm and placed at the base of the column to prevent soil particles from falling out the drain port.

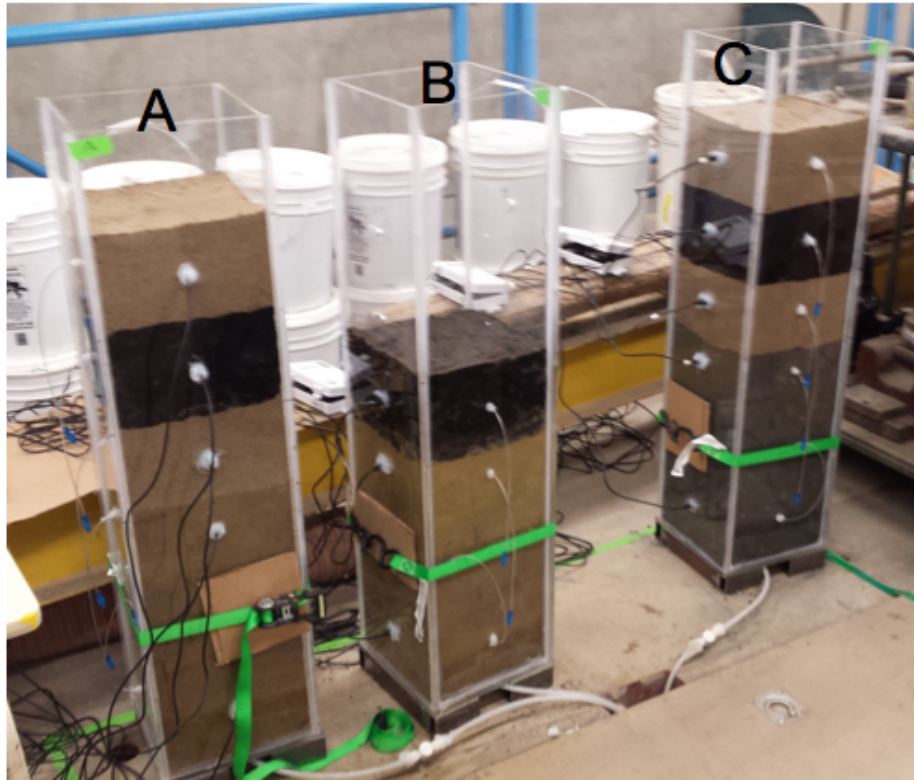


Figure 5-3. Photograph of instrumented columns at start of test period.

5.1.2 Instrumentation and Sensor Calibration

Each column was instrumented to collect volumetric water content, temperature, electrical conductivity, and suction data. METER Environmental 5TE sensors were used to monitor soil moisture, temperature, and EC, while METER Environmental Teros 21 sensors were used to monitor soil suction.

The 5TE sensors determine the volumetric water content by measuring the dielectric constant of the media using time domain reflectometry to calculate the dielectric constant of the soil medium, which can be related to volumetric water content using the Topp Equation shown in Equation 5-1.

$$VWC = (4.3 \cdot 10^{-6} \varepsilon_a^3) - (5.5 \cdot 10^{-4} \varepsilon_a^2) + (2.92 \cdot 10^{-2} \varepsilon_a) - 5.3 \cdot 10^{-2} \quad \text{Equation 5-1}$$

Where

VWC = volumetric water content

ϵ_a = dielectric permittivity (Farad per meter)

The dielectric constant is strongly dependent on the water content of the soil, and is almost independent of soil density, texture, and salt content, with no significant temperature dependence (Topp, Davis, et al., 1980). Independent calibrations were conducted for each cover material. Two methods of calibration were used; the first method of calibration used soils of known gravimetric water contents which were packed into tared 1 L containers and weighed, then sensors were inserted to read the VWC. Tests were repeated at several water contents for each soil type. The second method was to pack soil of a known gravimetric water content into a tared 1 L container, which was weighed and a sensor inserted, then a known mass of water was added and recorded at various time intervals. In the 5TE sensors an onboard thermistor measures temperature, and a stainless steel electrode array measures electrical conductivity.

When calculating the volumetric water content of the 1 L soil samples, the series of equations shown in Equation 5-2 was used to calculate the mass of soil in the 1 L sample, and the subsequent VWC.

$$GWC = \frac{m_{water}}{m_{solids}} \quad \text{Equation 5 – 2.1}$$

$$m_{water} = GWC \cdot m_{solids} \quad \text{Equation 5 – 2.2}$$

$$m_{soil} = m_{water} + m_{solids} \quad \text{Equation 5 – 2.3}$$

$$m_{soil} = GWC \cdot m_{solids} + m_{solids} \quad \text{Equation 5 – 2.4}$$

$$m_{soil} = (GWC + 1) \cdot m_{solids} \quad \text{Equation 5 – 2.5}$$

$$m_{solids} = \frac{m_{soil}}{GWC+1} \quad \text{Equation 5 – 2.6}$$

$$VWC = \frac{\left(\frac{m_{water}}{\rho_{water}}\right)}{\left(\frac{m_{solids}}{\rho_{solids}}\right) + \left(\frac{m_{water}}{\rho_{water}}\right) + \left(\frac{m_{air}}{\rho_{air}}\right)} \quad \text{Equation 5 – 2.7}$$

The calculated volumetric water content of the 1 L beakers was compared to the measured VWC from the 5TE sensors and used to establish a calibration curve for unoxidized tailings is shown in Figure 5-4, and calibration curve data are shown in Table 5-2.

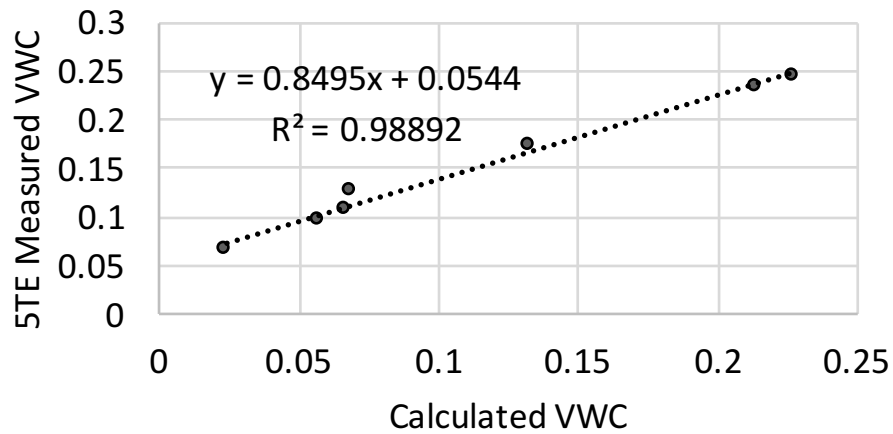


Figure 5-4. 5TE sensor volumetric water content calibration curve for unoxidized tailings

Table 5-2. 5TE sensor calibration curve parameters for different soil types

| Material | Slope | Intercept |
|-----------------------|--------|-----------|
| Sand | 0.5931 | 0.0696 |
| Unoxidized Tailings | 0.8495 | 0.0544 |
| Pre-oxidized Tailings | 1.3485 | 0.0391 |
| CRM | 1.0416 | 0.1246 |

Manufacturer application notes indicate that salinity and soil type effects on Decagon/METER moisture content sensors using TDR are negligible (Campbell, Campbell, et al., 2009). There are indications that extreme salinity can affect volumetric water content readings; soils up to 10 dS/m show good calibration results, however, soils with 30 dS/m or more may shift calibration of VWC readings (Campbell & Decagon Devices, 2001).

The calibration of the 5TE sensors resulted in a maximum VWC reading of 0.85 for the CRM biosolids material with a large degree in variability due to the sensor output at high water contents, and when used in conjunction with spot gravimetric water content samples to back-calculate the mass and volume of solids in each layer, may result in calculated degrees of saturation with a low level of precision and accuracy. The maximum VWC read by the sensors in the biosolids following

calibration corresponds to the saturated VWC of the biosolids materials calculated from axis translation and specific gravity tests.

The Teros 21 sensors are comprised of a porous ceramic disc sandwiched between dielectric permittivity sensors. The dielectric permittivity of the porous ceramic is dependent upon the amount of water present in the pore spaces. The ceramic discs are manufactured with a known SWCC, and therefore calculation of the water content from the dielectric permittivity allows for the suction pressure to be inferred from the water content of the ceramic. Sensors were factory calibrated prior to delivery using silica flour to develop a calibration curve and set on-board processor outputs. The AEV of the porous ceramic is approximately 9 kPa; this implies that the ceramic will not register changes in soil suctions lower than 9 kPa (METER Group, 2017).

The Teros 21 and 5TE sensors were connected to METER Environmental Em50 Dataloggers which stored data for the duration of the testing, and allowed for sampling intervals as short as 1 minute.

Rhizon Flex pore water samplers were used to withdraw soil pore-water samples from the columns. Rhizon flex samplers comprise of a fine porous ceramic with maximum pore sizes of 0.2 μm connected to a small sterile plastic tube with a luer attachment which could be sealed with a cap or attached to a syringe for sampling. The ceramic tip was inserted through the 3 mm diameter holes described in Section 5.1.1 and sealed in place. Caps were affixed to the ends of the samplers to maintain an air-tight environment within the columns. The small pore size of the samplers allowed for the withdrawal of water without significant disturbance or removal of solids from the columns.

5.1.3 Simulated Boundary Conditions

A simulated water table was implemented by establishing constant head reservoirs below the columns. The drain hoses from each column were passed through the floor of the laboratory, and secured within individual reservoirs which were maintained at a constant height to simulate a static water table depth. The elevation difference between the base of the columns and the water surface in the reservoirs was measured at 2 m.

Field weather conditions were not simulated during column testing. Instead, “worst-case” drying and wetting conditions were simulated by subjecting the columns to 35 days of drying without precipitation, followed by a period of flushing, and a second drying phase of 14 days. The temperature and relative humidity at the uppermost soil surface within each column was recorded using Lascar Electronics EasyLog Temperature & Humidity data loggers. A bucket of known surface area was partially filled with water and placed on a balance for the duration of the column testing. The mass of water, and height of water within the bucket was used as a proxy for the actual evaporation affecting each column. During flushing, the height of water ponded above the surface of each columns was used to corroborate the data obtained from the evaporation measurement bucket.

5.1.4 Initial Conditions

It was initially intended that tailings materials be mixed with water and deposited at an elevated water content (ie. in a slurry state) to simulate slurry deposition and to remove effects of grain size segregation related to sampling. All of the pre-oxidized tailings were obtained from within a fifty square meter area of P Area in the Copper Cliff Tailings facility which was deposited between 1960–1989. The unoxidized tailings were obtained from a two hundred square meter area of R2 deposition area and sampled along a rough grid extending from the deposition point in an effort to remove the effects of grain size segregation (ie. when mixed together should reasonably represent the tailings transported in the pipeline). The un-oxidized tailings were sampled from a section of the R2 area which had been deposited earlier in the day on which sampling occurred.

Due to the difficulty of mixing tailings in a slurry and placing a homogenized slurry in the columns, it was decided to mix tailings of the same type from all sample buckets to form a relatively homogeneous tailings pile which could be deposited in the acrylic columns. The un-oxidized tailings were mixed with water by hand to elevate their water content prior to deposition, however, the water content was below the liquid limit of the tailings to facilitate handling. Sand was mixed with water in a similar fashion prior to deposition. Unoxidized tailings were sampled at a saturated water content, and some consolidation occurred within the five gallon sample buckets. The

contents of the unoxidized tailings buckets were mixed together by hand to create a homogeneous tailings pile which was then deposited in the test column. Gravimetric water content samples were taken for all materials during deposition. The initial water contents of the columns are shown in Table 5-3 from gravimetric water content sampling during deposition.

Table 5-3. Column layer elevations, materials, and initial water content

| Elevation | Column A | | Column B | | Column C | |
|-------------|-----------------------|-------|-----------------------|------|------------------------|------|
| | Material | GWC | Material | GWC | Material | GWC |
| 0.80 – 0.95 | Sand | 0.06 | N/A | - | Sand | 0.06 |
| 0.65 – 0.80 | CRM | 2.39 | N/A | - | Custom Reclamation Mix | 2.12 |
| 0.50 – 0.65 | Sand | 0.048 | CRM | 2.30 | Sand | 0.05 |
| 0.00 – 0.50 | Pre-oxidized Tailings | 0.17 | Pre-oxidized Tailings | 0.20 | Unoxidized Tailings | 0.18 |

In Table 5-3 it can be seen that the biosolids materials were deposited at high water contents wet of optimum, and tailings were deposited slightly dry of optimum. Given the relatively small discrepancy between the OMC and the initial water content of the tailings materials, no significant effects on compaction or water retention were anticipated or observed. The sand layers were also deposited slightly dry of optimum which was not expected to significantly alter column results, and as described in Section 5.2.5 there were no significant volume changes associated with consolidation and material compaction. The deposition at drier water contents is in line with practical field application practices as sand would be delivered and applied in cover construction at low water contents.

5.1.5 Column Flushing

Column flushing was conducted with the intent of fully saturating the columns prior to a second round of drying, and to obtain pore water samples from regions of the columns which were otherwise too dry to obtain pore water samples without flushing. Flushing was also done in order to assess the effectiveness of biosolids covers to limit infiltration of water into the underlying tailings by simulating a “worst-case” scenario of hugely excessive precipitation. Flushing was conducted by initially adding 1 L of water to the top of each column and observing the effects of the added water. When it was determined that water was not penetrating the biosolids layer,

additional water was added in 1 L increments. Eventually it was observed that the upper sand layers in both capillary barrier columns became fully saturated without any noticeable effect on the underlying biosolids layer. The volumetric water content measured in the biosolids of Column A undergoes large swings throughout the flush period, but returns to a reading similar to that observed at the start of flushing when ponded water was removed at the end of flushing. This variability in water content reading was attributed to the changes in salinity during flushing affecting the sensor output, as well as changes in volume. In the monolayer column, some water was initially absorbed by the partially desaturated biosolids layer. Following initial saturation of the uppermost layers of each column, water was not observed to flow through the biosolids layers and a small volume of water remained ponded above the soil surface of each column.

The height of water ponded in the columns was measured over the course of the flushing period to observe the actual rate of evaporation affecting the surface of each soil column. The measurements from the weigh bucket and the temperature & humidity sensors were used to supplement the evaporation observations.

At the end of the flushing period (July 30th) the excess ponded water was removed from the columns using a peristaltic pump.

5.2 Column Test Results

Column testing results have been separated into three sections: initial drying, flushing, and secondary drying. Results are shown as depth profiles of volumetric water content, degree of saturation, suction, and soil pore water quality. Measures of pore water quality include pH, oxidation-reduction potential, and electrical conductivity. Concentrations of metal ions and nutrient anions were analyzed using Inductive Couple Plasma Mass Spectrometry and Emission Spectrophotometry conducted at the University of Ottawa Advanced Research Center.

5.2.1 Initial Drying Period Results

The initial drying period of testing spanned 35 days in duration between June 7th and July 12th, and was designed to simulate “worst-case” drying conditions for severely arid climates, as well as to observed the general responses of the covers to significant drying events.

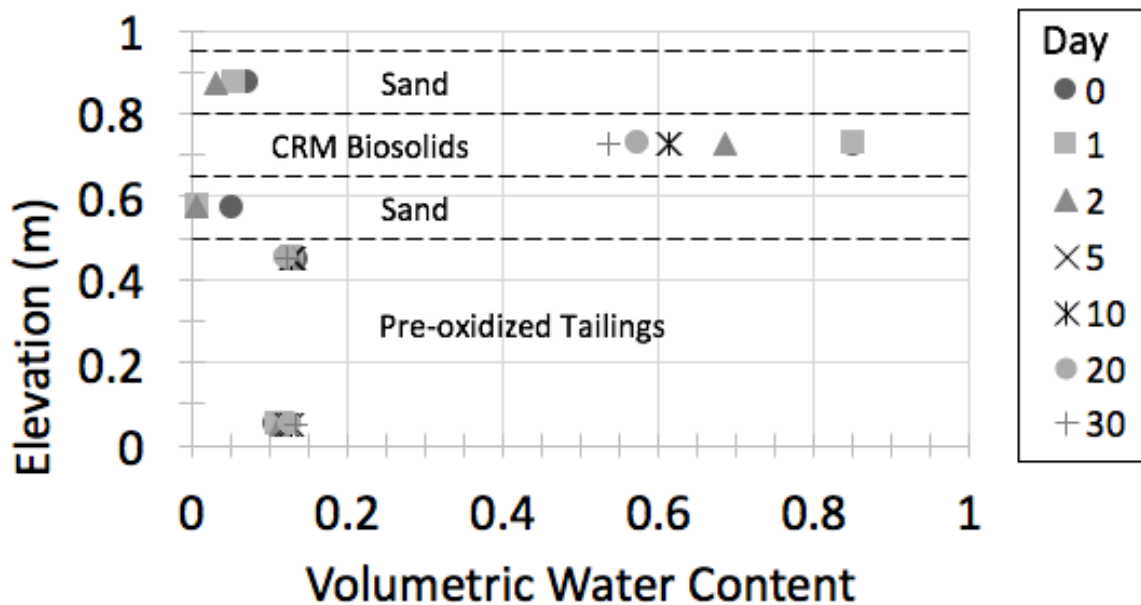


Figure 5-5. Volumetric water content profile of Column A (calibrated)

The volumetric water content profiles in Figure 5-5 and Figure 5-12 show the retention of water in the CRM biosolids layers within the CBC columns, Column A and Column C respectively. The biosolids in Column C appear to maintain a greater VWC compared to the biosolids in Column A.

The saturation profile of Column A is shown in Figure 5-6 highlighting the desaturation of the CRM biosolids layer within the cover. The degree of saturation within the columns was inferred using the developed SWCCs developed in Section 4. Saturation profiles of Column B and Column C are shown in Figure 5-9 and Figure 5-13 respectively. The sensors within the biosolids layer of Column C is report a higher volumetric water content throughout testing, however, the final state of the columns during deconstruction (Section 5.2.5.1) show similar degrees of saturation and water contents within the biosolids of both Column A and Column C despite significant differences in the 5TE Sensor readings. The differences in evaporative conditions at the surface of each column were modelled in SV-Flux (ie. modelling evaporative conditions for Column A applied to Column

C, and vice-versa) and do not noticeably alter the volumetric water content profiles or flux within the covers, indicating that the biosolids in Column A may not have desaturated to the extent reported by the sensor.

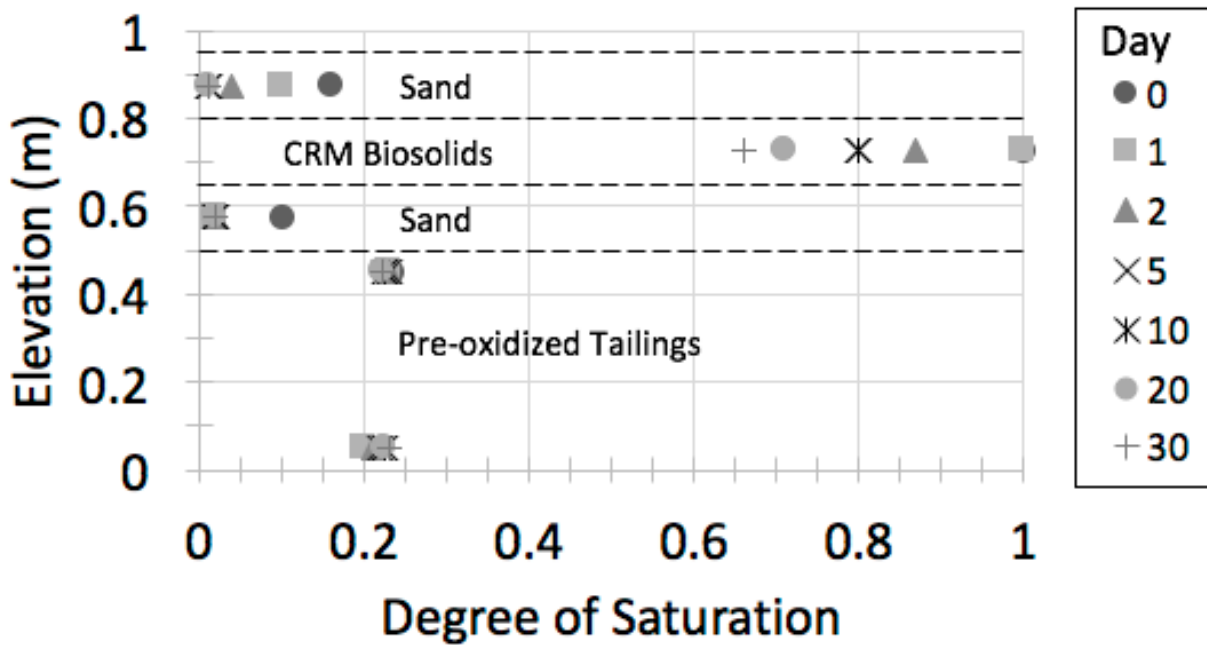


Figure 5-6. Calculated saturation profile for Column A

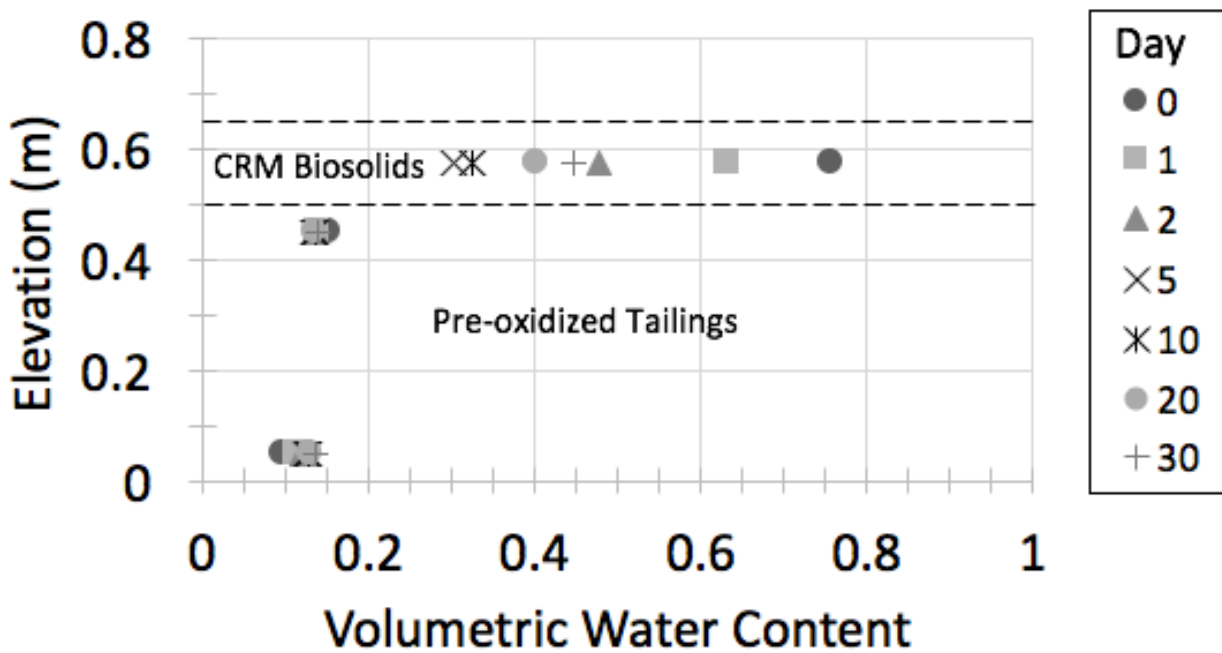


Figure 5-7. Volumetric water content profile of Column B (calibrated)

Despite deposition at low VWC, and low suctions within the tailings layer, no significant degree of re-wetting of the pre-oxidized tailings was found to have occurred in Column A and Column B due to the discontinuous nature of the water column to the reservoir; further explanation of the failed boundary condition can be found in Section 6.1.4.1.

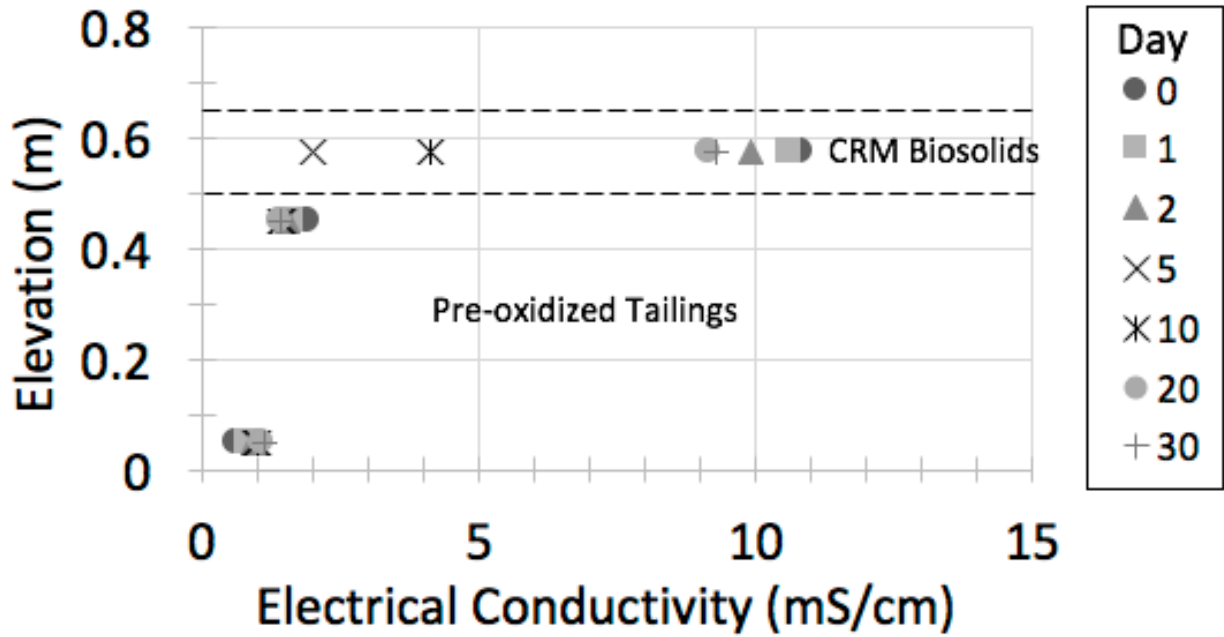


Figure 5-8. Electrical Conductivity profile of Column B from 5TE sensors

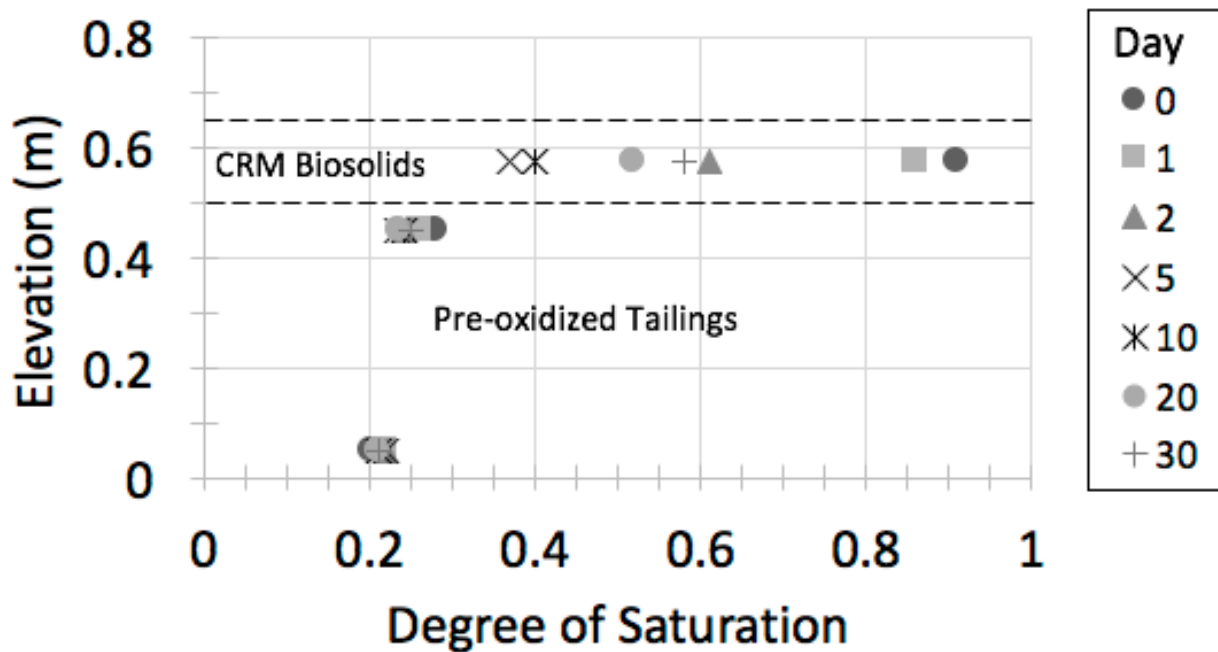


Figure 5-9. Calculated saturation profile of Column B

Significant cracking and volumetric deformation was observed in the upper half of the biosolids in the monolayer cover of Column B as shown in Figure 5-10. The lower half of the biosolids material did not appear to experience significant drying or deformation. The upper portion of the biosolids was observed to experience significant desaturation and drying with large cracks developing in the first week of drying. The crack volumes continued to increase throughout drying, and biosolids materials separated from the walls of the columns after approximately 10 days of drying.

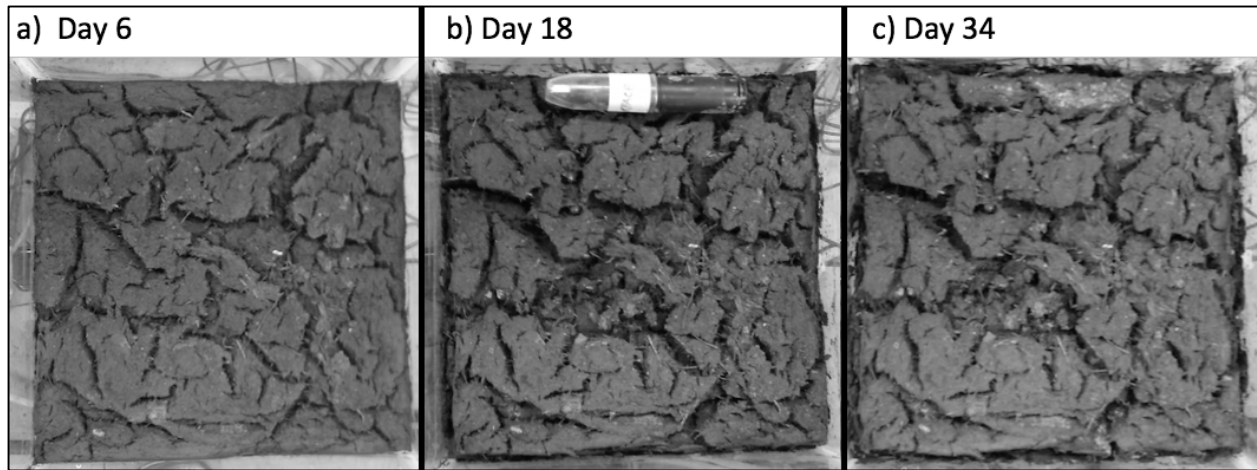


Figure 5-10. Cracking observed in the surface of the CRM biosolids in monolayer cover of Column B

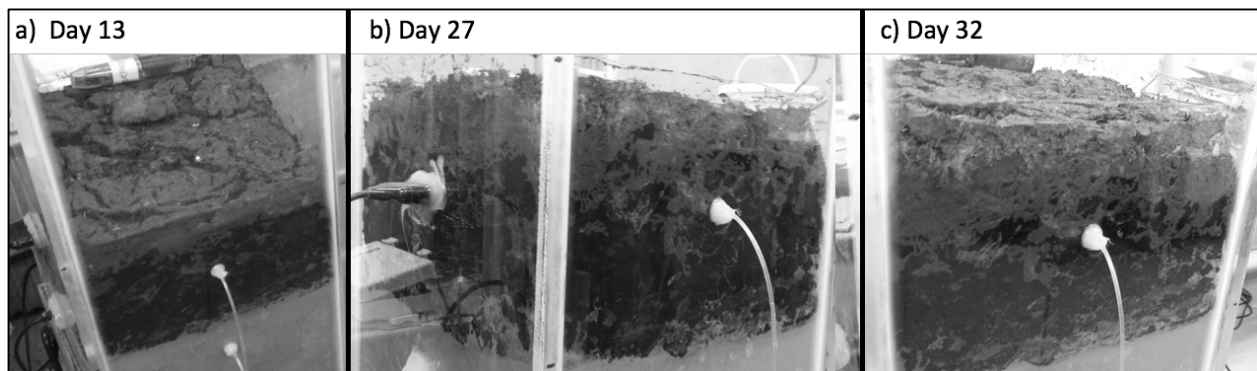


Figure 5-11. Biosolids monolayer shrinkage and separation from walls of Column B

From Figure 5-10 and Figure 5-11 it can be seen that significant shrinkage and volumetric deformation occurs at the surface of the biosolids of the monolayer cover. Crack formation continued through the drying period. In Figure 5-10 a small portion of the biosolids was sampled (slightly down and left of center) to assess the gravimetric water content and total suction within the biosolids. After Day 13, difficulty was encountered extracting surface samples due to

hardening of the biosolids surface, therefore sampling was conducted by removing small amounts of material from the inner edges of cracks in the biosolids surface. Eventually all sampling became impossible without significant risk of compromising the biosolids layer integrity, and sampling was ceased. The gravimetric water content of the surface samples indicated significantly greater degrees of drying at the cover surface relative to the volumetric water content and suction sensors embedded within the middle of the biosolids layer. As seen in of Figure 5-11, the drying and shrinkage front within the biosolids layer does not appear to reach the instrumentation and sampling port, and therefore suction measurement and volumetric water contents reported by the instrumentation are not representative of the full thickness of the CRM layer, however, the instrumentation and visual observation indicated that while the surface was drying, the lower portion of the CRM layer maintained a high water content and degree of saturation relative to the surface.

Table 5-4. Gravimetric water content of surface samples from Column B biosolids surface

| Day | Total Suction (kPa) | GWC (%) |
|-----|---------------------|---------|
| 0 | 0 | 231 |
| 6 | 20 | 177 |
| 13 | 600 | 118 |
| 18 | 940 | 88 |

Volumetric water content sensors report a large decrease in VWC from Day 0 to Day 10, with a subsequent small rebound from Day 11 to Day 35. The rebound in water content within the biosolids layer may be attributed to the following:

- Water flux upwards from the simulated water table reservoir, and the suction forces within the biosolids pulling water upwards from the base of the tailings. Unlikely due to failure of the simulated boundary condition.
- Accuracy of the volumetric water content sensors is $\pm 15\%$ of the measured value above a VWC of 0.4
- Increasing salinity and EC affecting sensor VWC output
- Volume change within the biosolids layer resulting in variation in the readings of water content within the sensor's volume of influence

- Decoupling of the sensor from the surrounding biosolids, causing the sensor to interact with air voids immediately surrounding the probe.

Numerical modelling results shown in Section 6.1.1 do not show a rebound in water content within the biosolids layer of monolayer columns when no precipitation is applied, and therefore the rebound in VWC is most likely not a result of water flux into the biosolids.

Analysis of a clustering of data from the 5TE sensor calibration indicates that there is little correlation between the real volumetric water content of the calibration samples and the electrical conductivity measurement, however, the measured volumetric water content of was shown to be weakly correlated to the electrical conductivity. Increasing electrical conductivity as read by the 5TE sensor was shown to correlate positively with an increased volumetric water content reading, even when the real volumetric water content remains relatively constant. This was not observed during initial calibration measurement prior to implementing the sensors in the column tests. Unfortunately, the data could not be normalized to remove the effects of salinity variation as the actual volumetric water content for each time interval is unknown. It is therefore likely that the decrease in water content shown by the sensor in the biosolids layer of Column B between Day 5 and Day 20 is caused by a substantial change in electrical conductivity. The change in electrical conductivity is suspected to be attributed to the migration of salts upwards towards the surface of the biosolids due to evaporation. The electrical conductivity profiles of Columns A and C do not change significantly throughout the test (Column A range 12.50 to 9.45, Column C range 10.40 to 8.75); the profiles are shown in Figures 5-19 to 5-24.

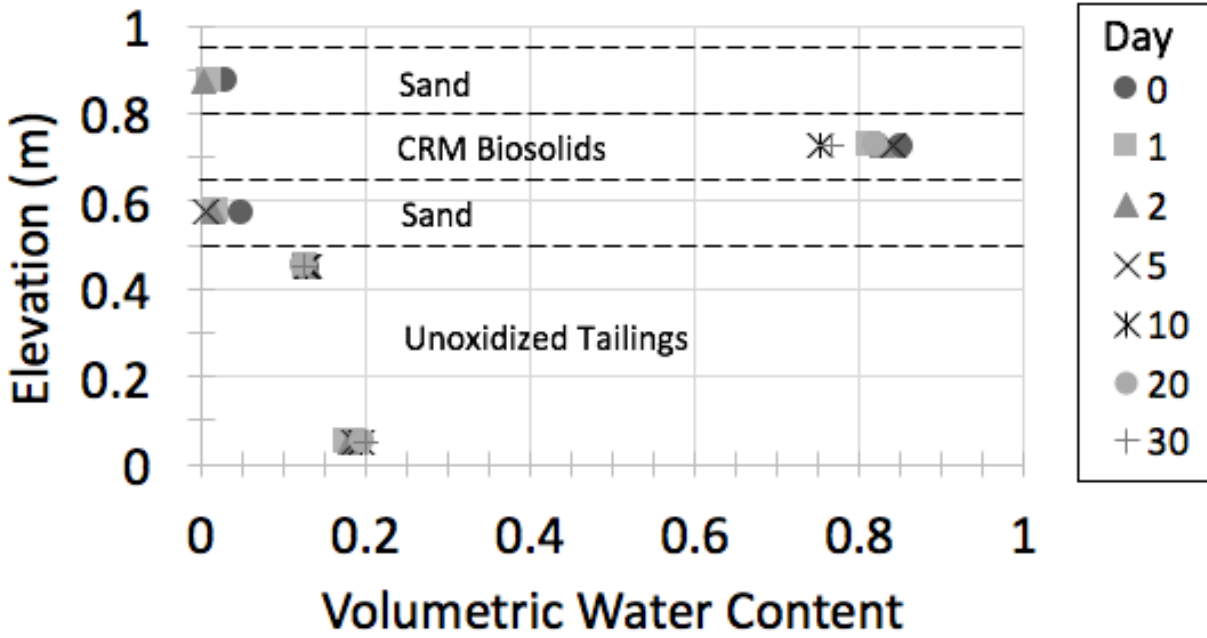


Figure 5-12. Volumetric Water content profile of Column C (calibrated)

In both capillary barrier covers the uppermost sand layer experienced significant drying.

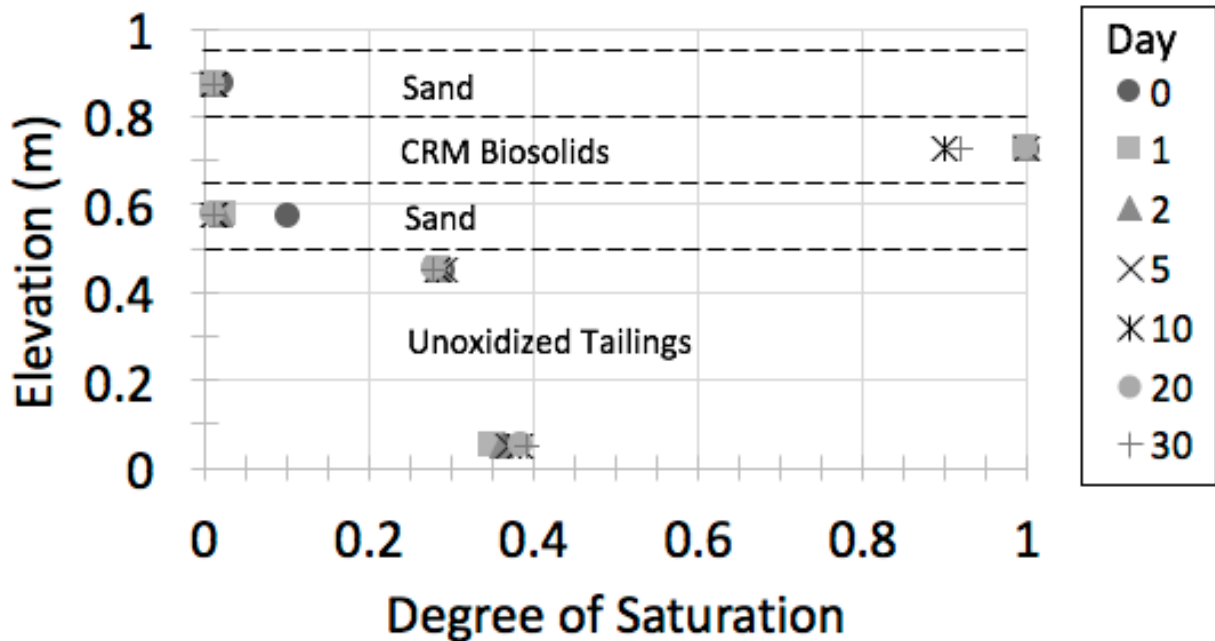


Figure 5-13. Saturation Profile of Column C (calibrated)

5.2.2 Column Flushing Results

During flushing of all columns, it was observed that the biosolids layers provided significant resistance to water infiltration. This was most evident where water remained ponded on the upper surfaces of all columns while the instrumentation in underlying layers reported insignificant change in the degree of saturation of the underlying soils.

Prior to flushing, the time to breakthrough was calculated as the time required for water to travel through the biosolids layer. The simple mathematical prediction is shown in Equation 5-3 and estimates a time to breakthrough of for water travelling through the CRM layers to be 412 days.

$$Time\ to\ breakthrough = \frac{biosolids\ layer\ thickness\ (m)}{biosolids\ saturated\ hydraulic\ conductivity\ \left(\frac{m}{day}\right)} \quad \text{Equation 5 - 3}$$

Despite the extensive estimated time to breakthrough, it was anticipated that there may be some displacement of water from the biosolids layer into the underlying sand layer during flushing.

During flushing it was observed that a small leak developed in a sensor port in the biosolids of Column B and a port in the tailings of Column A; both leaks were fixed with curing plumbing putty within a period of four hours after the leaks began on the morning of July 16th (10:00 to 14:00). During the period of leakage approximately 25 mL of water was lost from each column; the level of water ponded above the soil surface in the columns, and the volumetric water content readings were unchanged. From the lack of flux out of the column drains, and the observation of a leak in the sensor ports, it was determined that the column drains were plugged, inducing a “no-flow” boundary condition at the base of the columns. The effect of a “no-flow” boundary condition is discussed in Section 6.1.3.

The volumetric water content profile of the columns during flushing are shown below in Figure 5-14 where the x-axis measurement is the time since the beginning of flushing.

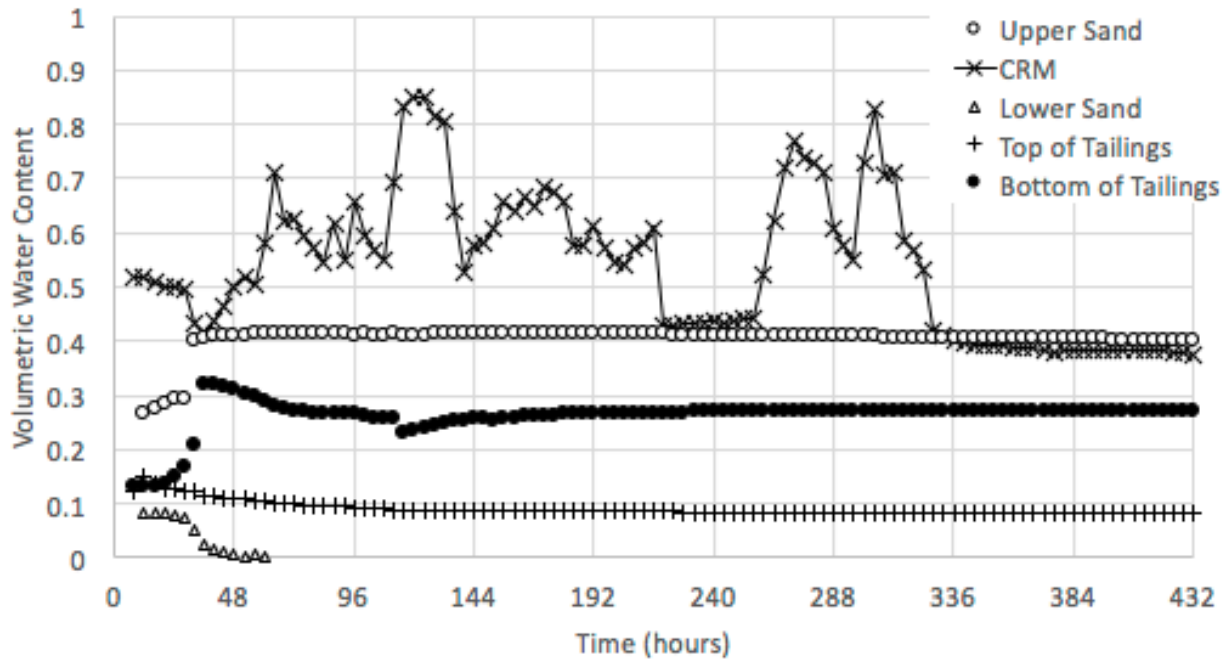


Figure 5-14 - A. Volumetric water content profile of Column A throughout flush period (calibrated)

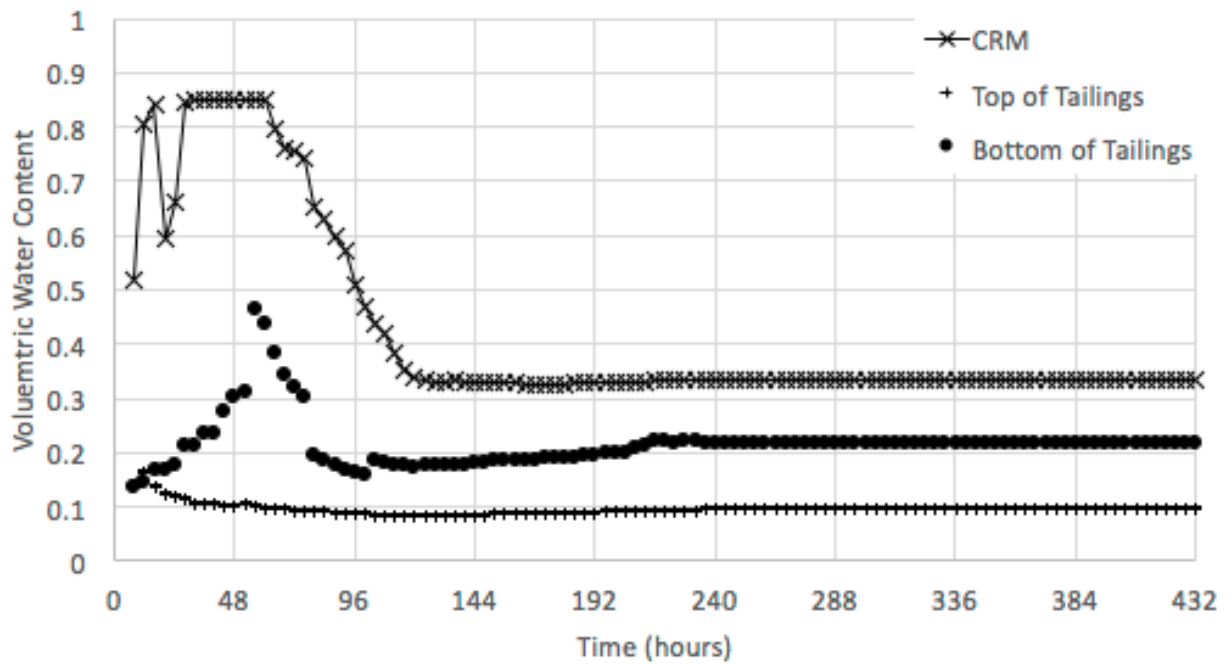


Figure 5-15. Volumetric water content profile of Column B throughout flush period (calibrated)

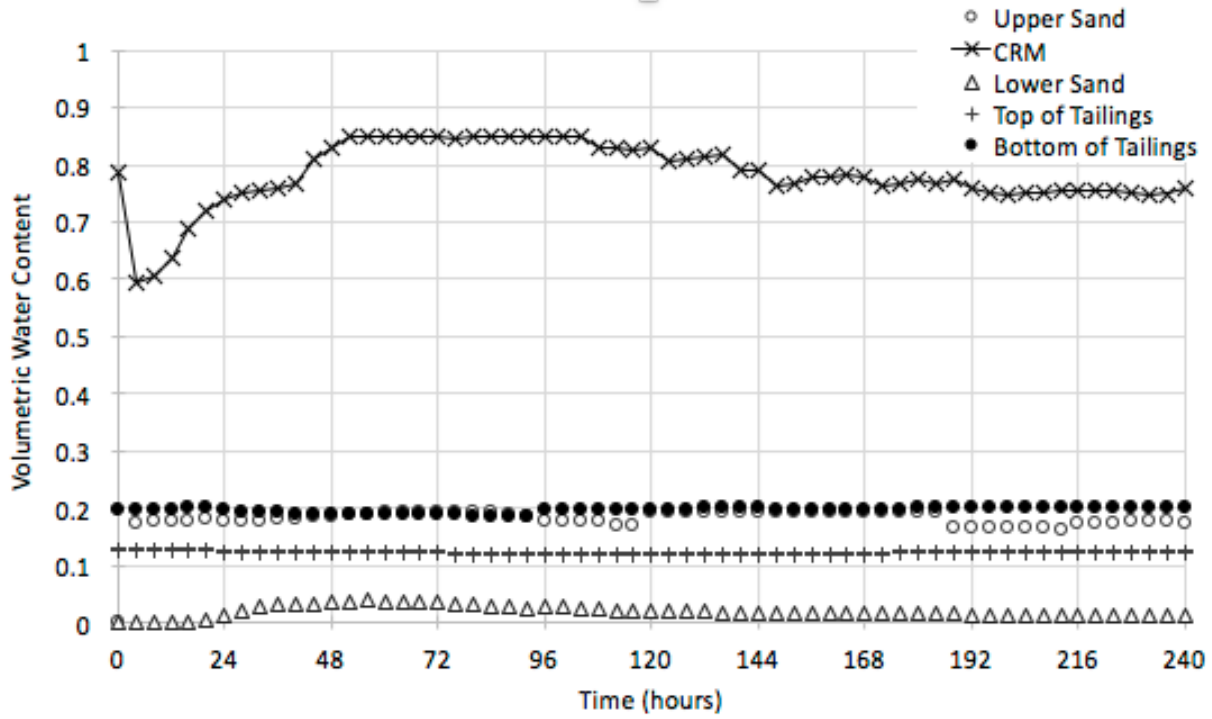


Figure 5-16. Volumetric water content profile of Column C throughout flush period (calibrated)

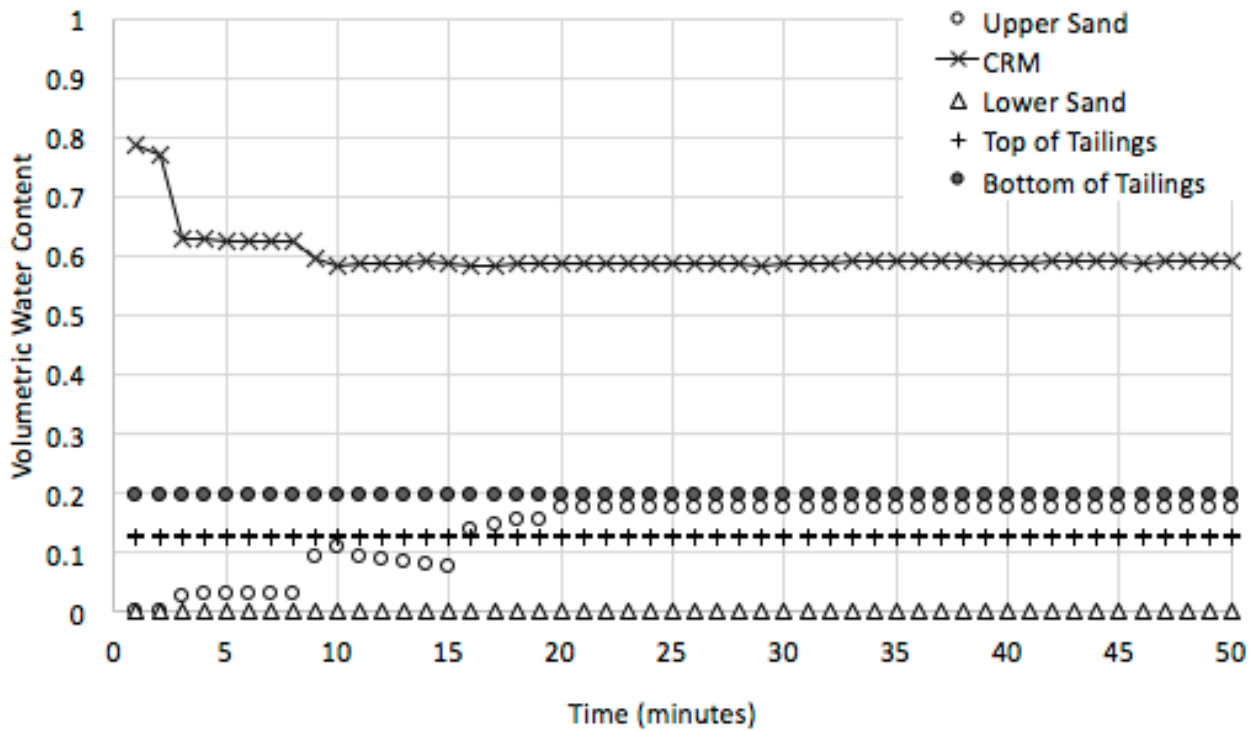


Figure 5-17. Volumetric Water Content profile of Column C at start of flush period (calibrated)

In Column C, it is apparent that the upper sand layer becomes saturated, and that the CRM biosolids layer VWC readings drop slightly. The volumetric water content of the biosolids layer recovers quickly as shown in Figure 5-16. The salinity of the pore water and volume of the layer remain steady during this time. The change in VWC of the biosolids is within the measurement error of the instrument, and there appears to be little effect on reduction of saturation within the biosolids layer.

From Figure 5-16 and Figure 5-17 it can be seen that there is no significant change in the volumetric water content readings of the tailings of Column C during flushing, indicating that flux through the cover is limited despite a large volume of water ponded on the cover surface. In Figure 5-16 the slight increase in water content of the lower sand layer between hours 24 and 120 may be a result of water passing through the sand layer, or it may be due to volumetric deformation and consolidation of the sand under the increased load of ponded water. No significant change occurs in the water content measured at the top of the tailings.

5.2.3 Post-Flush Drying Results

Post-flush drying was monitored for a period of 86 days between July 30th 2018 and October 24th, 2018. Post-flush drying results were found to be similar to initial drying results in all columns. The upper sand layers of the capillary barrier cover columns experienced significant reduction in volumetric water content and a corresponding increase in suction, while the biosolids layers in the CBC columns maintained a relatively high degree of saturation relative to the biosolids in the monolayer column. The surface of the monolayer column experienced further cracking and volumetric deformation during the second drying cycle as shown in Figure 5-18.

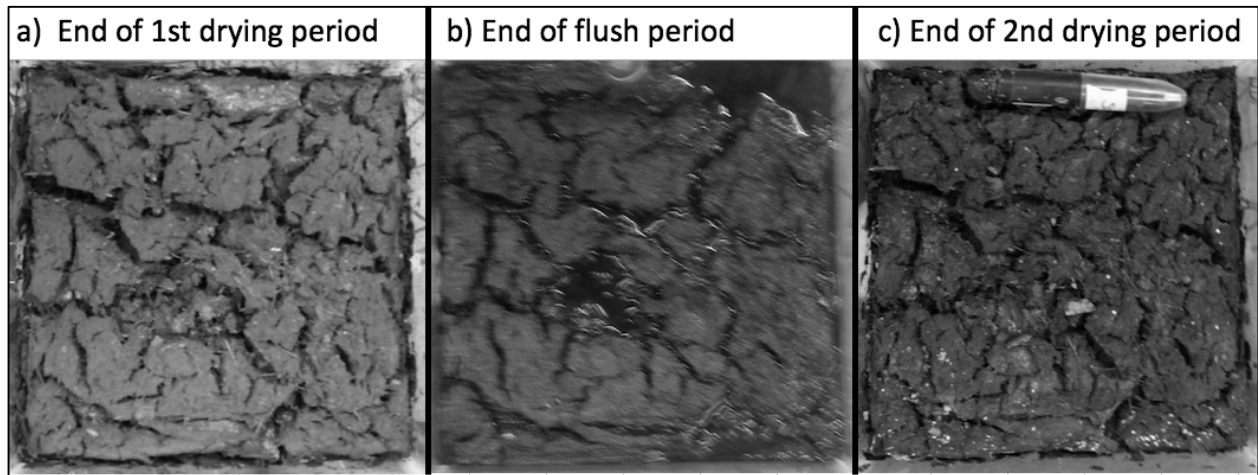


Figure 5-18. Drying of monolayer cover biosolids throughout duration of column testing

Slight swelling was observed in the biosolids during the flush period, however, visual observation of the biosolids surface following flushing shows that major cracks persist and volumetric deformation is not significantly reversed during the 14 days of flushing during which the biosolids were saturated and submerged beneath ponded water.

5.2.4 Pore-Water Quality Results

Soil pore-water samples were drawn from the ceramic samplers at the start of testing on June 7th, on July 7th prior to flushing, on July 27th near the end of the flushing period, and on August 30th to observe changes from secondary drying. All pore water quality results were normalized using a calculated dilution factor for each sample. Samples from the sand layers of Column A and Column C following initial and secondary drying do not exist as no pore water could be extracted.

The electrical conductivity of the pore water samples from Column A are shown in Figures 5-19 and 5-20. The “Initial” concentrations, pH, EC, and ORP values were obtained from saturation extraction methods similar to those described in Section 3.2.3.1. Acid leaching was not conducted as part of this project, however, numerous previous studies have examined the mineralogical and chemical composition of the Vale tailings.

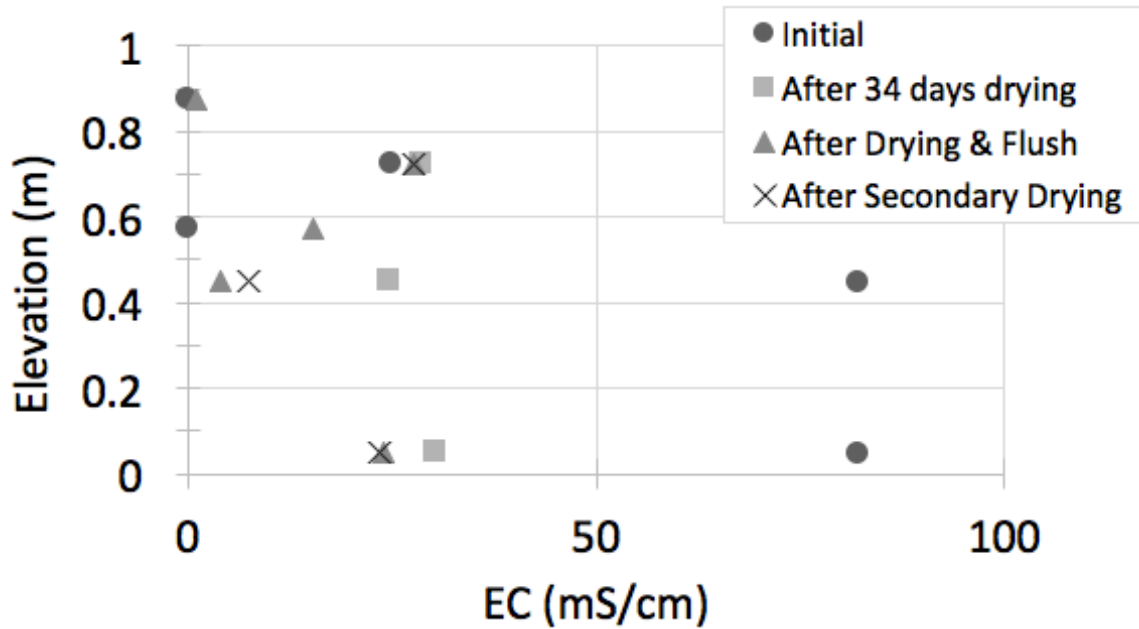


Figure 5-19. Electrical conductivity profile in Column A measured from pore water samples

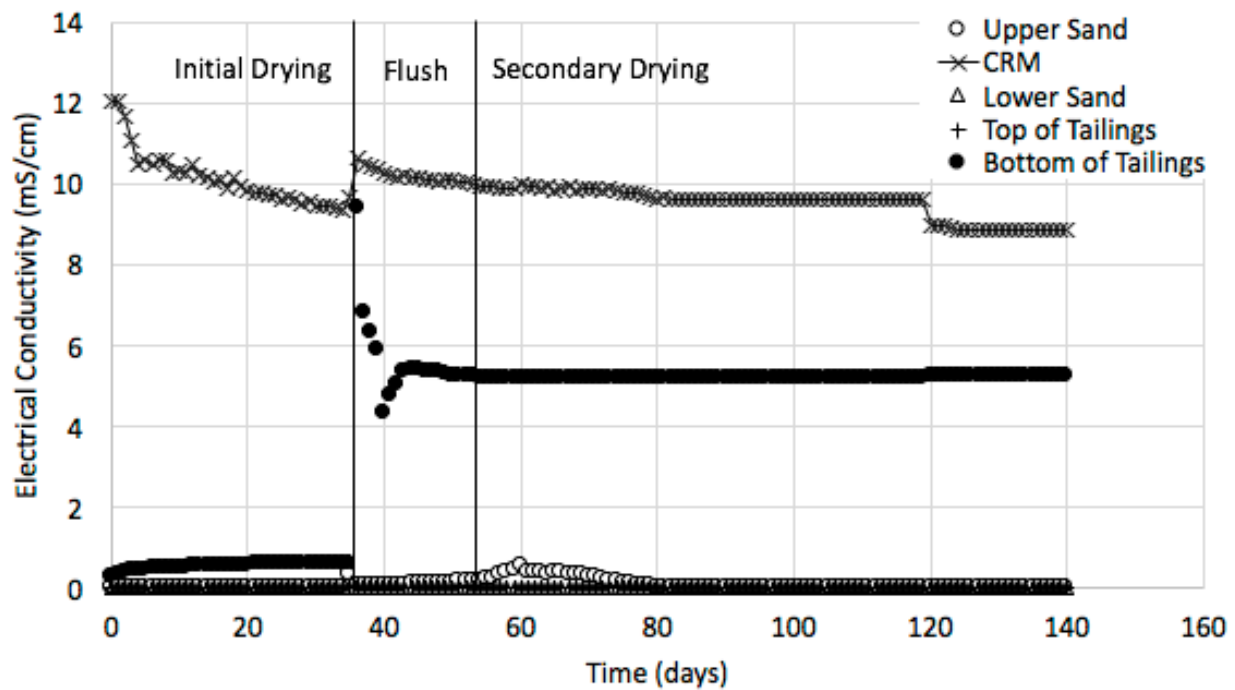


Figure 5-20. Electrical conductivity profile in Column A reported by 5TE sensors

The reduction in electrical conductivity of the tailings is shown to be greatest at the upper surface of the tailings. There is little change in the EC of the biosolids and sand layers.

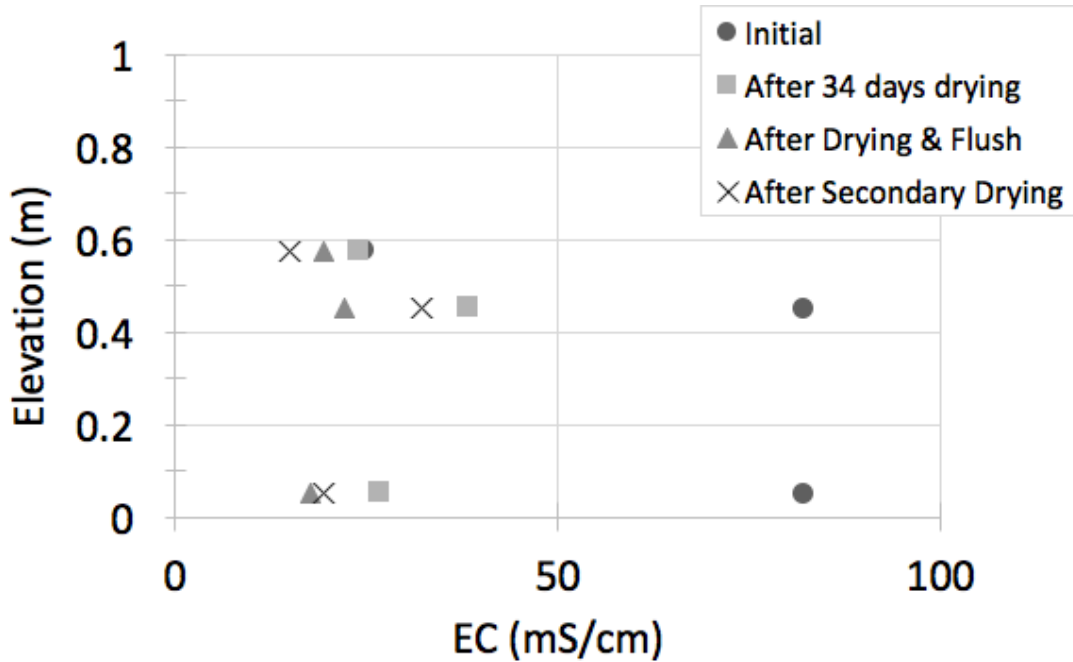


Figure 5-21. Electrical conductivity profile in Column B measured from pore water samples

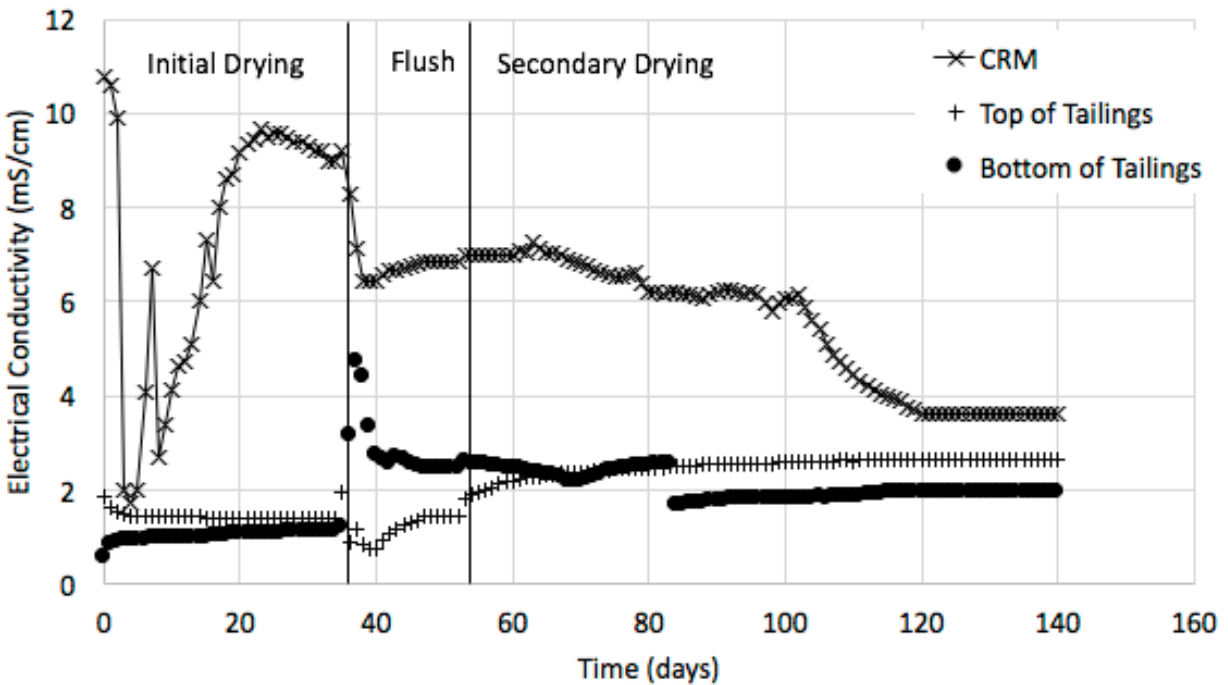


Figure 5-22. Electrical conductivity profile in Column B reported by 5TE sensors

Column B shows a similar reduction in tailings EC in Figure 5-21 and 5-22. Reduction of electrical conductivity within the tailings occurs throughout testing similar to column A; in Column B the lower section of the tailings layer demonstrate greater reduction of EC relative to the upper tailings

which is contrary to the observations of Column A. The biosolids layer in Column B shows a greater relative change of EC when compared to Column A, and the biosolids in Column B appear show a reduction in EC throughout testing.

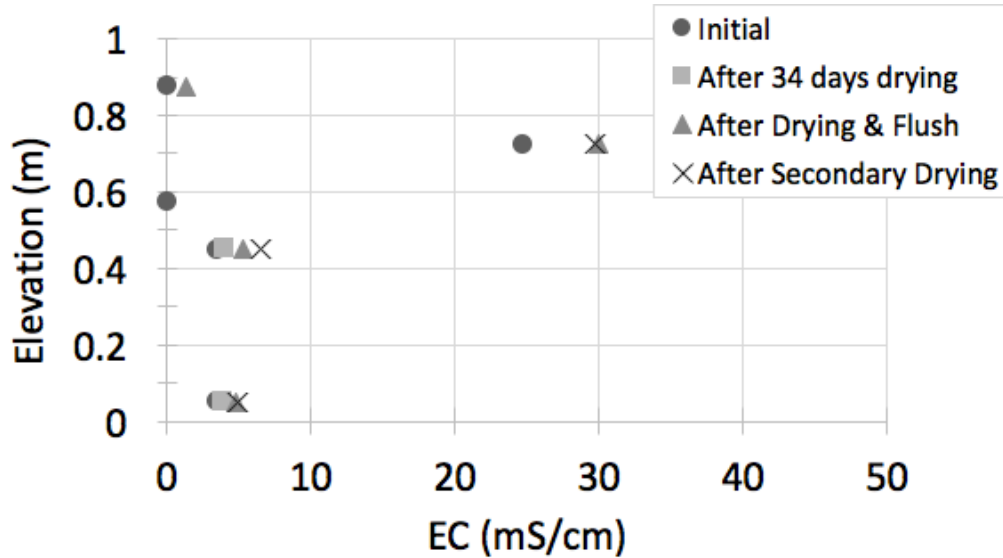


Figure 5-23. Electrical conductivity profile of Column C measured from pore water samples

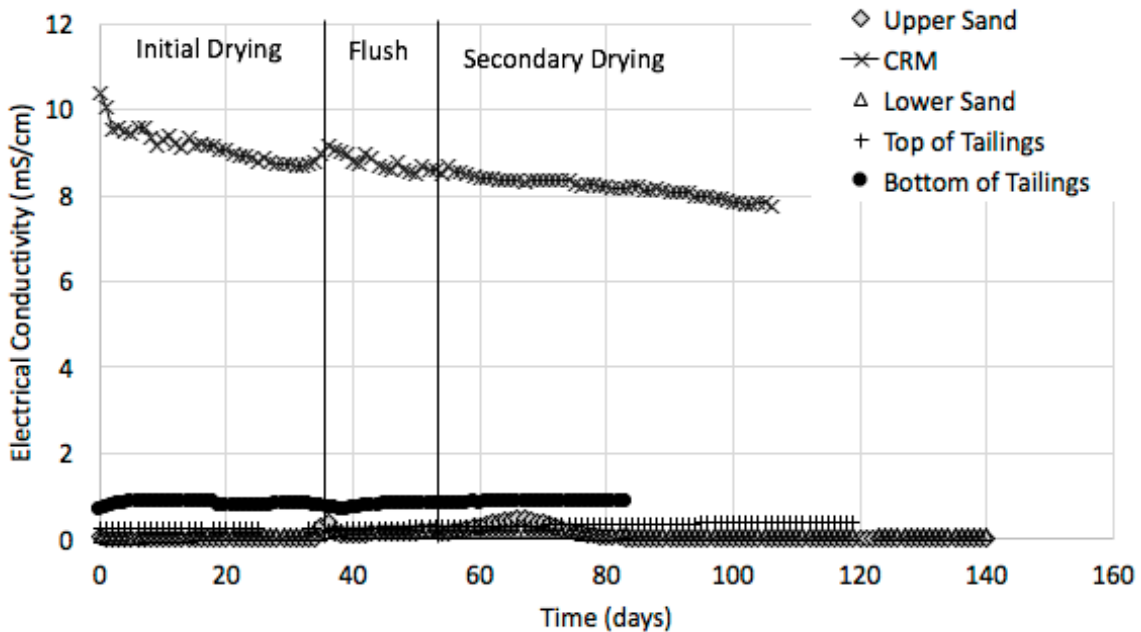


Figure 5-24. Electrical conductivity profile of Column C reported by 5TE sensors

Figure 5-23 shows a slight increase in electrical conductivity within the unoxidized tailings, indicating that dissolution of salts and metals is occurring within the tailings over the course of the

testing period. Contrary to the results of the unoxidized tailings columns, this indicates that the unoxidized tailings materials may be undergoing chemical oxidation, releasing metals, and generating ARD. The results of EC measurements can be used in tandem with the pH and ORP measurements displayed below to provide an improved understanding of the pore water quality changes within the columns.

The results of pH analysis from pore water samples in Column A are shown in Figure 5-25, the pH of the pre-oxidized tailings experiences a slight neutralization over the course of testing with a slight increase in pH of the biosolids and sand layers. The increase in pH of the sand layers is likely caused by migration of the alkaline biosolids pore water, and by the inaccuracy of normalization for small samples with high dilution factors. The pore water samples extracted from the desaturated sand layers were heavily diluted; the multiplication of $[H^+]$ or $[OH^-]$ by the dilution factor may significantly overestimate the change in pH caused by dilution. Additionally, for all samples with a measured pH near 7, there is no accounting for the auto-ionization of water at near neutral pH which results in further neutralization of pH at near-neutral values. These effects are largely irrelevant when solutions are strongly acidic or basic as $[H^+]$ and $[OH^-]$ are not significantly affected by multiplication of the linear dilution factor (remembering that the pH scale is logarithmic) and auto-ionization effects are minimal.

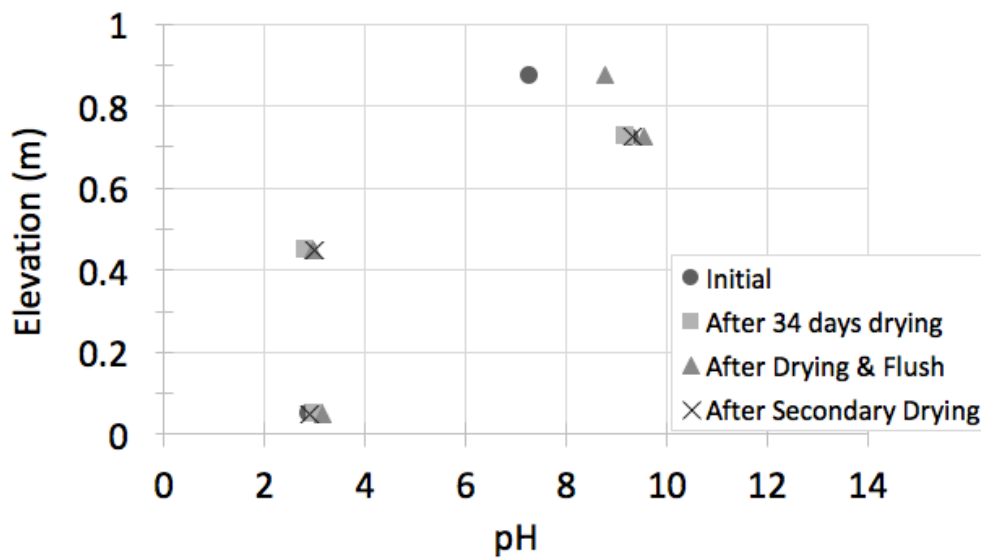


Figure 5-25. pH profile in Column A

There is effectively no change in the pH of the pre-oxidized tailings in Column A beneath the capillary barrier cover using municipal biosolids.

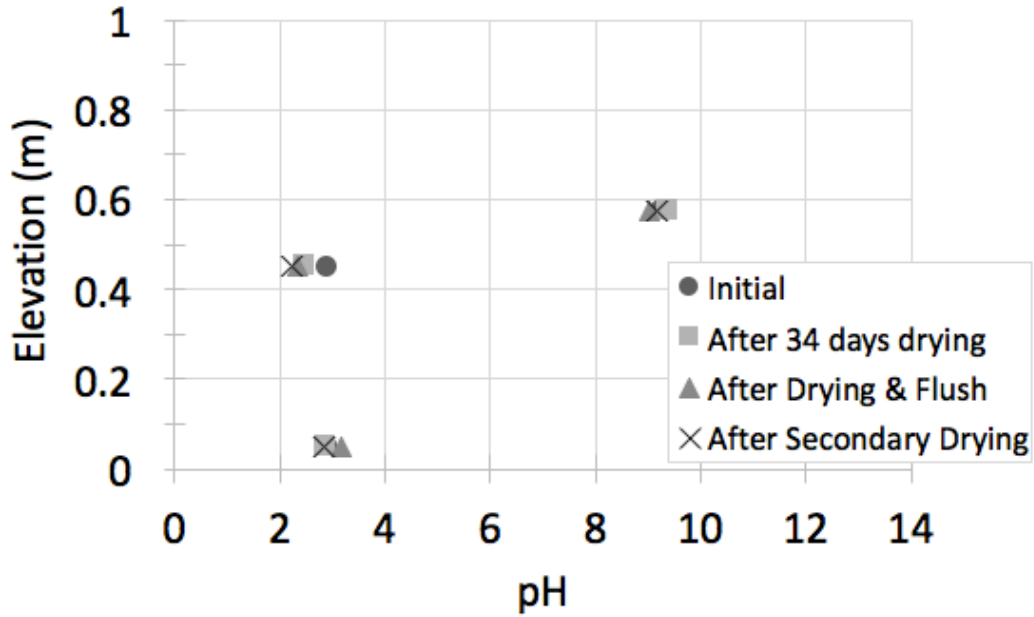


Figure 5-26. pH profile of Column B

Pore water samples from Column B show no apparent change in pH at the base of the tailings in Column B beneath the monolayer biosolids cover, however, the pH of the tailings near the interface beneath the biosolids shows a slight reduction in pH. The biosolids layer experiences no significant change in pH over the course of the testing period.

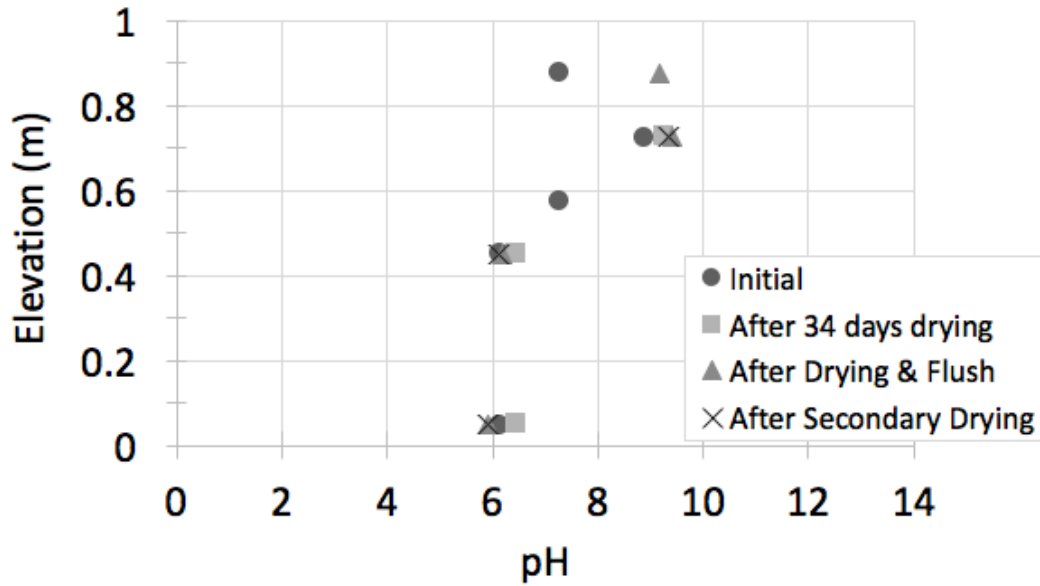


Figure 5-27. pH profile of Column C

The pH profile in Column C, shown in Figure 5-27 indicates that almost no change to the pH of the unoxidized tailings has occurred during the test period, indicating that little to no oxidation of the tailings within the column.

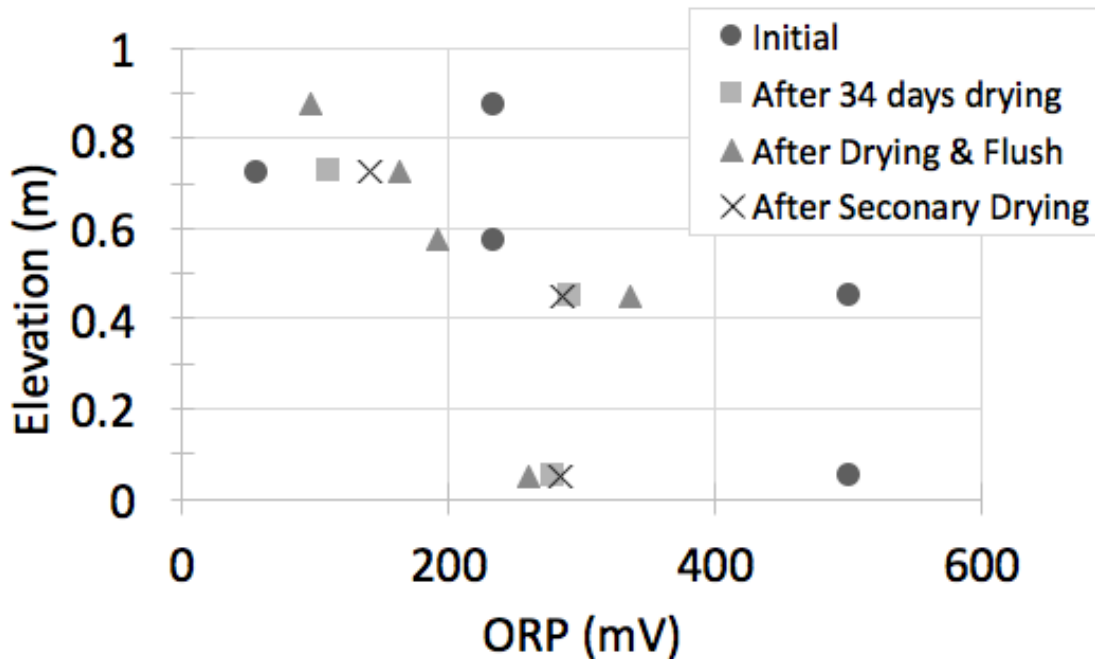


Figure 5-28. ORP profile of Column A

Figure 5-28 shows the diminishing ORP of the pre-oxidized tailings in Column A beneath the capillary barrier cover. The biosolids within the cover experience a slight increase in ORP.

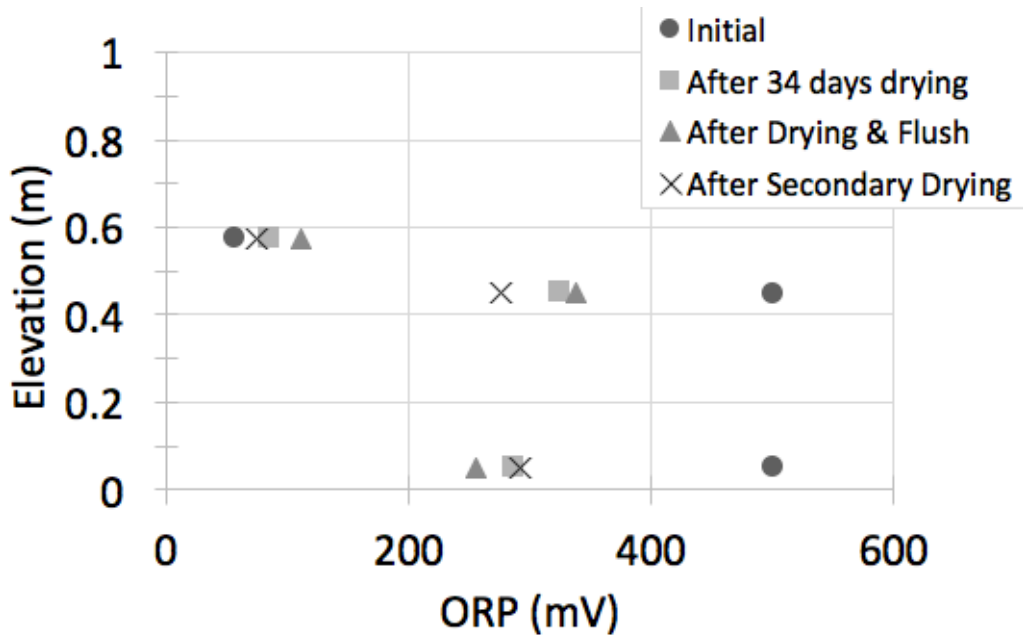


Figure 5-29. ORP profile of Column B

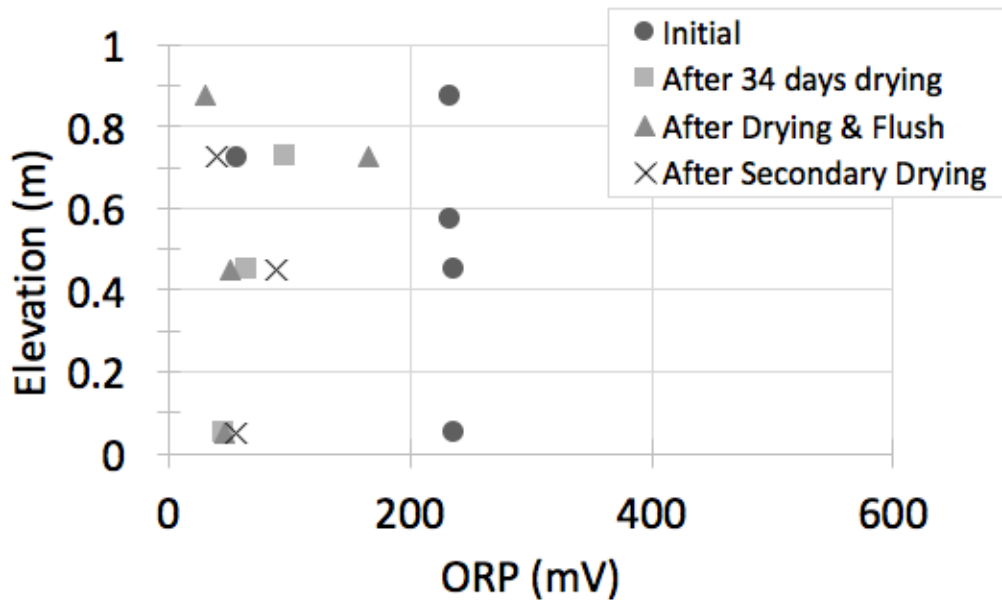


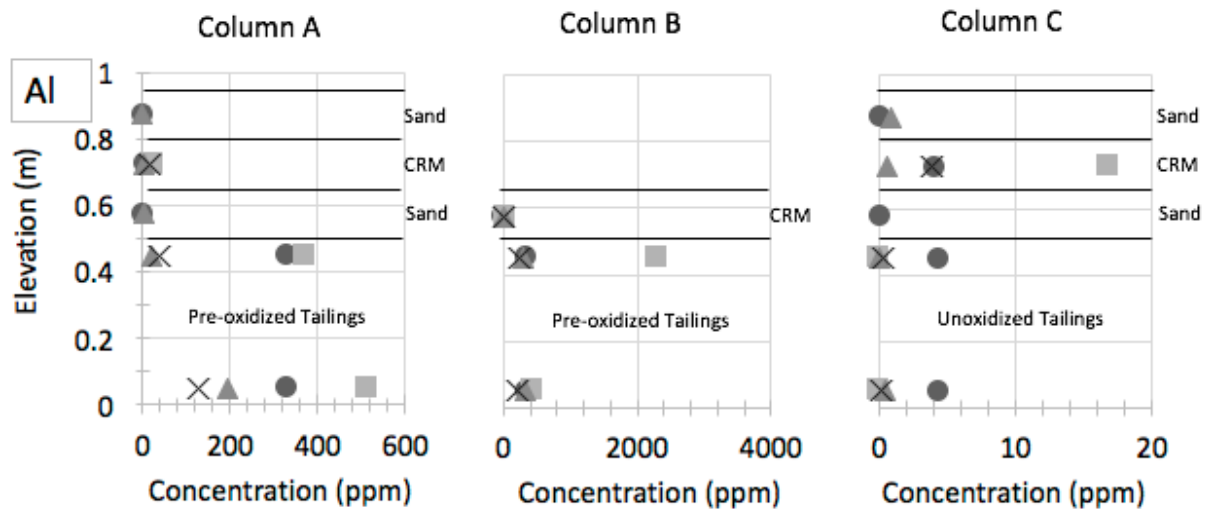
Figure 5-30. ORP profile of Column C

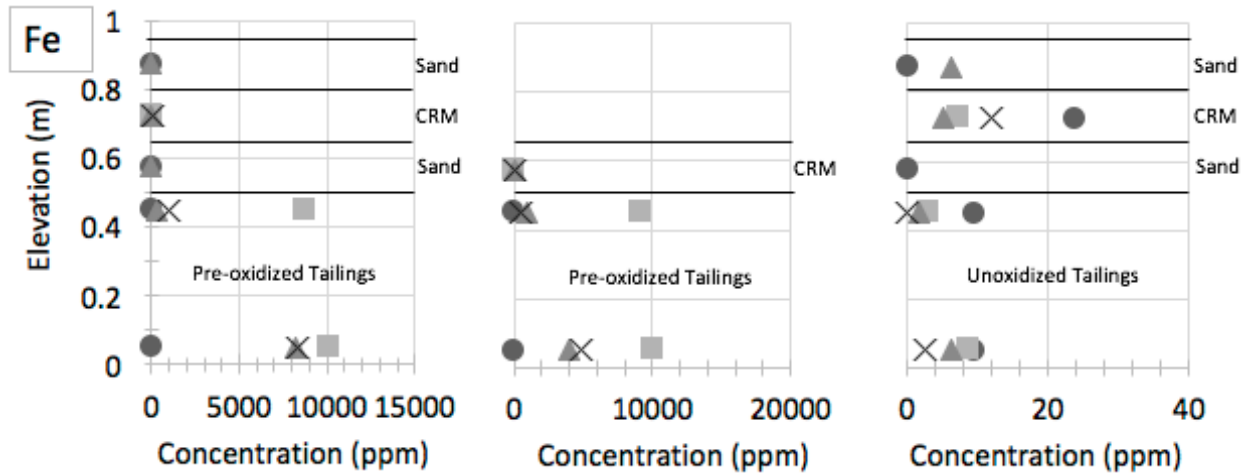
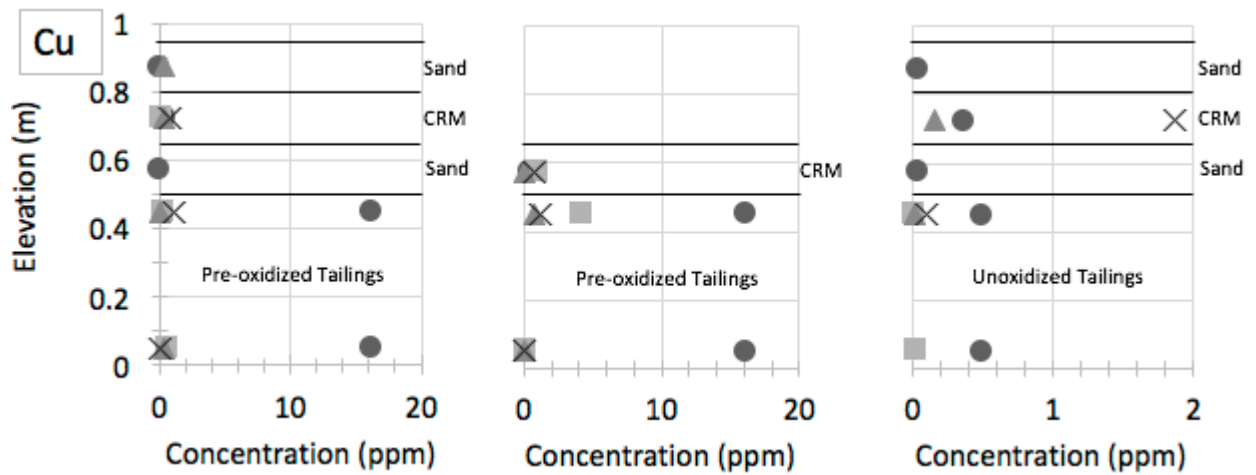
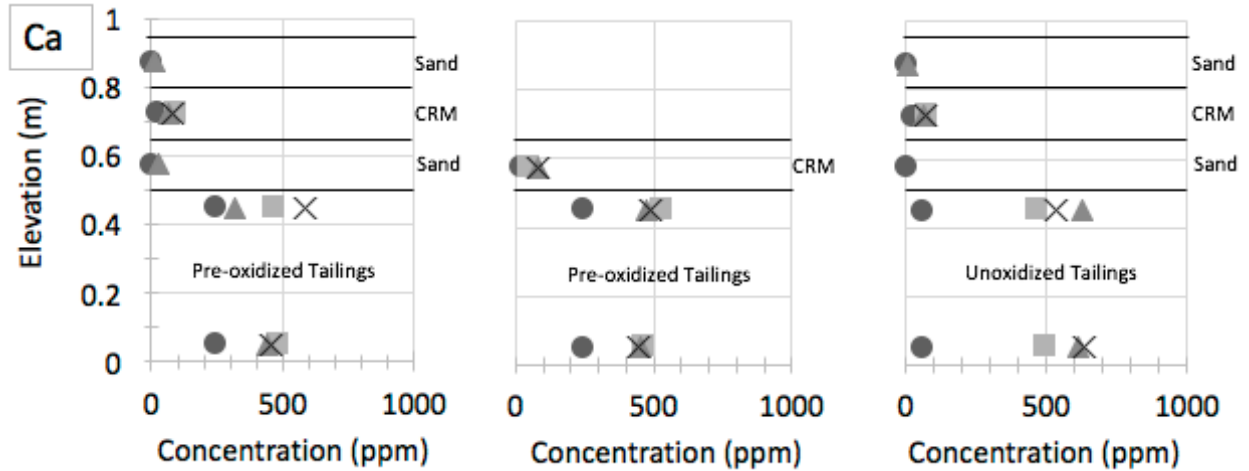
In all of the columns, the ORP of the biosolids layer increases during the initial drying, and throughout the flush period, and decreases during secondary drying. The change in ORP of the biosolids material is attributed to the ongoing degradation of the biosolids material. The change in

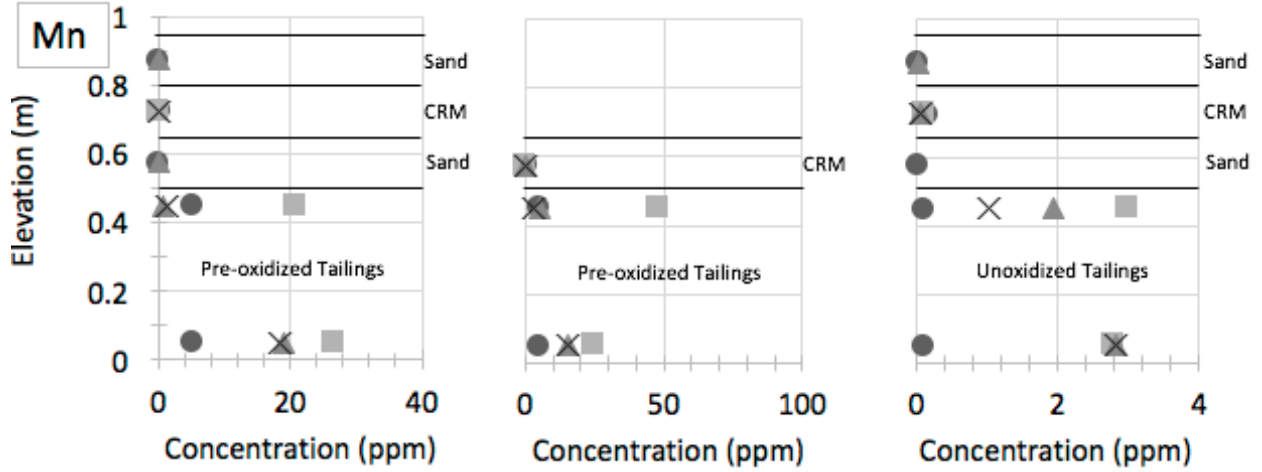
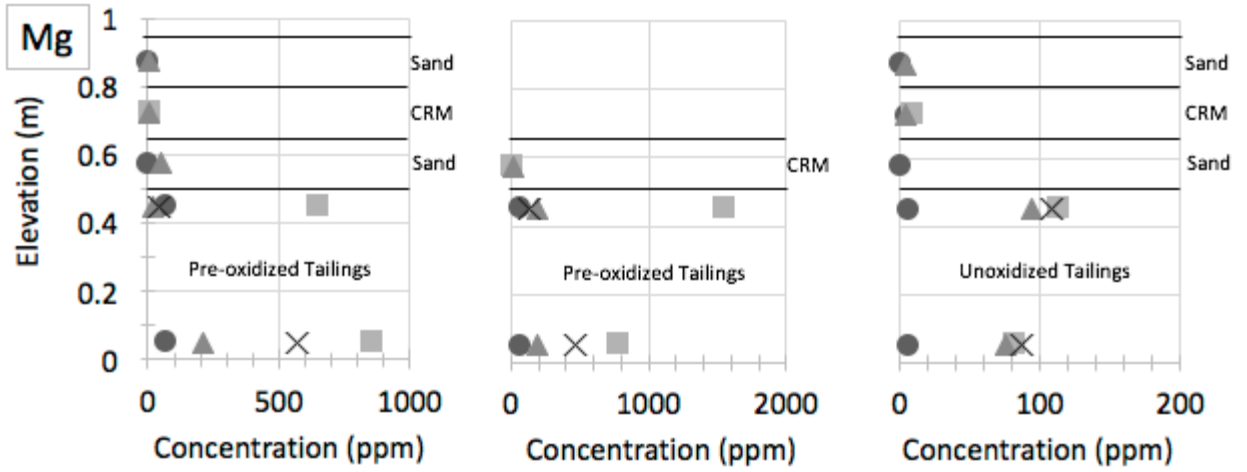
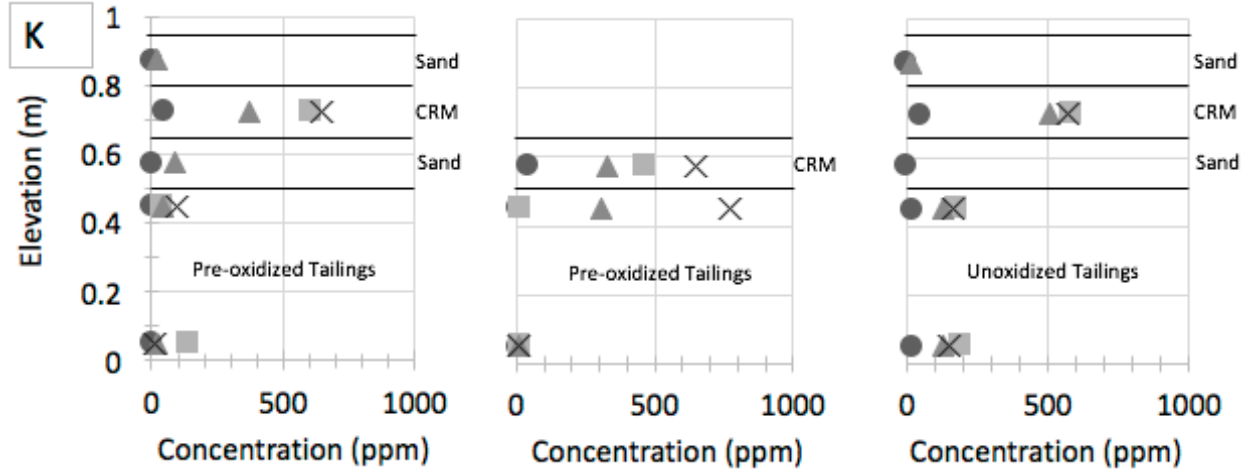
ORP and pH of the tailings materials does not indicate a significant change in iron speciation when observing the Pourbaix diagram shown in Section 2.3.1. From the Pourbaix diagram, iron in solution will be found predominantly as Fe^{2+} . Further speciation analysis was attempted using Visual MINTEQ, however, it was found that analysis lacked the ability to accurately estimate low pH values of pre-oxidized tailings; predicted values were consistently high, and iron speciation did not occur as a result unless forced to by user input of fixed species ratios. The discrepancy between estimated and measured pH values may be due to the program not incorporating the effects of bacterial interaction, and also having limited input from the analytes assessed via ICP analysis. When setting the pH and Eh values, speciation was not reported to have occurred between ferric and ferrous iron, only species of ferrous iron are formed. As such, speciation estimation results from Visual MINTEQ were not included in this report.

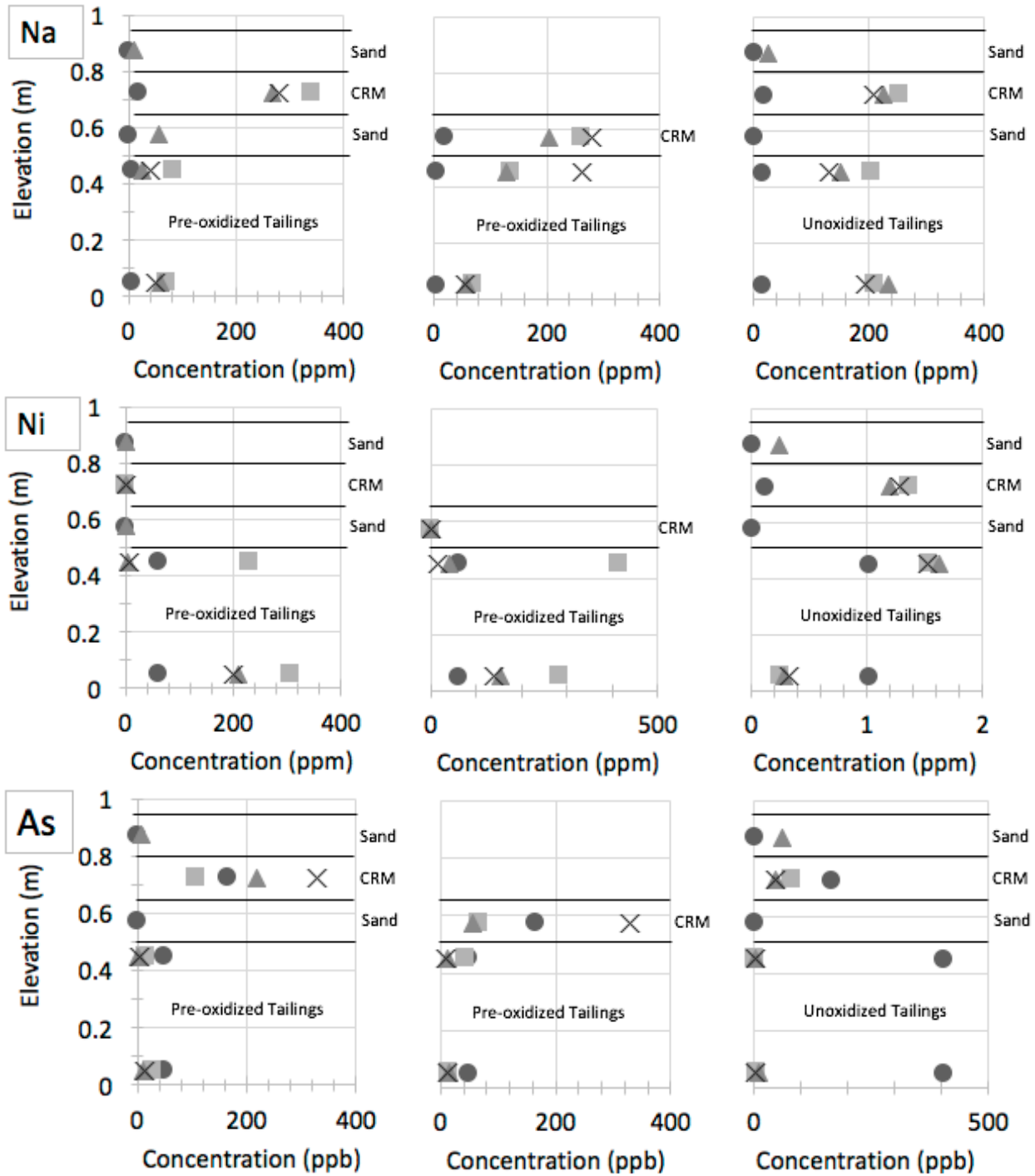
5.2.4.1 Pore water metals and nutrient analysis

Pore water samples were analyzed using Inductive Coupled Plasma Mass Spectrometry (ICP-MS) and Inductive Coupled Plasma Atomic Emission Spectrometry (ICP-AES). Metal concentrations were analyzed using ICP-MS with samples in a 1% HNO_3 solution, while nutrients and anions were analyzed using ICP-AES.









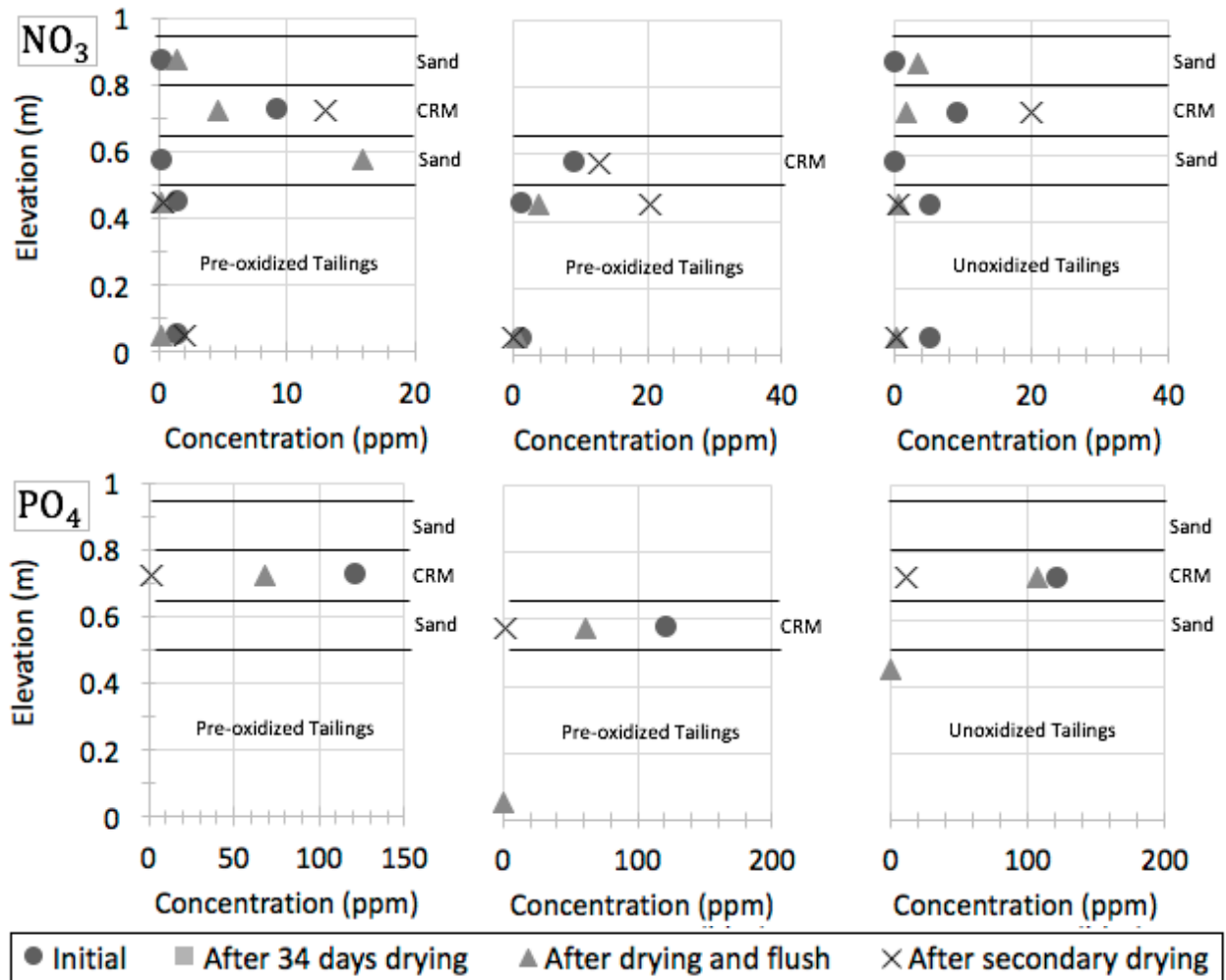


Figure 5-31. Concentration profiles for cations and anions throughout test duration

Tables of all cation and anion data from ICP testing can be found in Appendix B.

5.2.5 Additional Results and Observations from Column Testing

Throughout the duration of the column tests it was observed that the suction measurements reported for all biosolids cover layers did not experience any significant change as shown in Figure 5-32, 5-33, and 5-34. A brief increase in suction was shown in the biosolids of Column B prior to column deconstruction as shown in Figure 5-33. Additionally, suction measurements from layers underlying the biosolids layers did not change significantly. For the biosolids layers, the low levels of suction shown by the Teros 21 sensor was attributed to the continued saturation of the biosolids layer which did not allow the sensor ceramic to desaturate and measure suction change. The lack

of significant change in the lower sand layers of Column A and Column C may be indicative of the suction remaining lower than the AEV of the Teros 21 sensor, although this would thereby imply that the volumetric water content of these layers be quite high. The static suction levels observed in the tailings layers are attributed to high salinity pore water affecting the ability of the sensors to measure desaturation across the ceramic disks.

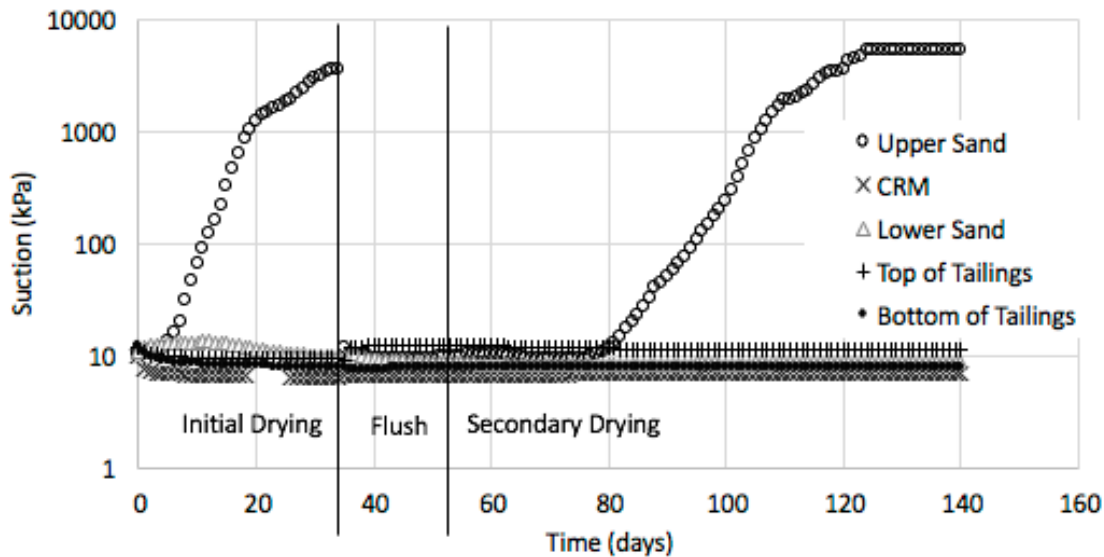


Figure 5-32. Suction profile in Column A measured by Teros 21 sensors throughout test duration

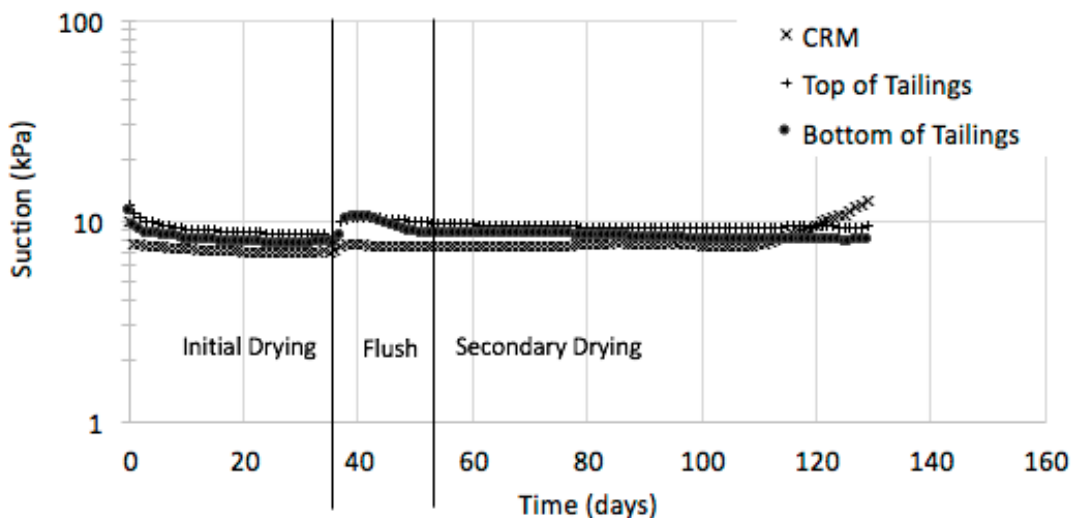


Figure 5-33. Suction profile in Column B measured by Teros 21 sensors throughout test duration

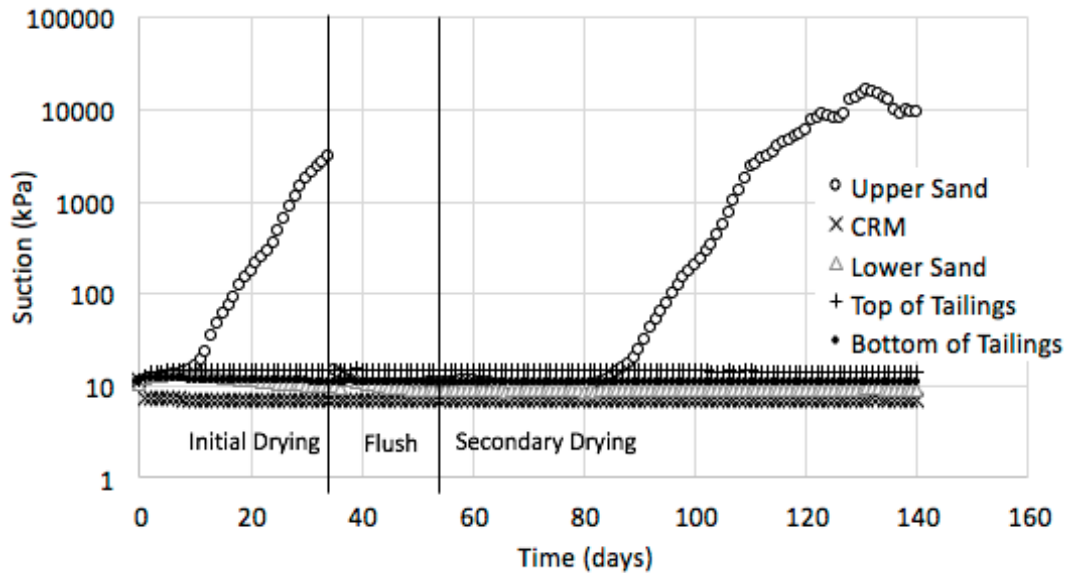


Figure 5-34. Suction profile in Column C measured by Teros 21 sensors throughout test duration

Minor volumetric deformation occurred in all columns throughout the course of testing. All observed volume change occurred during the flushing period. Measurements taken of the layer thicknesses throughout testing were used to calculate the change in layer thickness which is directly proportional to the volume.

Table 5-5. Layer thickness change observed during flush period

| Column | Layer | Layer thickness | | |
|--------|-----------|-----------------|------------|------------|
| | | Initial (cm) | Final (cm) | Change (%) |
| A | Sand | 15 | 12.6 | -16.0 |
| | Biosolids | 15 | 15.5 | 3.3 |
| | Sand | 15 | 14.7 | -2.0 |
| | Tailings | 50 | 49.8 | -0.4 |
| B | Biosolids | 15 | 15 | 0.0 |
| | Tailings | 50 | 48 | -4.0 |
| C | Sand | 15 | 14.6 | -2.7 |
| | Biosolids | 15 | 15.6 | 4.0 |
| | Sand | 15 | 14.3 | -4.7 |
| | Tailings | 50 | 50 | 0.0 |

Consolidation of the columns during flushing indicate that a continuous applied load from the ponded water resulted in further compaction of the cover layers. Additional volume change within

the biosolids layers during drying periods was estimated based on visual estimation of volumetric deformation caused by shrinkage and cracking.

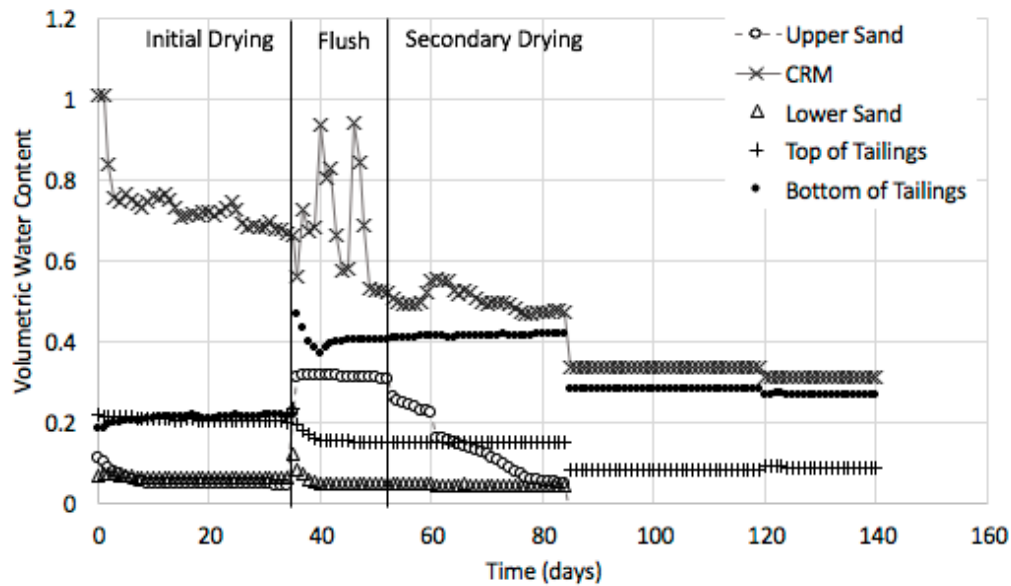


Figure 5-35. Volumetric Water Content profile of Column A throughout column test duration reported by 5TE sensors without calibration adjustment

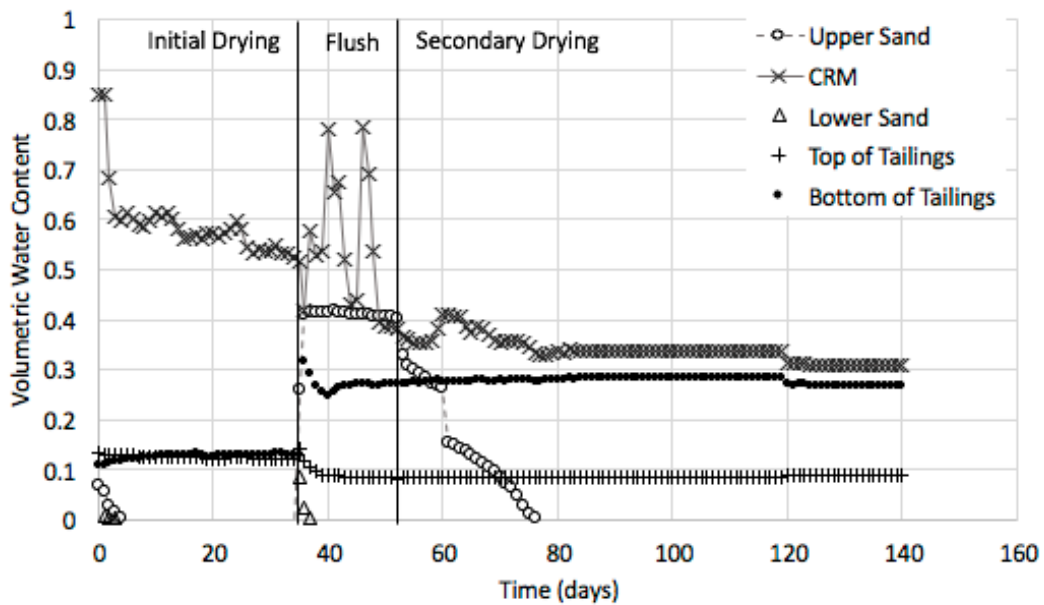


Figure 5-36. Volumetric Water Content profile of Column A throughout column test duration reported by 5TE sensors adjusted using determined calibration curves

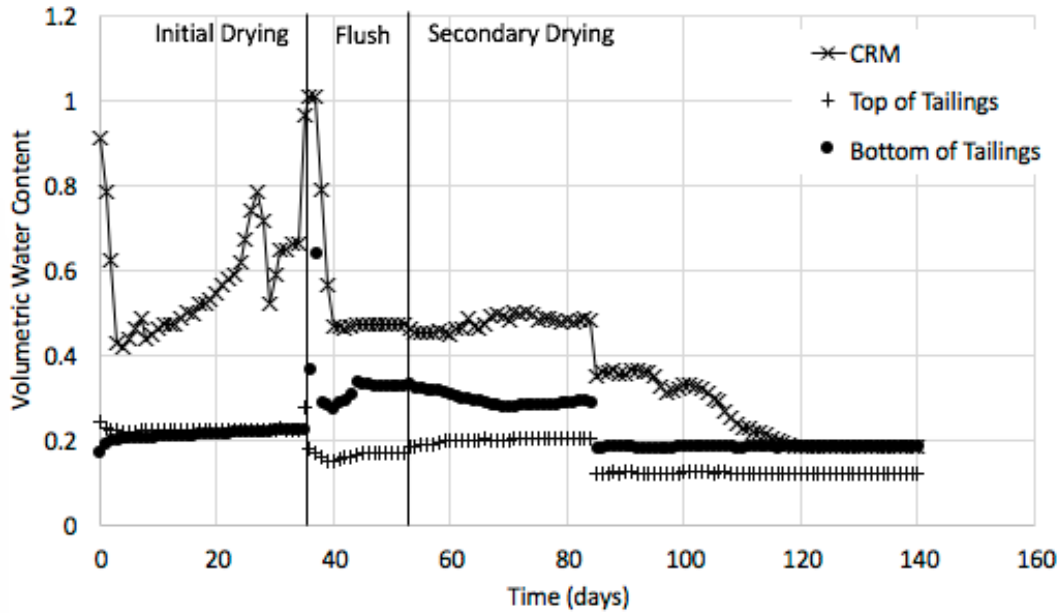


Figure 5-37. Volumetric Water Content profile of Column B throughout column test duration reported by 5TE sensors without calibration adjustment

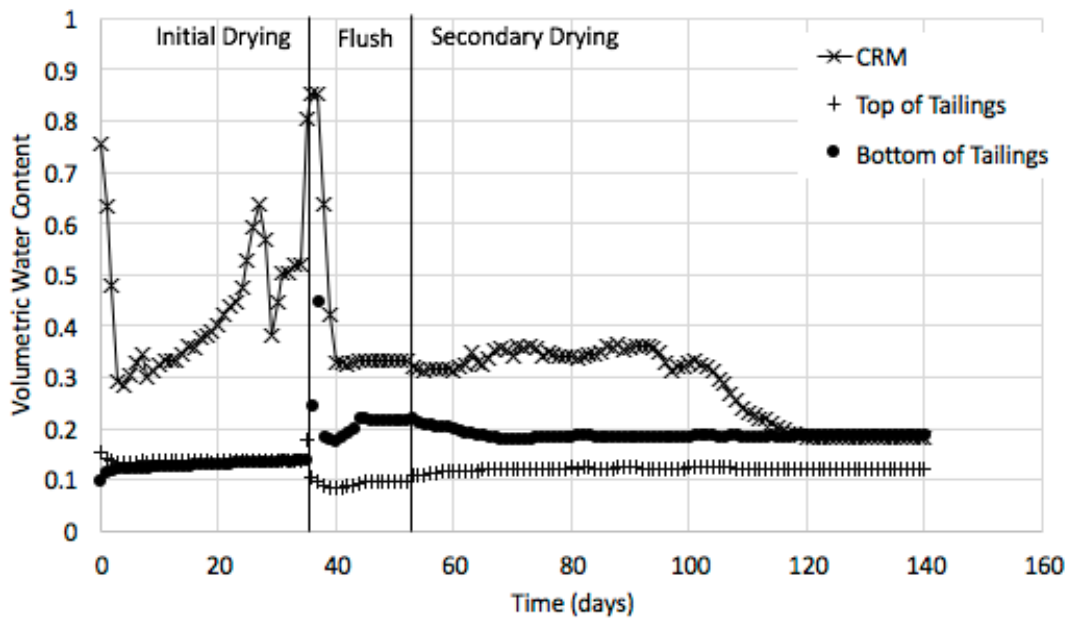


Figure 5-38. Volumetric Water Content profile of Column B throughout column test duration reported by 5TE sensors adjusted using determined calibration curves

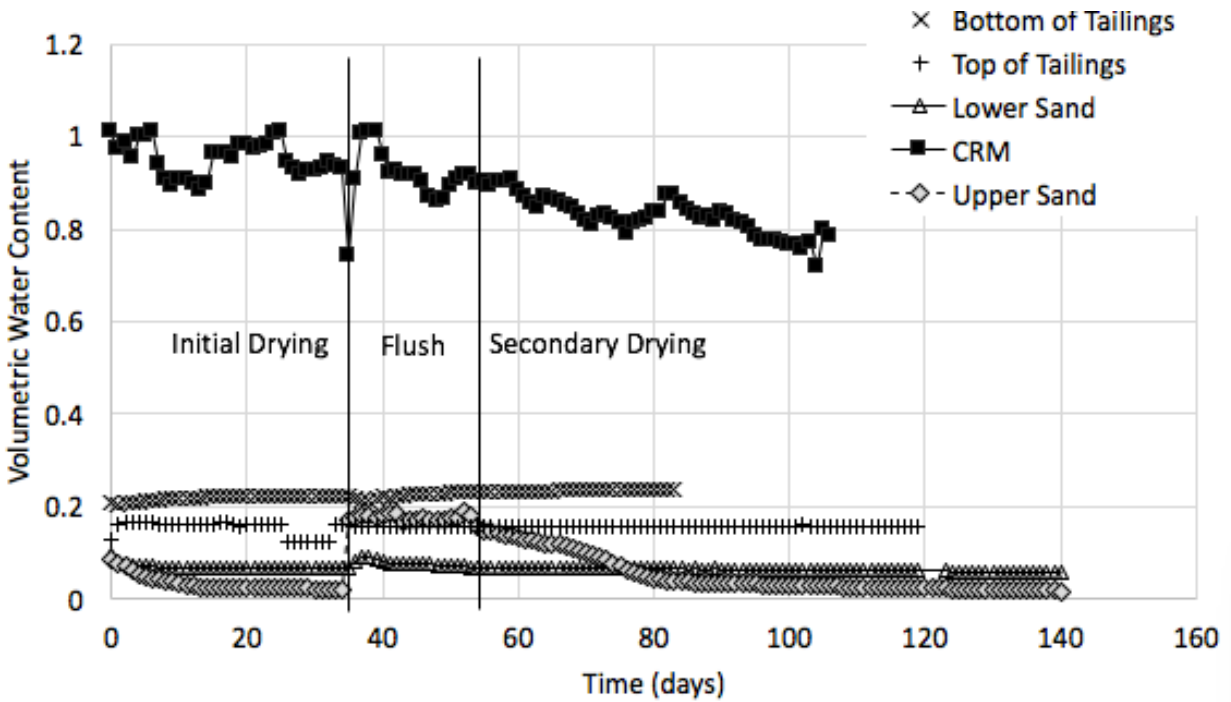


Figure 5-39. Volumetric Water Content profile of Column C throughout column test duration reported by 5TE sensors without calibration adjustment

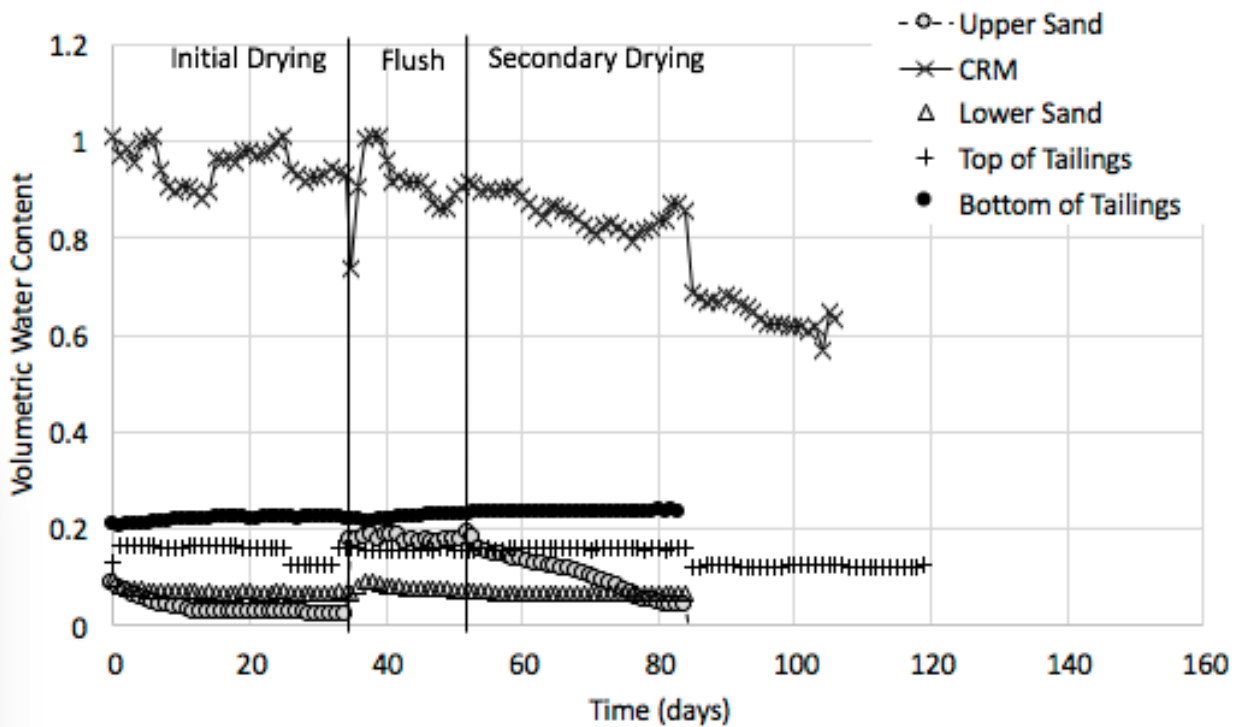


Figure 5-40. Volumetric Water Content profile of Column C throughout column test duration reported by 5TE sensors adjusted using determined calibration curves

Improved accuracy of volumetric water content measurement in the biosolids materials is strongly recommended for future work in order to observe the saturation characteristics of biosolids layers within the columns and to assess whether the biosolids can maintain full saturation within covers. The final water contents of the un-calibrated data appear to be a closer match to the deconstructed column water contents shown in Section 5.2.5.1, however, both the corrected, and uncorrected VWC readings show significant deviation from the final profile indicating sensor measurement error.

Figure 5-41 shows the reported VWC and suction measurements from the 5TE and Teros 21 sensors for the sand materials in the laboratory columns. A reasonable fit can be observed with the characterized SWCC for the sand material, however, it can be noted that the suction sensor does not accurately follow the SWCC of the sand material at suctions below the AEV of the Teros 21 sensor.

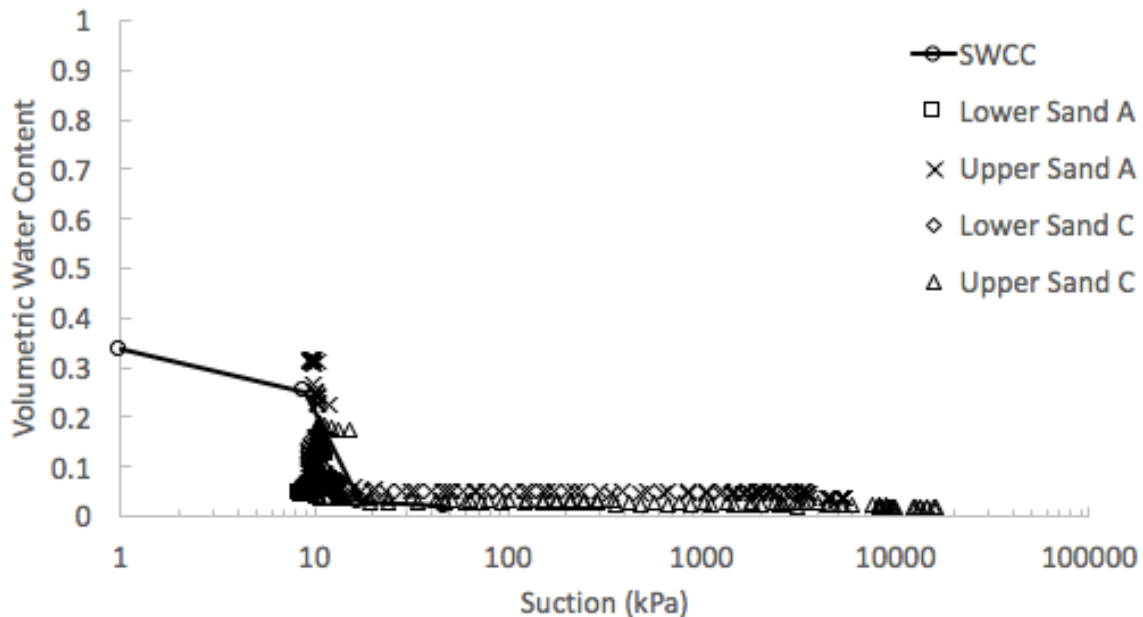


Figure 5-41. Paired VWC and Suction readings in the sand layers of laboratory columns overlying the characterized sand SWCC

Figure 5-42 shows a similar plot for the unoxidized tailings in Column C. The plot for pre-oxidized tailings is shown in Figure 5-43 and the plot for CRM biosolids is shown in Figure 5-44.

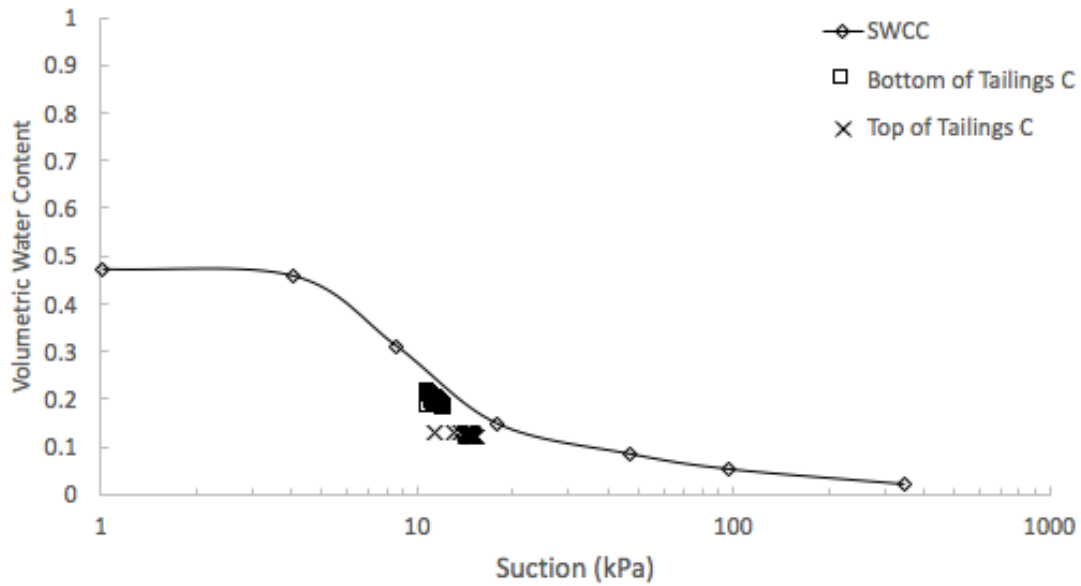


Figure 5-42. Paired VWC and Suction readings in the unoxidized tailings of laboratory column C overlying the characterized unoxidized tailings SWCC

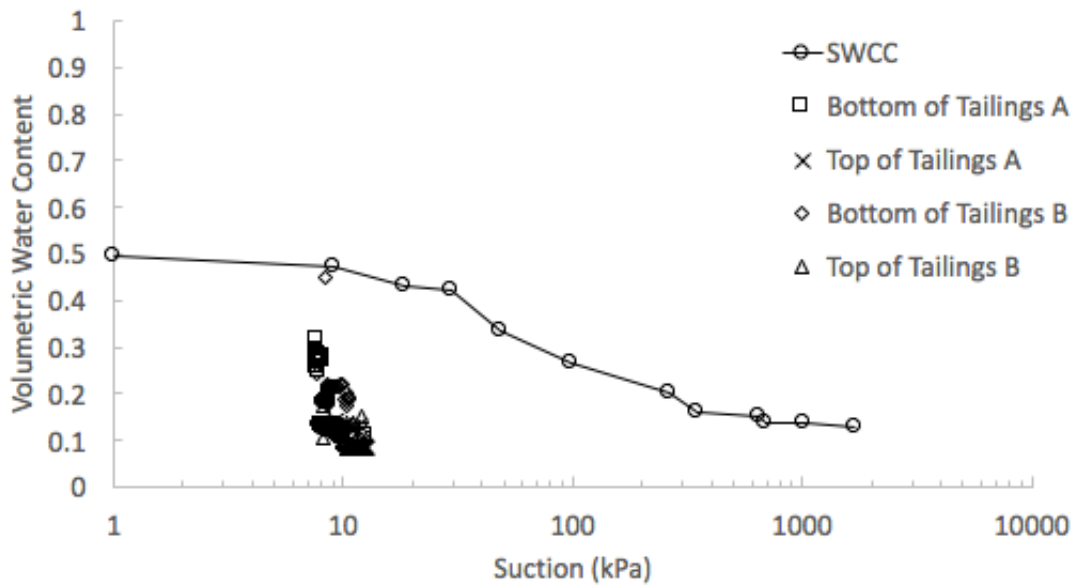


Figure 5-43. Paired VWC and Suction readings in the pre-oxidized tailings of laboratory columns A & B overlying the characterized pre-oxidized tailings SWCC

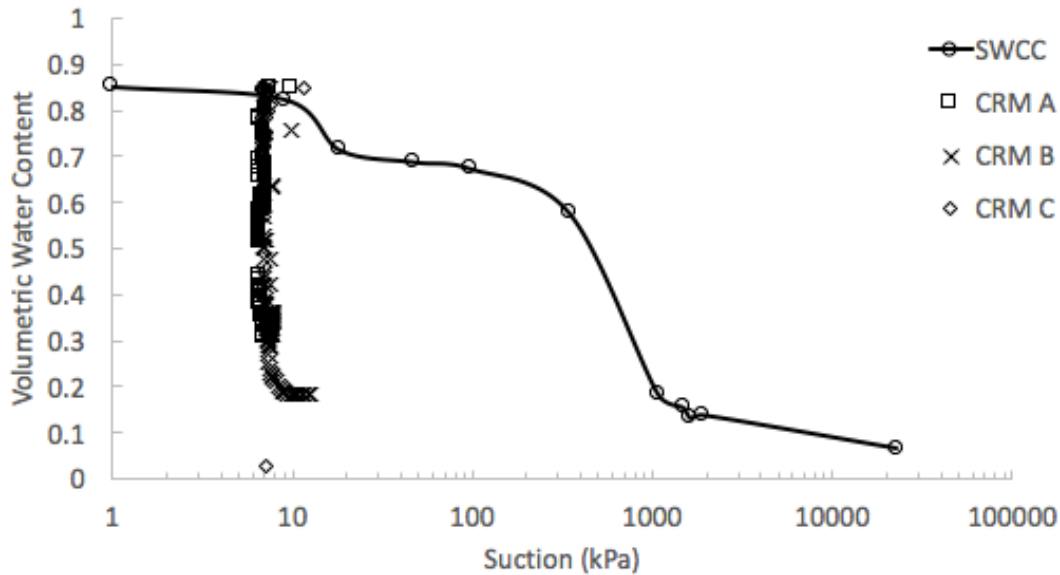


Figure 5-44. Paired VWC and Suction readings in the CRM biosolids of laboratory columns A, B, and C overlying the characterized CRM biosolids SWCC

From Figure 5-42 and 5-43 it can be seen that there is little change in the water content or suction profiles within the tailings throughout testing. In Figure 5-44 it can be seen that the volumetric water content readings do not correspond to the path predicted by the characterized SWCC; this further supports the notion the 5TE sensors are affected by salinity changes within the biosolids and decoupling from the biosolids throughout testing.

Preferential flow along the column walls, particularly in the corners of the columns, was considered as a possible explanation for limited changes in volumetric water content of tailings layers. It was determined that preferential flow was not significant as the drainage reservoirs below the columns experienced little volume change. Additionally, due to the very fine particle size of the biosolids (pore water withdrawn from biosolids layers through samplers with a pore size of 0.15 μm were black in colour) it was observed that the migration of very fine biosolids particles down the corner of the columns was minimal. Figure 5-45 shows the advection of biosolids particles in the pore water within the monolayer cover in Column B following the flushing period. No movement of biosolids particles was observed in the capillary barrier covers in Column A or Column C.



Figure 5-45. Advection of biosolids particles within the pore spaces of the pre-oxidized tailings in monolayer cover of Column B indicating slight preferential flow along the column wall.

5.2.5.1 Column Deconstruction

Column deconstruction was undertaken to determine the real volumetric water content of each column layer. Sample rings were used to extract a known volume of soil at specific depths within the layers, and the water content determined through oven drying. The volumetric water content profiles obtained during deconstruction are shown in Figures 5-46 to 5-48. Total suction measurements were also taken, along with additional gravimetric water content samples; data from these tests can be found in Appendix B.

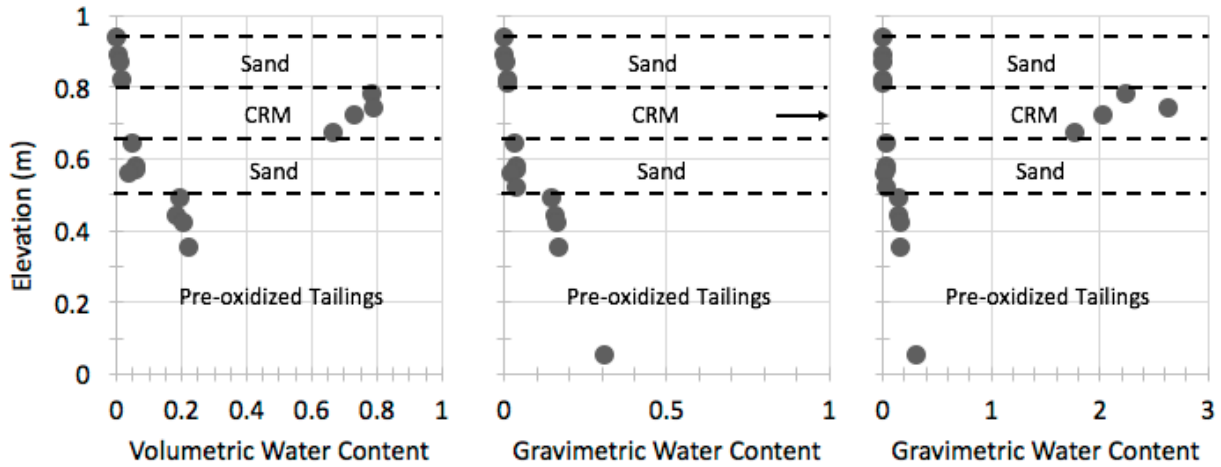


Figure 5-46. Water content profiles of Column A from soil sampling during deconstruction

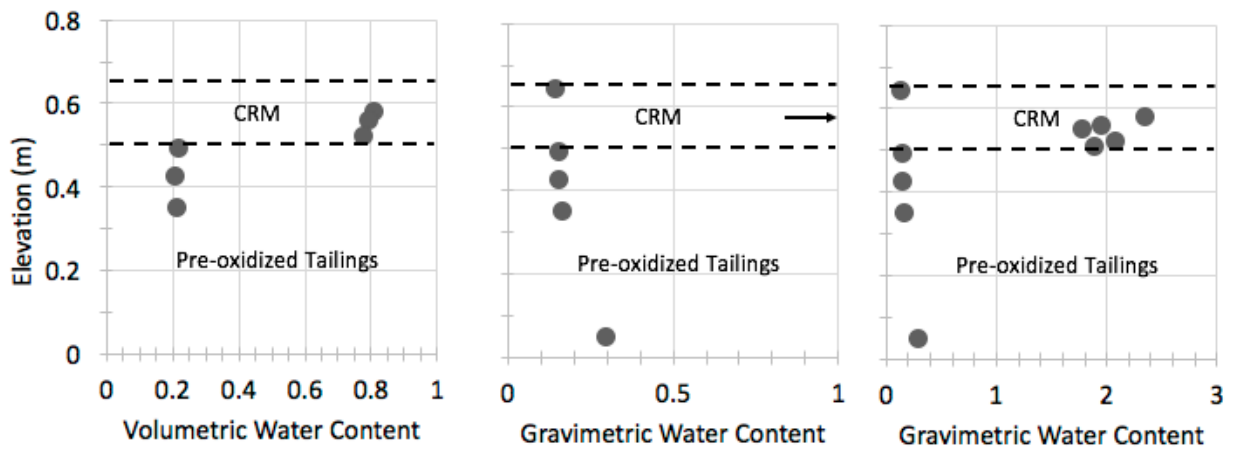


Figure 5-47. Water content profiles of Column B from soil sampling during deconstruction

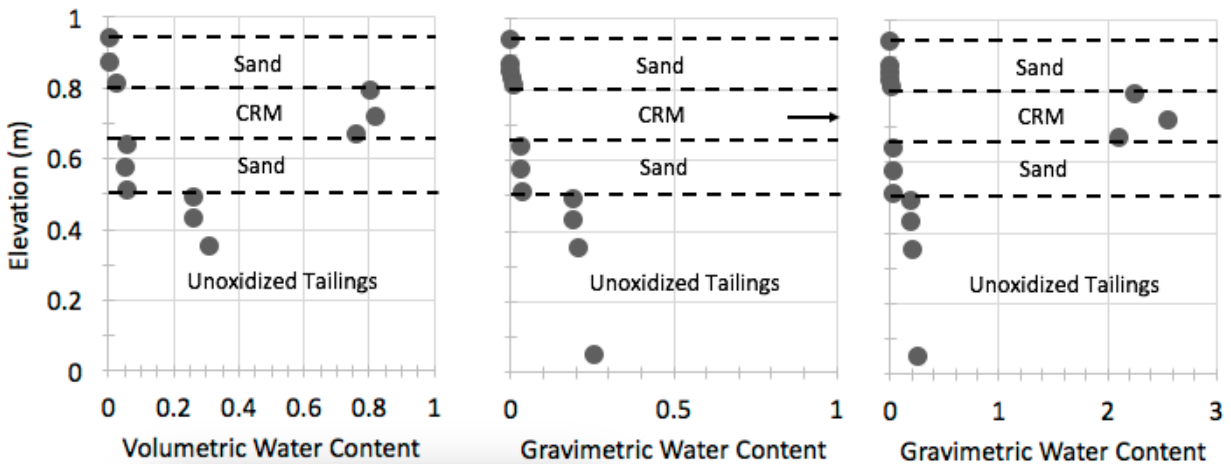


Figure 5-48. Water content profiles of Column C from soil sampling during deconstruction

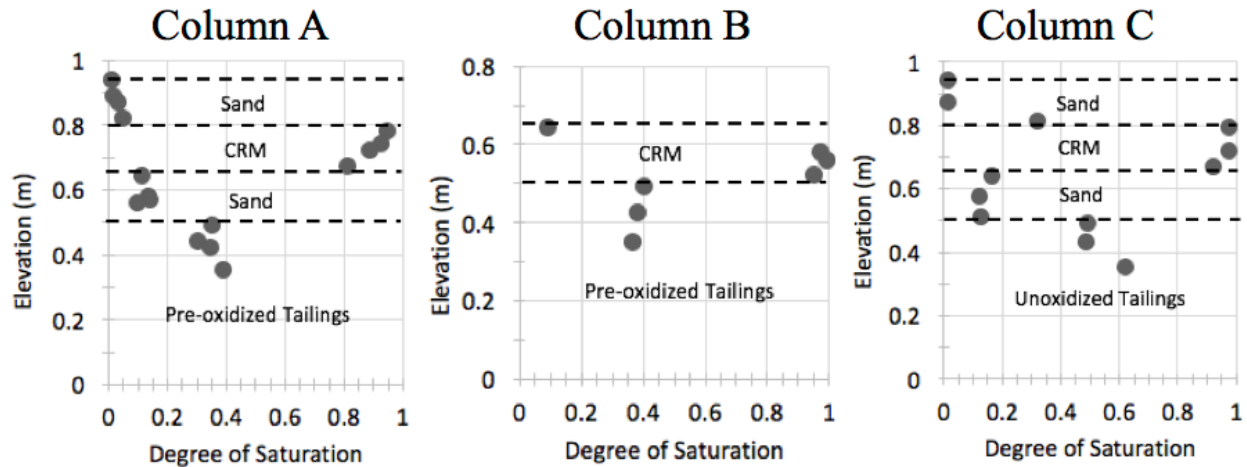


Figure 5-49. Degree of Saturation profiles from soil sampling during column deconstruction

5.3 Column Testing Discussion

It is evident that there is significant discrepancy between the data obtained from the multitude of tests conducted throughout the duration of column testing. This section seeks to provide clarity regarding which observations have the greatest impact on the assessment of cover performance assessment.

5.3.1 Volumetric Water Content

The most important finding from the volumetric water content testing was the high degree of saturation, and high volumetric water content within the biosolids layers during column deconstruction. While the 5TE sensors reported the establishment of the capillary barrier using sand and biosolids, the oven dried samples from column deconstruction give clear indication that the biosolids retain water over the course of the 86 day secondary drying period. As seen in Figure 5-50 the surface of the biosolids layer could not be sampled to determine the volumetric water content as the upper 5 cm underwent significant desiccation and drying which rendered the top layer impenetrable to sampling equipment. It can be seen in the photo that a layer of precipitates has formed at a depth of approximately 2 cm below surface. Below the crust, the biosolids were found to have a water content similar to the water content at initial column construction, and similar to the biosolids in the capillary barrier columns. This indicates that the drying front within the biosolids progresses slowly and that drying does not occur uniformly throughout the biosolids layer. Additionally, this indicates that the oxygen infiltration barrier does not become fully

compromised even after the extreme drying conditions (no precipitation for 35 days, and a subsequent 90 days) which the columns have been subjected to.

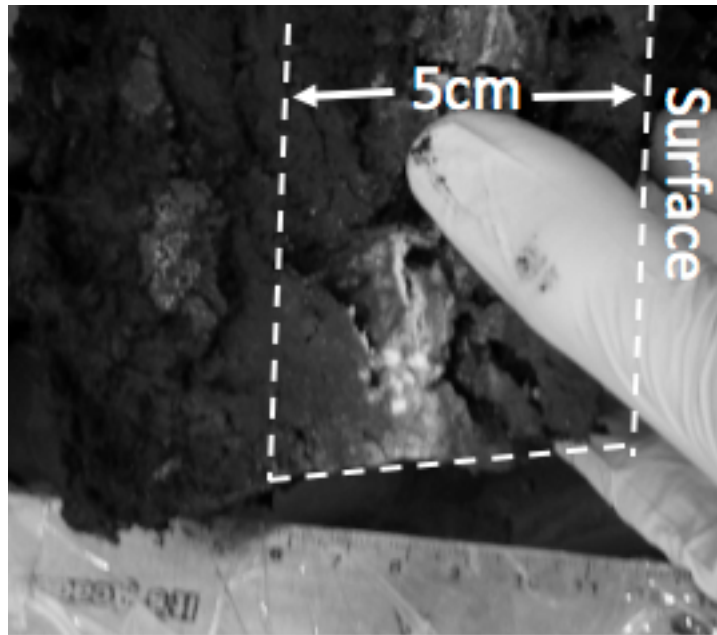


Figure 5-50. Surface crust formation in the CRM biosolids of the monolayer Column B

The volumetric water content reported by the sensors at the time of column deconstruction, and the measured water content of samples extracted from the columns are extremely different. The samples extracted and oven dried indicate that the biosolids layers maintain nearly complete saturation after an additional 90 days of drying after the column flushing. This is contradicted by the sensor output, and it is therefore up for discussion as to whether the 5TE volumetric water content readings are valid for the duration of the test period, for a portion of the observation period, or not valid whatsoever. Additionally, the calculated VWCs at time of deposition varies slightly from those reported by the 5TE sensors.

From the VWC profiles it is apparent the 5TE sensors do provide some indication of flux through the covers, and in the initial establishment of the capillary barrier in Column A and C. In all cases, the sensors at the top of the tailings experience no significant change in water content, however, the lower sand layers in both CBC columns, and the bottoms of the tailings in all columns show elevated VWC readings.

In Column A, the increase in VWC reported from the sensors in the lower sand and the top of the tailings occurs within minutes of adding water to the top of the column, and likely indicates consolidation of the sand and tailings under increased load. The same observation can be made in the top tailings layer of Column B, and the sand layer of Column C, although the change in the sand layer of Column C is slightly delayed. All of these layers experienced volumetric deformation during flushing in the form of consolidation as shown in Table 5-5.

In all columns, the increased VWC readings at the base of the column indicate the possibility of preferential flow along the column walls, with water bypassing the sensors in other column layers, and collecting at the base of the columns.

5.3.2 Suction Profiles

In Figure 5-32 and Figure 5-34 the Teros 21 sensors in the uppermost layers of each column demonstrate the expected response to drying conditions within the soil layers, however, when assessed in tandem with the VWC readings and deconstructed column profiles, the suction profile within the lower sand and tailings layers do not behave as may be expected from the SWCCs. According to the VWC profiles, the suctions corresponding to the measured and reported VWC in the lower layers of the columns should be elevated relative to those reported by the Teros 21 sensors. The sand layers may experience desaturation at suctions below the AEV of the porous ceramic sensor as described in Section 5.2.

5.3.3 Pore Water Quality Profiles

Several tests were conducted to assess changes within the pore water profiles of the columns. The discussion below outlines the observations from the profiles shown in Section 5.2.

5.3.3.1 pH Profiles

The pH profiles indicate that there is little change in pH conditions within the columns. The pre-oxidized tailings do not experience significant neutralization over the test period, nor do the unoxidized tailings show significant signs of acid generation. The time frame for study is likely too short to provide any strong indication of the neutralization and acid reduction potential from pH values alone.

The increase in pH values from the sand layers in Column A and Column C indicate hydraulic interaction between the sand and the biosolids. It should be noted that very small samples were extracted from the sand layers which required significant dilution prior to testing, and correction for dilution (by multiplication of the H^+ or OH^- concentration) may exaggerate the pH conditions in these sand samples.

5.3.3.2 Electrical Conductivity Profiles

It is evident that the electrical conductivity measured by the 5TE sensors, and that measured from saturation extraction and pore water sampling are different in magnitude. The 5TE sensors EC measurement spikes following flushing in the lower tailings profile of Columns A and B, providing further indication of preferential flow and transport of dissolved ions along the walls of the column to the base of the tailings. The spike, and subsequent continued high levels of electrical conductivity measured by the 5TE sensors at the base of Columns A and B, which is not replicated in the pore water samples, is likely caused by the increased level of saturation of the sensors; the sensors report low levels of EC at low water contents and spike following increases in water content indicating that further calibration of the sensors would be required for accurate EC measurement. Without calibration, it is still possible to use the EC reading as an indication of increasing soil salinity which may affect the VWC sensor reading, as explained in Section 5.2.1.

The electrical conductivity profiles from pore water sampling show a reduction in electrical conductivity of the pre-oxidized tailings throughout the profiles of Column A and Column B. In contrast, the electrical conductivity of the unoxidized tailings is shown to increase over the course of the test, indicating the dissolution of ions from the unoxidized tailings into the pore water. The conductivity of the biosolids in the CBC columns remain very stable, while the conductivity of the biosolids in the monolayer column is shown to decrease gradually over the course of the test period. The reduction of electrical conductivity in the pore water extracted from the biosolids layer of Column B may be caused by the transport of ions towards the biosolids surface as shown in Figure 5-50 where salt precipitation occurred at a horizon above the Rhizon Flex sampling port location.

5.3.3.3 ORP Profiles

The oxidation-reduction potential profiles show the high ORP of the pre-oxidized tailings, indicating that the pre-oxidized tailings are a reducing agent, and are prone to oxidation. The ORP of the pre-oxidized tailings appears to stay relatively constant at around 300 mV indicating that there exists further potential for oxidation of the tailings and for continued acid generation.

The unoxidized tailings in Column C show a slight increase in ORP over the course of testing, particularly in the upper horizon. This indicates that there may be small amounts of oxidation taking place at the tailings surface even underneath the CBC.

The biosolids are shown to be weak reducing agents, with increasing ORP over the course of testing. ORP is often related to pH in simple half-cell reactions, where positive ORP values indicate an acidic reducing agent according to the Nernst equation, and negative ORP values indicate basic oxidizing agents. In this application, the pore water chemistry is more chemically complex, and the dissolved ions from several different types of metals may act as strong reducing agents even in a basic pH environment. The high concentrations of reducing agents such as Na, K, Ca, Mg, Al, and Fe appear to cause the biosolids to be a reducing agent.

5.3.3.4 Metal Cation Concentration Profiles

The profiles shown in Figure 5-31 show high levels of metals within both the tailings and biosolids layers. Both pre-oxidized and unoxidized tailings report high levels of calcium ions with increasing concentrations at the tailings surface throughout testing.

Of considerable interest is the profile for iron, which shows significant concentrations of iron in the pre-oxidized tailings, but with very low concentrations in the pore water of the unoxidized tailings. Previous studies analyzing acid digestion of the tailings from Q and P areas show that the pre-oxidized tailings are typically ~20-25% iron by weight (Beauchemin, Clemente, et al., 2014), however, the very low concentrations from the initial saturation extraction indicate that the iron present in the tailings does not become liberated during saturation extraction. This indicates relatively low solubility in water which may point to the presence of iron oxide and iron hydroxide

compounds which are water insoluble, and therefore would not be extracted through short duration saturation in water.

Potassium concentrations within the biosolids layers increase throughout testing in all columns, indicating release of potassium to the pore water from the biosolids. Additionally, the concentration of potassium in the upper profile of the pre-oxidized tailings in the monolayer (Column B) show a distinct increase in concentration when compared to the capillary barrier covers. This indicates that the tailings/biosolids interface in the monolayer are hydraulically connected and that pore water travels from the biosolids into the tailings. The lower concentrations of analytes in the tailings of the capillary barrier covers indicate that the desaturated sand layer provides a hydraulic barrier to pore water flux, as theoretically described in Figure 2-26.

Concentrations of magnesium and manganese exhibit similar variations within the tailings profiles of each column; following initial drying the highest concentrations of manganese and magnesium are observed within the columns. Flushing appears to cause either transport or chemical removal of magnesium from the pore water. Magnesium has an oxidation state of +2 and can compete with manganese which has several oxidation states. Manganese is often associated with iron, and elevated concentrations may indicate chemical of iron compounds and the release of manganese. In the pre-oxidized tailings of Column A and B the concentrations of both magnesium and manganese decline following flushing. In Column C the concentration of magnesium remains elevated in the upper tailings profile, while the concentration of manganese declines; this could indicate either physical displacement, or the binding of manganese in solids within the tailings.

Comparison of sodium concentrations within the pre-oxidized tailings of Column A and Column B show an increase in sodium at the surface of the tailings in the monolayer cover. Within the unoxidized tailings, the sodium concentrations remain relatively constant following drying, flushing, and secondary drying.

Nickel concentrations in the unoxidized tailings column remain relatively low and unchanged throughout testing, while elevated concentrations are observed following initial drying of the pre-

oxidized tailings columns. The elevated nickel concentrations subsequently decline following flushing.

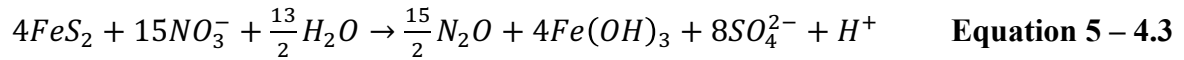
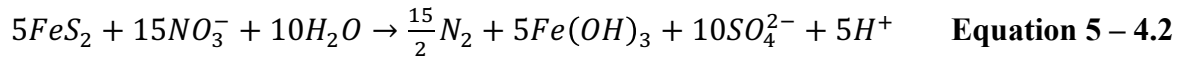
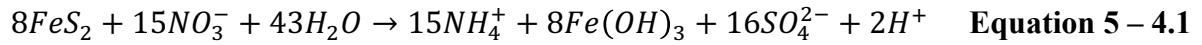
Arsenic concentrations are shown to be high in initial saturation extraction from the unoxidized tailings, however, arsenic concentrations within all other measured tailings are significantly lower. The arsenic concentrations in the unoxidized tailings drop to near zero throughout testing, and are generally near zero within the pre-oxidized tailings for the test duration. Lead concentrations show a similar trend with respect to an initially high concentration in saturation extraction, but low concentrations observed in pore water testing.

5.3.3.5 Nutrient Anion Concentration Profiles

Sulphate concentration profiles do not exhibit any significant changes throughout the testing period, with the exception that the initial saturation extract samples show elevated sulphate levels in the pre-oxidized tailings relative to the pore water samples extracted later during testing.

Nitrite concentrations decrease throughout the duration of testing in all layers of all columns. This indicates the presence of nitrifying bacteria which oxidize nitrite into nitrate.

Elevated levels of nitrate measured in the upper tailings profile of the monolayer column (Column B) indicate that nitrate is either released from the biosolids into the tailings through direct contact and advection, or that nitrate is produced through a change in pore water chemistry within the tailings from reaction of nitrite or other nitrogenous compounds. Since the increase in metal cation and nutrient anions is shown across a variety of analytes, it is most likely that simple advection and transport of nitrate from the biosolids into the tailings is occurring. Surface applied biosolids can provide favourable conditions for the microbial nitrification process (conversion of ammonia and ammonium into nitrate) within the biosolids, increasing the release of nitrates and leaching (Santibáñez et al., 2007). Nitrate may act as a replacement for oxygen in the oxidation of pyrite according to the following chemical reaction sequence shown in Equation 5-4 (Cravotta, 1998) and should therefore be seriously considered alongside oxygen flux when evaluating ARD mitigation.



Ammonium concentrations were not analyzed due to budgetary constraints, however, it is likely that ammonium contained within the biosolids may have undergone oxidation to produce nitrate, water, and hydrogen ions.

Phosphate levels were analyzed for all materials, however, only concentrations for the samples extracted from biosolids materials were returned from the University of Ottawa ICP lab due to equipment malfunction during sample analysis by University of Ottawa staff. Similar to nitrate, phosphate can also act as an oxidizing agent for iron (Mao, Pham, et al., 2011) and increase the reduction potential of mine waters (Tischler, Wiacek, et al., 2013) .

5.3.4 Key Findings from Column Testing

The establishment and preservation of the oxygen barrier layer using saturated municipal biosolids was confirmed by deconstructing the columns following 90 days of drying after flushing, and evaluating the column water content profiles.

Suction and volumetric water content profiles monitored throughout testing may be compromised due to elevated electrical conductivity in the pore water of the columns.

Interaction between the tailings and biosolids at the interface of the monolayer column is apparent from pore water analysis, and is largely absent in the capillary barrier columns, indicating a reduction in water flux through the desaturated sand layer between the biosolids and tailings.

Chapter 6 : Unsaturated Flow Modelling

Numerical modelling was conducted using Soil Vision SV-Flux software. 1D models were developed to assess material effectiveness for saturated/desaturated layers. Due to physical constraints of the equipment used at Vale's Copper Cliff Tailings Facility, biosolids application is limited to a 15 cm layer of material, and as such, the modelling and column testing were designed to simulate covers with a 15 cm layer of biosolids to assess their practical use in limiting oxygen transport and diffusion.

SoilVision's SV-Flux software is a 3D numerical modelling software which was used to develop 1-D transient models for monolayer and capillary barrier covers made using municipal biosolids.

6.1 One-Dimensional Model Parameters

1-D models were used to simplify model development and analysis, and were used to predict vertical water flux within the monolayer and capillary barrier covers, as well as the underlying tailings. The use of one dimensional models assumes lateral homogeneity and isotropy within the covers, it is assumed the material properties are the same in the X and Y direction at a given elevation.

SV-Flux uses finite element modelling, where model regions are discretized and computation of soil parameters are calculated at each individual node. Models constructed in SV-Flux used transient analysis to evaluate the behaviour of the cover configurations over time.

6.1.1 Model Dimensions

Models were developed to assess the effectiveness of 15 cm thick biosolids layers in monolayer and capillary barrier covers as this represented the practical maximum thickness of biosolids surface application currently implemented at Vale's Copper Cliff Tailings Facility. A 0.25 m model width was drawn to depict similarity to the laboratory columns, however, the model width did not affect results of 1D modelling. The modelled columns were divided into 203 vertical nodes for analysis in SV-Flux finite element modelling to provide enhanced resolution of modelling results by region.

Table 6-1. Cover configurations modelled in SV-Flux

| Cover type | | Elevation (cm) | Layer Thickness (cm) |
|------------|-----------|----------------|----------------------|
| Monolayer | CBC | | |
| N/A | Sand | 80 – 95 | 15 |
| N/A | Biosolids | 65 – 80 | 15 |
| Biosolids | Sand | 50 – 65 | 15 |
| Tailings | Tailings | 0 – 50 | 50 |

A visualization of the 1-D model setup from SV-Flux is shown in Figure 6-1.

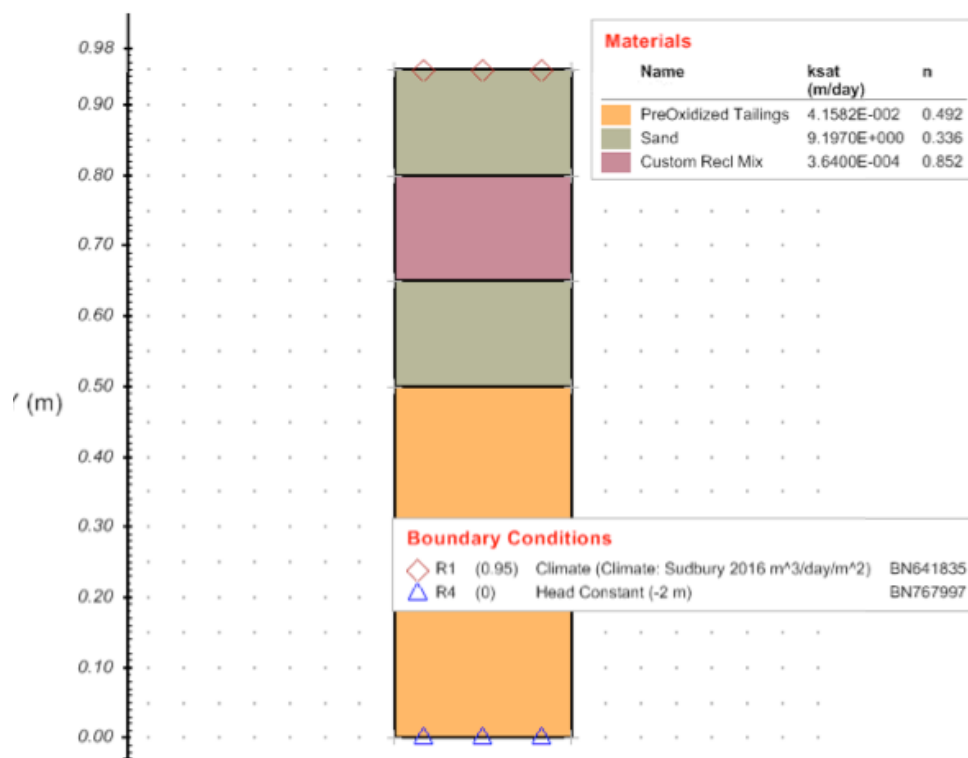


Figure 6-1. SV-Flux 1-D CBC column model setup

6.1.2 Material Properties

Several parameters determined from the characterization phase of testing were used in SV-Flux to define soil region properties. Characterized SWCC data and unsaturated hydraulic conductivity estimates were used as inputs. A Fredlund-Xing fit was used in the SV-Flux software to estimate water content at varying levels of soil suction and to fit a curve to SWCC data points measured in Section 4.1. The basis for the Fredlund-Xing function is shown in Equation 6-1 and uses algorithms to determine the fitting parameters a_f , n_f , m_f (D.G. Fredlund & Xing, 1994).

$$\theta(\psi) = \theta_s \cdot \left(1 - \frac{\ln\left(1 + \frac{\psi}{h_r}\right)}{\ln\left(1 + \frac{10^6}{h_r}\right)}\right) \cdot \left(\frac{1}{\left(\ln\left(\exp(1) + \left(\frac{\psi}{a_f}\right)^{n_f}\right)\right)^{m_f}}\right) \quad \text{Equation 6-1}$$

Where

$\theta(\psi)$ = gravimetric water content at any specified suction

θ_s = saturated gravimetric water content

h_r = residual soil suction (kPa)

a_f, n_f, m_f = fitting parameters

The Fredlund-Xing fit for pre-oxidized tailings is shown in Figure 6-2. The gravimetric water content is converted to volumetric water content using the specific gravity of the soil solids, and the porosity. The information used to generate the SWCC data points was entered in the program as VWC and corresponding suction values.

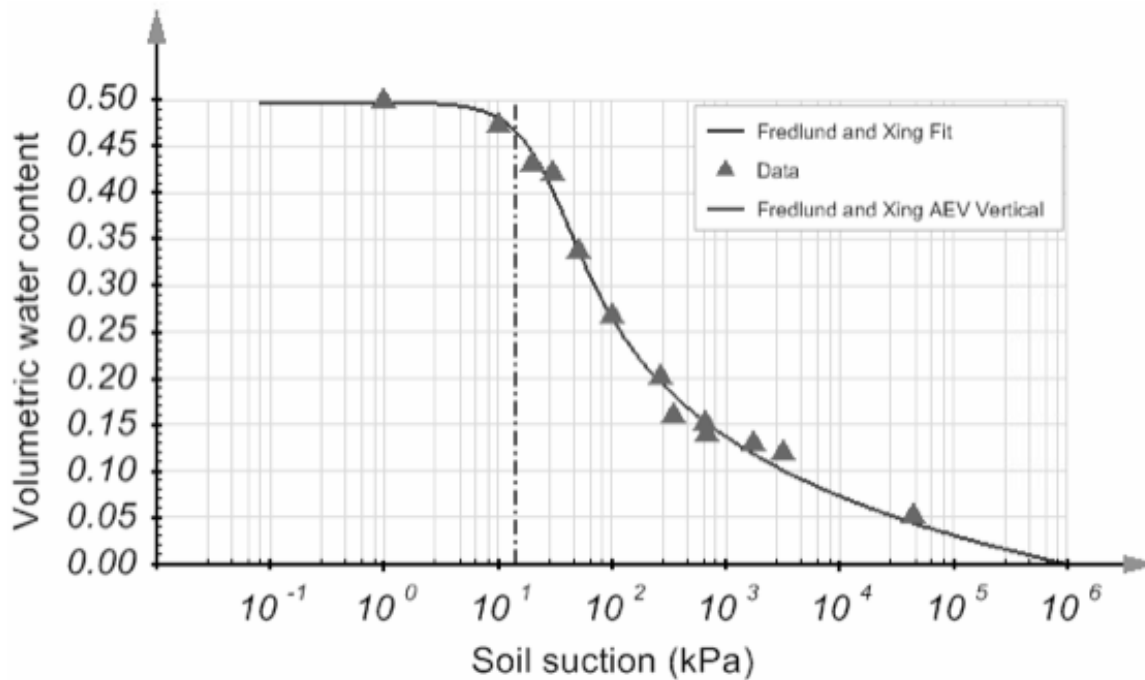


Figure 6-2. Fredlund-Xing fit used in SV-Flux modelling of pre-oxidized tailings

By default, models in SV-Flux are not constructed to account for volumetric deformation caused by shrinkage, the program assumes that changes in hydraulic conductivity are caused only by

desaturation. To incorporate the effects of shrinkage on hydraulic conductivity, the unsaturated conductivity was calculated using the Brooks-Corey estimation applied to a graph of Degree of Saturation vs. Suction as shown in Figure 6-3 where degree of saturation replaces the standard y-axis of volumetric water content.

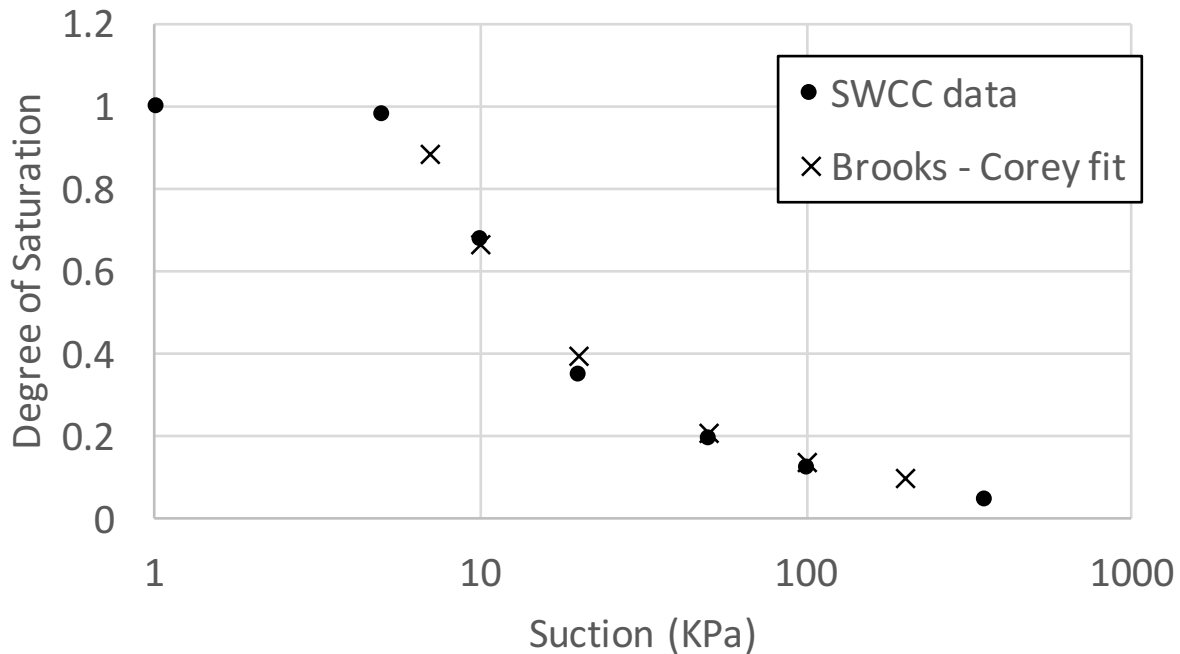


Figure 6-3. Brooks-Corey fit for determining unsaturated hydraulic conductivity calculation parameters of unoxidized tailings

The unsaturated hydraulic conductivity of the cover materials was predicted using the Brooks-Corey estimation method according to Equation 2-14 and Equation 2-15 in Section 2.4.3. The unsaturated hydraulic conductivity and suction values were entered in SV-Flux, and it was decided to use the Fredlund-Xing-Huang (FXH) estimation of unsaturated hydraulic conductivity to fit the data as the FXH estimation assigns a minimum hydraulic conductivity to soils according to the residual water content and degree of saturation, The minimum hydraulic conductivity is a constant at suctions greater than 1 MPa (D.G. Fredlund et al., 1994) where the Brooks-Corey estimation is linear with no lower bound to the unsaturated hydraulic conductivity.

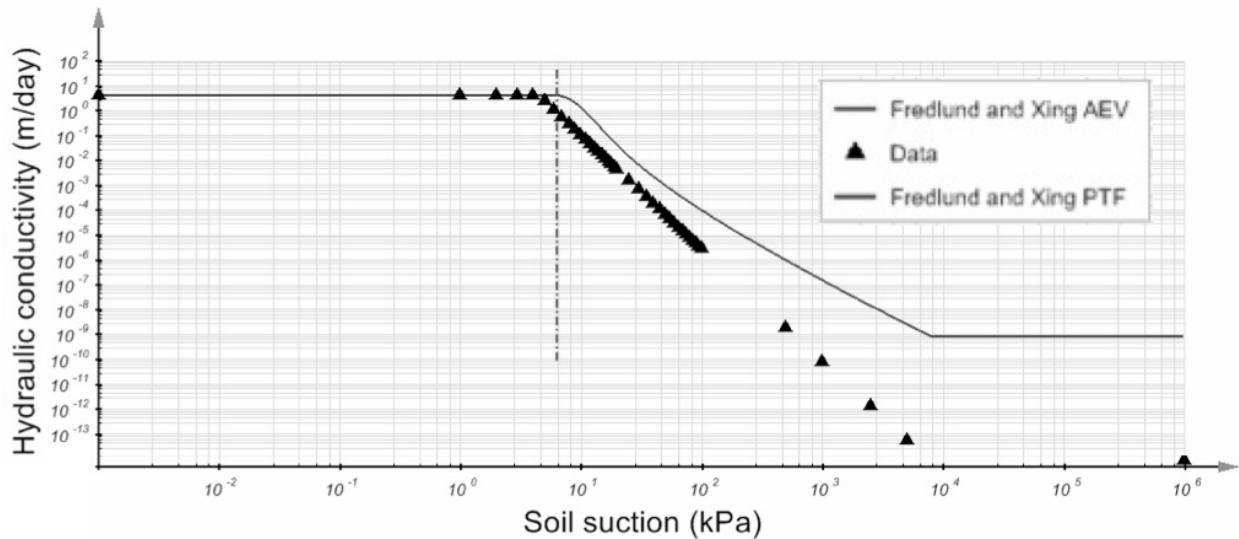


Figure 6-4. Fredlund-Xing-Huang function of unsaturated hydraulic conductivity used in SV-Flux for unoxidized tailings

The unsaturated hydraulic conductivity of the materials is shown to be marginally elevated when using the FXH estimation compared to the Brooks-Corey method, however, the FXH estimation was used in modelling due to the conservative nature of the modelling inputs (ie. results would show greater flux and desaturation of the cover with higher hydraulic conductivities). The general trend of both methods was visibly very similar.

6.1.2.1 Initial Volumetric Water Content

For preliminary model calibration to laboratory column data, initial volumetric water content was established by altering the pore water pressure (PWP) of the cover layers according to the negative PWP required to achieve the desired volumetric water content according to the SWCCs of each material established in Section 4.1. The initial VWC from both calibrated and unmodified 5TE sensor outputs were used in separate models to compare the different outputs for the initial drying period compared to the column data.

For the “What-If” analysis of hypothetical cover scenarios models were run from an initially saturated state, and from initial desaturated states in order to assess effects of initial conditions on the covers. Setup for fully saturated profile simulation was conducted by setting an initial head condition equal to the soil surface elevation.

6.1.3 Boundary Conditions

Boundary conditions were used to simulate weather effects and the depth from the cover surface to the water table.

6.1.3.1 *Climate Boundary*

Drying conditions modelling of the laboratory columns were recreated using measured temperature and relative humidity data collected with EasyLog sensors, and a linear fit was applied to data points using 6 hour point increments. Wind speed was back calculated from measured rates of evaporation in a proxy bucket and in the columns during flushing as described in Section 6.1.3.1.1 and Section 6.1.3.1.2.

Climate data for the City of Greater Sudbury was obtained from historical weather data (Government of Canada, 2018); it was decided to use a period of 91 days during the summer of 2016 from June 1 to August 31 for modelling of average weather conditions in the area. As per the scope of the project, winter months were not modelled as the freeze-thaw behaviour of the biosolids was not assessed as part of this study. Precipitation was applied according to the default parameters in SV-Flux which apply precipitation at specified intervals throughout each day and incorporate a correction for surface run-off on slopes.

Extreme drying conditions were simulated by applying a constant 20°C with 60% relative humidity and no precipitation for the 91 day simulation period.

6.1.3.1.1 Calculating Potential Evaporation and Calibrating Evaporation Inputs

Potential evaporation was measured in the laboratory by measuring the depth of water ponded above the surface of columns during flushing, as well as measuring the depth of water in a proxy bucket located near the columns throughout the duration of testing. The weight and depth of water in the bucket were measured throughout testing, and an average rate of evaporation was assumed between measurements.

Potential evaporation was assumed to be equal to the quantity of water evaporated from the proxy bucket measured by the change in depth in millimeters. The Penman-Monteith equation shown in Equation 6-2 incorporates mean temperature, relative humidity, mean wind speed, and solar radiation (Monteith, 1965), and was used to back-calculate the wind speed affecting evaporation at the surface of each column.

$$PE = \frac{1}{\lambda} \frac{\Delta(R_n - G) + \rho_a C_a \left[\frac{v_s - v_a}{r_a} \right]}{\Delta + \gamma \left(a + \frac{r_s}{r_a} \right)} \quad \text{Equation 6 - 2}$$

Where

PE = potential evaporation (mm/d)

λ = latent heat of vaporization (MJ/kg)

Δ = slope of the vapour pressure – temperature relationship (kPa⁰C)

R_n = albedo dependent net short and long-wave radiation (MJ/m²d)

G = soil heat flux (MJ/m²d)

ρ_a = density of air (kg/m³)

C_a = specific heat of air (MJ/kg⁰C)

γ = psychrometric constant (kPa⁰C)

v_s = vapour pressure at the soil surface (kPa)

v_a = vapour pressure in air above soil surface (kPa)

r_s = soil surface resistance factor

r_a = aerodynamic resistance factor

Simplification of the Penman-Monteith equation was done by eliminating solar radiation parameters since the column tests were conducted indoors, and the soil heat flux was assumed to be negligible (assuming constant equilibrium with atmospheric temperature), reducing the first term of Equation 6-3 to 0, and soil resistance factors assuming bare soil were used.

$$PE = \frac{0.408\Delta(R_n - G) + \gamma \frac{900}{T + 273.3} u_2 (e_s - e_a)}{\Delta + \gamma(1 + 0.43u_2)} \quad \text{Equation 6 - 3}$$

Where

T = mean temperature ($^{\circ}\text{C}$)

u_2 = wind speed (m/s)

e_s = saturation vapour pressure (kPa)

e_a = actual vapour pressure from relative humidity (kPa)

In Equation 6-3 the following simplifications can be made:

$$\Delta = \frac{4098 \left(0.6108 e^{\frac{17.27T}{T+273.3}} \right)}{(T+273.3)^2} \quad \text{Equation 6 – 3.1}$$

$$e_s = \frac{e^0(T_{max}) + e^0(T_{min})}{2} \quad \text{Equation 6 – 3.2}$$

$$e^0(T_i) = 0.6108 e^{\left(\frac{17.27T}{T+273.3} \right)} \quad \text{Equation 6 – 3.3}$$

$$e_a = \frac{e^0(T_{max})RH_{max} + e^0(T_{min})RH_{min}}{2} \quad \text{Equation 6 – 3.4}$$

Where

RH = the relative humidity

The simplified Penman Monteith equation was used to back calculate the wind speed affecting the columns, using the measured evaporation from the surface of each column during flushing and from the proxy bucket. The Solver function in Microsoft Excel was used to determine the average wind speed which resulted in the lowest sum of squared residuals between calculated PE and the measured PE over the course of data collection (lowest R^2 fit between measured and calculated data). An average windspeed of 2.07 m/s was applied to the SV-Flux simulation of laboratory conditions.

A sensitivity analysis was performed to assess the sensitivity of calculated potential evaporation to temperature, wind speed, and relative humidity; results are shown in Figure 6-5. In Figure 6-5 the values for relative humidity were reflected around the x-axis to simplify direct comparison with other factors. It was found that changes in relative humidity had the greatest effect on potential

evaporation. It should be noted that the change in evaporation caused by changes in wind speed is a polynomial relationship and there are diminishing returns of increasing wind speed on calculated PE.

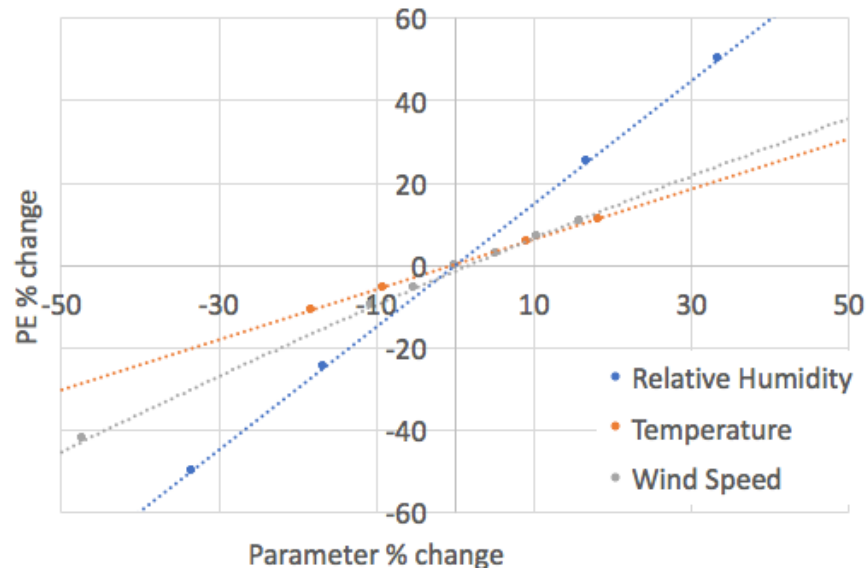


Figure 6-5. Sensitivity of Potential Evaporation calculation to various parameters

The results from evaporation calculated by SV-Flux from weather data compared to evaporation calculated using the Penman-Monteith equation were identical with respect to water flux and saturation profiles.

6.1.3.1.2 Calculating Actual Evaporation

Evaporation was included in all models. The actual evaporation was calculated in SV-Flux using the Modified Wilson Limiting Equation (1997), which incorporates the vapour pressure of the soil surface, soil, water, and air temperature, and the relative humidity measured in the air. The equation is best described by observing the series of equations shown in Equation 6-4 (Wilson, Fredlund, et al., 1997).

$$E = f(u)(e_s - e_a) \quad \text{Equation 6 - 4.1}$$

$$h_r = \exp\left(\frac{\psi g W_v}{RT}\right) \quad \text{Equation 6 - 4.2}$$

Where

E = rate of evaporation (mm/day)

$f(u)$ = transmission function dependent on characteristics of air above the evaporating surface

e_s = saturation vapour pressure at specific temperature above the water surface

e_a = vapour pressure of air in atmosphere above the water surface

h_r = relative humidity in the unsaturated soil voids (actual vapour pressure divided by saturation vapour pressure)

ψ = total suction in the liquid water phase expressed as matric suction (m)

g = acceleration (m/s^2)

W_v = molecular weight of water (0.018kg/mol)

R = universal gas constant (8.314 J/(mol · K))

T = temperature (K)

Combining Equation 6 – 4.1 and Equation 6 – 4.2, and assuming that $f(u)$ is the same at both the surface of the soil and the water surface yields Equation 6 – 4.3. Assuming that the temperature of the air, water, and soil are approximately the same, the equation can be expressed as follows in Equation 6 – 4.4. Where the phase temperatures are not equal Equation 6 – 4.2 and Equation 6 – 4.3 must be solved using the saturated vapour pressure at each temperature.

$$\frac{AE}{PE} = \frac{(e_o - e_a)}{(e_s - e_a)} \quad \text{Equation 6 – 4.3}$$

$$\frac{AE}{PE} = \left(\frac{\exp\left(\frac{\psi g W_v}{RT}\right) - h_a}{1 - h_a} \right) \quad \text{Equation 6 – 4.4}$$

Where

e_o = is the actual vapour pressure of the soil surface (kPa)

h_a = relative humidity of the air above the evaporating soil and water surfaces

The Modified Wilson Limiting Equation was developed using data obtained from very thin soil sections and does not account for recharge from soil subsurface. Extensive modelling has been conducted to attempt to refine calculation of actual evaporation, and surface suction corrections developed for individual soil types and incorporated into SV-Flux modelling capabilities (M. D. Fredlund, Tran, et al., 2015). No surface correction was applied for suction and relative humidity at the soil surface in this project as the parameters were unknown from the characterization work

conducted, and the accuracy of the Modified Wilson Limiting Equation were deemed to be sufficiently accurate for the scope of this project. The fit obtained for actual evaporation prediction in different soils using the Modified Wilson Limiting Equation is shown in Figure 6-6. When used in unsaturated flow modelling in SV-Flux the recharge from soil subsurface is accounted for by the water transport modelling.

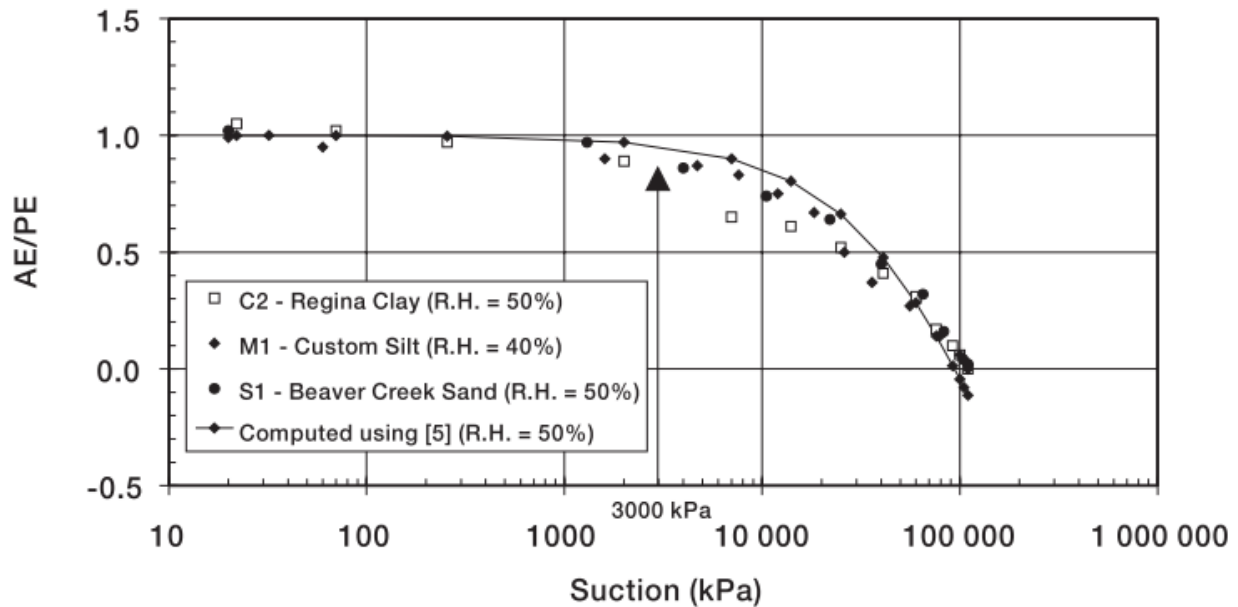


Figure 6-6. Calculation of AE/PE using Modified Wilson Limiting Equation relative to measurements in various soil types

6.1.3.2 Constant Head Boundary

Since soil suction increases with depth above the water table, it was decided to model several water table depths for the “What If” analyses. The depth from the ground surface to the water table was modelled by implementing a constant head boundary condition at the base of the tailings region. Constant head boundaries of -2 m, -5 m, and -20 m were implemented.

6.1.4 Model Calibration, Results, and Discussion

Initial modelling results of biosolids covers indicate significant potential suitability of a 15cm layer of biosolids in a capillary barrier cover for minimizing oxygen diffusion and water infiltration. The results from the first stage of modelling provided direction to continue to laboratory testing with the layer thicknesses specified in 5-3 of Section 5.1.1. Calibration of the models to fit laboratory

column data proved problematic due to volumetric water content sensor issues; efforts to calibrate the models are described in detail in Section 6.1.4.1.

6.1.4.1 SV-Flux Calibration to Laboratory Column Results

The initial intent of modelling the covers was to calibrate the model based upon laboratory column test results, and to utilize the calibrated model as a predictive tool for assessing the suitability of biosolids materials in covers subjected to weather conditions and varying climate and hydraulic head boundary conditions. As discussed in Chapter 5, the volumetric water content profiles reported from the 5TE sensors over the course of the column testing period may have significant deviation from the actual water content in the column layers, and therefore do not present a suitable basis for the calibration of model inputs. Prior to column deconstruction, several extensive attempts were made to match laboratory column water content and suction profiles to model outputs; this could only be accomplished by modification of the material soil-water characteristic curves. Additional axis-translation tests were run in an attempt to determine the changes in SWCC resulting from variation in initial water content and compaction pressures. Additionally, falling head tests were conducted on the CRM biosolids following column testing to determine if the hydraulic conductivity of the biosolids had changed over time; no increase in hydraulic conductivity of the biosolids was observed. The results are shown in Appendix A. In the models presented in this thesis, the original characterization results are used as model inputs; laboratory columns are recreated in SV-Flux, and several hypothetical “what-if” scenarios are analyzed. The use of a windspeed measuring 2.07 m/s was determined from calibration described in Section 6.1.3.1.1 and models were further calibrated by assessing the appropriateness of boundary conditions and soil properties. Model calibration did not use the time-period during or after flushing as the capability of SV-Flux to model ponded water in the columns was limited to a constant ponding depth for the entire duration of testing which was not representative of the water addition in the column tests. The small degree of volume change observed during flushing was not incorporated into the models. Recorded laboratory temperature and relative humidity conditions were applied to the models for the duration of the calibration period using a linear estimation of parameters between points recorded at 6-hour time intervals.

It was observed that modelling with no-flux boundary conditions more accurately simulated the water content profiles of the laboratory columns than when applying a -2 m constant head boundary, this further supports the assumption that the simulated boundary condition in the lab failed to establish a continuous hydraulic connection between the base of the columns and the reservoir 2 m below. As discussed in Section 5.2 it was deduced that the drain plugs at the base of the columns were plugged or restricted flow from the columns. Observations during testing further support the finding that the boundary condition may have failed as a discontinuous water column within the drainage tubes was observed shortly after the start of testing and no flow was observed in the tubing. Figure 6-7 shows the difference in the volumetric water content profiles simulated in SV Flux with varying boundary conditions overlaid with the water content profile observed in the laboratory.

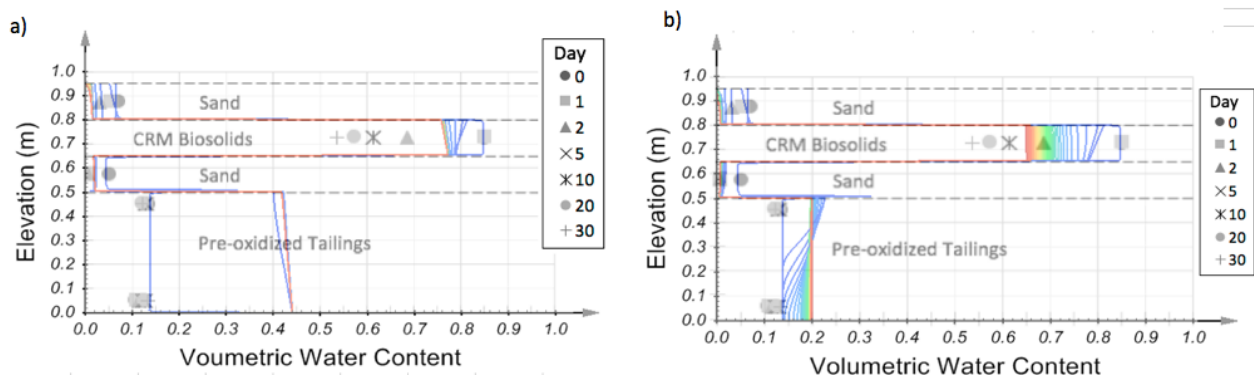


Figure 6-7 . Calibration of boundary conditions applied to simulation of Laboratory Column A in SV-Flux. -2m constant head boundary applied (a), and no-flux boundary condition (b).

Following the observation regarding the suitability of a no-flux bottom boundary condition, models were generated using the initial water content (with the exception of the biosolids layer) from the readings of the volumetric water content sensors prior to calibration correction and after calibration correction. The fit between sensor output and the model results are shown in Figures 6-8 to 6-11.

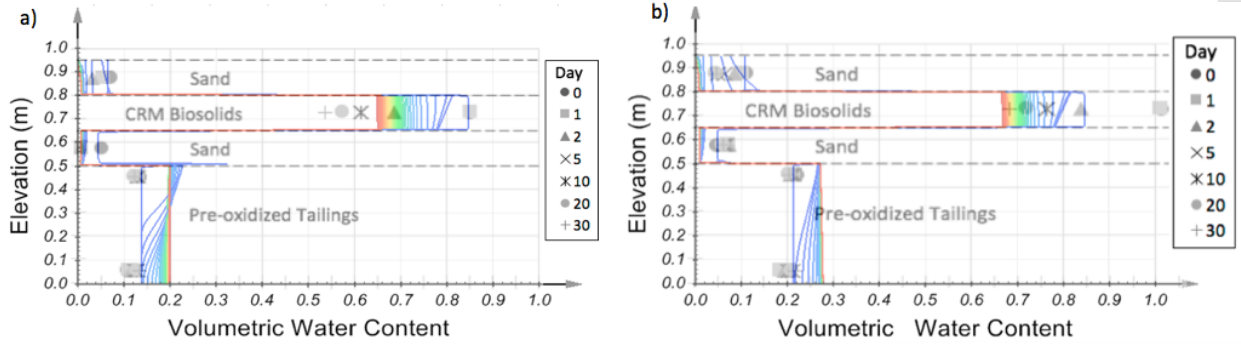


Figure 6-8. Column A Model results overlaid on initial drying profiles. Adjusted VWC (a) and unadjusted VWC values (b).

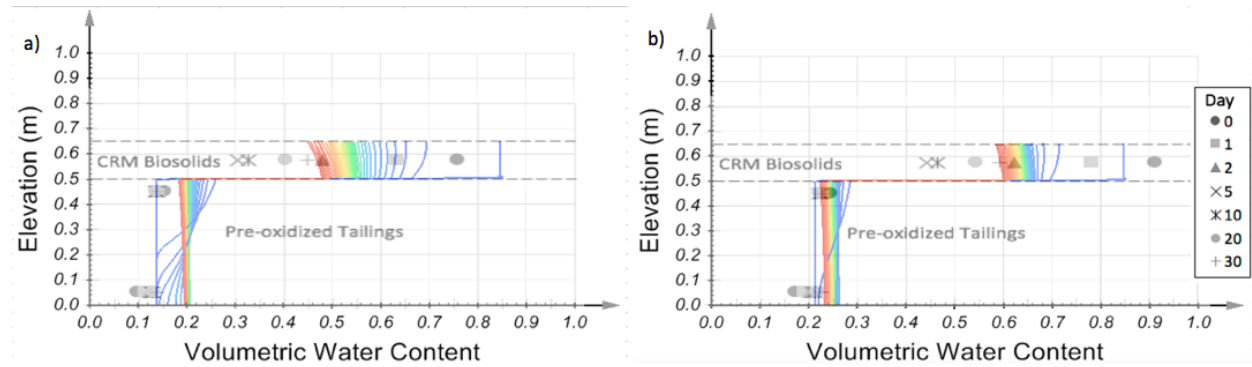


Figure 6-9. Column B Model results overlaid on initial drying profiles. Adjusted VWC (a) and unadjusted VWC values (b)

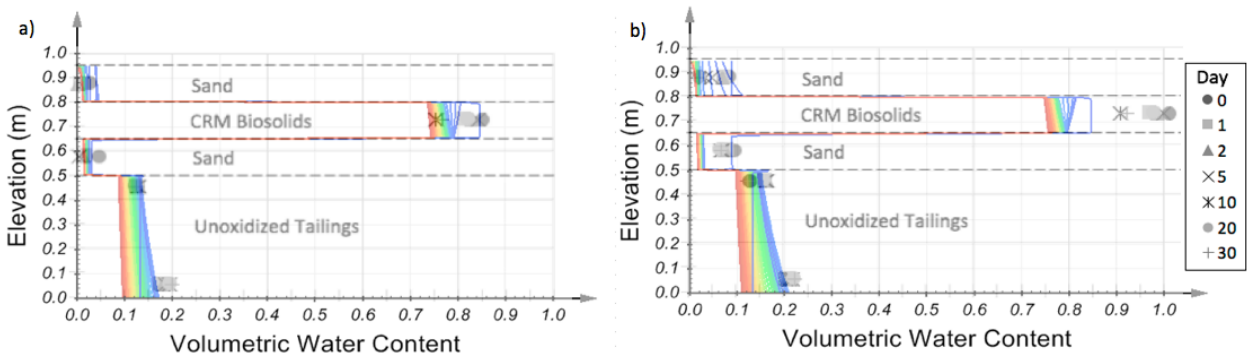


Figure 6-10. Column C Model results overlaid on initial drying profiles. Adjusted VWC (a) and unadjusted VWC values (b)

It was initially intended to calibrate the models to the laboratory column results in order to strengthen the validation of SV-Flux models as a predictive tool for biosolids cover performance. Due to the issues with sensor output from the volumetric water content sensors and suction sensors the matching of volumetric water content and suction profiles was not possible using the characterization data shown in Chapter 4. When initial pore water pressures were input to match

the volumetric water content profile of the columns, the matric suction profile within the modelled columns (see Figure 6-11) were found to be drastically elevated relative to the values reported by the Teros 21 sensors which were approximately 10 kPa for every soil layer with the exception of surface layers.

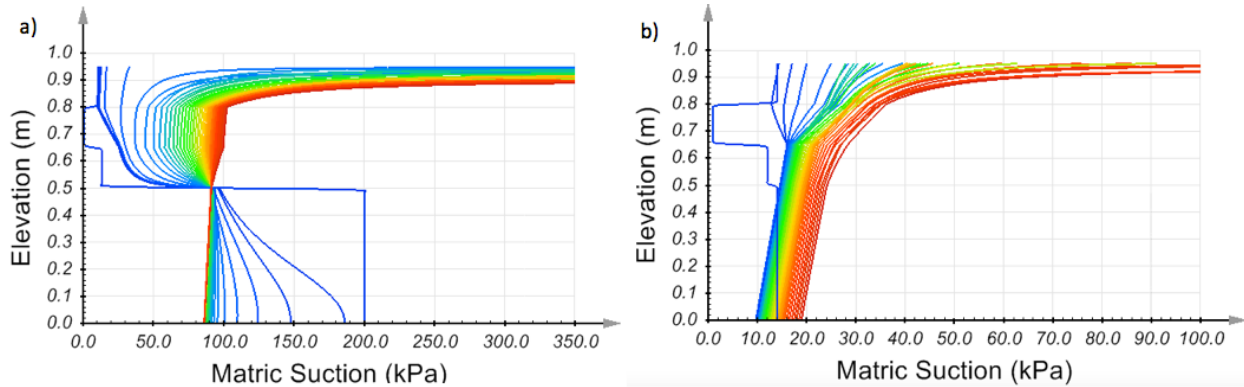


Figure 6-11. Matric Suction profiles for Column A (a) and Column C (b) from SV Flux modelling of initial drying period

While the suction and volumetric water content profiles could not be made to match the sensor output values from the laboratory using the established SWCCs, some attempts were made to use alternate SWCCs. Additional axis translation tests were performed which showed no significant change in the SWCC of the biosolids. Additionally, investigation in Section 6.1.5.3 indicates that the SWCC of the underlying tailings material has minimal impact on the degree of saturation of the overlying cover and flux through the cover.

6.1.4.2 Modelling of Secondary Drying Period

The post-flush drying period was modelled to in order to assess the modelled fit to the laboratory end states. In the modelled columns it was assumed that the biosolids layers and the upper sand layers of the CBCs were fully saturated, and that the lower sand and tailings were desaturated according to the unadjusted VWC values reported by the 5TE sensors at the end of flushing.

Modelling of an osmotic crust, and of a physical crust at the biosolids surface were attempted in SV Flux, however, neither option could be appropriately utilized in the secondary drying period. The osmotic crust simulates a reduction in evaporation, and the physical crust is applied by the program following precipitation events. Neither crust method was found to be suitable, however,

a reduction in the saturated and unsaturated hydraulic conductivity of the biosolids material was able to simulate a drying front more representative of the final measured volumetric water content profiles observed during column deconstruction. Figures 6-12, 6-13, and 6-14 shows the results of application of the reduced hydraulic conductivity in the biosolids material.

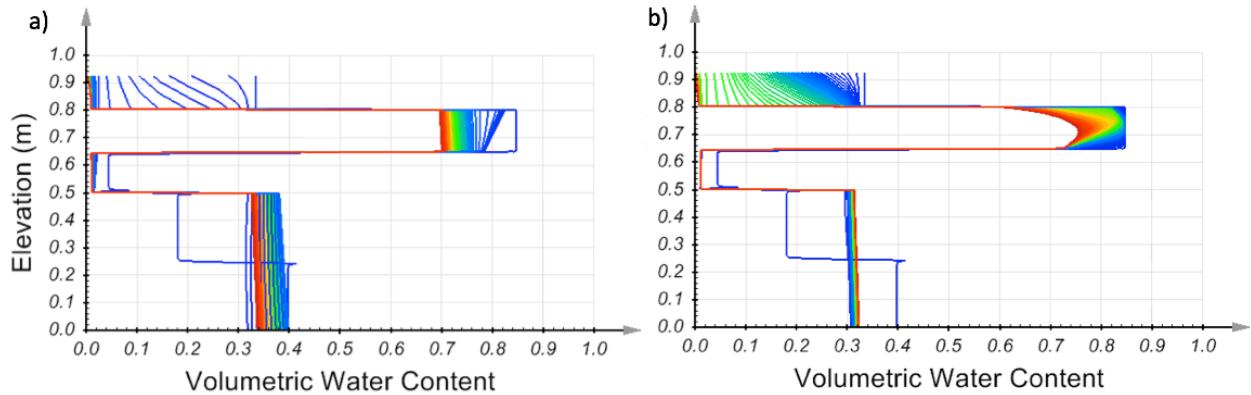


Figure 6-12. Volumetric Water Content profile of Column A with original hydraulic conductivity (a) and a lowered hydraulic conductivity (b)

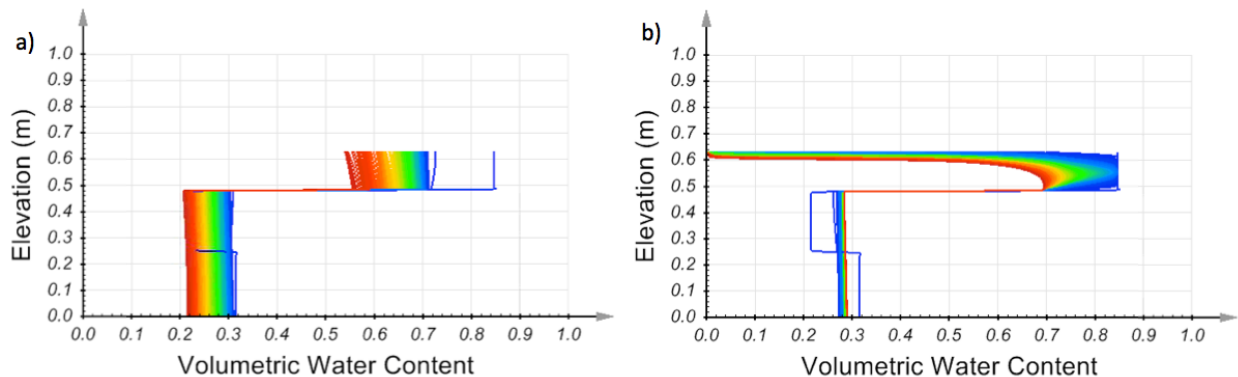


Figure 6-13. Volumetric Water Content profile of Column B with original hydraulic conductivity (a) and a lowered hydraulic conductivity creating a drying front (b)

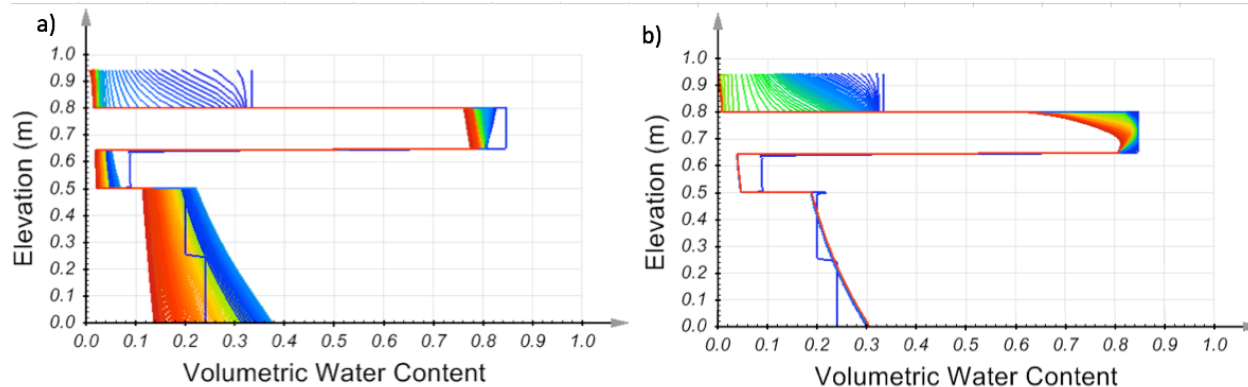


Figure 6-14. Volumetric Water Content profile of Column C with original hydraulic conductivity (a) and a lowered hydraulic conductivity (b)

The drying front was established by a 450 fold reduction in hydraulic conductivity (reduced from 3.64×10^{-4} m/day to 8×10^{-7} m/day). Uniform drying of the biosolids occurs at the higher hydraulic conductivities as shown in Figure 6-13 and drying of the surface layer only could not be modelled without decreasing the hydraulic conductivity by over two orders of magnitude. The reduction in hydraulic conductivity prevents replenishment of water available at the biosolids surface during evaporation, and also reduces flux within the tailings. This is a massive decrease in the hydraulic conductivity, and was therefore not incorporated in any of the further “What – If” analyses. The hydraulic conductivity of the biosolids materials stored separately in sample buckets was measured at the end of the column testing period, and found to be within the range of previous tested samples (5.03×10^{-4} m/day and 2.91×10^{-4} m/day). Flux at the tailings interface in all covers drops to effectively 0 (between 0.00001 and 0.00004 m³/day, a reduction of 3 orders of magnitude relative to the higher k values employed) with the lower hydraulic conductivity in the biosolids.

The hydraulic conductivity was not reduced for the “What If” analyses, as the formation of the surface crust (both physical and osmotic) could not be appropriately predicted using the model inputs, and reduction of the hydraulic conductivity by such a large degree could not be justified given the results of the falling head tests which indicated no significant change in the hydraulic conductivity from initial testing. All simulations of cover functionality in Section 6.1.5 therefore incorporate the original saturated hydraulic conductivity estimate obtained during characterization testing, and may therefore report increased desaturation of the biosolids and flux at the tailings interface, particularly in the monolayer covers. Therefore the analyses presented in this dissertation

are deemed to be conservative, in the sense that they will predict poorer cover performance with respect to desaturation and water flux than may be experienced in actual biosolids covers.

6.1.5 Simulated Cover Functionality

Table 6-2 shows some of the scenarios which were modelled as part of this project; more than 50 different scenarios were modelled. In Table 6-2 the tailings types are listed as Pre-Oxidized Tailings (POT) and Unoxidized Tailings (UT). Further models were conducted to

Table 6-2. Scenarios initially modelled in SV-Flux

| Cover Type | Climate Boundary | Tailings Type | Barrier Material | Initial Conditions | Depth to Water Table (m) | |
|---------------------------------------------------|----------------------|---------------|------------------------|--------------------|--------------------------|----------|
| Municipal Biosolids Capillary Barrier Covers | Sudbury Weather Data | POT | Custom Reclamation Mix | Saturated | 2, 20 | |
| | | UT | | | 2, 20 | |
| | | POT | | Toronto Amendment | Unsaturated | 2, 5, 20 |
| | | UT | | | | 2, 5, 20 |
| | POT | 2, 20 | | | | |
| | UT | 2, 20 | | | | |
| | No Precipitation | POT | Custom Reclamation Mix | 2, 20 | | |
| | | UT | | 2, 20 | | |
| Monolayer Covers | Sudbury Weather Data | POT | Custom Reclamation Mix | Unsaturated | | 2, 20 |
| | | UT | | | | 2, 20 |
| | | POT | Toronto Amendment | | 2, 20 | |
| | | UT | | | 2, 20 | |
| | No Precipitation | POT | Custom Reclamation Mix | | 2, 20 | |
| | | UT | | | 2, 20 | |
| 15cm Evaporative Sand Barrier over 15cm Biosolids | Sudbury Weather Data | POT | Custom Reclamation Mix | Unsaturated | 2, 20 | |
| | No Precipitation | | | | 2, 20 | |

6.1.5.1 Simulated Weather Condition Results

Modelling results with simulated weather conditions indicate that the capillary barrier covers utilizing CRM maintain the highest degree of saturation and experience the lowest water flux into the underlying tailings of all covers modelled. All capillary barrier covers were observed to provide

abatement of water flux relative to monolayer covers, and all capillary barriers maintained higher degrees of saturation within the biosolids layers when compared to monolayer covers.

Modelled covers in this section are referred to by the nomenclature outlined in Table 6-3.

Table 6-3. Modelled cover nomenclature

| Name | Model description |
|---------------|-----------------------------------------------------------------------------------------------------------------------------------------------------------------------------------------------------------------------------------------|
| Cover CBC-1A | Capillary barrier cover with CRM biosolids layer overlying pre-oxidized tailings. Sudbury weather data applied, initial pore water pressure applied, constant -2 m head boundary at base of column. |
| Cover Mono-1A | Monolayer cover with CRM biosolids layer overlying pre-oxidized tailings. Sudbury weather data applied, initial pore water pressure applied, constant -2 m head boundary at base of column. |
| Cover CBC-1B | Capillary barrier cover with CRM biosolids layer overlying pre-oxidized tailings. Sudbury weather data applied, initial pore water pressure applied, constant -20 m head boundary at base of column. |
| Cover Mono-1B | Monolayer cover with CRM biosolids layer overlying pre-oxidized tailings. Sudbury weather data applied, initial pore water pressure applied, constant -2 m head boundary at base of column. |
| Cover TBS-1A | 15 cm biosolids layer overlying pre-oxidized tailings. Biosolids covered with 15 cm of sand for evaporative barrier. Sudbury weather data applied, initial pore water pressure applied, constant -2 m head boundary at base of column. |
| Cover TBS-1B | 15 cm biosolids layer overlying pre-oxidized tailings. Biosolids covered with 15 cm of sand for evaporative barrier. Sudbury weather data applied, initial pore water pressure applied, constant -20 m head boundary at base of column. |
| Cover TA-1A | Capillary barrier cover with TA biosolids layer overlying pre-oxidized tailings. Sudbury weather data applied, initial pore water pressure applied, constant -2 m head boundary at base of column. |
| Cover TA-1B | Capillary barrier cover with TA biosolids layer overlying pre-oxidized tailings. Sudbury weather data applied, initial pore water pressure applied, constant -20 m head boundary at base of column. |
| Cover TA-ML | Monolayer cover with TA biosolids layer overlying pre-oxidized tailings. Sudbury weather data applied, initial pore water pressure applied, constant -20 m head boundary at base of column. |

6.1.5.1.1 Comparison of Cover Configuration

From Figure 6-15 and Figure 6-16 it is apparent that the upper horizon of the biosolids layer experiences greater desaturation in the monolayer cover (Cover Mono-1A) without the evaporative

barrier provided by the sand cover at the surface of the capillary barrier cover. A similar degree of saturation is observed throughout the modelled time period for the tailings layer.

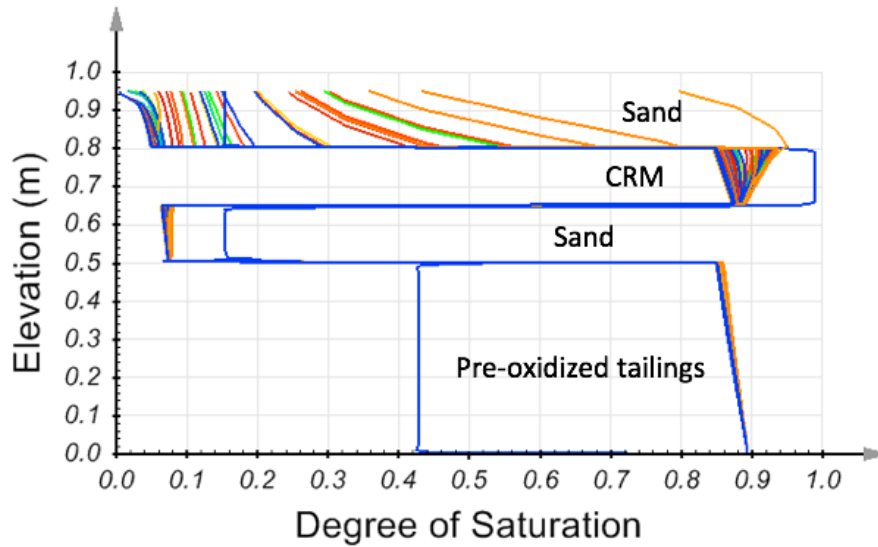


Figure 6-15. Saturation profile of Cover CBC-1A

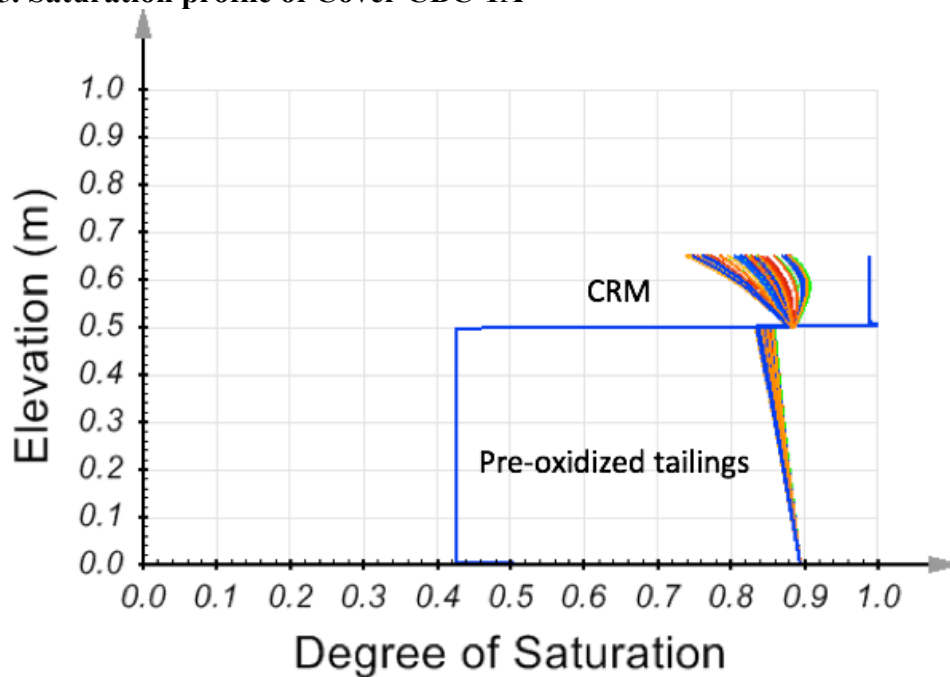


Figure 6-16. Saturation profile of Cover Mono-1A

While the monolayer cover maintains a relatively high degree of saturation, the water flux through the cover reported from the SV-Flux models indicate that the capillary barrier cover achieves a significantly greater reduction in water flux at tailings interface.

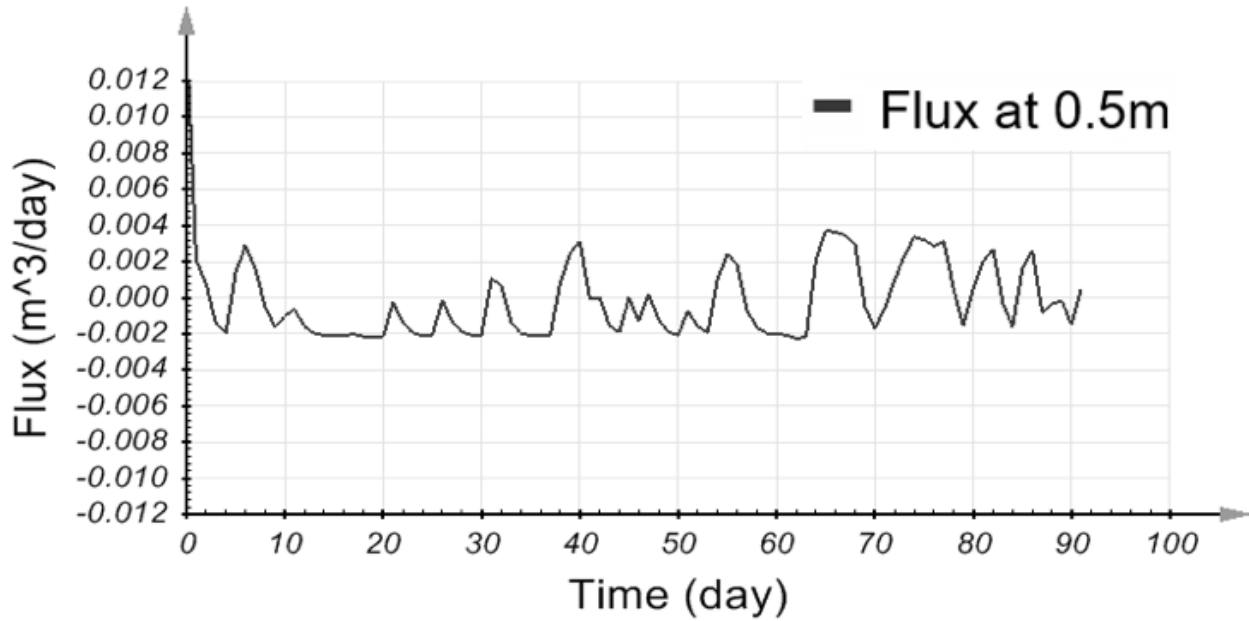


Figure 6-17. Reported flux at the sand/tailings interface of Cover CBC-1A

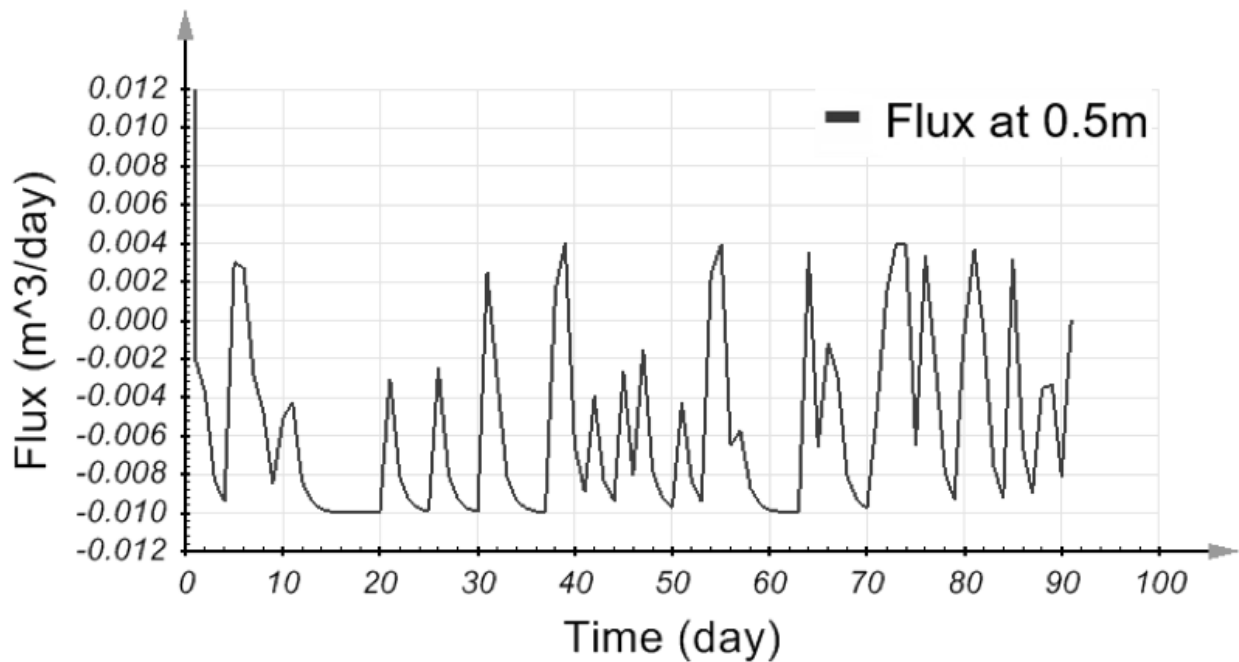


Figure 6-18. Reported flux at the biosolids/tailings interface of Cover Mono-1A

The effectiveness of an evaporative sand barrier overlying the biosolids monolayer was assessed; the saturation profile is shown in Figure 6-20 and the reported flux is shown in Figure 6-21. The evaporative barrier reduces the desaturation of the biosolids layer and results in a similar reported flux at the tailings interface when compared to the capillary barrier cover. A greater degree of

upwards water flux is observed in the monolayer cover, likely due to increased suction in within the slightly drier biosolids layer. To evaluate the flux abatement of both covers Figure 6-19 shows the flux at the pre-oxidized tailings surface when no cover is used under the same model conditions (-2 m constant head boundary at base of tailings).

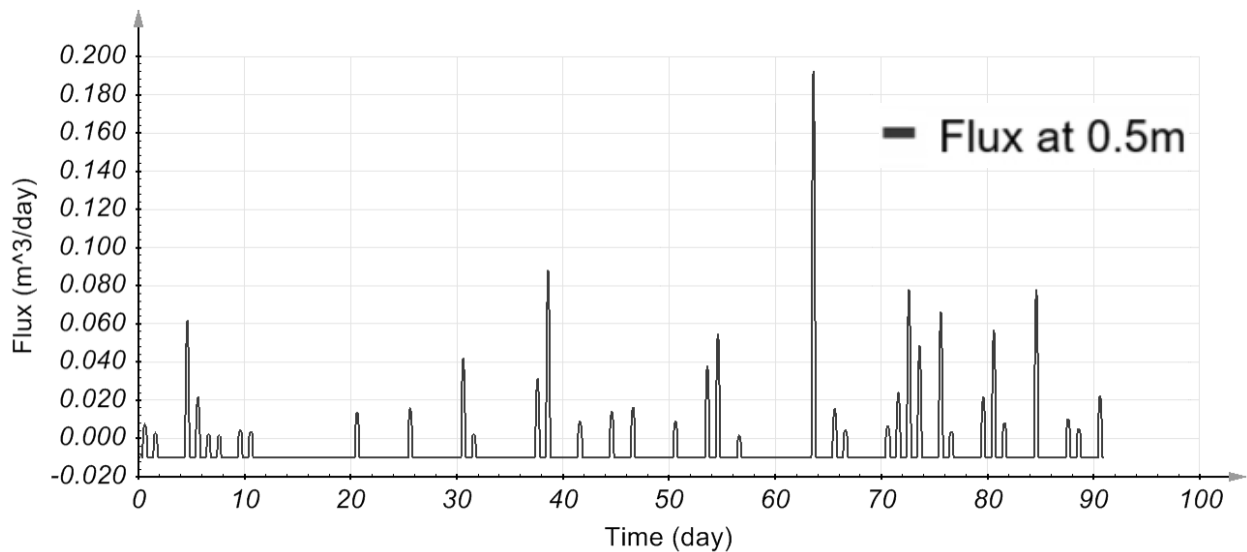


Figure 6-19. Flux at the tailings surface when no cover is applied over pre-oxidized tailings and -2m constant head boundary at the base of the tailings

It is evident that both the capillary barrier cover and monolayer serve to significantly reduce the flux of water at the upper boundary of the tailings relative to simulations with no covers. The reduction of peak flux from 0.2 m³/day with no cover to 0.004 m³/day with a CRM biosolids capillary barrier represents a 98% reduction in water flux at the tailings surface.

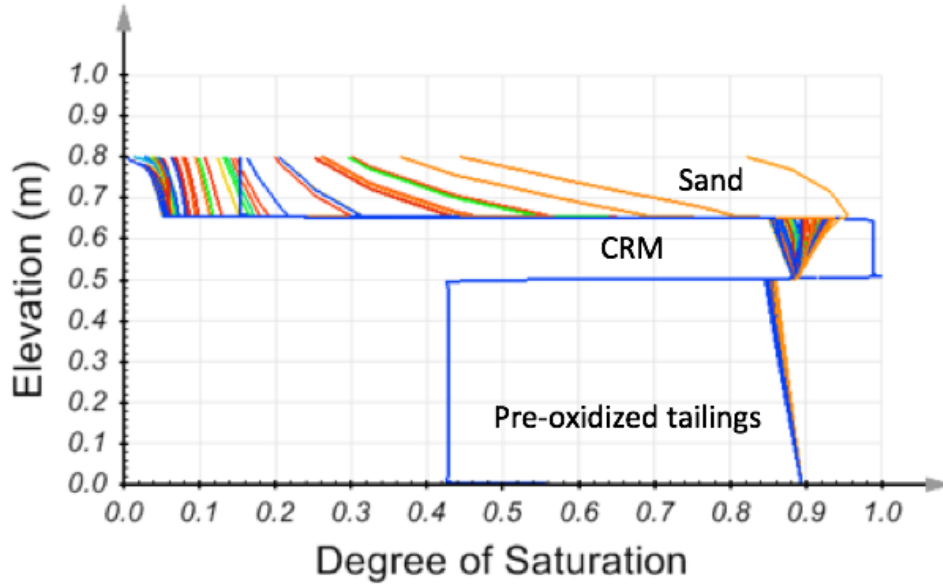


Figure 6-20. Saturation profile of Cover TBS-1A

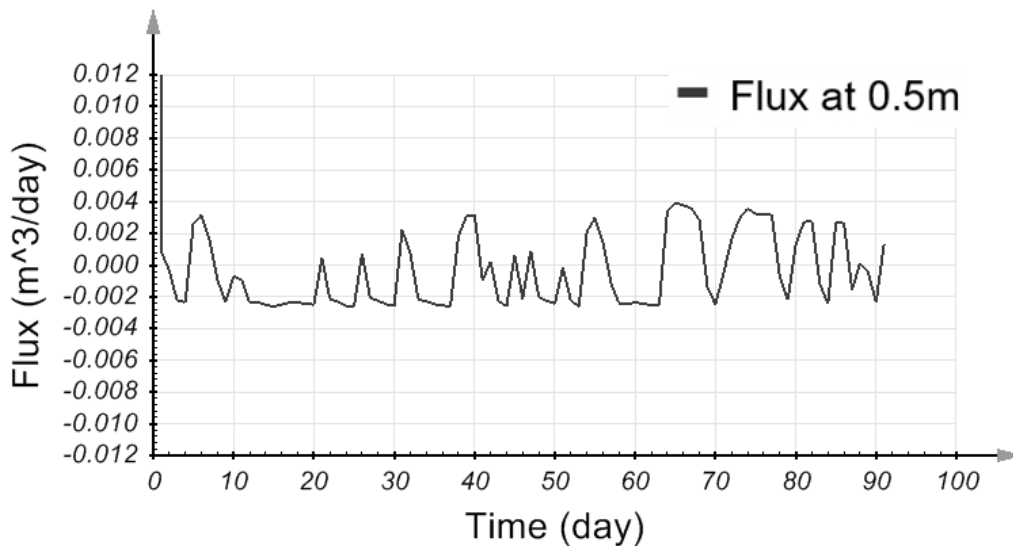


Figure 6-21. Reported flux at the biosolids/tailings interface of Cover TBS-1A

With a shallow modelled depth to the water table implemented by a -2 m constant head boundary, the saturation of the monolayer cover, capillary barrier cover, and biosolids with an evaporative sand barrier achieve relatively similar results. In the following pages a modelled constant head boundary of -20 m was implemented to simulate an increased depth to the water table and elevated levels of soil suction. At increased levels of soil suction it can be seen that the capillary barrier covers made from CRM greatly out perform other modelled covers with respect to maintaining saturation within the biosolids layer and controlling water flux at the tailings surface.

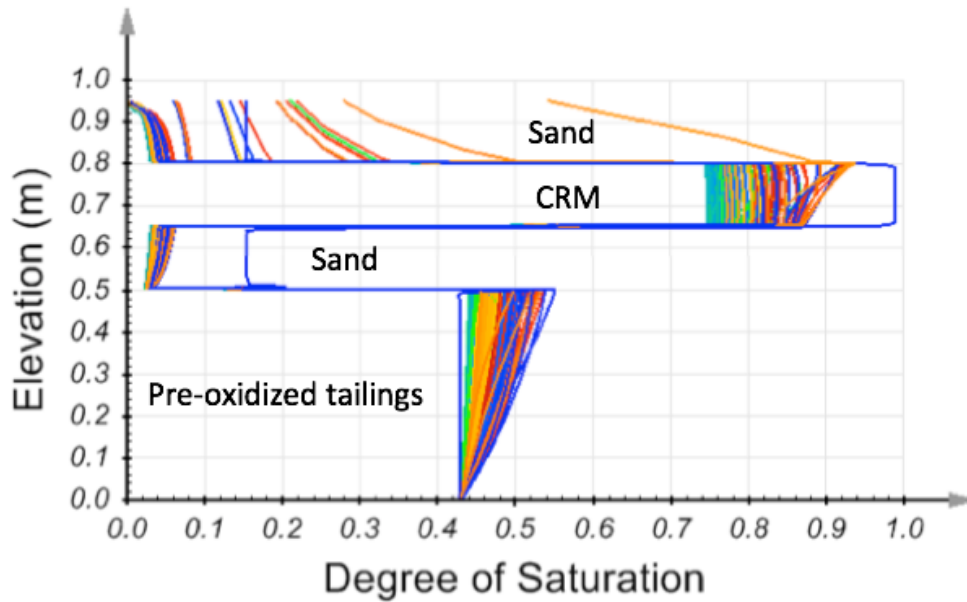


Figure 6-22. Saturation profile of Cover CBC-1B

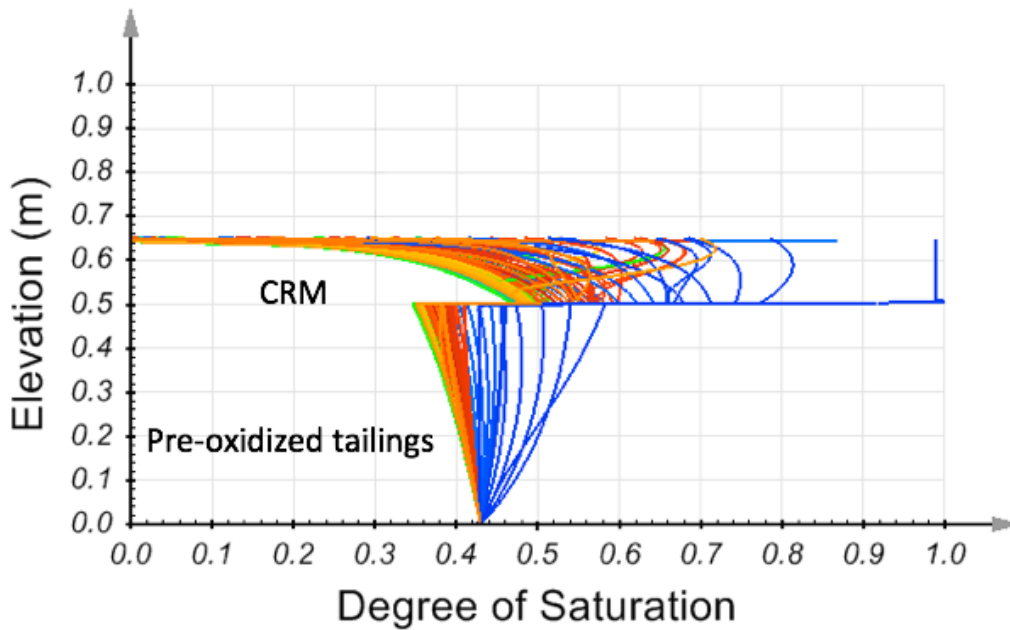


Figure 6-23. Saturation profile of Cover Mono-1B

Figure 6-22 and Figure 6-23 show the ability of the capillary barrier cover to maintain saturation within the biosolids layer even under extreme drying conditions imposed by a -20 m constant head boundary at the base of the column. The minimum calculated degree of saturation within the biosolids in Cover CBC-1B is approximately 0.75, while the biosolids in the monolayer of Cover Mono-1B report a minimum degree of saturation of 0.46 at the tailings interface. In addition to

experiencing a significantly greater degree of desaturation in the cover layers, there is a marked difference in water flux between the monolayer and capillary barrier covers. Figure 6-24 shows a positive flux at the tailings interface in Cover CBC-1B, indicating that water is being transported downwards into the tailings through the lower sand layer of the capillary barrier cover with no upwards flux of water from the tailings. Conversely, the results from the monolayer cover in Figure 6-25 show an almost constant upwards water flux, indicating that water is being transported from the tailings layer into the biosolids of the monolayer cover.

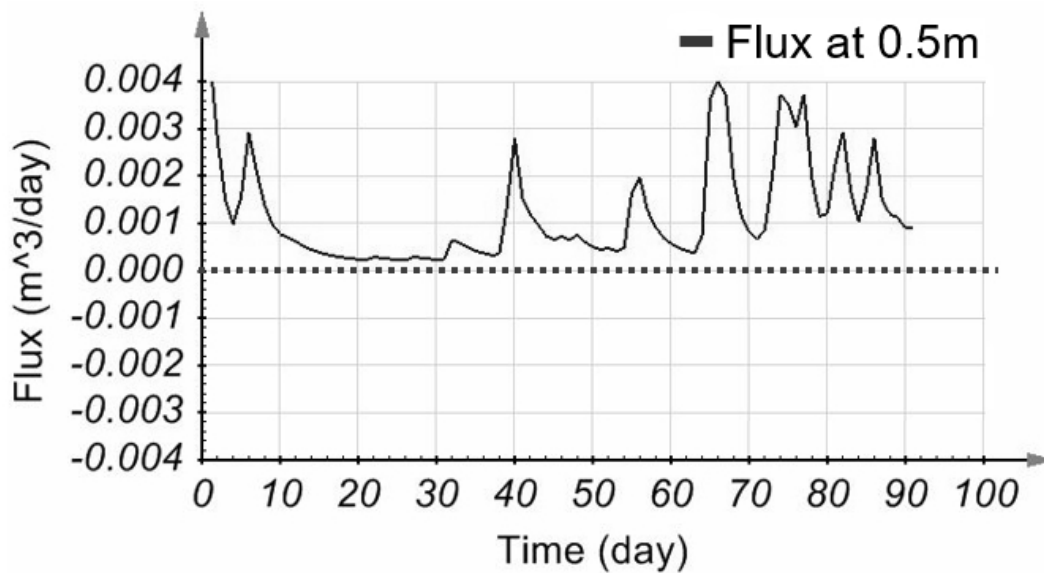


Figure 6-24. Flux at the tailings interface of Cover CBC-1B

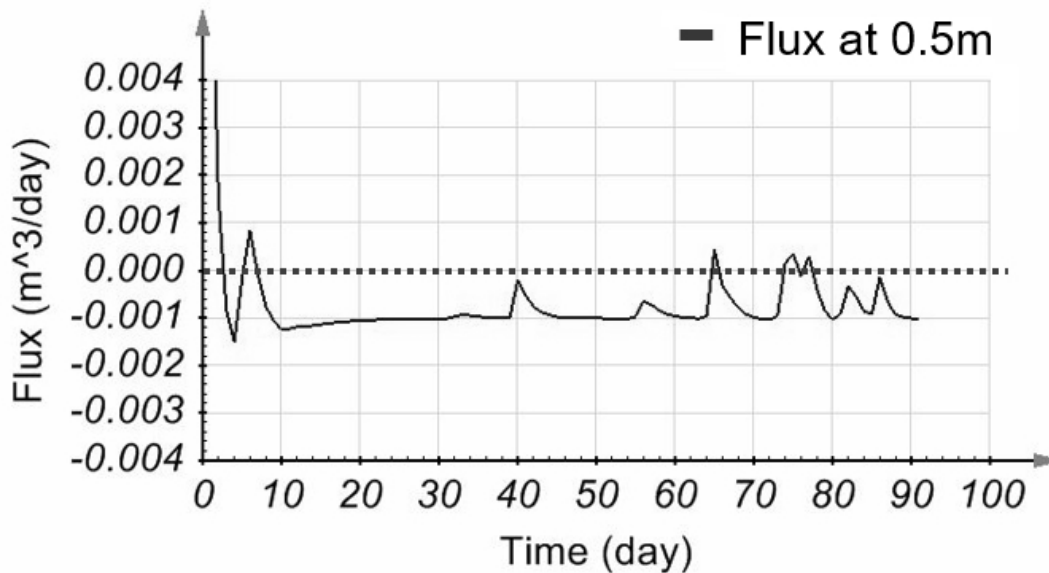


Figure 6-25. Flux at the tailings interface of Cover Mono-1B

The desaturation of the biosolids layer using a monolayer cover indicate that a monolayer cover constructed with 15 cm of CRM may be insufficient to prevent ARD when high levels of soil suction are present below the cover.

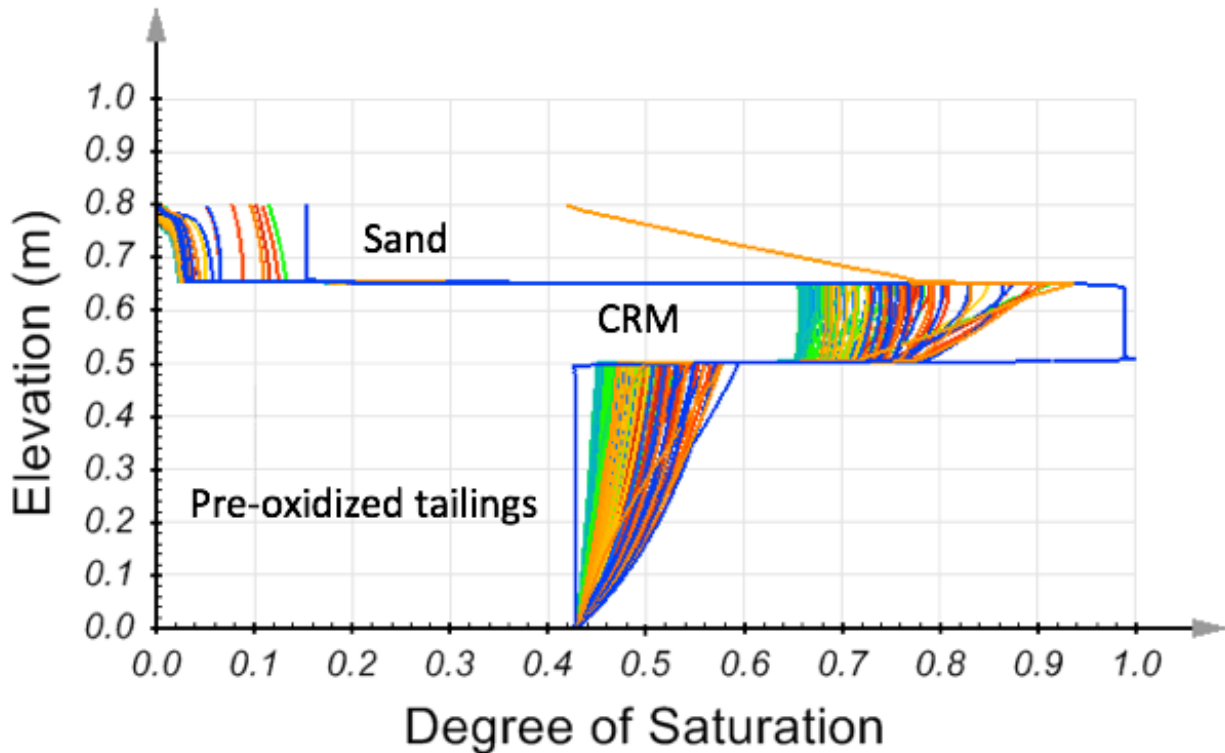


Figure 6-26. Saturation profile of Cover TBS-1B

Modelling of a cover utilizing a 15 cm layer of biosolids with an evaporative barrier comprised of 15 cm of sand was conducted and the results shown in Figure 6-26 and Figure 6-27 (-20 m constant head boundary condition at the base of the tailings). When compared to Cover CBC-1B, the biosolids layer in TBS-1B experiences a relatively greater degree of desaturation (0.65 compared to 0.75 for the CBC).

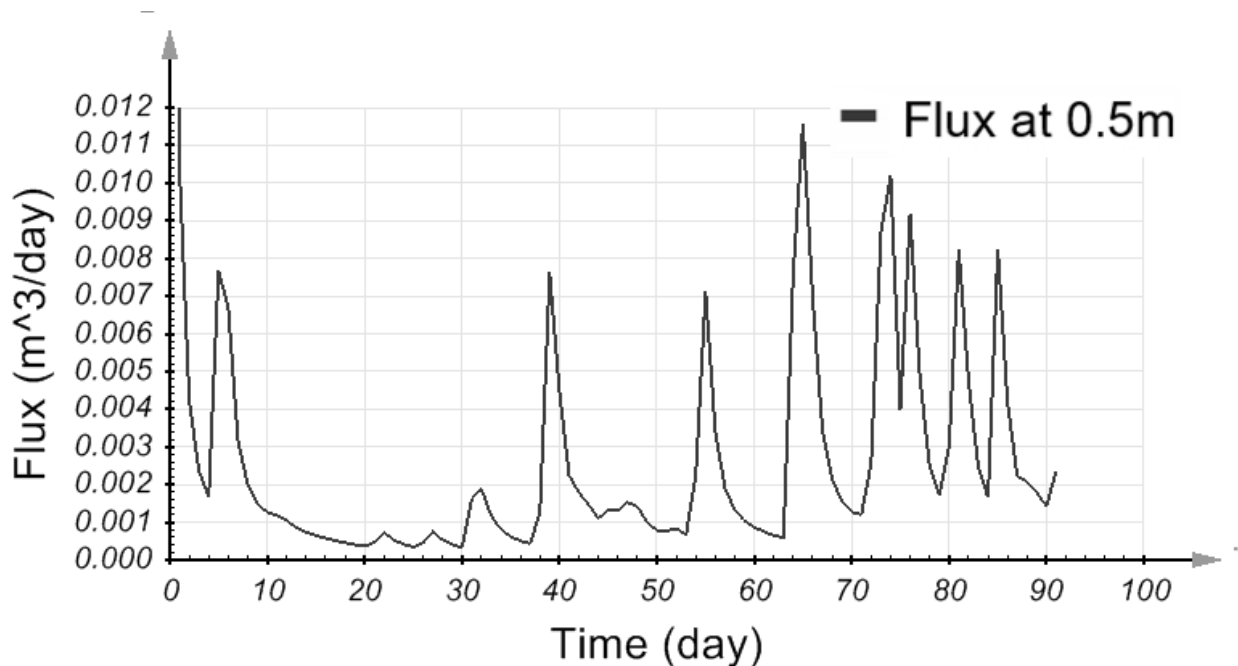


Figure 6-27. Flux at the tailings interface of Cover TBS-1B

The flux at the tailings surface when using a biosolids cover with an evaporative sand barrier (Cover TBS-1B) is significantly greater than when employing a capillary barrier cover. This is likely due to the low unsaturated hydraulic conductivity within the desaturated lower sand layer in the capillary barrier cover which reduces movement of water between the tailings and biosolids. Cover TBS-1B experiences water flux approximately 300% greater than the flux in Cover CBC-1B.

6.1.5.1.2 Comparison of Cover Materials

Both the Toronto Amendment and Custom Reclamation Mix biosolids were modelled in various cover configurations and conditions to assess cover performance. It was observed that the TA biosolids desaturated at a significantly greater rate than the CRM biosolids when used in monolayer covers at greater levels of soil suction below the covers, and generally resulted in poor control of flux at the tailings interface relative to covers modelled with CRM. The TA biosolids did maintain a high degree of saturation within CBC covers, however, it was noted that control of water flux was greatly reduced when TA biosolids were used in all cover types.

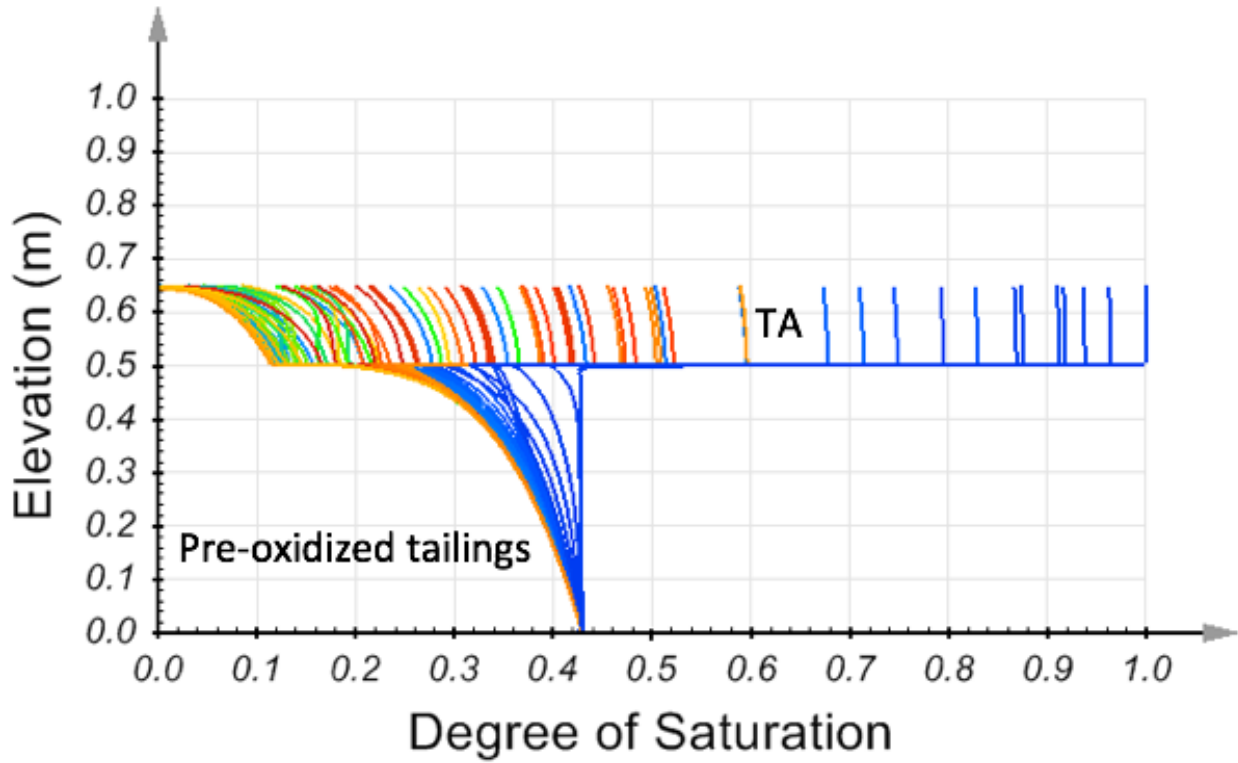


Figure 6-28. Saturation profile of TA-ML

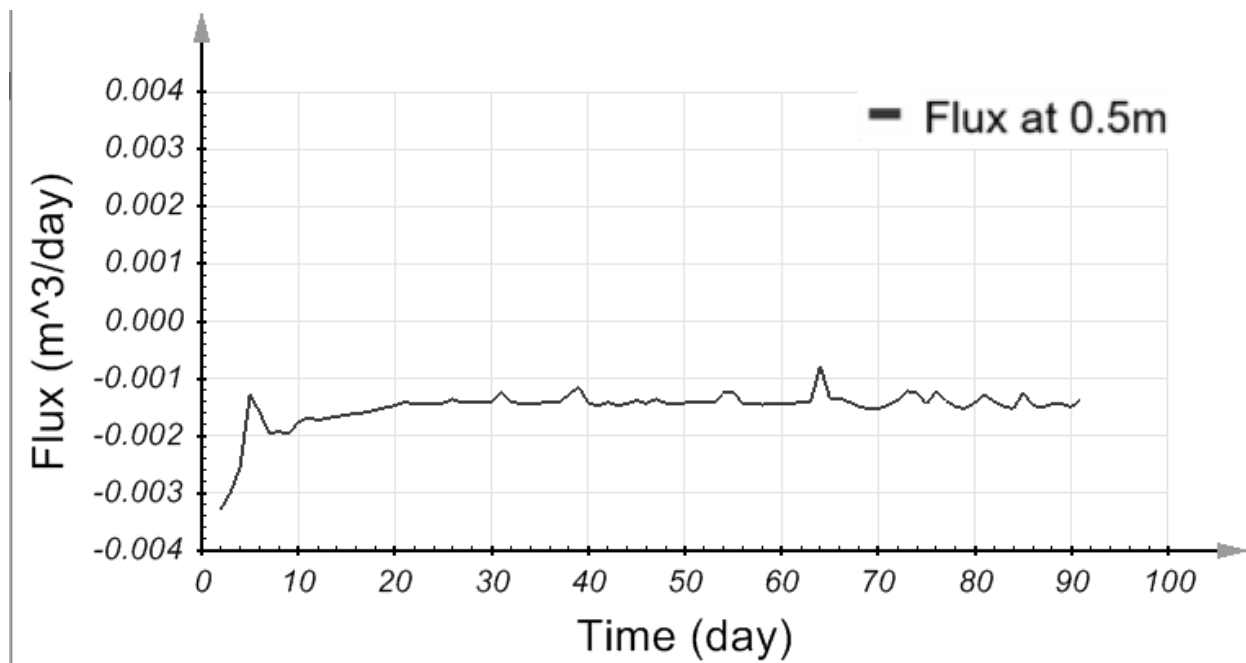


Figure 6-29. Flux at the tailings interface of Cover TA-ML

Figure 6-28 and Figure 6-29 show the nearly complete desaturation of a monolayer cover using TA biosolids under elevated soil suction conditions (-20 m constant head boundary at the base of the tailings), and a constant upwards flux of water from the tailings into the biosolids. From these results it can be inferred that monolayer covers utilizing TA biosolids may prove to be ineffective at reducing oxygen diffusion and tailings water may be drawn upwards into the biosolids.

Figure 6-30 and Figure 6-31 show the output from modelling of a CBC cover with TA biosolids and a -20m constant head boundary at the base of the tailings. While the tailings maintain a high degree of saturation, the flux control at the tailings interface is significantly reduced compared to CBC covers with CRM biosolids; water flux is approximately 275% greater in the TA covers relative to covers with CRM biosolids.

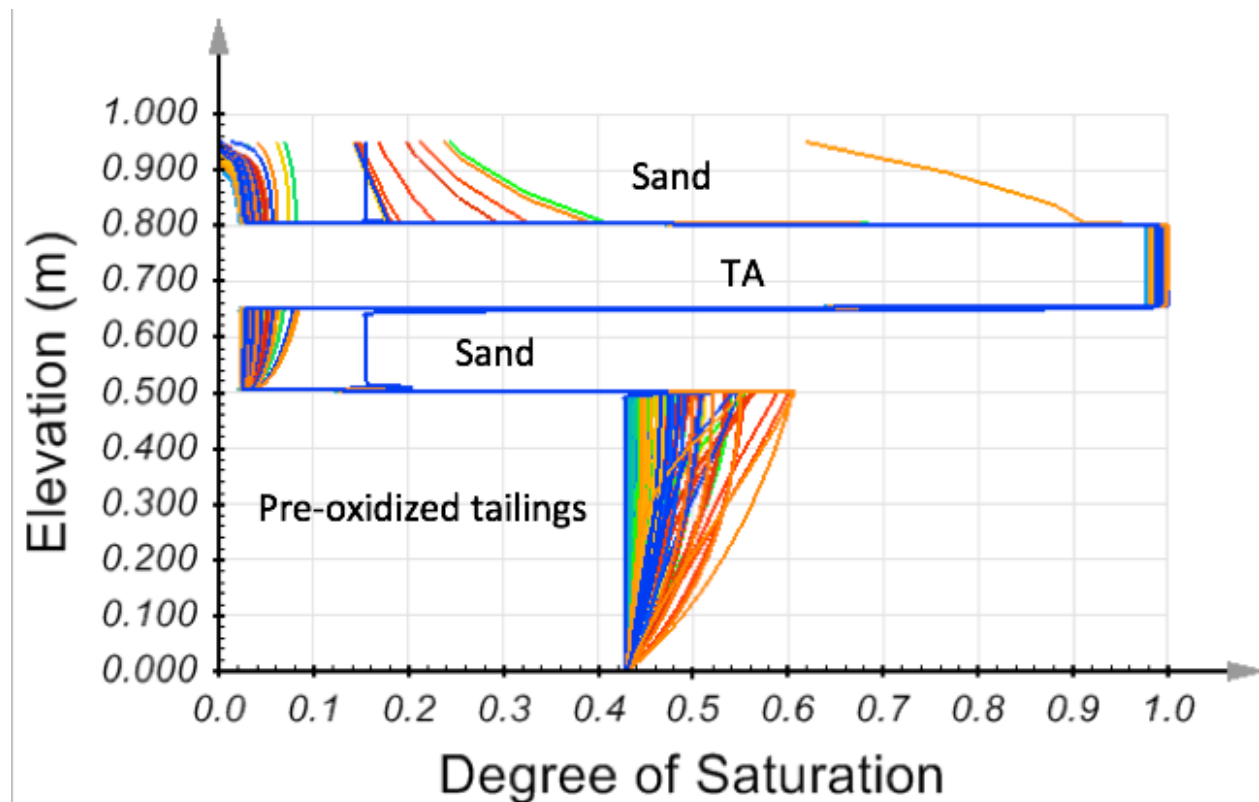


Figure 6-30. Saturation profile of Cover TA-1B

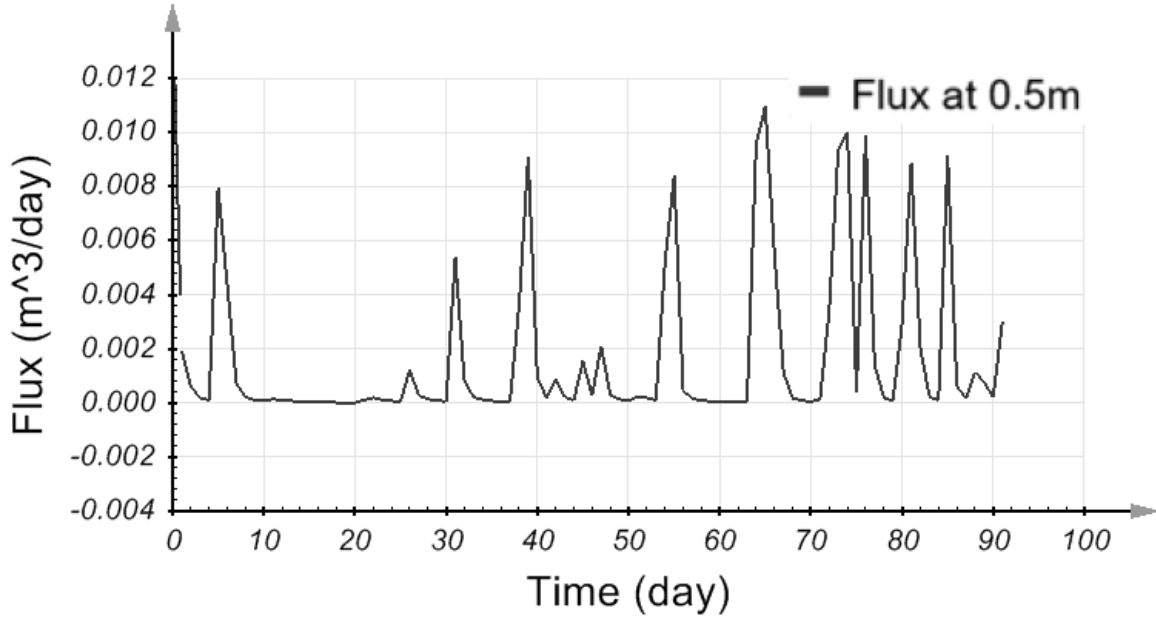


Figure 6-31. Flux at the tailings interface in Cover TA-1B

Figure 6-31 shows the flux predicted in a CBC cover using TA biosolids with a -2m constant head boundary; when comparing to a similar CBC cover using CRM biosolids (Figure 6-17) it is evident that the flux is significantly greater within the column using TA biosolids. The flux in a TA CBC cover with a -20m head boundary at the base of the pre-oxidized tailings is shown in Figure 6-32.

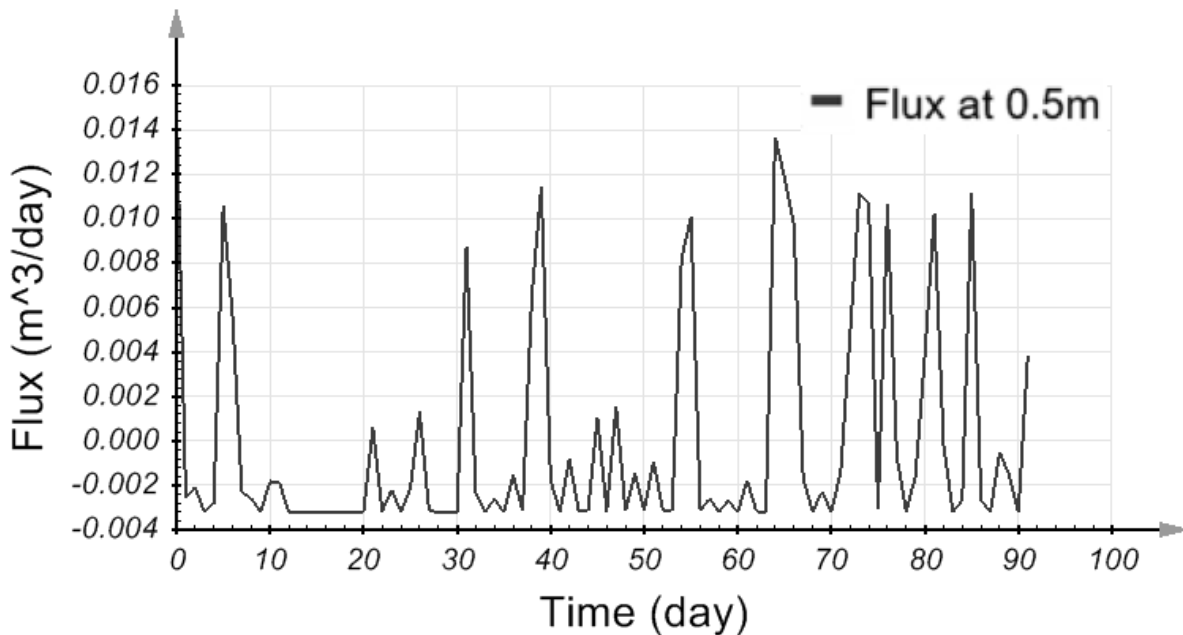


Figure 6-32. Flux at the tailings interface in Cover TA-1A

6.1.5.2 Simulated Extreme Drying Condition Results

Modelling of extreme drying conditions indicate that monolayer covers undergo significant desaturation relative to capillary barrier covers. The significant desaturation of the monolayer covers implies that a greater degree of oxygen diffusion may occur through the covers and result in elevated levels of tailings oxidation and ARD.

As stands to reason, biosolids layers in all covers experience a greater degree of desaturation when exposed to extreme drying conditions when compared to covers modelled with precipitation. Comparison of CBC saturation profiles are shown in Figure 6-33 and monolayer saturation profiles are shown in Figure 6-34.

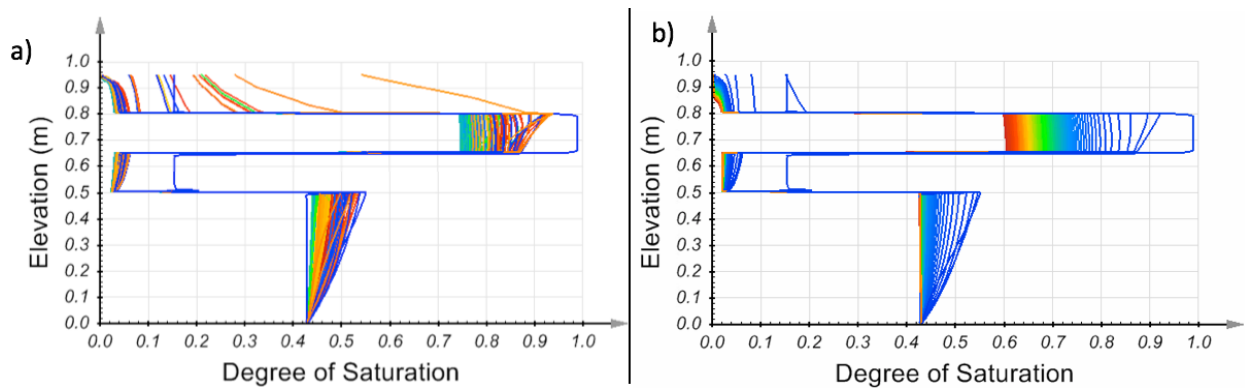


Figure 6-33. Comparison of saturation profiles for CRM biosolids CBC with -20m constant head boundary at the base of the pre-oxidized tailings. Precipitation applied (a) compared to extreme drying conditions (b).

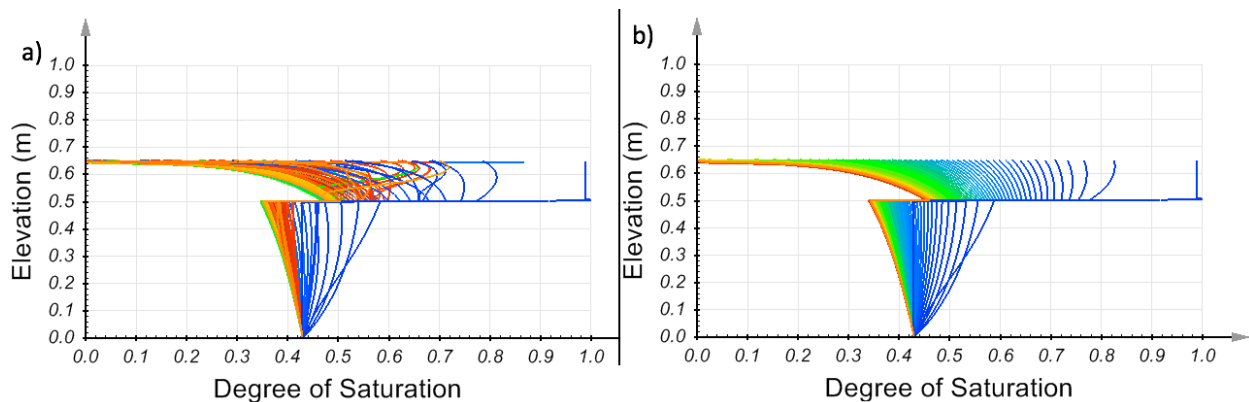


Figure 6-34. Comparison of saturation profiles for CRM monolayer covers with -20m constant head boundary at the base of the pre-oxidized tailings. Precipitation applied (a) compared to extreme drying conditions (b).

6.1.5.3 Model Input Sensitivity

Modelling results indicate that the initial water content and negative pore water pressure of the sand and tailings within the columns have little effect on the volumetric water content and negative pore water pressure profiles within the columns following the first few days of testing (similar behaviour between columns is observed between 1-7 days after initiation depending on the column configuration). Identical saturation profiles and boundary flux results are observed in the later stages of modelling regardless of whether the sand and tailings were initially saturated or desaturated. It can therefore be inferred that cover construction might be carried out following a period of drying and decanting without significantly affecting the cover effectiveness.

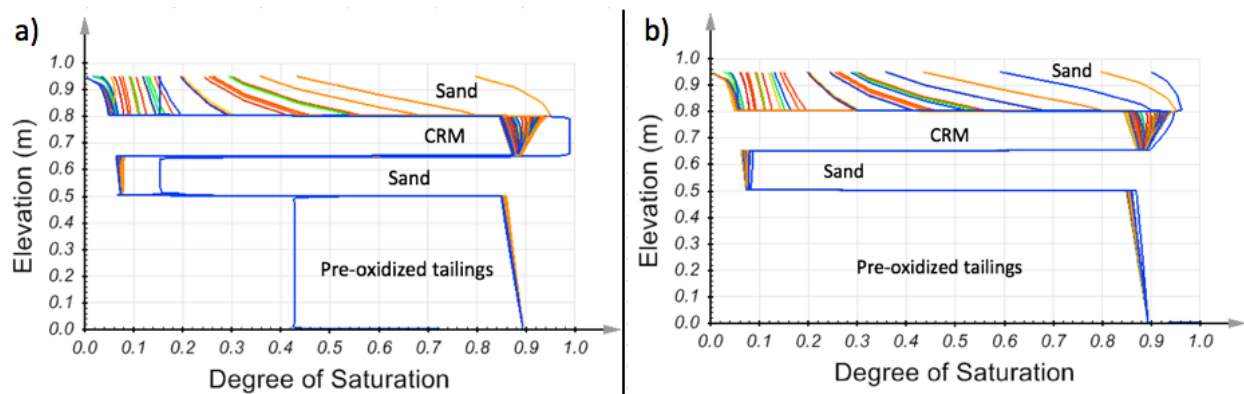


Figure 6-35. Saturation profile of CBC covers with identical inputs (-2m constant head boundary at base), with the exception of initial saturation conditions. Unsaturated (a) compared to initial Fully Saturated (b) conditions.

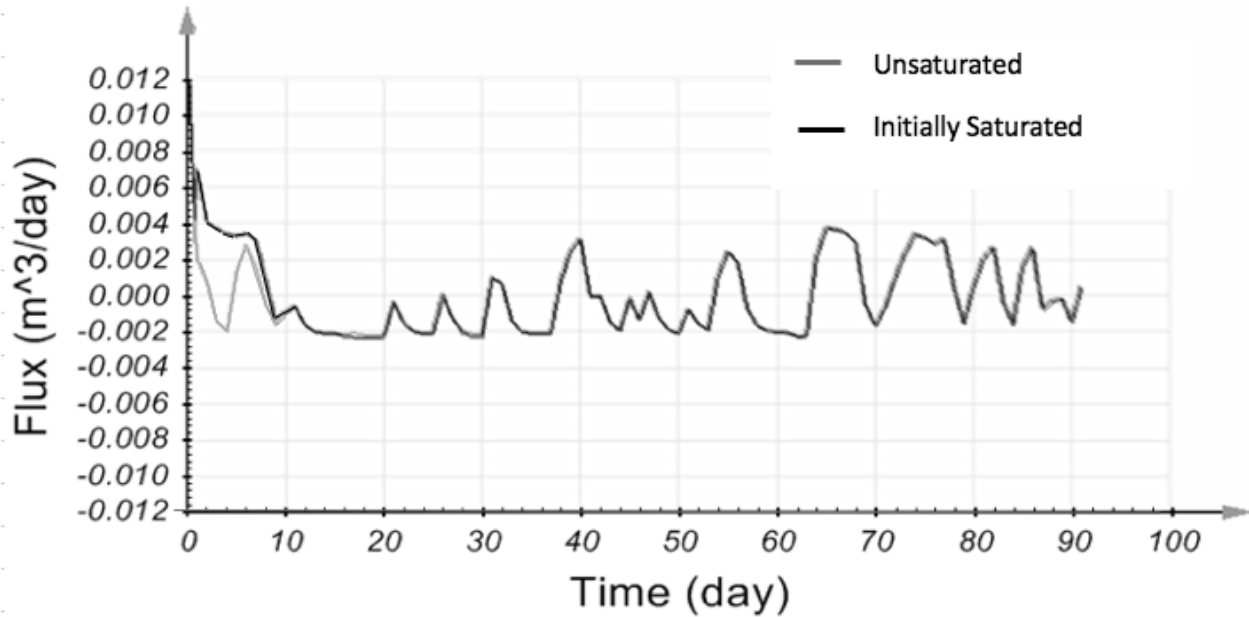


Figure 6-36. Flux at the tailings interface for identical CBC covers (-2m constant head boundary at base of tailings) with unsaturated initial conditions and fully saturated initial conditions.

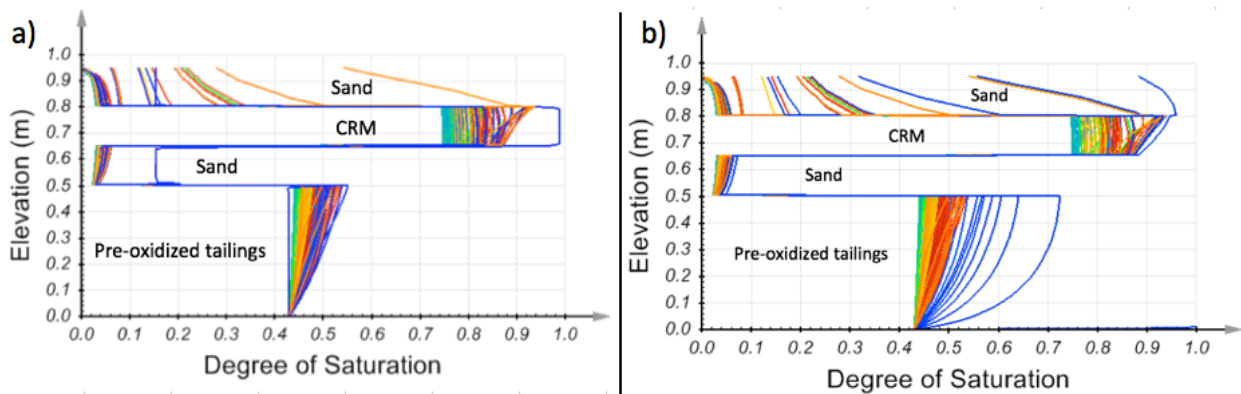


Figure 6-37. Saturation profile of CBC covers with identical inputs (-20m constant head boundary at base), with the exception of initial saturation conditions. Unsaturated (a) compared to initial Fully Saturated (b) conditions.

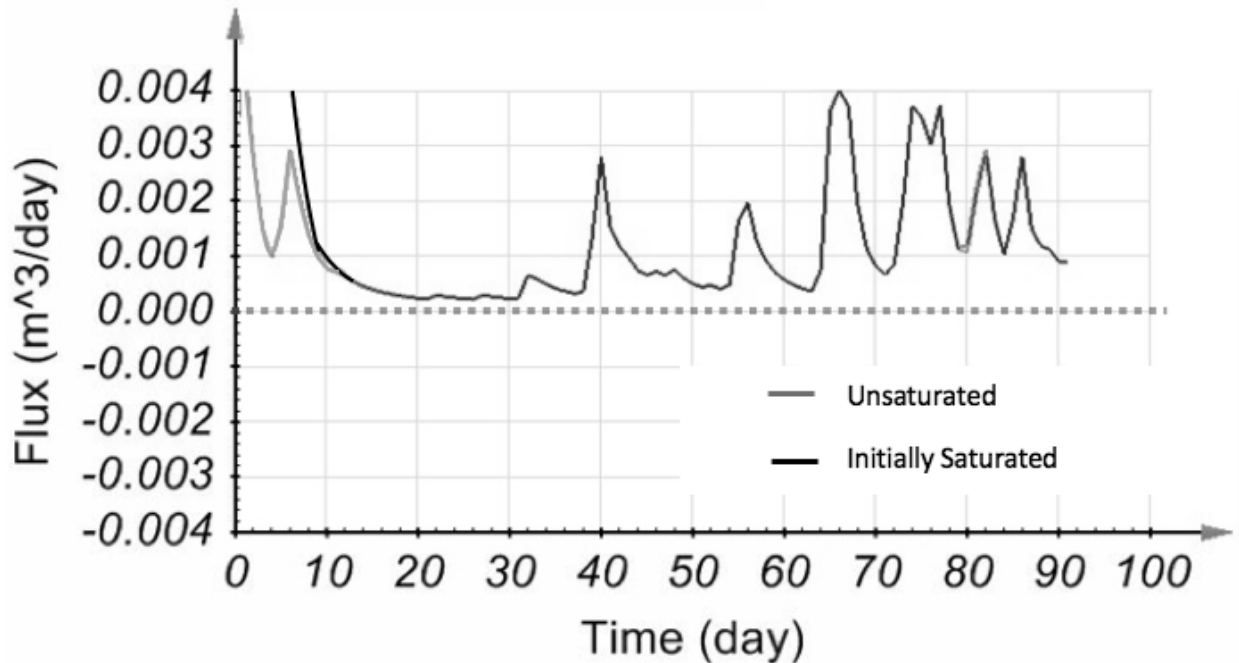


Figure 6-38. Flux at the tailings interface for identical CBC covers (-20m constant head boundary at base of tailings) with unsaturated initial conditions and fully saturated initial conditions

As shown in Figure 6-35, Figure 6-36, Figure 6-37 and Figure 6-38, the initial saturation conditions have no observable effect on the saturation profile and flux observed within the covers after 10 days.

Models were run with both pre-oxidized and unoxidized tailings. It was observed that saturation profiles within the biosolids layers varied only slightly when using different tailings. Only the tailings displayed different levels of saturation throughout modelling; the sand and biosolids appeared largely unaffected. Water flux at the tailings surface was nearly identical for both modelled tailings types with the exception of monolayer covers subjected to large negative constant head boundaries as shown in Figure 6-39. These results indicate that the covers perform similarly over top of both tailings types.

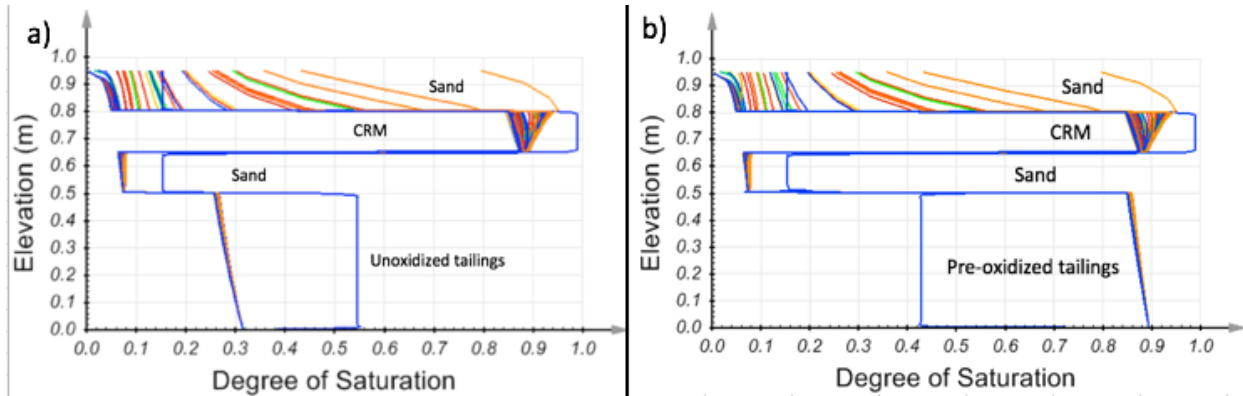


Figure 6-39. Comparison of CBC saturation profiles with unoxidized tailings (a) and pre-oxidized tailings (b) with a -2m constant head boundary at the base of the tailings

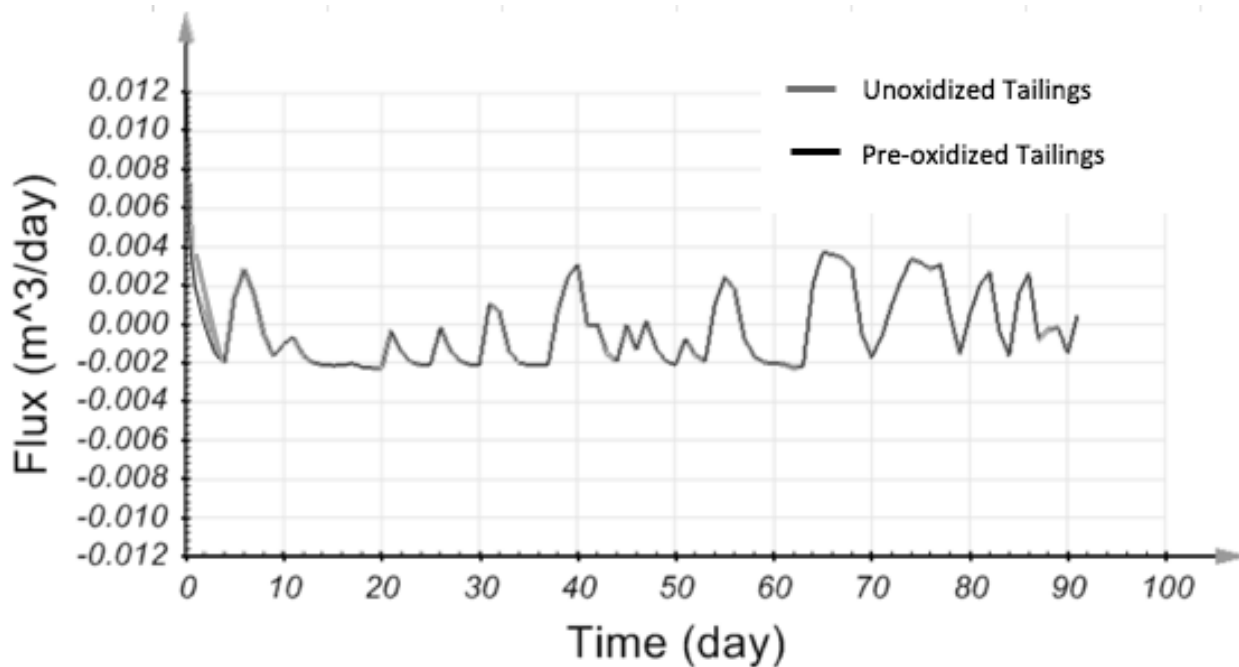


Figure 6-40. Flux at the tailings interface in a CBC cover with CRM biosolids and a -2m constant head boundary at the tailings base

Where boundary conditions are present to control the desaturation of the tailings materials and the water flux at material boundaries, the difference between tailings types is minimal. These results differ from those in Section 5.2.1 and the modelled column tests in Section 6.1.4.1.1 where a no-flux boundary condition is present.

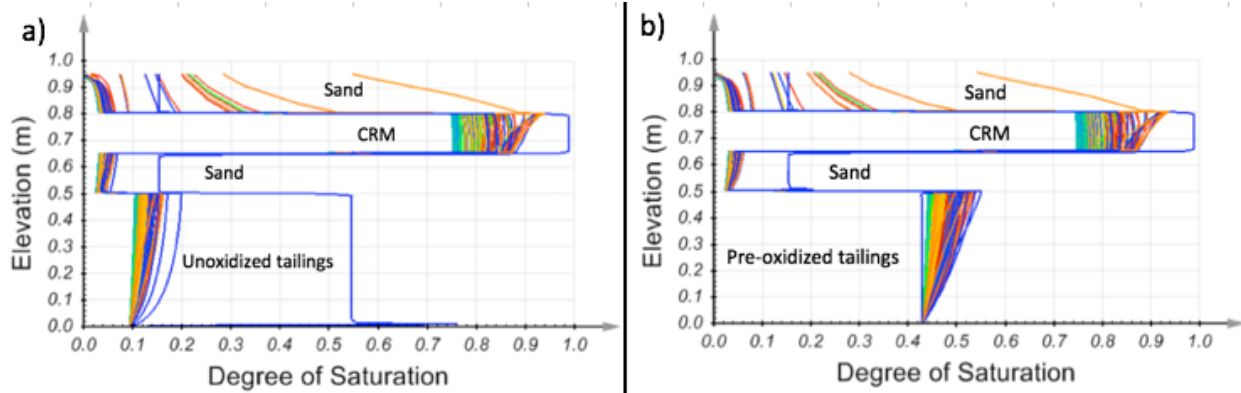


Figure 6-41. Comparison of saturation profiles of CBCs using CRM biosolids with a -20m constant head boundary at the base of the tailings layer

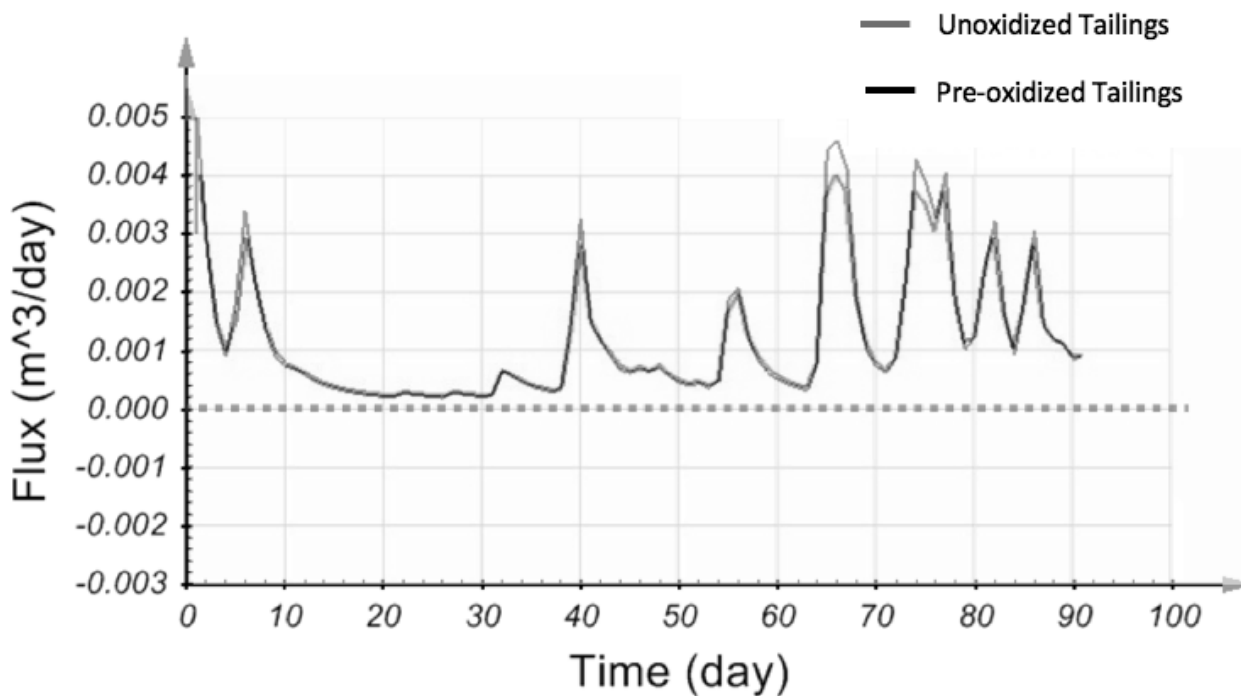


Figure 6-42. Water flux at the tailings interface of CBCs using CRM biosolids with a -20m constant head boundary with covers placed over pre-oxidized and unoxidized tailings

When a highly negative boundary condition is applied at the base of the tailings in the capillary barrier cover models with different tailings types, the degree of saturation within the biosolids barrier is unchanged, however, the flux at the tailings interface is slightly elevated in the coarser unoxidized tailings (+ 10% at peak flux).

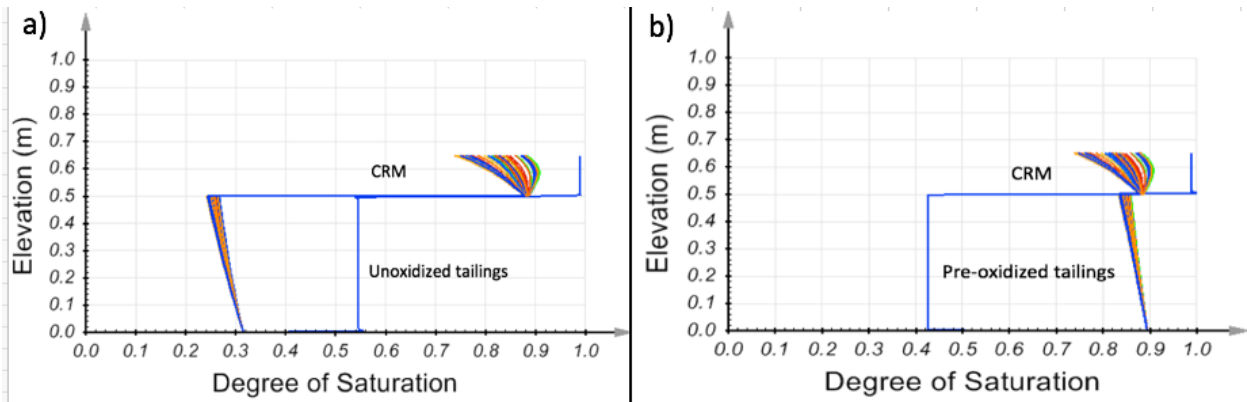


Figure 6-43. Comparison of saturation profiles of monolayer covers using CRM biosolids with a -2m constant head boundary at the base of the tailings layer

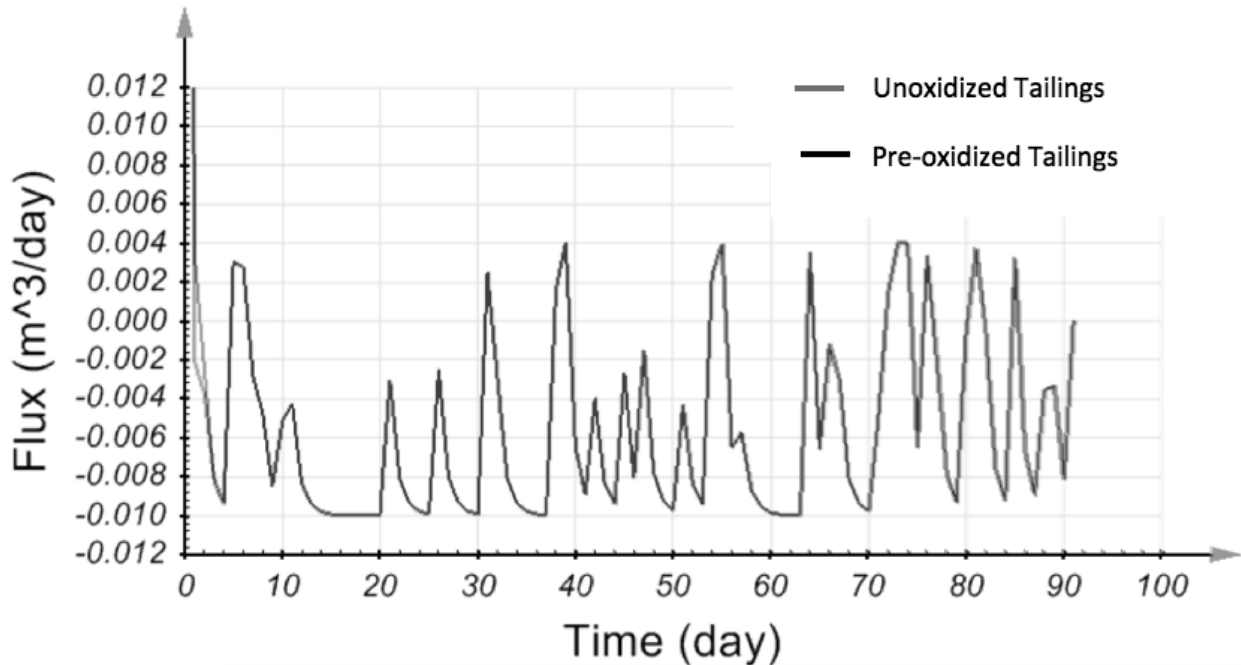


Figure 6-44. Comparison of water flux at the tailings interface when using a monolayer CRM cover with a -2m constant head boundary at the base of the tailings

With low applied suctions at the base of the tailings, the saturation profiles of the biosolids cover and flux at the tailings interface are virtually identical regardless of the type of tailings over which the monolayer is created. SV-Flux model results are shown in Figure 6-43 and Figure 6-44.

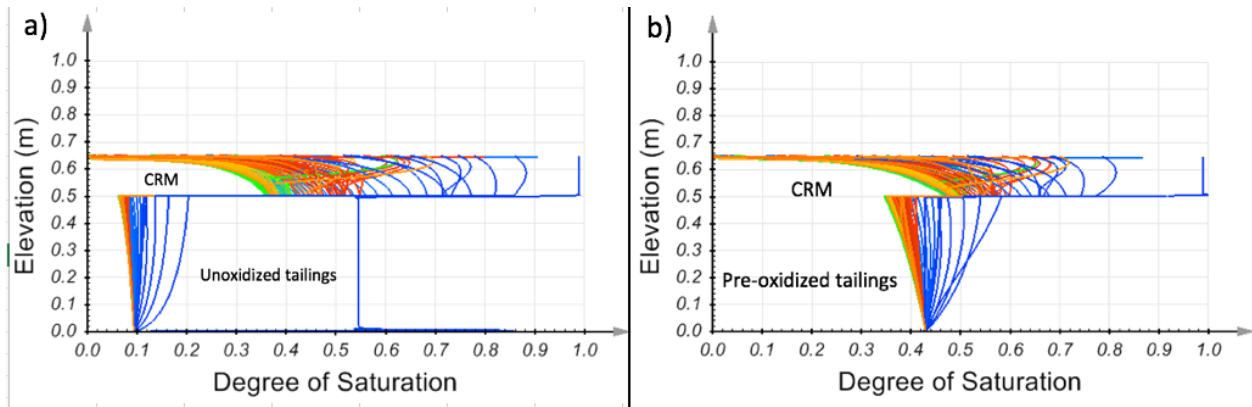


Figure 6-45. Comparison of saturation profiles of monolayer covers using CRM biosolids with a -20m constant head boundary at the base of the tailings layer

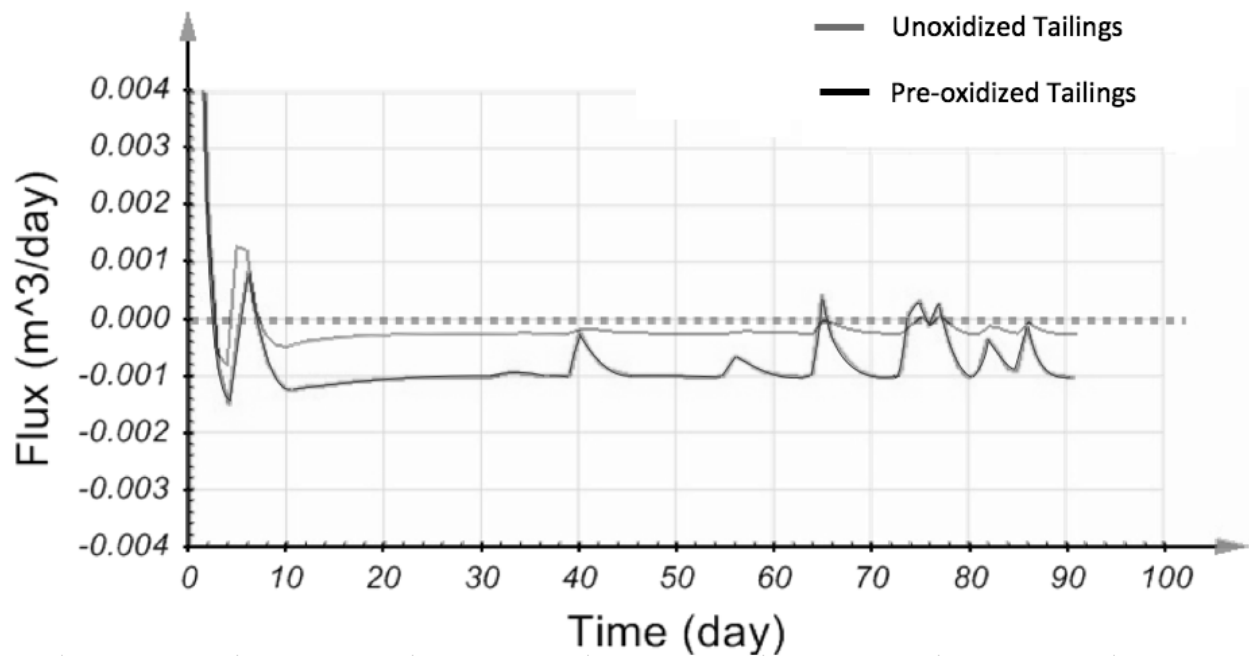


Figure 6-46. Comparison of flux at the tailings interface for monolayer cover over unoxidized and pre-oxidized tailings using CRM biosolids with a -20m constant head boundary at the base of the tailings

Similar to the results of modelling biosolids CBCs above different tailings types, with high levels of suction applied by boundary conditions, the biosolids monolayer over the coarser unoxidized tailings desaturates to a greater degree than the monolayer placed over the finer pre-oxidized tailings as seen in Figure 6-45. Additionally, Figure 6-46 shows the increased upwards flux of water into the biosolids from the tailings in the monolayer overlying the pre-oxidized tailings.

The results from Section 6.1.5.3 indicate that capillary barrier covers made with municipal biosolids may provide effective reduction in flux at the tailings interface and in maintaining a saturated oxygen diffusion barrier layer. It is worth noting that the unoxidized tailings desaturate in the laboratory columns and the numerical models. This is not attributed to the oxidation state of the tailings, but rather to the soil particle size and water retention properties. The desaturation of the tailings may lead to oxidation as some oxygen becomes available via transport through the cover, or in a field scenario, by lateral ingress from any cover perforations in the surrounding area. This reduced level of oxidation can be avoided by practitioners designing covers over top of suitably fine tailings which will maintain saturation, or by combining the biosolids CBC with an elevated water table. In this project the unoxidized tailings had to be sampled relatively close to the deposition spigot, resulting in very coarse tailings due to grain size segregation, and these may not be representative of the size of unoxidized reactive tailings throughout the entirety of the tailings area, or more importantly, of unoxidized reactive tailings at other operations worldwide.

The results from SV-Flux modelling using different cover configurations and materials indicate that capillary barriers constructed with Custom Reclamation Mix biosolids present the greatest ability to maintain saturation within the cover layers, and to reduce water flux at the tailings interface.

Chapter 7 : Summary and Conclusions

7.1 Summary

Laboratory studies and numerical modelling indicate that municipal biosolids exhibit the necessary properties for use in capillary barrier covers to reduce reactive tailings oxidation and subsequent acid rock drainage.

7.2 Characterization

Characterization tests have shown that municipal biosolids, and municipal biosolids amended with leaf and yard waste show high potential for use as materials in capillary barrier covers. The biosolids materials exhibit low hydraulic conductivity (4.21×10^{-7} m/s) and good water retention properties as determined by establishment of the biosolids soil water characteristic curve.

7.3 Column Tests

7.3.1 Saturation and water flux

Laboratory column testing showed the successful establishment of a capillary barrier using municipal biosolids to cover both coarse and fine mine tailings. The biosolids layers were shown to remain almost fully saturated throughout extensive drying periods of 34 and 90 days without precipitation. The biosolids layers were also found to significantly limit water flux during flushing, where water was ponded on the surface of the columns for 16 days.

Deconstruction of the columns revealed the formation of a substantial crust at the surface of the biosolids within the monolayer cover, and the accumulation of salts near the biosolids surface.

7.3.2 Pore water analysis

Pore water analysis shows a reduction in nutrient transport at the tailings interface when employing a capillary barrier cover compared to a monolayer cover. In particular, nitrates were found to be present at the surface of the tailings in the monolayer column, and were not observed in high concentrations in the capillary barrier columns. Leaching of potassium and sodium were also observed in the monolayer column at the tailings/biosolids interface, while increases in potassium and sodium concentrations were measured in the biosolids in all three columns. The biosolids and

sand capillary barrier acts as intended to reduce flux through the desaturated sand layer and limit water flux, and solute transport through to the underlying tailings.

A significant change in pH within the tailings profiles was not observed in any of the columns, however, the time period over which testing was conducted was relatively short.

7.4 Modelling

Modelling results show that the water flux at the tailings interface was found to be greatly reduced when applying biosolids in both monolayer and capillary barrier cover configurations. Modelled capillary barrier covers were shown to reduce flux at the tailings interface by 98% under identical climate and precipitation conditions compared to uncovered tailings. The capillary barrier covers reduced water flux at the tailings interface by 300% relative to monolayer biosolids covers and covers without a desaturated sand layer underlying the biosolids. Modelled capillary barrier covers outperformed monolayer covers with respect to the retention of water within the oxygen barrier layer (biosolids). Additionally, modelling results indicate that the Custom Reclamation Mix biosolids outperform the straight biosolids (Toronto Amendment) in reducing water flux at the tailings interface, and in maintaining a saturated oxygen diffusion barrier layer.

6.5 Other Findings

Other findings of interest throughout the testing period include the relative stability of the biosolids over the course of the testing period. The Custom Reclamation Mix biosolids did not exhibit a significant change in hydraulic conductivity over a 15-month aging period, and the soil-water characteristic curve for the aged material was nearly identical to the original samples.

Chapter 8 : Recommendations for Future Work

As this was the first test of municipal biosolids in capillary barrier covers, there were several avenues for research which were not explored, but which could have significant impact on the long-term viability biosolids CBCs. Additionally, further research may shed light on additional uses for biosolids and residuals products.

With respect to changing material properties, the study of any of the following mechanisms would be of great use in understanding the long-term suitability of biosolids for use in engineering applications:

- Improvement in sensor function within biosolids materials to obtain water content and suction readings without interference from dissolved salts and metals.
- Examination of freeze-thaw behaviour of biosolids materials with a particular emphasis on the water retention properties and hydraulic conductivity would provide a vastly improved understanding of how biosolids CBCs would perform over multiple seasons in a variable climate.
- Investigation of the hysteresis of biosolids materials SWCC would provide insight into the sustainability of cover function through drying and wetting cycles, as well as the effects of deformation on the biosolids SWCC.
- Long-term composting effects on SWCC and cover function of municipal biosolids. Organic degradation of the biosolids materials may have significant effect on performance in the long-term. The oxygen consumption during the aerobic stages of biosolids composting may be worth investigating as this mechanism may help to further reduce oxygen flux through to the underlying tailings; this process may also be finite in duration as biosolids undergo structural and biological change.

The use of biosolids in reclamation of mine impacted sites is still relatively new; the possibilities for future research are abundant and exciting.

References

- Abedi-Koupai, J., & Mehdizadeh, H. (2008). Estimation of osmotic suction from electrical conductivity and water content measurements in unsaturated soils. *Geotechnical Testing Journal*, 31(2), 142–148. <https://doi.org/10.1520/GTJ100322>
- Ahn, J. S., Chon, C. M., Moon, H. S., & Kim, K. W. (2003). Arsenic removal using steel manufacturing byproducts as permeable reactive materials in mine tailing containment systems. *Water Research*, 37(10), 2478–2488. [https://doi.org/10.1016/S0043-1354\(02\)00637-1](https://doi.org/10.1016/S0043-1354(02)00637-1)
- Al, T. A., & Blowes, D. W. (1995). *A GEOCHEMICAL, HYDROGEOLOGICAL AND HYDROLOGICAL STUDY OF THE TAILINGS IMPOUNDMENT AT THE FALCONBRIDGE LIMITED, KIDD CREEK DIVISION METALLURGICAL SITE, TIMMINS, ONTARIO.*
- ASTM. (2017a). ASTM D6836-16: Standard Test Methods for Determination of the Soil Water Characteristic Curve for Desorption Using a Hanging Column , Pressure Extractor , Chilled Mirror Hygrometer , and / or Centrifuge. West Conshohocken, PA: ASTM International. <https://doi.org/10.1520/D6836-02R08E02.characteristic>
- ASTM. (2017b). ASTM D7928 – 17 : Standard Test Method for Particle-Size Distribution (Gradation) of Fine-Grained Soils Using the Sedimentation (Hydrometer) Analysis. *American Standard Test Methods*. <https://doi.org/10.1520/D7928-17>
- ASTM. (2018). ASTM D5298-16 Standard test method for measurement of soil potential (suction) using filter paper. West Conshohocken, PA: ASTM International. <https://doi.org/10.1520/D5298-16.2>
- Aubertin, M., Bussière, B., Pabst, T., James, M., & Mbonimpa, M. (2016). Review of the Reclamation Techniques for Acid-Generating Mine Wastes upon Closure of Disposal Sites. In *Geo-Chicago 2016* (pp. 1–16). Chicago, United States: American Society of Civil Engineers. <https://doi.org/10.1061/9780784480137.034>
- Awoh, A. S., Mbonimpa, M., & Bussiere, B. (2014). Laboratory Study of Highly Pyritic Tailings Submerged Beneath a Water Cover Under Various Hydrodynamic Conditions. *Mine Water Environ*, 33, 241–255. <https://doi.org/10.1007/s10230-014-0264-x>
- Azam, S., & Li, Q. (2010). Tailings dam failures: A review of the last one hundred years. *Geotechnical News*, 28(4), 50–53.
- Bear, J. (1972). *Dynamics of Fluids in Porous Media*. Haifa, Israel: American Elsevier Publishing Company.
- Beauchemin, S., Clemente, J. S., Mackinnon, T., Tisch, B., Lastra, R., Smith, D., & Kwong, J. (2014). Metal Leaching in Mine Tailings: Short-Term Impact of Biochar and Wood Ash Amendments, 275–285. <https://doi.org/10.2134/jeq2014.04.0195>

- Bianchi, M., Assumpção, M., Schimmel, M., Collaço, B., Ciardelli, C., Barbosa, J. R., & Calhau, J. (2016). The tailings dam failure of 5 November 2015 in SE Brazil and its preceding seismic sequence. *Geophysical Research Letters*, 4929–4936. <https://doi.org/10.1002/2016GL069257>. Received
- Blight, G. E., & Bentel, G. M. (1983). The behaviour of mine tailings during hydraulic deposition. *Journal of The South African Institute of Mining and Metallurgy*, (APRIL), 73–86.
- Blowes, D. W., & Jambor, J. L. (1990). The pore-water geochemistry and the mineralogy of the vadose zone. *Applied Geochemistry*, 5, 327–346. [https://doi.org/10.1016/0883-2927\(90\)90008-S](https://doi.org/10.1016/0883-2927(90)90008-S)
- Brooks, R. H., & Corey, a T. (1964). Hydraulic properties of porous media. *Hydrology Papers, Colorado State University. Fort Collins CO*, 3(3), 27 pgs. <https://doi.org/citeulike-article-id:711012>
- Buckingham, E. (1907). *Studies on the Movement of Soil Moisture. Bureau of Soils---Bulletin No. 38*. <https://doi.org/10.1017/CBO9781107415324.004>
- Bussière, B., & Aubertin, M. (2016). Development and Application of Mine Site Reclamation Methods to Control Acid Generation in Canada. In *West Virginia Mine Drainage Task Force Symposium*.
- Campbell, C. S., Campbell, G. S., Cobos, D. R., & Bissey, L. L. (2009). Calibration and evaluation of an improved low-cost soil moisture sensor. *Available At: Http://Www.Decagon.Com/Education/Calibration-and-Evaluation-of-an-Improved-Low-Cost-Soil-Moisture-Sensor-13492-01-An/*. Pullman, WA: Decagon Devices.
- Campbell, C. S., & Decagon Devices. (2001). *Calibrating ECH2O Soil Moisture Probes*. Pullman, WA: Decagon Devices.
- Carman, P. C. (1937). FLUID FLOW THROUGH GRANULAR BEDS *. *Transactions - Institution of Chemical Engineers*, 15. [https://doi.org/10.1016/S0263-8762\(97\)80003-2](https://doi.org/10.1016/S0263-8762(97)80003-2)
- Chalkley, M. E. (1989). Tailings and Effluent Management : proceedings of the International Symposium on Tailings and Effluent Management, Halifax, August 20-24, 1989. In B. R. Conard, V. I. Lakshmanan, & K. G. (eds. . Wheeland (Eds.), *Hydrometallurgy Section of the Metallurgical Society of CIM* (p. 336). Halifax, NS: Pergamon Press.
- Choo, L.-P. (1996). *Evaluation of Water Flow in Unsaturated Soils for Multi-Layered Mine Waste Covers*. University of Western Ontario.
- Cravotta, C. A. (1998). Effect of sewage sludge on formation of acidic ground water at a reclaimed coal mine. *Ground Water*. <https://doi.org/10.1111/j.1745-6584.1998.tb01061.x>
- Cronney, D., & Coleman, J. D. (1954). SOIL STRUCTURE IN RELATION TO SOIL SUCTION. *Journal of Soil Science*, 5(1), 75–84. <https://doi.org/10.1111/j.1365->

- Darcy, H. (1856). *Les Fontaines Publiques de La Ville de Dijon*. (V. Dalmont, Ed.). Paris: Libraire des Corps Imperiaux des Ponts et Chaussees et des Mines. Retrieved from https://books.googleusercontent.com/books/content?req=AKW5QadJUCFwfVxTZYpP7wXihAFC_P_URY7h4v66oRBglSGVkoj7ODpfPLfII74ygXyRvxABPWkR1a7GprgufPLewdmITDxFVrSBQDm27DzzVPfajlA61ElniR5rjihVjVhBmkeaHhRKcNM7gTifOkkYJ8XhWXCAwDnRhflECcUzd2ji5--wvrm06ovfX0FavzCka8ckq
- Das, B. (2008). *Advanced Soil Mechanics* (3rd ed.). New York: Taylor & Francis.
- Das, B., & Sivakugan, N. (2017). *Fundamentals of Geotechnical Engineering* (Fifth). Boston, MA: Cengage Learning.
- DeSisto, S. L., Jamieson, H. E., & Parsons, M. B. (2017). *Arsenic mobility in weathered gold mine tailings under a low-organic soil cover*. *Environmental Earth Sciences* (Vol. 76). Springer Berlin Heidelberg. <https://doi.org/10.1007/s12665-017-7041-7>
- Dobchuk, B., Nichol, C., Ward Wilson, G., & Aubertin, M. (2013). Evaluation of a single-layer desulphurized tailings cover. *Canadian Geotechnical Journal*, (50), 777–792.
- Duffy, D., Garg, S., Washer, C., Grammatikopoulos, T., & Papangelakis, V. G. (2015). Mineralogical characterization of Sudbury pyrrhotite tailings: evaluating the bioleaching potential. *Conference of Metallurgists Hosting America's Conference on Aluminum Alloys*, (July 2016), 315–329.
- Edlefsen, N. E., & Anderson, A. B. C. (1943). Thermodynamics of soil moisture. *Journal of Agricultural Science Published by The California Agricultural Experiment Station*, 15(2), 31–298. <https://doi.org/10.3733/hilg.v15n02p031>
- Elberling, B., Nicholson, R. V., Reardon, E. J., & Tibble, R. (1994). Evaluation of sulphide oxidation rates: a laboratory study comparing oxygen fluxes and rates of oxidation product release. *Canadian Geotechnical Journal*, 31(3), 375–383. <https://doi.org/10.1139/t94-045>
- Fernandes, F., Lopes, D. D., Andreoli, C. V., & da Silva, S. M. C. P. (2007). *Biological Wastewater Treatment Vol.6: Sludge Treatment and Disposal*. (C. v. Andreoli, M. von Sperling, & F. Fernandes, Eds.), *Sludge treatment and disposal*. London: IWA Publishing. <https://doi.org/10.1016/B978-1-85617-705-4.00021-6>
- Forsberg, L. S., & Ledin, S. (2006). Effects of sewage sludge on pH and plant availability of metals in oxidising sulphide mine tailings. *Science of the Total Environment*, 358(1–3), 21–35. <https://doi.org/10.1016/j.scitotenv.2005.05.038>
- Fowler, T. A., Holmes, P. R., & Crundwell, F. K. (1999). Mechanism of pyrite dissolution in the presence of *Thiobacillus ferrooxidans*. *Applied and Environmental Microbiology*, 65(7), 2987–2993. <https://doi.org/10.1016/j.jnuemat.2005.06.023>
- Fredlund, D. G., & Houston, S. L. (2013). Interpretation of soil-water characteristic curves when

- volume change occurs as soil suction is changed. *Advances in Unsaturated Soils, c*, 15–31. <https://doi.org/doi:10.1201/b14393-410.1201/b14393-4>
- Fredlund, D. G., Rahardjo, H., & Fredlund, M. D. (2012). *Unsaturated Soil Mechanics in Engineering Practice*. Hoboken, NJ, USA: John Wiley & Sons, Inc. <https://doi.org/10.1002/9781118280492>
- Fredlund, D. G., & Xing, A. (1994). Equations for the soil-water characteristic curve. *Canadian Geotechnical Journal*, 31(6), 1026–1026. <https://doi.org/10.1139/t94-120>
- Fredlund, D. G., Xing, A., & Huang, S. (1994). Predicting the permeability function for unsaturated soils using the soil-water characteristic curve. *Canadian Geotechnical Journal*, 31(4), 533–546. <https://doi.org/10.1139/t94-062>
- Fredlund, M. D., Tran, D. T. Q., & Fedlund, D. G. (2015). The calculation of actual evaporation from an unsaturated soil surface. In A. Brown (Ed.), *10th International Conference on Acid Rock Drainage & IMWA Annual Conference* (pp. 1–13). Santiago, Chile: Mine Environment Neutral Drainage (MEND).
- Gambrell, R. P., Wiesepape, J. B., Patrick, W. H., & Duff, M. C. (1991). The effects of pH, redox, and salinity on metal release from a contaminated sediment. *Water, Air, and Soil Pollution*, 57–58(1), 359–367. <https://doi.org/10.1007/BF00282899>
- Garnder, W. (2013). *Copper Mine Tailings Reclamation With Biosolids*.
- GCTS. (2014). SWC-150 Fredlund SWCC Device User Manual. Tempe, AZ: GCTS Testing Systems.
- Government of Canada. (2018). Station Results - Historical Data - Climate - Environment and Climate Change Canada. Retrieved August 16, 2018, from http://climate.weather.gc.ca/historical_data/search_historic_data_stations_e.html?searchType=stnProv&timeframe=1&lstProvince=ON&optLimit=yearRange&StartYear=1990&EndYear=2017&Year=1996&Month=8&Day=30&selRowPerPage=25&txtCentralLatMin=0&txtCentralLatSec=0&
- Hatch Mott MacDonald Group. (2010). *Mid Halton Wastewater (Sewage) Treatment Plant Phase IV & V Expansion Class Environmental Assessment Table of Contents*. Burlington.
- Hazen, A. (1893). *Some physical properties of sand and gravels, with special reference to their use in filtration*.
- Heidarian, P. (2012). *Effect of initial water content and stress history on water-retention behaviour of mine tailings*.
- Hillel, D. (2004). *Introduction to Environmental Soil Physics*. Amsterdam: Academic Press.
- Hulshof, A. H. M., Blowes, D. W., & Douglas Gould, W. (2006). Evaluation of in situ layers for treatment of acid mine drainage: A field comparison. *Water Research*, 40(9), 1816–1826.

<https://doi.org/10.1016/j.watres.2006.03.003>

- Independent Expert Engineering Investigation and Review Panel. (2015). Report on Mount Polley Tailings Storage Facility Breach, 1–147. Retrieved from <https://www.mountpolleyreviewpanel.ca/final-report>
- Johnson, R. H., Blowes, D. W., Robertson, W. D., & Jambor, J. L. (2000). The hydrogeochemistry of the Nickel Rim mine tailings impoundment, Sudbury, Ontario. *Journal of Contaminant Hydrology*, 41(1–2), 49–80. [https://doi.org/10.1016/S0169-7722\(99\)00068-6](https://doi.org/10.1016/S0169-7722(99)00068-6)
- Jones, P. H. (1978). Wastewater Treatment Technology. Toronto: Institute for Environmental Studies, University of Toronto.
- Kimball, B. A., & Lemon, E. R. (1970). *EFFECTS OF AIR TURBULENCE UPON GAS EXCHANGE FROM SOIL*. Cornell University.
- Krumbein, W. C. (1937). Size frequency distribution of sediments. *Journal of Sedimentary Petrology*, 7(1), 3–17.
- Lewis, E. L. (1980). The Practical Salinity Scale 1978 and Its Antecedents. *IEEE Journal of Oceanic Engineering*, 5(1), 3–8. <https://doi.org/10.1109/JOE.1980.1145448>
- Lipinski, M. J., & Golebiewska, A. (2000). A study of granulation distribution in a beach of tailings dam. In J. D. Nelson, D. Cave, & W. A. Cincilla (Eds.), *Tailings and Mine Waste '00* (pp. 159–168). Fort Collins, Colorado: A.A. Balkema. <https://doi.org/9789058091260>
- Little, L., Mainza, A. N., Becker, M., & Wiese, J. G. (2016). Using mineralogical and particle shape analysis to investigate enhanced mineral liberation through phase boundary fracture. *Powder Technology*, 301, 794–804. <https://doi.org/10.1016/j.powtec.2016.06.052>
- López-Vázquez, C. M., Hooijmans, C. M., Brdjanovic, D., Gijzen, H. J., & van Loosdrecht, M. C. M. (2008). Factors affecting the microbial populations at full-scale enhanced biological phosphorus removal (EBPR) wastewater treatment plants in The Netherlands. *Water Research*, 42(10–11), 2349–2360. <https://doi.org/10.1016/j.watres.2008.01.001>
- Lottermoser, B. (2007). *Mine Wastes. Mine Wastes (Second Edition): Characterization, Treatment and Environmental Impacts* (Second). Berlin: Springer. <https://doi.org/10.1007/978-3-540-48630-5>
- Mao, Y., Pham, A. N., Rose, A. L., & Waite, T. D. (2011). Influence of phosphate on the oxidation kinetics of nanomolar Fe (II) in aqueous solution at circumneutral pH, 75, 4601–4610. <https://doi.org/10.1016/j.gca.2011.05.031>
- Maqsood, A., Bussière, B., Aubertin, M., Chouteau, M., & Mbonimpa, M. (2011). Field investigation of a suction break designed to control slope-induced desaturation in an oxygen barrier. *Canadian Geotechnical Journal*, 48(1), 53–71. <https://doi.org/10.1139/T10-045>

- Marinho, F. A. M., Take, W. A., & Tarantino, A. (2008). Measurement of Matric Suction Using Tensiometric and Axis Translation Techniques. *Geotechnical and Geological Engineering*, 26(6), 615–631. <https://doi.org/10.1007/s10706-008-9194-3>
- McGregor, R. G., Blowes, D. W., Jambor, J. L., & Robertson, W. D. (1998). The solid-phase controls on the mobility of heavy metals at the Copper Cliff Tailings Area, Sudbury, Ontario, Canada. *Journal of Contaminant Hydrology*, 33(3–4), 247–271. [https://doi.org/10.1016/S0169-7722\(98\)00060-6](https://doi.org/10.1016/S0169-7722(98)00060-6)
- Metcalf & Eddy, Tchobanoglous, G., Stensel, D., Tsuchihashi, R., & Burton, F. (2014). *Wastewater Engineering: Treatment and Resource Recovery* (5th ed.). New York: McGraw-Hill Education.
- Meter group. (2018). *WP4C Dew Point Potential Meter Operators manual*. Retrieved from www.metergroup.com
- METER Group. (2017). Teros 21 User Manual. Pullman, WA.
- Metso. (2015). *Basics in minerals processing*.
- Miller, D., & Nelson, J. (2006). Osmotic Suction in Unsaturated Soil Mechanics. In G. Miller, C. Zapata, S. Houston, & D. Fredlund (Eds.), *Unsaturated Soils 2006* (pp. 2186–2197). Carefree, Arizona: American Society of Civil Engineers. <https://doi.org/9780784408025>
- Minerals and metals facts | Natural Resources Canada. (n.d.). Retrieved March 11, 2018, from <http://www.nrcan.gc.ca/mining-materials/facts/20507>
- Monteith, J. L. (1965). Evaporation and environment. In *Symposia of the Society for Experimental Biology* (Vol. 19, pp. 205–234). Cambridge, England: University Press, Cambridge. <https://doi.org/10.1613/jair.301>
- Moses, C. O., Kirk Nordstrom, D., Herman, J. S., & Mills, A. L. (1987). Aqueous pyrite oxidation by dissolved oxygen and by ferric iron. *Geochimica et Cosmochimica Acta*, 51(6), 1561–1571. [https://doi.org/10.1016/0016-7037\(87\)90337-1](https://doi.org/10.1016/0016-7037(87)90337-1)
- Nagaraj, D. R. (2005). Minerals Recovery and Processing. In *Kirk-Othmer Encyclopedia of Chemical Technology* (pp. 595–668). Hoboken, NJ, USA: John Wiley & Sons, Inc. <https://doi.org/10.1002/0471238961.1309140514010701.a01.pub2>
- Neczaj, E., Fija, K., Grobelak, A., & Grosser, A. (2017). Sewage sludge disposal strategies for sustainable development, 156(January), 39–46. <https://doi.org/10.1016/j.envres.2017.03.010>
- Ng, C. W. W., & Pang, Y. W. (2000). INFLUENCE OF STRESS STATE ON SOIL-WATER CHARACTERISTICS AND SLOPE STABILITY. *Journal of Geotechnical and Geoenvironmental Engineering*, 126(February), 157–166.
- Nicholson, R. V., Gillham, R. W., Cherry, J. A., & Reardon, E. J. (1989). Reduction of acid generation in mine tailings through the use of moisture-retaining cover layers as oxygen

- barriers. *Canadian Geotechnical Journal*, 26(1), 1–8. <https://doi.org/10.1139/t89-001>
- Oleszkiewicz, J. A., & Mavinic, D. S. (2002). Wastewater biosolids: an overview of processing, treatment, and management. *Journal of Environmental Engineering and Science*, 1(2), 75–88. <https://doi.org/10.1139/s02-010>
- Oleszkiewicz, J., Kruk, D. J., Devlin, T., Lashkarizadeh, M., & Yuan, Q. (2015). Options for Improved Nutrient Removal and Recovery from Municipal Wastewater in the Canadian Context. *Environmental Technology*, 20(7)(March), 681–695. Retrieved from <http://www.cwn-rce.ca/assets/resources/pdf/Oleszkiewicz-Nutrients/Oleszkiewicz-KI-Report-March-2015.pdf>
- Paktunc, D. (2013). Mobilization of arsenic from mine tailings through reductive dissolution of goethite influenced by organic cover. *Applied Geochemistry*, 36, 49–56. <https://doi.org/10.1016/j.apgeochem.2013.05.012>
- Penman, H. L. (1948). Natural evaporation from open water, bare soil and grass. *Proceedings of the Royal Society of London. Series A. Mathematical and Physical Sciences*, 193(1032), 120–145.
- Petrucchi, R. H., Herring, F., Maduor, J. D., & Bissonnette, C. (2016). *General Chemistry - Principles and Modern Applications* (11th ed.). Upper Saddle River, N.J.: Pearson.
- Pond, A. P., White, S. A., Milczarek, M., & Thompson, T. L. (2005). Accelerated Weathering of Biosolid-Amended Copper Mine Tailings. *Journal of Environment Quality*, 34(4), 1293. <https://doi.org/10.2134/jeq2004.0405>
- Pourbaix, M., Muylder, J., & Schmets, J. (2009). Pourbaix Diagrams. <https://doi.org/10.1016/B0-08-043152-6/01399-1>
- Rahardjo, H., Santoso, V. A., Leong, E. C., Ng, Y. S., Tam, C. P. H., & Satyanaga, A. (2013). Use of recycled crushed concrete and Secudrain in capillary barriers for slope stabilization. *Canadian Geotechnical Journal*, 50(6), 662–673. <https://doi.org/10.1139/cgj-2012-0035>
- Richards, L. A. (1931). *Capillary Conduction of Liquids Through Porous Mediums*. Cornell University. <https://doi.org/10.1063/1.1745010>
- Richards, L., Allison, L. E., Bernstein, L., Bower, C. A., Brown, J. W., Fireman, M., ... Wilcox, L. V. (1954). *Diagnosis and Improvement of Saline and Alkaline Soils*. (L. A. Richards, Ed.), *Soil Science Society of America Journal* (Vol. 18). Washington, D.C.: United States Department of Agriculture. <https://doi.org/10.2136/sssaj1954.03615995001800030032x>
- Richardson, L. F. (1922). *Weather Prediction by Numerical Process*. Cambridge, England: Cambridge University Press.
- Santibáñez, C., Ginocchio, R., & Teresa Varnero, M. (2007). Evaluation of nitrate leaching from mine tailings amended with biosolids under Mediterranean type climate conditions. *Soil Biology and Biochemistry*, 39(6), 1333–1340. <https://doi.org/10.1016/j.soilbio.2006.12.009>

- Simms, P., Daliri, F., & Sivathayalan, S. (2016). Method-dependent variation of yield stress in a thickened gold tailings explained using a structure based viscosity model. *Minerals Engineering*, 98, 40–48. <https://doi.org/10.1016/j.mineng.2016.07.011>
- Simms, P., Soleimani, S., Mizani, S., Daliri, F., Dunmola, A., Rozina, E., & Innocent-Bernard, T. (2017). Cracking, salinity and evaporation in mesoscale experiments on three types of tailings. *Environmental Geotechnics*, 1–15. <https://doi.org/10.1680/jenge.16.00026>
- Singer, P., & Stumm, W. (1970). Acidic Mine Drainage : The Rate-Determining Step. *American Association for the Advancement Of Science*, 167(3921), 1121–1123.
- Spinosa, L., & Vesilind, P. (2001). *Sludge Into Biosolids: Processing, Disposal, Utilization*. London: IWA Publishing.
- Sridharan, A., & Nagaraj, H. B. (2005). Plastic limit and compaction characteristics of fine-grained soils. *Ground Improvement*, 9(1), 17–22. <https://doi.org/10.1680/grim.9.1.17.58544>
- Terzaghi, K. (1943). *Theoretical Soil Mechanics*. London: Chapman and Hall Limited.
- Tindall, J. A., & Kunkel, J. R. (1998). *Unsaturated Zone Hydrology for Scientists and Engineers* (1st ed.). Upper Saddle River, N.J.: Pearson.
- Tisch, B., Zinck, J., & Vigneault, B. (2008). *GREEN MINES GREEN ENERGY: ESTABLISHING PRODUCTIVE LAND ON MINE TAILINGS*.
- Tischler, J. S., Wiacek, C., Janneck, E., & Schlo, M. (2013). Bench-scale study of the effect of phosphate on an aerobic iron oxidation plant for mine water treatment, 8(0). <https://doi.org/10.1016/j.watres.2013.09.049>
- Topp, G. C., Davis, J. L., & Annan, A. P. (1980). Electromagnetic Determination of Soil Water Content: Measurements in Coaxial Transmission Lines. *Water Resources Research*, 16(3), 574–582. <https://doi.org/10.1029/WR016i003p00574>
- United States Federal Law. Federal Water Pollution Control Act, Public health reports (Washington, D.C. : 1896) § (1962). United States of America. <https://doi.org/10.1111/j.1744-1714.1974.tb00320.x>
- Vanapalli, S. K., Fredlund, D. G., & Pufahl, D. E. (1999). Influence of soil structure and stress history on the soil water characteristics of a compacted till. *Géotechnique*, 49(2), 143–159.
- Verdugo, C., Sánchez, P., Santibáñez, C., Urrestarazu, P., Bustamante, E., Silva, Y., ... Ginocchio, R. (2011). Efficacy of lime, biosolids, and mycorrhiza for the phytostabilization of sulfidic copper tailings in chile: A greenhouse experiment. *International Journal of Phytoremediation*, 13(2), 107–125. <https://doi.org/10.1080/15226510903535056>
- Vick, S. G. (1983). *Planning, design, and analysis of tailings dams*. Vancouver, Canada: BiTech.
- Vigneault, B., & Campbell, P. G. C. (2001). GEOCHEMICAL CHANGES IN SULFIDIC MINE

TAILINGS STORED UNDER A SHALLOW WATER COVER. *Water Resources*, 35(4), 1066–1076.

Villavicencio, G., Espinace, R., Palma, J., Fourie, A., & Valenzuela, P. (2014). Failures of sand tailings dams in a highly seismic country. *Canadian Geotechnical Journal*, 51(4), 449–464. <https://doi.org/10.1139/cgj-2013-0142>

Wang, L., Shammass, N., & Hung, Y.-T. (2007). *Biosolid Treatment Process*. *Journal of Chemical Information and Modeling* (Vol. 53). <https://doi.org/10.1017/CBO9781107415324.004>

Warren, B. L. P., & Church, P. E. (1996). *Comparison of Hydraulic Conductivities for a Sand and Gravel Aquifer in Southeastern Massachusetts, Estimated by Three Methods U. S. Geological Survey Water-Resources Investigations Report 95-4160*. Marlborough, Massachusetts.

Wastewater Systems Effluent Regulations. (2012). Retrieved July 19, 2018, from <http://laws-lois.justice.gc.ca/eng/regulations/SOR-2012-139/FullText.html>

Williams, L. O., Hoyt, D. L., Dwyer, S. F., Hargreaves, G. A., & Zornber. (2011). Design Criteria and Construction of a Capillary Barrier Cover System: The Rocky Mountain Arsenal Experience L.O. In *Geo-Frontiers* (pp. 996–1005).

Wills, B. A., & Finch, J. A. (2015). *Wills' Mineral Processing Technology: An Introduction to the Practical Aspects of Ore Treatment and Mineral Recovery* (8th ed.). Butterworth-Heinemann. Retrieved from <http://proquest.safaribooksonline.com.proxy.library.carleton.ca/book/chemical-engineering/9780080970547/firstchapter#X2ludGVybmFsX0h0bWxWaWV3P3htbGlkPTk3ODAwODA5NzA1NDclMkZzdDAxMTVfaHRtbCZxdWVyeT0=>

Wilson, G. W., Fredlund, D. G., & Barbour, S. L. (1994). Coupled soil-atmosphere modelling for soil evaporation. *Canadian Geotechnical Journal*, 31(2), 151–161. <https://doi.org/10.1139/t94-021>

Wilson, G. W., Fredlund, D. G., & Barbour, S. L. (1997). The effect of soil suction on evaporative fluxes from soil surfaces: Discussion. *Canadian Geotechnical Journal*, 34, 145–155. <https://doi.org/10.1139/t98-034>

Witteman, M. L. (2013). *Unsaturated Flow In Hydrating Porous Media: Application to Cemented Paste Backfill*. Carleton University.

Woysner, M. R., & Yanful, E. K. (1995). Modelling and field measurements of water percolation through an experimental soil cover on mine tailings. *Canadian Geotechnical Journal*, 32(4), 601–609. <https://doi.org/10.1139/t95-062>

Yanful, E. (1994). Oxygen Diffusion through Soil Covers on Sulphidic Mine Tailings. *Journal of Geotechnical Engineering*, 119(8), 1207–1228.

- Yanful, E. K., Bell, A. V., & Woyshner, M. R. (1993). Design Of A Composite Soil Cover For An Experimental Waste Rock Pile Near Newcastle, New-Brunswick, Canada. *Canadian Geotechnical Journal*, 30(4), 578–587. <https://doi.org/10.1139/t93-050>
- Yanful, E. K., & Choo, L.-P. (1997). Measurement of evaporative fluxes from candidate cover soils. *Canadian Geotechnical Journal*, 34(3), 447–459. <https://doi.org/10.1139/t97-002>
- Yanful, E. K., Simms, P. H., Rowe, R. K., & Stratford, G. (1999). Monitoring an experimental soil waste cover near London, Ontario, Canada. *Geotechnical and Geological Engineering*, 17(2), 65–84. <https://doi.org/10.1023/A:1008986103460>
- Yanful, E., & Simms, P. (1997). *REVIEW OF WATER COVER SITES AND RESEARCH PROJECTS*. London.
- Yang, S. X., Liao, B., Yang, Z. H., Chai, L. Y., & Li, J. T. (2016). Revegetation of extremely acid mine soils based on aided phytostabilization: A case study from southern China. *Science of the Total Environment*, 562, 427–434. <https://doi.org/10.1016/j.scitotenv.2016.03.208>

Appendix A – Material Characterization Data and Results

A – 1 : Specific Gravity Test data and Results

| Pycnometer Calibration | | | | | | | |
|------------------------|---------------------|----------------|--------|--------|--------|--------|---------|
| | | Empty Mass (g) | | | | | |
| Pycnometer | Nominal Volume (mL) | 1 | 2 | 3 | 4 | 5 | Average |
| 500mL | 500 | 164.14 | 164.15 | 164.15 | 164.14 | 164.14 | 164.144 |
| 500mL - 1 | 500 | 160.93 | 160.94 | 160.94 | 160.93 | 160.94 | 160.936 |
| 250mL | 250 | 122.29 | 122.29 | 122.29 | 122.29 | 122.29 | 122.29 |
| 201 | 200 | 81.06 | 81.06 | 81.07 | 81.05 | 81.06 | 81.06 |
| 202 | 200 | 92.88 | 92.88 | 92.89 | 92.87 | 92.88 | 92.88 |
| 203 | 200 | 80.07 | 80.07 | 80.07 | 80.06 | 80.06 | 80.066 |
| 1L | 1000 | 257.81 | 257.8 | 257.82 | 257.81 | 257.81 | 257.81 |
| 1L - 1 | 1000 | 249.7 | 249.71 | 249.7 | 249.69 | 249.7 | 249.7 |

| | | Full Mass (g) | | | | | |
|------------|---------------------|---------------|--------------------|--------------------|--------------------|--------------------|--------------------|
| | | 1 | 2 | 3 | 4 | 5 | |
| Pycnometer | Nominal Volume (mL) | Full mass | Post Equilibration |
| 500mL | 500 | 662.23 | 662.23 | 662.27 | 662.2 | 662.24 | 662.21 |
| 500mL - 1 | 500 | 659.41 | 659.42 | 659.48 | 659.46 | 659.42 | 659.44 |
| 250mL | 250 | 371.22 | 371.22 | 371.15 | 371.25 | 371.2 | 371.22 |
| 201 | 200 | 280.4 | 280.4 | 280.41 | 280.38 | 280.41 | 280.39 |
| 202 | 200 | 292.02 | 292.02 | 292 | 291.98 | 292.05 | 292.03 |
| 203 | 200 | 279.48 | 279.49 | 279.49 | 279.45 | 279.48 | 279.49 |
| 1L | 1000 | 1253.5 | 1253.5 | 1253.55 | 1253.51 | 1253.56 | 1253.47 |
| 1L - 1 | 1000 | 1245.4 | 1245.4 | 1245.36 | 1245.35 | 1245.42 | 1245.41 |

| | | Volume | | | | | | |
|------------|---------------------|---------|---------|---------|---------|---------|---------|--------------------|
| Pycnometer | Nominal Volume (mL) | 1 | 2 | 3 | 4 | 5 | Average | Standard Deviation |
| 500mL | 500 | 499.314 | 499.354 | 499.284 | 499.324 | 499.294 | 499.314 | 0.0246 |
| 500mL - 1 | 500 | 499.713 | 499.773 | 499.753 | 499.713 | 499.733 | 499.737 | 0.0234 |
| 250mL | 250 | 249.544 | 249.474 | 249.574 | 249.524 | 249.544 | 249.532 | 0.0332 |
| 201 | 200 | 199.832 | 199.842 | 199.812 | 199.842 | 199.822 | 199.830 | 0.0117 |
| 202 | 200 | 199.631 | 199.611 | 199.591 | 199.661 | 199.641 | 199.627 | 0.0242 |
| 203 | 200 | 199.916 | 199.916 | 199.876 | 199.906 | 199.916 | 199.906 | 0.0155 |
| 1L | 1000 | 998.145 | 998.196 | 998.155 | 998.206 | 998.115 | 998.163 | 0.0332 |
| 1L - 1 | 1000 | 998.155 | 998.115 | 998.105 | 998.176 | 998.165 | 998.143 | 0.0279 |

| | |
|---------------------|---------|
| Temperature (deg C) | 23 |
| density at temp | 0.99754 |

| Unoxidized Tailings | | | | | | | | | |
|---------------------|-------------|----------------------|----------------|---------------|---------|---------|---------|---------|-------|
| Pycnometer | Volume (mL) | Weight of Solids (g) | Full mass @ EQ | Temp (deg C) | Mp | Vp | Mpw,t | pw,t | Gt |
| 500 | 500 | 82.43 | 717.01 | 23.8 | 164.144 | 499.314 | 662.135 | 0.99735 | 2.991 |
| 250 | 250 | 45.39 | 401.37 | 23.8 | 122.29 | 249.532 | 371.161 | 0.99735 | 2.990 |
| 203 | 200 | 34.23 | 302.12 | 23.8 | 80.066 | 199.906 | 279.442 | 0.99735 | 2.963 |
| 203 | 200 | 34.42 | 302.36 | 22.8 | 80.066 | 199.906 | 279.490 | 0.99759 | 2.980 |
| | | | | | | | | Average | 2.981 |

| Pre-oxidized Tailings | | | | | | | | | |
|-----------------------|-------------|----------------------|--------------------|--------------|---------|---------|---------|---------|-------|
| Pycnometer | Volume (mL) | Weight of Solids (g) | Mass Full @ EQ (g) | Temp (deg C) | Mp | Vp | Mpw,t | pw,t | Gt |
| 500-1 | 500 | 96.15 | 723.26 | 23.8 | 160.936 | 499.737 | 659.349 | 0.99735 | 2.982 |
| 201 | 200 | 29.1 | 299.91 | 23.8 | 81.06 | 199.830 | 280.360 | 0.99735 | 3.047 |
| 202 | 200 | 31.32 | 312.87 | 23.8 | 92.88 | 199.627 | 291.978 | 0.99735 | 3.003 |
| 202 | 200 | 33.42 | 314.5 | 22.8 | 92.88 | 199.627 | 292.026 | 0.99759 | 3.053 |
| | | | | | | | | Average | 3.022 |

| Toronto Amendment Biosolids | | | | | | | | | |
|-----------------------------|-------------|----------------------|--------------------|--------------|---------|---------|---------|---------|-------|
| Pycnometer | Volume (mL) | Weight of Solids (g) | Mass Full @ EQ (g) | Temp (deg C) | Mp | Vp | Mpw,t | pw,t | Gt |
| 500-1 | 500 | 82.66 | 694.96 | 24 | 160.936 | 499.737 | 659.324 | 0.9973 | 1.758 |
| 202 | 200 | 47.99 | 312.63 | 24 | 92.88 | 199.627 | 291.968 | 0.9973 | 1.756 |
| 203 | 200 | 32.83 | 293.6 | 24 | 80.066 | 199.906 | 279.432 | 0.9973 | 1.759 |
| | | | | | | | | Average | 1.758 |

| Fish Compost Amendment | | | | | | | | | |
|------------------------|-------------|----------------------|--------------------|--------------|---------|---------|---------|---------|-------|
| Pycnometer | Volume (mL) | Weight of Solids (g) | Mass Full @ EQ (g) | Temp (deg C) | Mp | Vp | Mpw,t | pw,t | Gt |
| 500 | 500 | 41.97 | 685.39 | 24.8 | 164.144 | 499.314 | 662.010 | 0.9971 | 2.258 |
| 250 | 250 | 19.34 | 381.9 | 24.8 | 122.29 | 249.532 | 371.098 | 0.9971 | 2.265 |
| 201 | 200 | 26.17 | 294.79 | 24.8 | 81.06 | 199.830 | 280.310 | 0.9971 | 2.239 |
| | | | | | | | | Average | 2.254 |

| Leaf and Yard Amendment | | | | | | | | | |
|-------------------------|-------------|----------------------|--------------------|--------------|---------|---------|---------|---------|-------|
| Pycnometer | Volume (mL) | Weight of Solids (g) | Mass Full @ EQ (g) | Temp (deg C) | Mp | Vp | Mpw,t | pw,t | Gt |
| 500 | 500 | 56.36 | 690.91 | 24 | 164.144 | 499.314 | 662.110 | 0.9973 | 2.045 |
| 250 | 250 | 38.09 | 388.74 | 24 | 122.29 | 249.532 | 371.148 | 0.9973 | 1.858 |
| 201 | 200 | 37.8 | 300.7 | 24 | 81.06 | 199.830 | 280.350 | 0.9973 | 2.166 |
| | | | | | | | | Average | 2.023 |

| Custom Reclamation Mix Biosolids | | | | | | | | | |
|----------------------------------|-------------|----------------------|--------------------|--------------|---------|---------|---------|---------|-------|
| Pycnometer | Volume (mL) | Weight of Solids (g) | Mass Full @ EQ (g) | Temp (deg C) | Mp | Vp | Mpw,t | pw,t | Gt |
| 500-1 | 500 | 62.38 | 690.88 | 24 | 160.936 | 499.737 | 659.324 | 0.9973 | 2.024 |
| 202 | 200 | 38.81 | 312.79 | 24 | 92.88 | 199.627 | 291.968 | 0.9973 | 2.158 |
| 203 | 200 | 33.19 | 297.02 | 24 | 81.06 | 199.906 | 280.426 | 0.9973 | 2.000 |
| | | | | | | | | Average | 2.060 |

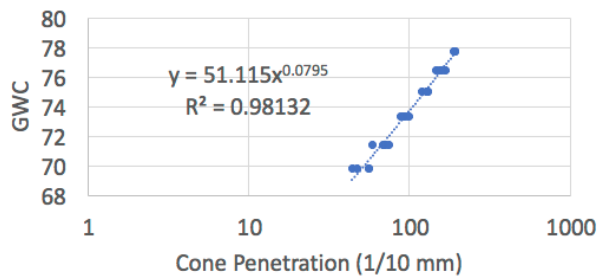
| Domtar Papermill Biosolids | | | | | | | | | |
|----------------------------|-------------|----------------------|--------------------|--------------|---------|---------|---------|---------|-------|
| Pycnometer | Volume (mL) | Weight of Solids (g) | Mass Full @ EQ (g) | Temp (deg C) | Mp | Vp | Mpw,t | pw,t | Gt |
| 500 | 500 | 58.67 | 697.88 | 25 | 164.144 | 499.314 | 661.985 | 0.99705 | 2.576 |
| 201 | 200 | 32.1 | 299.79 | 25 | 81.06 | 199.830 | 280.300 | 0.99705 | 2.546 |
| 203 | 200 | 29.19 | 297.07 | 25 | 80.066 | 199.906 | 279.382 | 0.99705 | 2.538 |
| | | | | | | | | Average | 2.553 |

| Sand | | | | | | | | | |
|------------|-------------|----------------------|--------------------|--------------|---------|---------|---------|---------|-------|
| Pycnometer | Volume (mL) | Weight of Solids (g) | Mass Full @ EQ (g) | Temp (deg C) | Mp | Vp | Mpw,t | pw,t | Gt |
| 500 | 500 | 120.63 | 739.09 | 24.9 | 164.144 | 499.314 | 661.995 | 0.997 | 2.771 |
| 201 | 200 | 63.09 | 320.5 | 24.9 | 81.06 | 199.830 | 280.304 | 0.997 | 2.756 |
| 203 | 200 | 59.5 | 317.25 | 24.9 | 80.066 | 199.906 | 279.386 | 0.997 | 2.750 |
| | | | | | | | | Average | 2.759 |

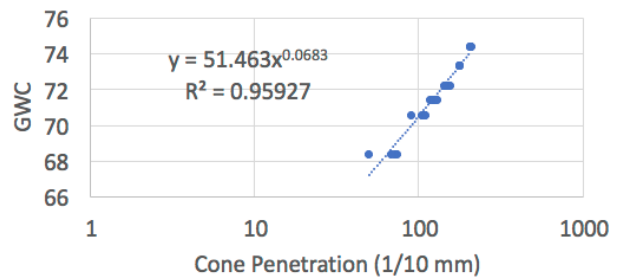
A – 2 : Fall Cone Test result plots

| Material | GWC | Test | | | | Material | GWC | Test | | | |
|------------------------|-------|-------|-----|------|------|---------------------|----------------------------|-------|-----|-----|-----|
| | | 1 | 2 | 3 | 4 | | | 1 | 2 | 3 | 4 |
| Leaf and Yard Waste | 69.81 | 56 | 44 | 47.5 | 56 | Unoxidized Tailings | 0.00 | 146 | 135 | 185 | |
| | 71.44 | 59.5 | 69 | 71 | 74.5 | | 9.09 | 45 | 38 | 47 | 52 |
| | 73.35 | 91 | 94 | 99 | 89 | | 13.04 | 35 | 37 | 31 | 39 |
| | 75.00 | 130 | 130 | 121 | 128 | | 16.67 | 35 | 34 | 29 | 41 |
| | 76.49 | 169 | 146 | 155 | 160 | | 20.10 | 34 | 34 | 35 | 34 |
| | 77.78 | 192.5 | 191 | 191 | 190 | | 23.12 | 104 | 100 | 124 | 120 |
| Custom Reclamation Mix | 68.41 | 73.5 | 50 | 71.5 | 68 | | 19.97 | 25 | 18 | 25 | 22 |
| | 70.59 | 107.5 | 90 | 105 | 110 | | 20.73 | 33 | 36 | 34 | 32 |
| | 71.45 | 122.5 | 118 | 123 | 130 | | 21.30 | 41 | 80 | 62 | 38 |
| | 72.22 | 155 | 145 | 151 | 143 | | 21.86 | 82 | 40 | 50 | 69 |
| | 73.33 | 177 | 179 | 178 | 178 | | 22.81 | 101 | 104 | 102 | 45 |
| Fish Compost | 74.38 | 205 | 208 | 205 | 206 | | Domtar Papermill Biosolids | 52.88 | 92 | 96 | 80 |
| | 41.76 | 105 | 93 | 88 | 108 | 54.20 | | 135 | 139 | 136 | 130 |
| | 47.37 | 41 | 60 | 75 | 65 | 55.23 | | 165 | 172 | 166 | 170 |
| | 53.52 | 42 | 40 | 41 | 40 | 56.12 | | 185 | 185 | 186 | 184 |
| | 56.53 | 89.5 | 104 | 80 | 96 | Sand | 0.31 | 93 | 87 | 88 | 92 |
| | 60.03 | 175 | 177 | 190 | 191 | | 2.78 | 45 | 52 | 76 | 49 |
| 61.54 | 220 | 220 | 227 | 218 | 6.12 | | 53 | 52 | 54 | 50 | |
| Pre-oxidized Tailings | 26.39 | 70 | 85 | 66 | | | 9.61 | 46 | 46 | 39 | 38 |
| | 28.57 | 162 | 158 | 133 | 154 | | 11.20 | 44 | 40 | 37 | 38 |
| | 29.85 | 210 | 220 | 219 | 221 | | 12.34 | 35 | 29 | 21 | 24 |
| Toronto Amendment | 73.60 | 75 | 75 | 74 | 77 | | 14.64 | 36 | 38 | 37 | 38 |
| | 75.00 | 91 | 91 | 90 | 90 | | 14.92 | 40 | 55 | 45 | 48 |
| | 75.60 | 94 | 94 | 93 | 94 | 16.16 | 65 | 70 | 77 | 83 | |
| | 76.49 | 106.5 | 104 | 105 | 104 | 16.34 | 72 | 79 | 61 | 68 | |
| | 77.01 | 114 | 110 | 111 | 110 | | | | | | |
| | 77.78 | 121 | 123 | 120 | 122 | | | | | | |

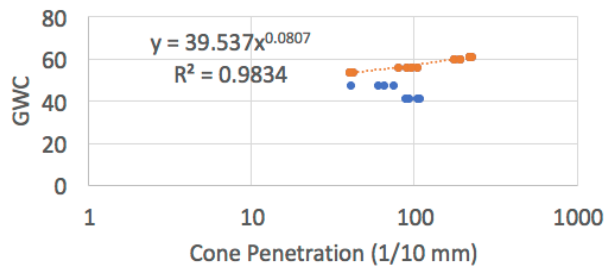
Leaf and Yard Waste - Fall Cone Data



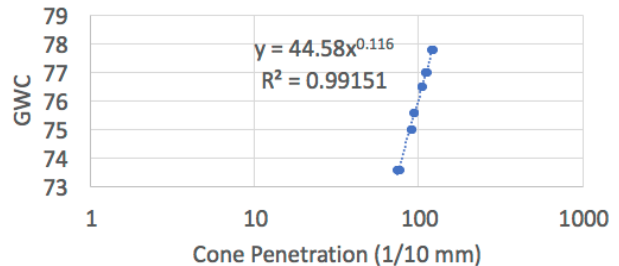
Custom Reclamation Mix - Fall Cone Data

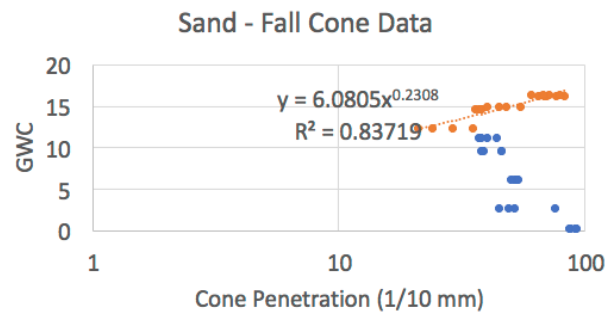
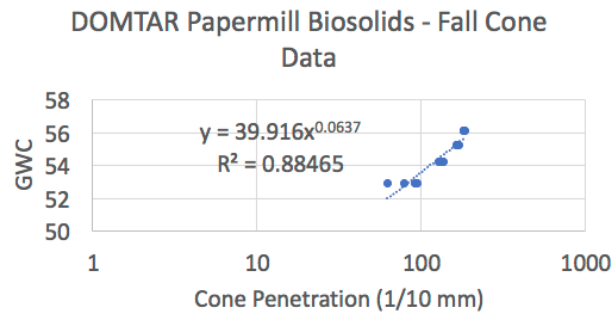
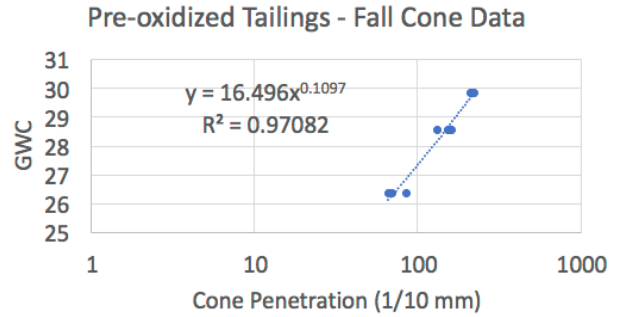
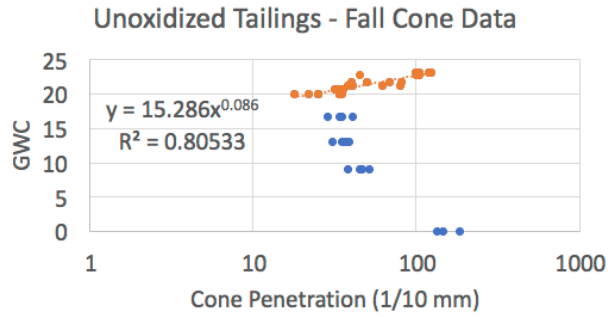


Fish Compost Amendment - Fall Cone Data



Toronto Amendment Biosolids - Fall Cone Data





A – 3 : Saturated Hydraulic Conductivity data and results

| Unoxidized Tailings Test 1 | | | | | | |
|----------------------------|---------|---------|---------------|----------|------------|------------|
| Volume (mL) | Minutes | Seconds | Total Seconds | K (cm/s) | L (cm) | 14.5 |
| 400 | 2 | 57 | 177 | 5.76E-03 | A (cm^2) | 45.7234463 |
| 500 | 3 | 58 | 238 | 4.18E-03 | h (cm) | 124.5 |
| 600 | 4 | 42 | 282 | 5.79E-03 | | |
| 700 | 5 | 16 | 316 | 7.49E-03 | | |
| 800 | 5 | 55 | 355 | 6.53E-03 | K total | |
| 1000 | 7 | 40 | 460 | 4.85E-03 | 0.00553735 | |
| AVERAGE | | | | 5.77E-03 | | |
| Unoxidized Tailings Test 2 | | | | | | |
| Volume | Minutes | Seconds | Total Seconds | K (cm/s) | L (cm) | 14.4 |
| 500 | 3 | 5 | 185 | 6.84E-03 | A (cm^2) | 45.7234463 |
| 600 | 3 | 48 | 228 | 5.88E-03 | h (cm) | 124.5 |
| 700 | 4 | 20 | 260 | 7.91E-03 | | |
| 800 | 4 | 50 | 290 | 8.43E-03 | K total | |
| 1000 | 6 | 10 | 370 | 6.32E-03 | 0.00683679 | |
| AVERAGE | | | | 7.08E-03 | | |
| Unoxidized Tailings Test 3 | | | | | | |
| Volume | Minutes | Seconds | Total Seconds | K (cm/s) | L (cm) | 14.5 |
| 400 | 4 | 3 | 243 | 4.19E-03 | A (cm^2) | 45.7234463 |
| 500 | 5 | 0 | 300 | 4.47E-03 | h (cm) | 124.5 |
| 600 | 6 | 12 | 372 | 3.54E-03 | | |
| 700 | 6 | 55 | 415 | 5.92E-03 | | |
| 800 | 8 | 16 | 496 | 3.14E-03 | K total | |
| 1000 | 10 | 6 | 606 | 4.63E-03 | 0.00420327 | |
| AVERAGE | | | | 4.32E-03 | | |

| Unoxidized Tailings Test 4 | | | | | | |
|----------------------------|---------|---------|---------------|----------|----------------------|------------|
| Volume | Minutes | Seconds | Total Seconds | K (cm/s) | | |
| 200 | 2 | 12 | 132 | 3.86E-03 | | |
| 400 | 4 | 32 | 272 | 3.64E-03 | L (cm) | 14.5 |
| 500 | 5 | 42 | 342 | 3.64E-03 | A (cm ²) | 45.7234463 |
| 600 | 6 | 54 | 414 | 3.54E-03 | h (cm) | 124.5 |
| 700 | 8 | 1 | 481 | 3.80E-03 | | |
| 800 | 9 | 9 | 549 | 3.75E-03 | K total | |
| 900 | 10 | 21 | 621 | 3.54E-03 | 0.00367029 | |
| 1000 | 11 | 34 | 694 | 3.49E-03 | | |
| | | | AVERAGE | 3.66E-03 | | |

| Pre-oxidized tailings test 1 | | | | | |
|------------------------------|---------------|------------|------------|-------------------------|-------------|
| Monometer Reading | total seconds | total head | K (cm/s) | | |
| 80 | 0 | 107 | | | |
| 70 | 33 | 97 | 0.00046728 | L (cm) | 12.2 |
| 60 | 65 | 87 | 0.00053436 | Diameter (cm) | 6.3 |
| 50 | 110 | 77 | 0.00042644 | Area (cm ²) | 31.17245311 |
| 40 | 183 | 67 | 0.0002995 | | |
| 35 | 228 | 62 | 0.00027087 | Total | |
| 30 | 264 | 57 | 0.00036707 | delta t | 396 |
| 25 | 300 | 52 | 0.0004008 | first term | 0.000396873 |
| 20 | 346 | 47 | 0.0003454 | second term | 0.935159216 |
| 15 | 396 | 42 | 0.00035354 | K (cm/s) | 0.00037114 |
| | | Average | 0.00038503 | | |

| Pre-oxidized tailings test 2 | | | | | |
|------------------------------|---------------|------------|----------|-------------------------|-------------|
| Monometer Reading | total seconds | total head | K (cm/s) | | |
| 99 | 0 | 126 | | | |
| 98 | 95 | 125 | 1.62E-05 | L (cm) | 15 |
| 95 | 329 | 122 | 2.01E-05 | Diameter (cm) | 6.3 |
| 90 | 724 | 117 | 2.05E-05 | Area (cm ²) | 31.17245311 |
| 85 | 1140 | 112 | 2.03E-05 | | |
| 80 | 1591 | 107 | 1.96E-05 | Total | |
| 75 | 2079 | 102 | 1.89E-05 | delta t | 5223 |
| 65 | 3177 | 92 | 1.82E-05 | first term | 3.69963E-05 |
| 60 | 3805 | 87 | 1.72E-05 | second term | 0.492476485 |
| 50 | 5223 | 77 | 1.66E-05 | K (cm/s) | 1.82E-05 |
| | | Average | 1.86E-05 | | |

| Pre-oxidized tailings test 3 | | | | | |
|------------------------------|---------------|------------|----------|-------------------------|-------------|
| Monometer Reading | total seconds | total head | K (cm/s) | | |
| 99 | 0 | 126 | | | |
| 98 | 41 | 125 | 3.76E-05 | L (cm) | 15 |
| 95 | 170 | 122 | 3.64E-05 | Diameter (cm) | 6.3 |
| 90 | 405 | 117 | 3.44E-05 | Area (cm ²) | 31.17245311 |
| 85 | 669 | 112 | 3.20E-05 | | |
| 80 | 952 | 107 | 3.12E-05 | | |
| 70 | 1588 | 97 | 2.98E-05 | Total | |
| 65 | 1957 | 92 | 2.77E-05 | delta t | 3288 |
| 60 | 2373 | 87 | 2.60E-05 | first term | 5.87688E-05 |
| 55 | 2810 | 82 | 2.62E-05 | second term | 0.492476485 |
| 50 | 3288 | 77 | 2.54E-05 | k | 2.89E-05 |
| | | Average | 3.07E-05 | | |

| Pre-oxidized tailings test 4 | | | | | | |
|------------------------------|---------------|------------|----------|---------------|-------------|--|
| Monometer Reading | total seconds | total head | K (cm/s) | | | |
| 99 | 0 | 126 | | | | |
| 98 | 41 | 125 | 3.76E-05 | L (cm) | 15 | |
| 95 | 170 | 122 | 3.64E-05 | Diameter (cm) | 6.3 | |
| 90 | 405 | 117 | 3.44E-05 | Area (cm^2) | 31.17245311 | |
| 85 | 669 | 112 | 3.20E-05 | | | |
| 80 | 952 | 107 | 3.12E-05 | | | |
| 70 | 1588 | 97 | 2.98E-05 | Total | | |
| 65 | 1957 | 92 | 2.77E-05 | delta t | 3288 | |
| 60 | 2373 | 87 | 2.60E-05 | first term | 5.87688E-05 | |
| 55 | 2810 | 82 | 2.62E-05 | second term | 0.492476485 | |
| 50 | 3288 | 77 | 2.54E-05 | K (cm/s) | 2.89E-05 | |
| | | Average | 3.07E-05 | | | |

| Sand Constant Head Test 1 | | | | | | |
|---------------------------|---------|---------|---------------|----------|----------------|------------|
| Volume | Minutes | Seconds | Total Seconds | K (cm/s) | | |
| 200 | 0 | 44 | 44 | 1.16E-02 | L (cm) | 14.5 |
| 400 | 1 | 24 | 84 | 1.27E-02 | Diameter (cm) | 7.63 |
| 500 | 1 | 48 | 108 | 1.06E-02 | Area (cm^2) | 45.7234463 |
| 600 | 2 | 13 | 133 | 1.02E-02 | | |
| 800 | 3 | 0 | 180 | 1.08E-02 | Total K (cm/s) | |
| 1000 | 3 | 38 | 218 | 1.34E-02 | 0.011684313 | |
| | | | AVERAGE | 1.16E-02 | | |

| Sand Constant Head Test 2 | | | | | | |
|---------------------------|---------|---------|---------------|----------|----------------|------------|
| Volume | Minutes | Seconds | Total Seconds | K (cm/s) | | |
| 400 | 1 | 49 | 109 | 9.28E-03 | L (cm) | 14.4 |
| 600 | 2 | 50 | 170 | 8.29E-03 | Diameter (cm) | 7.63 |
| 800 | 3 | 46 | 226 | 9.03E-03 | Area (cm^2) | 45.7234463 |
| 1000 | 4 | 40 | 280 | 9.37E-03 | Total K (cm/s) | |
| | | | AVERAGE | 9.00E-03 | 0.009034334 | |

| Sand Constant Head Test 3 | | | | | | |
|---------------------------|---------|---------|---------------|----------|----------------|------------|
| Volume | Minutes | Seconds | Total Seconds | K (cm/s) | | |
| 400 | 1 | 29 | 89 | 1.14E-02 | L (cm) | 14.5 |
| 600 | 2 | 12 | 132 | 1.16E-02 | Diameter (cm) | 7.63 |
| 800 | 3 | 1 | 181 | 1.13E-02 | Area (cm^2) | 45.7234463 |
| 1000 | 3 | 47 | 227 | 1.12E-02 | Total K (cm/s) | |
| | | | AVERAGE | 1.14E-02 | 0.011221059 | |

| Custom Reclamation Mix Biosolids Test 1 | | | | | | |
|-----------------------------------------|---------------|------------|---------|----------|----------------|----------|
| Monometer Reading | total seconds | total head | delta t | k (cm/s) | | |
| 96.8 | 0 | 126.3 | | | L (cm) | 12.5 |
| 94.3 | 600 | 123.8 | 600 | 2.33E-06 | Diameter (cm) | 6.3 |
| 88.8 | 3900 | 118.3 | 3300 | 9.63E-07 | Area (cm^2) | 3.12E+01 |
| 78 | 36600 | 107.5 | 32700 | 2.05E-07 | Total delta t | 36600 |
| | | | AVERAGE | 1.17E-06 | Total k (cm/s) | 3.08E-07 |

| Custom Reclamation Mix Biosolids Test 2 | | | | | | |
|-----------------------------------------|---------------|------------|---------|----------|---------------|----------|
| Monometer Reading | total seconds | total head | delta t | k (cm/s) | | |
| 99.3 | 0 | 128.8 | | | L (cm) | 12.5 |
| 97.4 | 600 | 126.9 | 600 | 1.73E-06 | Diameter (cm) | 6.3 |
| 92.1 | 3900 | 121.6 | 3300 | 9.04E-07 | Area (cm^2) | 3.12E+01 |
| 86.6 | 36600 | 116.1 | 32700 | 9.90E-08 | Total delta t | 36600 |
| | | | AVERAGE | 9.12E-07 | k | 1.98E-07 |

| Custom Reclamation Mix Biosolids Test 3 | | | | | | | |
|-----------------------------------------|---------------|------------|---------|----------|--|---------------|----------|
| Monometer Reading | total seconds | total head | delta t | k (cm/s) | | L (cm) | 12.5 |
| 98.2 | 0 | 127.7 | | | | Diameter (cm) | 6.3 |
| 95.9 | 600 | 125.4 | 600 | 2.12E-06 | | Area (cm^2) | 3.12E+01 |
| 87.8 | 3900 | 117.3 | 3300 | 1.42E-06 | | | |
| 56.4 | 36600 | 85.9 | 32700 | 6.66E-07 | | Total delta t | 36600 |
| | | | AVERAGE | 1.40E-06 | | k | 7.58E-07 |

| Custom Reclamation Mix Biosolids Test 4 - (aged 15 months) | | | | | | | |
|------------------------------------------------------------|--------------|------------|---------|----------|--|---------------|----------|
| Monometer Reading | Total Second | Total Head | delta t | k (cm/s) | | L (cm) | 12.5 |
| 99.5 | 0 | 129 | | | | Diameter (cm) | 6.3 |
| 99.2 | 300 | 128.7 | 300 | 5.43E-07 | | Area (cm^2) | 3.12E+01 |
| 99 | 600 | 128.5 | 300 | 3.63E-07 | | | |
| 98.3 | 1800 | 127.8 | 1200 | 3.18E-07 | | Total delta t | 39600 |
| 96.8 | 3600 | 126.3 | 1800 | 4.59E-07 | | k | 5.82E-07 |
| 91.7 | 10800 | 121.2 | 7200 | 4.00E-07 | | | |
| 63.3 | 39600 | 92.8 | 28800 | 6.48E-07 | | | |
| | | | AVERAGE | 4.55E-07 | | | |

| Custom Reclamation Mix Biosolids Test 5 (aged 15 months) | | | | | | | |
|----------------------------------------------------------|---------------|------------|---------|----------|--|---------------|----------|
| Monometer Reading | total seconds | total head | delta t | k (cm/s) | | L (cm) | 12.5 |
| 98.9 | 0 | 128.4 | | | | Diameter (cm) | 6.3 |
| 98.7 | 300 | 128.2 | 300 | 3.63E-07 | | Area (cm^2) | 3.12E+01 |
| 98.5 | 600 | 128 | 300 | 3.64E-07 | | | |
| 98 | 1800 | 127.5 | 1200 | 2.28E-07 | | Total delta t | 39600 |
| 97.2 | 3600 | 126.7 | 1800 | 2.45E-07 | | k | 3.37E-07 |
| 93.5 | 10800 | 123 | 7200 | 2.88E-07 | | | |
| 76.6 | 39600 | 106.1 | 28800 | 3.59E-07 | | | |
| | | | AVERAGE | 3.08E-07 | | | |

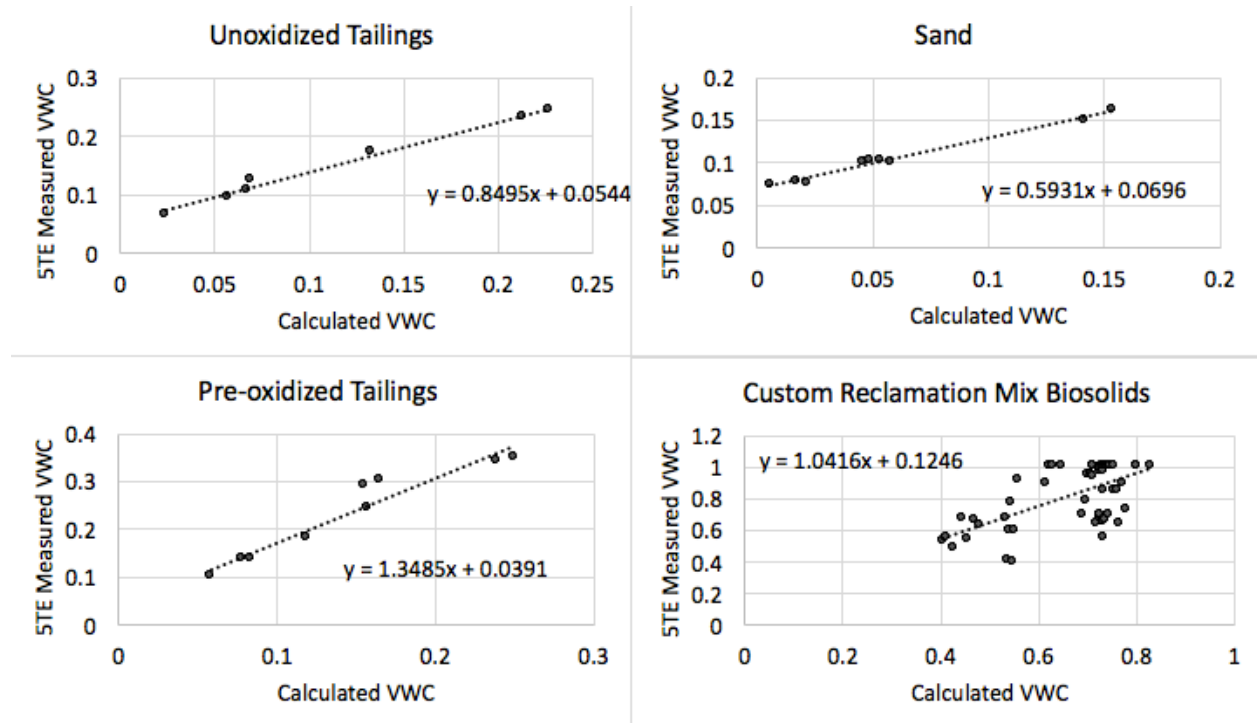
| Toronto Amendment Biosolids Test 1 | | | | | | | |
|------------------------------------|---------------|------------|---------|----------|--|----------------|----------|
| Monometer reading | Total Seconds | Total Head | Delta t | K (cm/s) | | L (cm) | 15 |
| 99.2 | 600 | 126.2 | 600 | | | Diameter (cm) | 6.3 |
| 97 | 1200 | 124 | 600 | 2.46E-06 | | Area (cm^2) | 31.17 |
| 95.2 | 1800 | 122.2 | 600 | 2.05E-06 | | | |
| 93.4 | 2400 | 120.4 | 600 | 2.08E-06 | | | |
| 91.7 | 3000 | 118.7 | 600 | 1.99E-06 | | Total | |
| 90.3 | 3600 | 117.3 | 600 | 1.66E-06 | | delta t | 10200 |
| 88.7 | 4200 | 115.7 | 600 | 1.92E-06 | | first term | 1.89E-05 |
| 87.4 | 4800 | 114.4 | 600 | 1.58E-06 | | second term | 8.32E-02 |
| 86.3 | 5400 | 113.3 | 600 | 1.35E-06 | | Total K (cm/s) | 1.58E-06 |
| 77.2 | 10800 | 104.2 | 5400 | 1.30E-06 | | | |
| | | | AVERAGE | 1.82E-06 | | | |

| Toronto Amendment Biosolids Test 2 | | | | | | | |
|------------------------------------|---------------|------------|---------|----------|--|----------------|----------|
| Monometer reading | Total Seconds | Total Head | Delta t | K (cm/s) | | L (cm) | 15 |
| 96.4 | 0 | 123.4 | | | | Diameter (cm) | 6.3 |
| 94.6 | 600 | 121.6 | 600 | 2.06E-06 | | Area (cm^2) | 31.17 |
| 93.5 | 1200 | 120.5 | 600 | 1.27E-06 | | | |
| 92.4 | 1800 | 119.4 | 600 | 1.28E-06 | | | |
| 91.3 | 2400 | 118.3 | 600 | 1.29E-06 | | Total | |
| 90.3 | 3000 | 117.3 | 600 | 1.19E-06 | | delta t | 10800.00 |
| 89.4 | 3600 | 116.4 | 600 | 1.08E-06 | | first term | 1.79E-05 |
| 86.8 | 4200 | 113.8 | 600 | 3.16E-06 | | second term | 9.92E-02 |
| 84 | 4800 | 111 | 600 | 3.48E-06 | | Total K (cm/s) | 1.77E-06 |
| 81.6 | 5400 | 108.6 | 600 | 3.06E-06 | | | |
| 71.2 | 10800 | 98.2 | 5400 | 1.56E-06 | | | |
| | | | AVERAGE | 1.94E-06 | | | |

| Custom Reclamation Mix Biosolids | | | | | | | | | |
|----------------------------------|----------|---------|--------------|---------|----------------------|--------------------|------------------------------|--------|---------|
| Hydrometer Reading | | | | | | | | Test | Control |
| Elapsed Time (minutes) | Solution | Control | Temp (deg C) | % finer | Effective Depth (cm) | Particle Size (um) | | | |
| 1 | 22.5 | 0.75 | 23 | 49.97 | 12.78 | 58.66 | Dispersant (g) | 5.03 | 5.02 |
| 2 | 22 | 0.5 | 23 | 49.39 | 12.81 | 41.54 | Water (g) | 100 | 100 |
| 5 | 21 | 0.75 | 23 | 46.52 | 13.00 | 26.47 | Soil (g) | 182.47 | |
| 8 | 20.5 | 1 | 23.5 | 44.80 | 13.12 | 20.89 | GWC | 246.46 | |
| 15 | 20.75 | 0.5 | 23.5 | 46.52 | 13.00 | 15.19 | | | |
| 30 | 20 | 0.5 | 23.5 | 44.80 | 13.12 | 10.79 | Diameter of test column (cm) | | 5.8 |
| 60 | 18.75 | 0.75 | 23.5 | 41.35 | 13.35 | 7.70 | % passing 200 mesh | | 52.53 |
| 240 | 18.25 | 1 | 23 | 39.63 | 13.46 | 3.89 | specific gravity of soil | | 2.06 |
| 1440 | 17 | 0.5 | 23 | 37.91 | 13.57 | 1.59 | dry mass of soil (g) | | 52.67 |
| | | | | | | | volume of suspension (mL) | | 1000 |

Appendix B – Column Testing Parameters, Data, and Results

B – 1 : 5TE Volumetric Water Content sensor calibration curves

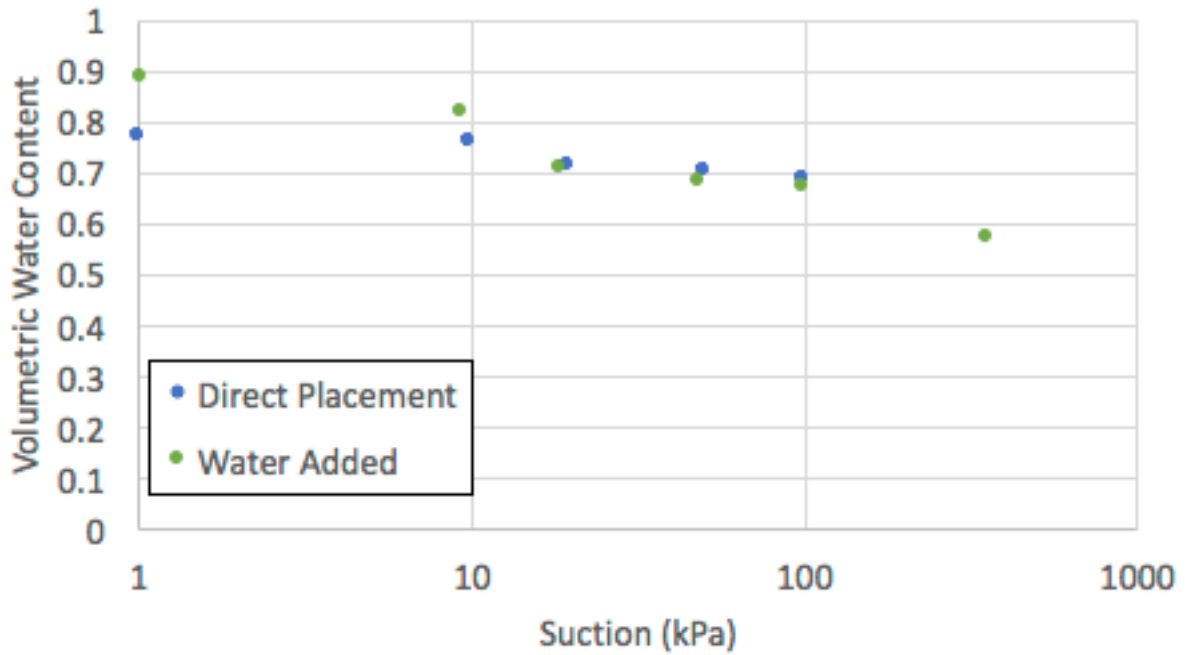


B – 2: Column pore water analysis results

| Time Period | Sample | Description | pH | EC (mS/cm) | Concentration (ppm) | | | | | | | | | | | | | | | |
|------------------------|----------------|--------------------------------------|------|------------|---------------------|--------|-------|----------|--------|---------|-------|--------|--------|----------|----------|----------|----------|----------|--------|-----|
| | | | | | Al | Ca | Cu | Fe | K | Mg | Mn | Na | Ni | As (ppb) | Pb (ppb) | SO4 | NO2 | NO3 | PO4 | |
| After Initial Drying | CH 7/11 - 001 | Column A Lower Tailings Port | 3.02 | 30.46 | 515.81 | 489.01 | 0.58 | 10119.22 | 144.07 | 859.10 | 26.81 | 73.25 | 306.76 | 29.24 | 37.92 | n/a | n/a | n/a | n/a | |
| | CH 7/11 - 002 | Column A Upper Tailings Port | 2.83 | 24.66 | 371.79 | 469.91 | 0.37 | 8785.02 | 41.68 | 653.68 | 20.88 | 85.58 | 231.70 | 15.33 | 20.59 | n/a | n/a | n/a | n/a | |
| | CH 7/11 - 003 | Column A CRM Port | 9.19 | 28.54 | 22.81 | 94.15 | 0.23 | 13.12 | 609.51 | 14.61 | 0.16 | 340.66 | 2.48 | 109.69 | 15.88 | n/a | n/a | n/a | n/a | |
| | CH 7/11 - 004 | Column B Lower Tailings Port | 2.86 | 26.80 | 443.02 | 468.91 | 0.18 | 10031.29 | 16.40 | 792.10 | 25.23 | 69.68 | 285.74 | 14.69 | 8.84 | n/a | n/a | n/a | n/a | |
| | CH 7/11 - 005 | Column B Upper Tailings Port | 2.47 | 38.22 | 2308.04 | 529.26 | 4.22 | 9274.54 | 17.33 | 1552.93 | 47.77 | 136.63 | 414.08 | 44.26 | 7.59 | n/a | n/a | n/a | n/a | |
| | CH 7/11 - 006 | Column B CRM Port | 9.37 | 23.99 | 37.38 | 53.71 | 1.10 | 12.93 | 470.57 | 18.52 | 0.26 | 262.32 | 2.49 | 66.12 | 44.33 | n/a | n/a | n/a | n/a | |
| | CH 7/11 - 007 | Blank | | | 1.51 | 0.16 | 0.01 | 0.22 | 0.60 | 0.21 | 0.00 | 0.28 | 0.02 | -0.04 | 2.01 | n/a | n/a | n/a | n/a | |
| | CH 7/11 - 008 | Column C Lower Tailings Port | 6.47 | 3.87 | 0.08 | 501.73 | 0.03 | 8.98 | 191.65 | 82.62 | 2.80 | 212.60 | 0.25 | 5.66 | 1.48 | n/a | n/a | n/a | n/a | |
| | CH 7/11 - 009 | Column C Upper Tailings Port | 6.47 | 4.01 | 0.05 | 470.46 | 0.02 | 3.29 | 177.76 | 114.18 | 3.01 | 204.95 | 1.54 | 2.38 | 0.84 | n/a | n/a | n/a | n/a | |
| | CH 7/11 - 010 | Column C CRM Port | 9.27 | 41.12 | 16.82 | 76.06 | -0.04 | 7.38 | 586.22 | 10.32 | 0.12 | 254.12 | 1.38 | 81.28 | 7.49 | n/a | n/a | n/a | n/a | |
| Original State | CH 7/13 - 011 | Original State Sand | 7.26 | 0.00 | 0.15 | 1.95 | 0.04 | 0.21 | 0.16 | 0.34 | 0.01 | 0.33 | 0.00 | 0.62 | 22.86 | 14.84 | 1.13 | 0.25 | n/a | |
| | CH 7/13 - 012 | Original State Unoxidized Tailings | 6.08 | 2.25 | 3.06 | 68.24 | 0.80 | 6.55 | 16.02 | 5.40 | 0.09 | 16.41 | 1.00 | 329.31 | 312.28 | 208.60 | 29960.53 | 29291.89 | 0.15 | n/a |
| | CH 7/13 - 013 | Original State Pre-Oxidized Tailings | 2.78 | 32.20 | 247.39 | 213.14 | 11.98 | 9.24 | 3.60 | 49.68 | 3.91 | 2.16 | 44.09 | 42.52 | 1819.47 | 22.29 | 1819.47 | 22.29 | 8.06 | n/a |
| | CH 7/13 - 014 | Original State CRM | 9.27 | 24.72 | 4.09 | 23.19 | 0.36 | 23.93 | 44.40 | 4.63 | 0.16 | 19.18 | 0.13 | 165.59 | 149.24 | 4439.49 | 1616.15 | 9.26 | 122.05 | n/a |
| | CH 7/13 - 015 | Original State Pre-Oxidized Tailings | 6.11 | 2.15 | 5.80 | 54.11 | 0.18 | 12.41 | 22.26 | 6.57 | 0.13 | 15.73 | 1.05 | 478.82 | 633.34 | 1335.61 | 26.47 | 2.42 | n/a | n/a |
| | CH 7/27 - 016 | Original State Pre-Oxidized Tailings | 2.88 | 52.22 | 408.77 | 275.22 | 20.28 | 11.34 | 3.83 | 93.77 | 6.55 | 7.95 | 76.42 | 52.97 | 96.42 | 47478.67 | 46537.78 | 2.74 | n/a | n/a |
| | CH 7/27 - 017 | Column A Lower Tailings Port | 3.15 | 24.01 | 193.60 | 439.16 | 0.28 | 8178.51 | 22.75 | 209.62 | 19.06 | 58.83 | 210.64 | 9.36 | 15.98 | 23510.15 | 20923.13 | 0.21 | n/a | n/a |
| | CH 7/27 - 018 | Column A Upper Tailings Port | 2.97 | 4.03 | 19.87 | 321.39 | 0.03 | 307.08 | 42.78 | 21.55 | 0.68 | 26.00 | 5.43 | 1.84 | 5.20 | 1941.26 | 2299.17 | 0.15 | n/a | n/a |
| | CH 7/27 - 019 | Column A Lower Sand Port | 9.52 | 15.54 | 4.20 | 25.10 | -0.77 | 4.04 | 89.72 | 47.66 | 0.09 | 57.38 | 0.66 | -2.31 | 7.68 | 140.64 | 140.68 | 15.87 | n/a | n/a |
| | CH 7/27 - 020 | Column A CRM Port | 9.53 | 28.17 | 1.13 | 66.16 | 0.34 | 4.53 | 374.71 | 7.35 | -0.05 | 268.86 | 1.28 | 217.79 | 50.72 | n/a | 285.55 | 4.67 | 68.51 | n/a |
| Post Flush | CH 7/27 - 021 | Column A Upper Sand Port | 8.76 | 0.93 | 0.18 | 15.08 | 0.27 | 0.36 | 22.56 | 4.93 | 0.01 | 10.47 | 0.00 | 6.78 | 17.93 | 69.04 | 5.80 | 1.36 | n/a | n/a |
| | CH 7/27 - 022 | Column B Lower Tailings Port | 3.16 | 17.62 | 338.53 | 449.30 | 0.01 | 3952.20 | 10.93 | 189.20 | 15.67 | 60.15 | 152.08 | 15.16 | 5.99 | 14886.93 | 13754.40 | 3.78 | 0.10 | n/a |
| | CH 7/27 - 023 | Column B Upper Tailings Port | 2.35 | 22.21 | 300.35 | 473.07 | 0.74 | 981.51 | 310.04 | 192.57 | 4.93 | 127.21 | 41.57 | 12.14 | 21.61 | 10136.38 | 11464.09 | 3.78 | n/a | n/a |
| | CH 7/27 - 024 | Column B CRM Port | 9.02 | 19.56 | 1.21 | 81.59 | 0.02 | 3.10 | 332.48 | 11.69 | 0.06 | 204.04 | 0.98 | 56.68 | 13.53 | 644.33 | 55.46 | n/a | 61.95 | n/a |
| | CH 7/27 - 025 | Blank | | | 0.03 | 0.03 | 0.01 | 0.04 | -0.25 | 0.05 | 0.00 | -0.25 | 0.00 | 0.13 | 0.81 | 0.02 | 1.48 | 0.27 | n/a | n/a |
| | CH 7/27 - 026 | Column C Lower Tailings Port | 5.90 | 4.83 | 0.43 | 611.83 | -0.02 | 6.40 | 128.20 | 75.14 | 2.83 | 235.17 | 0.28 | 10.55 | 18.29 | 1755.47 | 0.55 | 0.26 | n/a | n/a |
| | CH 7/27 - 027 | Column C Upper Tailings Port | 6.18 | 5.25 | 0.08 | 625.27 | 0.02 | 1.68 | 130.56 | 93.79 | 1.94 | 150.42 | 1.63 | 4.78 | 2.72 | 1738.94 | 0.66 | 0.46 | 0.42 | n/a |
| | CH 7/27 - 028 | Column C Lower Sand Port (Blank) | | | 0.02 | 0.07 | 0.70 | 5.11 | -0.23 | 0.16 | 0.00 | -0.27 | 0.00 | 0.10 | 33.88 | 0.47 | 1.43 | 0.31 | 1.87 | n/a |
| | CH 7/27 - 029 | Column C CRM Port | 9.40 | 30.13 | 0.52 | 62.65 | 0.16 | 5.04 | 507.10 | 5.07 | 0.05 | 225.73 | 1.20 | 48.32 | 22.07 | n/a | 250.49 | 1.87 | 107.72 | n/a |
| | CH 7/27 - 030 | Column C Upper Sand Port | 9.16 | 1.34 | 0.87 | 7.46 | -0.01 | 6.35 | 12.78 | 3.77 | 0.02 | 27.20 | 0.25 | 62.00 | 1.80 | 166.81 | 5.81 | 3.57 | n/a | n/a |
| After Secondary Drying | CH 08/30 - 101 | Column A Lower Tailings Port | 2.88 | 23.59 | 127.94 | 466.81 | 0.09 | 8276.60 | 15.47 | 571.06 | 18.53 | 49.77 | 200.25 | 12.31 | 7.46 | 23142.99 | 20261.61 | 2.06 | n/a | n/a |
| | CH 08/30 - 102 | Column A Upper Tailings Port | 2.97 | 7.38 | 39.57 | 586.16 | 1.12 | 935.73 | 95.88 | 38.86 | 1.18 | 41.80 | 7.05 | 5.21 | 60.23 | 4134.53 | 4622.19 | 0.36 | n/a | n/a |
| | CH 08/30 - 103 | Column A CRM Port | 9.31 | 27.87 | 16.39 | 83.23 | 0.77 | 21.04 | 646.86 | -0.44 | 0.15 | 279.17 | 1.59 | 329.31 | 72.48 | 12.75 | 239.10 | 12.99 | 1.64 | n/a |
| | CH 08/30 - 104 | Column B Lower Tailings Port | 2.85 | 19.37 | 212.50 | 445.05 | 0.07 | 4880.76 | 10.64 | 468.24 | 15.29 | 55.11 | 139.20 | 12.79 | 4.84 | 14998.00 | 13945.95 | 0.13 | n/a | n/a |
| | CH 08/30 - 105 | Column B Upper Tailings Port | 9.23 | 32.42 | 238.39 | 488.07 | 1.23 | 429.61 | 771.83 | 137.51 | 3.07 | 261.65 | 14.26 | 10.66 | 28.32 | 11906.33 | 34.87 | 20.34 | n/a | n/a |
| | CH 08/30 - 106 | Column B CRM Port | 9.19 | 14.95 | 2.44 | 55.09 | 0.43 | 4.15 | 318.42 | 3.22 | 0.05 | 151.66 | 0.68 | 53.93 | 17.14 | 246.28 | 85.88 | 9.72 | 22.15 | n/a |
| | CH 08/30 - 107 | Column C Lower Tailings Port | 5.92 | 4.89 | 0.18 | 632.94 | -0.01 | 2.69 | 147.43 | 87.71 | 2.83 | 194.03 | 0.33 | 5.65 | 4.37 | 1757.62 | 0.62 | 0.25 | n/a | n/a |
| | CH 08/30 - 108 | Column C Upper Tailings Port | 6.11 | 6.55 | 0.25 | 536.91 | 0.10 | 0.03 | 161.28 | 108.98 | 1.04 | 130.04 | 1.52 | 4.47 | 3.22 | 2063.10 | 0.70 | 0.45 | n/a | n/a |
| | CH 08/30 - 109 | Column C CRM Port | 9.35 | 29.88 | 3.89 | 68.77 | 1.87 | 11.94 | 567.70 | -1.08 | 0.07 | 208.44 | 1.29 | 46.91 | 105.45 | n/a | 411.13 | 19.89 | 11.89 | n/a |
| | CH 08/30 - 110 | Blank | | | | | | | | | | | | | | | | | | |

B – 3 Column Deconstruction data

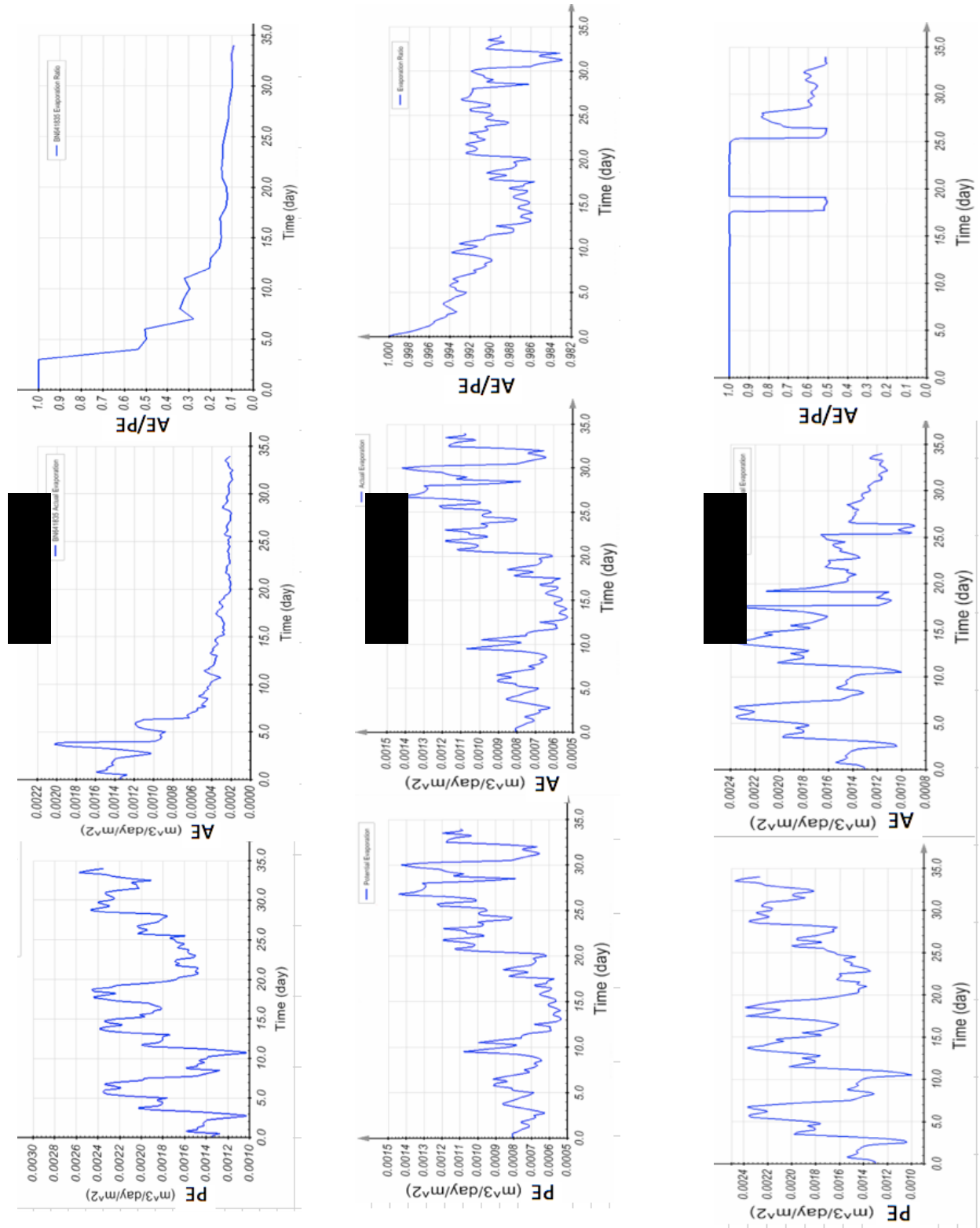
| Column | Layer | Sample | GWC | | | | Suction | | | Volumetric Water Content | | | | | | | | | |
|--------|-------------------|-------------------------------------|----------|---------|---------|--------|---------|------|-------|--------------------------|-------------------|------------|--------------------------------|-----------------------------------|------------|-------------------------------------|-----------|------|--|
| | | | Dish (g) | Wet (g) | Dry (g) | GWC | Mpa | pF | DP | Ring (g) | Ring + Sample (g) | Sample (g) | Disc volume (cm ³) | Bulk Density (g/cm ³) | Solids (g) | Solids Density (g/cm ³) | Water (g) | VWC | |
| A | Upper Sand | A5 TOP | 2.0152 | 79.193 | 79.01 | 0.0024 | 69.6 | 5.86 | 24.8 | 83.62 | 236.77 | 153.15 | 86.65 | 1.77 | 152.79 | 1.76 | 0.36 | 0.00 | |
| | | A5 MIDDLE | 2.0012 | 83.937 | 83.691 | 0.003 | | | | 86.33 | 244.87 | 158.54 | 86.65 | 1.83 | 158.06 | 1.82 | 0.48 | 0.01 | |
| | | T21 | 2.0015 | 25.038 | 24.938 | 0.0044 | 43.4 | 5.65 | 24.8 | | | | | | | | | | |
| | | VWC | 2.0318 | 90.381 | 89.84 | 0.0062 | | | | 86.33 | 247.23 | 160.9 | 86.65 | 1.86 | 159.91 | 1.85 | 0.99 | 0.01 | |
| | | BOTTOM | 1.9987 | 94.806 | 93.843 | 0.0105 | 0.84 | 3.94 | 24.8 | 86.34 | 239.56 | 153.22 | 86.65 | 1.77 | 151.63 | 1.75 | 1.59 | 0.02 | |
| | | INTERFACE 1 | 2.0309 | 26.85 | 26.498 | 0.0144 | | | | | | | | | | | | | |
| | INTERFACE 2 | 2.0584 | 39.436 | 38.97 | 0.0126 | | | | | | | | | | | | | | |
| | CRM | TOP EDGE | 2.0084 | 17.074 | 7.0885 | 1.9656 | | | | | | | | | | | | | |
| | | TOP CENTER | 2.0252 | 47.602 | 16.033 | 2.2537 | 0.49 | 3.7 | 24.7 | 86.34 | 184.86 | 98.52 | 86.65 | 1.14 | 30.28 | 0.35 | 68.24 | 0.79 | |
| | | ABOVE | 2.0286 | 20.167 | 8.2066 | 1.936 | | | | | | | | | | | | | |
| | | VWC | 2.0071 | 37.692 | 12.992 | 2.2486 | | | | | | | | | | | | | |
| | | MIDDLE | 2.0227 | 19.957 | 7.5767 | 2.229 | | | | | | | | | | | | | |
| | | T21 | 2.0078 | 18.505 | 7.1583 | 2.203 | 0.63 | 3.81 | 24.7 | | | | | | | | | | |
| | | BELOW | 1.9805 | 32.427 | 12.025 | 2.0311 | | | | 86.37 | 181.06 | 94.69 | 86.65 | 1.09 | 31.24 | 0.36 | 63.45 | 0.73 | |
| | | BOTTOM | 2.0118 | 22.438 | 9.3604 | 1.7796 | 0.57 | 3.77 | 24.8 | 86.35 | 176.58 | 90.23 | 86.65 | 1.04 | 32.46 | 0.37 | 57.77 | 0.67 | |
| | | Axis Translat | 1.7352 | 13.213 | 4.8906 | 2.6374 | | | | 86.32 | 180.99 | 94.67 | 86.65 | 1.09 | 26.03 | 0.30 | 68.64 | 0.79 | |
| | | Axis Translat | 1.6714 | 12.664 | 4.874 | 2.4325 | | | | | | | | | | | | | |
| | | Axis translation sample from column | | | | | | | | 143.84 | 255.04 | 111.2 | 99.28 | 1.12 | | | | | |
| | | Axis translation sample from column | | | | | | | | 86.34 | 183.09 | 96.75 | 86.65 | 1.12 | | | | | |
| | Lower Sand | VWC | 1.6218 | 66.068 | 63.638 | 0.0392 | | | | 41.88 | 106.45 | 64.57 | 39.90 | 1.62 | 62.14 | 1.56 | 2.43 | 0.06 | |
| | | T21 | 1.633 | 30.5 | 29.457 | 0.0375 | 0.62 | 3.81 | 24.8 | 41.87 | 108.36 | 66.49 | 39.90 | 1.67 | 64.09 | 1.61 | 2.40 | 0.06 | |
| | | TOP | 1.6033 | 67.931 | 65.779 | 0.0335 | 0.63 | 3.81 | 24.7 | 41.4 | 104.42 | 63.02 | 39.90 | 1.58 | 60.98 | 1.53 | 2.04 | 0.05 | |
| | | MIDDLE | 1.6221 | 63.295 | 61.721 | 0.0262 | | | | 41.87 | 107.56 | 65.69 | 39.90 | 1.65 | 64.01 | 1.60 | 1.68 | 0.04 | |
| | | BOTTOM | 1.6148 | 67.189 | 64.582 | 0.0414 | 0.54 | 3.75 | 24.7 | | | | | | | | | | |
| | Oxidized Tailings | TOP | 1.6263 | 61.942 | 54.087 | 0.1497 | 0.5 | 3.71 | 24.8 | 41.87 | 102.51 | 60.64 | 39.90 | 1.52 | 52.74 | 1.32 | 7.90 | 0.20 | |
| | | MIDDLE | 1.6241 | 55.248 | 47.965 | 0.1572 | | | | 41.39 | 95.86 | 54.47 | 39.90 | 1.37 | 47.07 | 1.18 | 7.40 | 0.19 | |
| | | VWC | 1.6214 | 58.433 | 50.321 | 0.1666 | | | | 41.87 | 99.3 | 57.43 | 39.90 | 1.44 | 49.23 | 1.23 | 8.20 | 0.21 | |
| | | T21 | 1.6018 | 21.694 | 18.87 | 0.1635 | 0.39 | 3.48 | 24.8 | | | | | | | | | | |
| 15CM | | 1.5916 | 61.949 | 53.069 | 0.1725 | 0.29 | 3.48 | 24.8 | 41.87 | 102.61 | 60.74 | 39.90 | 1.52 | 51.80 | 1.30 | 8.94 | 0.22 | | |
| BASE | 1.615 | 44.179 | 34.038 | 0.3128 | 0.17 | 3.24 | 24.8 | | | | | | | | | | | | |
| B | CRM | Surface | 1.6203 | 19.913 | 17.54 | 0.149 | 15.4 | 5.2 | 24.8 | | | | | | | | | | |
| | | Middle | 1.6155 | 47.518 | 15.281 | 2.3591 | 0.7 | 3.86 | 24.7 | 41.88 | 88.03 | 46.15 | 39.90 | 1.16 | 13.74 | 0.34 | 32.41 | 0.81 | |
| | | VWC | 1.6172 | 49.393 | 17.787 | 1.9547 | | | | 41.88 | 89.94 | 48.06 | 39.90 | 1.20 | 16.27 | 0.41 | 31.79 | 0.80 | |
| | | T21 | 1.6208 | 43.268 | 16.573 | 1.7853 | 0.47 | 3.69 | 24.7 | | | | | | | | | | |
| | | Bottom | 1.636 | 47.449 | 16.474 | 2.0876 | | | | 41.88 | 87.99 | 46.11 | 39.90 | 1.16 | 14.93 | 0.37 | 31.18 | 0.78 | |
| | Interface | 1.6288 | 24.586 | 9.5604 | 1.8944 | | | | | | | | | | | | | | |
| | Oxidized Tailings | Surface/Interface | 1.6289 | 65.068 | 56.34 | 0.1595 | 1.5 | 4.19 | 24.8 | 41.38 | 105.17 | 63.79 | 39.90 | 1.60 | 55.01 | 1.38 | 8.78 | 0.22 | |
| | | T21 | 1.6044 | 23.417 | 20.28 | 0.168 | 0.35 | 3.5 | 24.8 | | | | | | | | | | |
| | | VWC | 1.6051 | 63.5 | 55.154 | 0.1559 | | | | 41.38 | 103.78 | 62.4 | 39.90 | 1.56 | 53.99 | 1.35 | 8.41 | 0.21 | |
| | | 15CM | 1.6379 | 60.246 | 51.813 | 0.1681 | 0.19 | 3.29 | 24.8 | 41.38 | 100.44 | 59.06 | 39.90 | 1.48 | 50.56 | 1.27 | 8.50 | 0.21 | |
| Base | | 1.6286 | 26.618 | 20.889 | 0.2975 | | | | | | | | | | | | | | |
| C | Upper Sand | Surface | 1.3347 | 44.408 | 44.316 | 0.0021 | 184 | 6.28 | 24.6 | 41.38 | 121.17 | 79.79 | 39.90 | 2.00 | 79.62 | 2.00 | 0.17 | 0.00 | |
| | | VWC | 1.3226 | 43.789 | 43.653 | 0.0032 | | | | 41.4 | 114.7 | 73.3 | 39.90 | 1.84 | 73.06 | 1.83 | 0.24 | 0.01 | |
| | | T21 | 1.3435 | 41.775 | 41.653 | 0.003 | 118 | 6.09 | 24.8 | | | | | | | | | | |
| | | Bottom | 1.3362 | 39.524 | 39.259 | 0.007 | | | | | | | | | | | | | |
| | | Interface | 1.3229 | 20.426 | 20.171 | 0.0136 | 4.19 | 4.64 | 24.8 | 41.39 | 118.02 | 76.63 | 39.90 | 1.92 | 75.60 | 1.89 | 1.03 | 0.03 | |
| | CRM | Surface | 1.3134 | 47.165 | 15.429 | 2.2483 | 0.46 | 3.68 | 24.8 | 41.38 | 87.91 | 46.53 | 39.90 | 1.17 | 14.32 | 0.36 | 32.21 | 0.81 | |
| | | VWC | 1.3445 | 44.407 | 13.435 | 2.5615 | 0.77 | 3.9 | 24.8 | 41.39 | 87.07 | 45.68 | 39.90 | 1.14 | 12.83 | 0.32 | 32.85 | 0.82 | |
| | | T21 | 1.3463 | 22.722 | 7.5257 | 2.4592 | | | | | | | | | | | | | |
| | | Bottom | 1.3183 | 45.046 | 15.368 | 2.1124 | | | | 41.39 | 86.17 | 44.78 | 39.90 | 1.12 | 14.39 | 0.36 | 30.39 | 0.76 | |
| | | Surface | 1.3157 | 38.953 | 37.801 | 0.0316 | 0.69 | 3.86 | 24.8 | 70.5 | 136.43 | 65.93 | 35.29 | 1.87 | 63.91 | 1.81 | 2.02 | 0.06 | |
| | Lower Sand | Middle VWC/T21 | 1.3132 | 22.991 | 22.264 | 0.0347 | | | | 41.38 | 105.74 | 64.36 | 39.90 | 1.61 | 62.20 | 1.56 | 2.16 | 0.05 | |
| | | Bottom/Interface | 1.3331 | 27.975 | 27.003 | 0.0379 | | | | 41.38 | 104.81 | 63.43 | 39.90 | 1.59 | 61.11 | 1.53 | 2.32 | 0.06 | |
| | | Surface | 1.3214 | 39.013 | 32.963 | 0.1912 | 0.19 | 3.08 | 24.9 | 41.37 | 107.33 | 65.96 | 39.90 | 1.65 | 55.37 | 1.39 | 10.59 | 0.27 | |
| | FT | VWC/T21 | 1.3234 | 21.875 | 18.572 | 0.1915 | | | | 41.38 | 106.73 | 65.35 | 39.90 | 1.64 | 54.85 | 1.37 | 10.50 | 0.26 | |
| | | 15cm | 1.339 | 34.764 | 28.985 | 0.209 | | | | 41.38 | 113.15 | 71.77 | 39.90 | 1.80 | 59.36 | 1.49 | 12.41 | 0.31 | |
| Base | | 1.3276 | 32.53 | 26.128 | 0.2582 | | | | | | | | | | | | | | |



B – 4 Axis translation tests on Custom Reclamation Mix Biosolids with different initial water contents.

Appendix C – Numerical Modelling Addenda

C-1 Simulated evaporation values



C -2 Example of reduced k_{sat} affecting matric suction and AE/PE ratio.

Biosolids $k_{sat} = 8E-7m/day$

